Prediction of Leakage in Elastomeric Seals for High Pressure Applications

Travis Werner Hohenberger

Submitted in partial fulfillment of the requirements of the Degree of Doctor of Philosophy

The School of Engineering and Materials Science

Queen Mary University of London

327 Mile End Road

London E1 4NS

October 2022

## Declaration

I, Travis Werner Hohenberger, confirm that the research included within this thesis is my own work or that where it has been carried out in collaboration with, or supported by others, that this is duly acknowledged below and my contribution indicated. Previously published material is also acknowledged below.

I attest that I have exercised reasonable care to ensure that the work is original, and does not to the best of my knowledge break any UK law, infringe any third party's copyright or other Intellectual Property Right, or contain any confidential material.

I accept that the College has the right to use plagiarism detection software to check the electronic version of the thesis.

I confirm that this thesis has not been previously submitted for the award of a degree by this or any other university.

The copyright of this thesis rests with the author and no quotation from it or information derived from it may be published without the prior written consent of the author.

Signature:

Date: October 24th, 2022

# Abstract

Elastomeric seals are mechanical devices that are used to prevent the leakage of fluids across a boundary. Most commonly, a leak is driven by differential pressure acting across a seal, and failure occurs due to elastic leak, fracture, or a combination thereof. A pure elastic leak occurs when fluid bypasses a seal without imparting mechanical damage, so when the differential pressure is reduced sufficiently, the device recovers some or all of its sealing capability. When seal fracture occurs, it may be followed by elastic leak of the damaged seal, nearly always with a reduction in the maximum sealing ability. When severe enough, fracture can render a seal completely useless. It is important to understand both failure modes, but rubber fracture has received much more attention in the literature than elastic leak. Hence, this thesis focuses strictly on elastic leak failures.

To reduce cost and development time, it is advantageous to predict elastic leaks during the design process. Some reasonably accurate analytical models to assess sealing performance exist for simple geometries such as O-rings, but non-standard seal configurations are notoriously difficult to design and model. Although the basic operating principles of rubber seals are simple, complexities arise due to many factors such as the tribological conditions, finite deformations, time-dependent mechanical properties, and thermal effects. Thus, custom seal design remains an empirical and iterative process. Some challenges are partially mitigated with numerical techniques such as finite-element analysis (FEA), but the subtleties to accurately simulate fluid leakage are neither well-described nor resolved in the literature.

FEA has been used to simulate seal leakage for at least two decades, but no systematic, comprehensive study of the modelling parameters that affect leak simulations has been disclosed. This thesis closes this gap with numerical sensitivity analyses that consider the following: the hyperelastic material model and its validation; stress relaxation; volumetric compressibility; friction models; mesh sensitivity; contact interactions; static versus dynamic solvers; discretisation of pressures into nodal forces; the fluid pressure penetration algorithm; and the leak criterion. This latter parameter which tells the solver when to propagate fluid pressure from one node to the next is of primary importance in this thesis. Two leak criteria that were previously proposed in the literature are studied.

Researchers have attempted to experimentally validate simulated leak pressures, but there is no comprehensive discussion of the variables that affect test measurements and model predictions. The present work addresses this gap by conducting experimental tests on bonded rubber seals to validate leak simulation studies and provides the following details: the materials tested including their formulations; manufacturing and material model validation tests; justification for critical settings in finite-element models; and potential sources of error in the experimental tests and numerical models. Poor correlations are found between the laboratory and numerically simulated leak pressures. It is argued that the primary source of error is the leak criterion, and it should be the focal point for future validation attempts. An alternative leak criterion, which is yet to be numerically implemented, is proposed for further investigation.

**Details of collaborations:**

**Details of publications:**

T.W. Hohenberger & J.J.C. Busfield, (2022). "A Method to Generate Accurate Elastic and Hyperelastic Uniaxial Tension Stress-Strain Data without an Extensometer". *Rubber Chemistry & Technology*. In press.

R.J. Windslow, T.W. Hohenberger, & J.J.C. Busfield, (2020). "Determination of the Loading Mode Dependence of the Proportionality Parameter for the Tearing Energy of Embedded Flaws in Elastomers under Multiaxial Deformations". In: *Fatigue Crack Growth in Rubber Materials*. *Advances in Polymer Science* **286**. Eds. G. Heinrich, R. Kipscholl, & R. Stocek.

T.W. Hohenberger, R.J. Windslow, N.M. Pugno, & J.J.C. Busfield, (2019). "A Constitutive Model for both Low and High Strain Nonlinearities in Highly Filled Elastomers and Implementation with User-Defined Material Subroutines in Abaqus". *Rubber Chemistry and Technology*, **92** (4), 653-686.

**Details of conference proceedings:**

T. Hohenberger, W. Lan, H. Jin, N. Pugno, & J.J.C. Busfield, (2020). "Numerical leak prediction of elastomeric seals". In *25th International Conference on Fluid Sealing*, Manchester, UK, March 4th–5th, 2020. Ed. A. Bickley. BHR Group, Bedfordshire, UK.

T. Hohenberger, W. Lan, H. Jin, N. Pugno, & J.J.C. Busfield, (2019). "A strain-energy function to model low and high strain non-linearities in highly filled elastomers". In *Constitutive Models for Rubber XI: Proceedings of the 11th ECCMR*, Nantes, France, June 25–27, 2019. Eds. B. Huneau, J.-B. Le Cam, Y. Marco, and E. Verron. CRC Press, Boca Raton, FL.

**Details of conference presentations:**

"The Challenges of Modelling Large Rubber Seals for Oilfield Applications". *PhD Seminar on Rubber Chemistry and Technology*. Lodz, Poland. April 23–25, 2018.

"The Challenges of Modelling Large Rubber Seals for Oilfield Applications". *194th Technical Meeting of the Rubber Division, ACS*. Louisville, Kentucky. October 9–11, 2018.

"Strain Energy Functions for Oilfield Elastomers". *Schlumberger Modelling and Simulation Eureka Workshop*. Katy, Texas. October 16–17, 2018.

"The Challenges of Modelling Large Rubber Seals for Oilfield Applications". *Sealing Material Development for Critical Industrial Applications Forum*. Berlin, Germany. May 16–17, 2019.

"A strain-energy function to model low and high strain non-linearities in highly filled elastomers". *European Conference on Constitutive Models for Rubber XI*. Nantes, France. June 25–27, 2019.

"Numerical Leak Prediction of Elastomeric Seals". *International Rubber Conference 2019*. London, United Kingdom. September 3–5, 2019.

"Numerical Leak Prediction of Elastomeric Seals". *25th International Conference on Fluid Sealing*. Manchester, United Kingdom. March 4–5, 2020.

"Numerical Leak Prediction of Elastomeric Seals". *197th Technical Meeting of the Rubber Division*, ACS. Online Presentation. April 28-30, 2020.

"Preventing Blowouts in Oil Wells through Simulation of Seal Leakage". *3rd Russell Binions Research Symposium*. May 18-21, 2020.

*A mi Pinguina, por atravesar la vida lado a lado.*

*To Theodore, for your incredible patience.*

*To Annelise, for making me smile when I am dark.*

*To my sisters Kacie, Lexi, and Keely, for whom I have always tried to set a good example.*

# Acknowledgements

# Contents

## List of Figures

## List of Tables

## List of Symbols and Abbreviations

The subscripts "1, 2, 3…" are not shown on some symbols, but when used, "1" usually designates a value in an initial (or undeformed) configuration, whereas larger numbers denote values at later configurations. In other instances, the indices map to coordinate directions per the convention $(1,2,3) = (x, y, z)$.

| | |
|---|---|
| $\mathbf{A}$ | an arbitrary tensor |
| $A$ | area, or a model fitting parameter |
| $A_a$ | nominal axial surface area of a uniaxial compression button |
| $\hat{A}_a$ | deformed axial surface area of a uniaxial compression button |
| $A'$ | area of the section of a body after an oblique cut |
| $A_r$ | radial surface area of the perimeter of an equibiaxial tension specimen, or nominal radial surface area around the perimeter of a button in uniaxial compression |
| $\hat{A}_r$ | deformed radial surface area around perimeter of uniaxial compression button |
| $\mathbf{a}$ | an arbitrary vector |
| $a_P$ | TPS shift factor |
| $a_T$ | TTS shift factor for WLF model |
| $a_{T,P}$ | TTPS shift factor for FMT model |
| $\mathbf{B}$ | left Cauchy-Green strain tensor |
| $\mathbf{B}^*$ | auxiliary left Cauchy-Green strain tensor for FE implementation in a VUMAT |
| $\bar{\mathbf{B}}$ | modified left Cauchy-Green strain tensor |
| $\bar{\mathbf{B}}^*$ | modified auxiliary left Cauchy-Green strain tensor for FE implementation in a VUMAT |
| $\bar{\bar{\mathbf{B}}}$ | deviatoric part of the modified left Cauchy-Green strain tensor |
| $B$ | point in space, or a material point in a solid body, or a model fitting parameter |
| $b$ | scaling factor in a Gaussian probability density function for molecular chain length |
| $C$ | circumference of an O-ring |
| $C_1$ | fitting parameter for WLF and FMT models (for TTS & TTPS, respectively) |
| $C_2$ | fitting parameter for WLF and FMT models (for TTS & TTPS, respectively) |
| $C_{ij}$ | coefficient(s) for an incompressible Rivlin-type polynomial expansion SEFs |
| $C_{ijk}$ | coefficient(s) for a compressible Rivlin-type polynomial expansion SEFs |
| $c$ | a constant |
| $c_d$ | dilational wave speed of a material |
| $c_p$ | isobaric specific heat capacity |
| cm | centimetre |
| C=C | carbon-carbon double bond |
| C≡C | carbon-carbon triple bond |
| $D$ | fitting parameter in the DDT SEF |
| $\mathbf{D}$ | rate of deformation tensor |
| $D_1$ | a volumetric compressibility parameter used in Abaqus |
| $d_f$ | deformed diameter of a compression button |
| $d_o$ | initial diameter of a compression button |
| $d$ | diameter |
| dN | decanewton |
| d$Q$ | differential amount of heat transfer |
| d$\mathbf{s}$ | differential line element (a vector quantity) |
| d$V$ | differential volume |
| d$x$ | edge length of a differential volume in the $x$-direction |
| d$y$ | edge length of a differential volume in the $y$-direction |
| d$z$ | edge length of a differential volume in the $z$-direction |
| $\mathbf{E}$ | elasticity tensor for infinitesimal deformations |
| $E$ | Young's modulus |
| $E'$ | storage modulus during uniaxial deformation |
| $E''$ | loss modulus during uniaxial deformation |
| e | Euler's number, the mathematical constant, 2.71828 ... |
| $e_R$ | relative error |
| $\mathbf{F}$ | deformation gradient |
| $\bar{\mathbf{F}}$ | deformation gradient with volumetric contributions removed |
| $\boldsymbol{F}$ | force vector |
| $\boldsymbol{F}_\parallel$ | force vector parallel to the surface of a section after an oblique cut (shear force) |
| $\boldsymbol{F}_\perp$ | force vector normal to the surface of a section after an oblique cut |
| $\mathcal{F}$ | an arbitrary function, particularly in a material (undeformed) reference frame |

| | |
|---|---|
| $F$ | force magnitude |
| $F_a$ | axial force on uniaxial compression button |
| $F_c$ | compressive force on a seal |
| $F_r$ | radial force on the perimeter of an equibiaxial tension or uniaxial compression test specimen |
| $F_{uc}$ | compressive force on a button held in uniaxial compression |
| $F'_{uc}$ | equivalent compressive force on a button held in equibiaxial tension |
| $F_\parallel$ | force magnitude parallel to the surface of a section after an oblique cut (shear force) |
| $F_\perp$ | force magnitude normal to the surface of a section after an oblique cut |
| $f$ | frequency, or a function |
| $f_s$ | shape factor in the Guth-Gold equation |
| $G$ | shear modulus |
| $G_o$ | shear modulus of unfilled rubber in Smallwood and Guth-Gold equations |
| $G^*$ | complex modulus in shear |
| $G'$ | storage modulus in shear |
| $G''$ | loss modulus in shear |
| GHz | gigahertz |
| GPa | gigapascal |
| gm | gram |
| $h$ | thickness of an equibiaxial test specimen, or height of a rectangular seal |
| $h_f$ | deformed height of a compression button |
| $h_g$ | height of a gauge ring that resists extrusion of a seal |
| $h_o$ | initial height of a compression button |
| hrs | hours |
| $\mathbf{I}$ | identity tensor |
| $I_1$ | $1^{st}$ invariant of a stretch or strain tensor |
| $I_2$ | $2^{nd}$ invariant of a stretch or strain tensor |
| $I_3$ | $3^{rd}$ invariant of a stretch or strain tensor |
| $\bar{I}_1$ | modified 1st invariant of a stretch or strain tensor |
| $\bar{I}_2$ | modified $2^{nd}$ invariant of a stretch or strain tensor |
| $\bar{I}_3$ | modified $3^{rd}$ invariant of a stretch or strain tensor |
| $I_A$ | number of iteration attempts in an implicit step in Abaqus/Standard |
| i | summation index, or imaginary unit $(\sqrt{-1})$ |
| in | inch |
| J | Joule |
| $J$ | volume ratio or Jacobian determinate |
| j | summation index, or the rank of an arbitrary tensor |
| $K_i$ | coefficients for the generalised Yeoh strain-energy function, i = (1,2,3) |
| k | summation index, or arbitrary tensor rank |
| $k_B$ | Boltzmann's constant |
| kg | kilogram |
| kJ | kilojoule |
| kN | kilonewton |
| kPa | kilopascal |
| $\mathbf{L}$ | spatial velocity gradient |
| L | litre |
| $L$ | length of a rectangular seal |
| $L_e$ | length of the smallest edge in a finite-element mesh |
| $L_{grip}$ | grip separation in a uniaxial tension test |
| $L_i$ | length of an n-block in a dumbbell |
| $L_T$ | total length of a dumbbell in a uniaxial extension |
| lbf | pounds force |
| $l_m$ | length of idealised molecular units in a polymer chain |
| m | metre |
| $m$ | mass, or a rational exponent in the gen-Yeoh strain-energy function |
| min | minute |
| mJ | millijoules |
| mm | millimetre |
| mol | mole |
| $M_h$ | maximum torque in a rheometer curve |
| $M_l$ | minimum torque in a rheometer curve |
| MPa | Megapascal |
| N | Newton |

| | |
|---|---|
| $N_p$ | number of data points considered in an error calculation |
| n | model order of a strain-energy function |
| $\boldsymbol{n}$ | unit normal vector perpendicular to a planar area |
| $n_m$ | number of idealised molecular units in a polymer chain |
| nm | nanometre |
| $N_c$ | number of chains in a rubber network, or crosslink density |
| $N_p$ | total number of data points considered in an error calculation |
| $O$ | origin of a coordinate system |
| $P$ | hydrostatic pressure, or differential pressure during experimental testing |
| $P_1$ | leak pressure on a bonded rubber seal during its first pressure application |
| $P_{apply}$ | an applied pressure, often equivalent to a fluid pressure |
| $P_{contact}$ | contact pressure |
| $P_{crack}$ | critical pressure at which pressure begins to propagate during a leak simulation |
| $P_f$ | fluid pressure |
| $P_g$ | glass transition pressure |
| $P_{leak}$ | pressure at which fluid leaks past a seal |
| psi | pounds per square inch |
| $P(x, y, z)$ | probability of the end of a molecular chain lying at point $(x, y, z)$ in space |
| $p(x, y, z)$ | probability density governing the location of the end of a molecular chain in space |
| $p$ | a rational exponent in the gen-Yeoh strain-energy function |
| $P\text{-}T_g$ | pressure-glass transition temperature relationship |
| $\mathbf{Q}$ | an orthogonal tensor |
| $q$ | a rational exponent in the gen-Yeoh strain-energy function |
| $\mathbf{R}$ | rotation tensor |
| $R_1$ | concave arc radius on an ASTM dumbbell |
| $R_2$ | convex arc radius on an ASTM dumbbell |
| $R^2$ | correlation coefficient computed in Microsoft Excel |
| $R_a$ | surface roughness parameter |
| $\boldsymbol{r}$ | position vector for: (a) ends of a molecular chain; or (b) material point in a body |
| $r_i$ | radius of a cylindrical dumbbell in an $n$-block model |
| $\boldsymbol{r}_{o,i}$ | vector joining the ends of the i$^{th}$ molecular chain in an undeformed rubber network |
| $\overline{r_o^2}$ | average end-to-end squared vector length of an undeformed rubber network |
| s | second |
| $s_1$ | absolute entropy of an ideal crosslinked molecular chain in an undeformed state |
| $s_2$ | absolute entropy of an ideal crosslinked molecular chain in a deformed state |
| $T$ | temperature |
| $T_g$ | glass transition temperature |
| $T_{ref}$ | reference temperature for WLF and FMT models (TTS and TTPS, respectively) |
| $t$ | time, or thickness of a dumbbell |
| $t_{90}$ | time to achieve 90% cure in a rheometer test |
| $t_{s2}$ | scorch time as defined by a rheometer test |
| $\mathbf{U}$ | right stretch tensor |
| $\overline{\mathbf{U}}$ | modified right stretch tensor |
| $\boldsymbol{u}$ | displacement vector as defined by two position vectors such as $\boldsymbol{r}_1$ and $\boldsymbol{r}_2$ |
| $u$ | displacement in the $x$-direction |
| $u'$ | displacement in the $x'$-direction |
| $V$ | bulk volume of a material |
| $V_f$ | free volume, or final volume of a deformed body |
| $V_o$ | initial volume of a body before a deformation |
| $V_1$ | undeformed volume of an element in a body |
| $V_2$ | deformed volume of an element in a body |
| $\boldsymbol{v}_2$ | velocity field in a spatial (deformed) reference frame |
| $V\text{-}P$ | isothermal volume-pressure relationship of a rubber |
| $V\text{-}T$ | isobaric volume-temperature relationship of a rubber |
| W | Watt |
| $W$ | work applied to a rubber network, or a strain-energy (density) function |
| $W_{iso}$ | distortional (isometric) part of the strain-energy density (function) |
| $W_{vol}$ | dilatational (volumetric) part of the strain-energy density (function) |
| $w_i$ | width of an n-block in a dumbbell |
| $w_i'$ | half-width of an n-block in a dumbbell |
| $x$ | $x$-coordinate |

| | |
|---|---|
| $x_{o,i}$ | undeformed $x$-coordinate of the end of the $i^{th}$ molecular chain in a rubber network |
| $x'$ | direction corresponding to the rotation of an $x$-axis, or $x$-coordinate in a $(\circ)'$ frame |
| $x_\perp$ | $x$-coordinate of intersection of tangent arcs in an ASTM dumbbell |
| $Y$ | height of a cube in simple shear |
| $y$ | $y$-coordinate |
| $y_i$ | vertical location of an n-block in a dumbbell |
| $y_{o,i}$ | undeformed $y$-coordinate of the end of the $i^{th}$ molecular chain in a rubber network |
| $y'$ | direction corresponding to the rotation of a $y$-axis, or $y$-coordinate in a $(\circ)'$ frame |
| $y_\perp$ | $y$-coordinate of intersection of tangent arcs in an ASTM dumbbell |
| $z$ | $z$-coordinate |
| $z'$ | $z$-coordinate in a $(\circ)'$ frame |
| $z_{o,i}$ | undeformed $z$-coordinate of the end of the $i^{th}$ molecular chain in a rubber network |
| | |
| $\alpha$ | biaxiality in a body or finite-element, or a model parameter, or angle joining arc centres |
| $\beta_j$ | fitting parameter in Ogden SEF |
| $\gamma$ | shear strain |
| $\gamma_o$ | initial (instantaneous) shear strain, or peak dynamic shear strain |
| $\gamma_e$ | elastic shear strain |
| $\gamma_p$ | plastic shear strain |
| $\dot{\gamma}$ | shear strain rate |
| $\gamma_\infty$ | equilibrium shear strain |
| $\Delta c_p$ | change in isobaric specific heat through the glass transition temperature |
| $\Delta d$ | cross-sectional compression of an O-ring |
| $\Delta h$ | compression of height in a rectangular seal |
| $\Delta H$ | latent heat of vaporisation |
| $\Delta M$ | difference between maximum and minimum torque in a rheometer test |
| $\Delta Q$ | total change in heat transfer |
| $\Delta S$ | total change in entropy in a thermodynamic system or rubber network |
| $\Delta U$ | total change in internal energy of a rubber network |
| $\Delta W$ | total change in work applied to a rubber network |
| $\Delta s$ | change in entropy in a single molecular chain |
| $\Delta s_i$ | change in entropy of the $i^{th}$ molecular chain in a rubber network |
| $\Delta t_c$ | critical time increment in an explicit finite-element simulation |
| $\Delta \alpha_p$ | change in isobaric thermal expansivity through the glass transition temperature |
| $\Delta \kappa_t$ | change in isothermal compressibility through the glass transition temperature |
| $\delta$ | loss tangent during harmonic excitation, or displacement of a dumbbell in uniaxial tension |
| $\boldsymbol{\varepsilon}$ | infinitesimal strain tensor |
| $\varepsilon$ | nominal (engineering) strain, or average compressive strain in a seal |
| $\varepsilon_a$ | nominal (engineering) axial strain in a compression button |
| $\varepsilon_r$ | nominal (engineering) radial strain in a compression button |
| $\bar{\varepsilon}$ | average strain across an equibiaxial test specimen |
| $\hat{\varepsilon}$ | "equivalent" compression in a laterally constrained O-ring |
| $\Phi$ | an arbitrary scalar |
| $\phi_v$ | volume fraction of filler in a rubber compound or solute in a solvent |
| $\eta$ | (bulk) shear viscosity |
| $\eta_o$ | shear viscosity of pure solvent in Einstein's mixture equation |
| $\kappa$ | bulk modulus |
| $\kappa_1$ | volumetric fitting parameter for a strain-energy function |
| $\kappa_2$ | volumetric fitting parameter for a strain-energy function |
| $\lambda$ | stretch (a measure of strain) |
| $\lambda_a$ | axial stretch in a uniaxial compression button |
| $\lambda_{et}$ | stretch in an equibiaxial extension/tension deformation |
| $\lambda_i$ | principal stretch (i = 1,2,3) |
| $\bar{\lambda}_i$ | modified principal stretch (i = 1,2,3) |
| $\lambda_{max}$ | the stretch at fracture or the maximum stretch in a simulation |
| $\lambda_r$ | radial stretch in a uniaxial compression button |
| $\lambda_T$ | total stretch in a dumbbell during a uniaxial extension |
| $\lambda_{uc}$ | axial stretch in a uniaxial compression deformation |
| $\lambda_{ut}$ | axial stretch in a uniaxial tension deformation |
| $\lambda_{ut.max}$ | the maximum stretch (or stretch at fracture) in uniaxial tension |
| $\lambda_z$ | stretch in the $z$-coordinate direction |
| $\mu$ | coefficient of friction |

| | |
|---|---|
| $\mu_j$ | fitting parameter in Ogden SEF |
| $\mu_{max}$ | peak coefficient of friction in a contact pressure-dependent friction model |
| $\mu m$ | micrometre |
| $\nu$ | Poisson's ratio |
| $\Pi$ | Prigogine-Defay ratio |
| $\pi$ | pi, the mathematical constant, 3.14159 ... |
| $\theta$ | angle defining normal of a section after an oblique cut, or the angle of shear strain, or an angle measured from a horizontal $x$-axis. |
| $\rho$ | mass density |
| $\sigma$ | nominal (engineering) stress magnitude |
| $\sigma_1$ | one standard deviation |
| $\sigma_c$ | contact pressure (or stress) at a sealing interface |
| $\sigma_{c.max}$ | maximum contact pressure (or stress) at a sealing interface |
| $\sigma_{et}$ | nominal (engineering) stress in an equibiaxial tension deformation mode, or nominal radial stress around the perimeter of a uniaxial compression button |
| $\hat{\sigma}_{et}$ | true stress around the perimeter of a uniaxial compression button, or true stress on an equibiaxial tension specimen |
| $\sigma_{pt}$ | nominal stress in a planar extension/tension deformation |
| $\sigma_{i.data}$ | stress measured at index i in a set of data |
| $\sigma_{i.SEF}$ | stress of a strain-energy function at the stretch of data point with index i |
| $\sigma_o$ | initial (instantaneous) shear stress, or a peak dynamic shear stress, or or an initial contact stress |
| $\sigma_u$ | nominal (engineering) stress in a uniaxial tension or compression deformation |
| $\sigma_{uc}$ | nominal (engineering) stress in a uniaxial compression deformation |
| $\hat{\sigma}_{uc}$ | true axial stress on a compression button |
| $\sigma_{ut}$ | nominal (engineering) stress in a uniaxial extension/tension deformation |
| $\hat{\sigma}$ | true stress magnitude, or reduced stress |
| $\boldsymbol{\hat{\sigma}}$ | Cauchy (true) stress tensor |
| $\boldsymbol{\hat{\sigma}}_{co}$ | Cauchy (true) stress tensor in corotational form |
| $\boldsymbol{\hat{\sigma}}_{gn}$ | Green-Naghdi objective stress rate |
| $\boldsymbol{\hat{\sigma}}_{jz}$ | Jaumann-Zaremba objective stress rate |
| $\boldsymbol{\hat{\sigma}}_o$ | spherical part of the Cauchy (true) stress tensor |
| $\boldsymbol{\hat{\sigma}}_{tr}$ | Truesdell objective stress rate |
| $\boldsymbol{\bar{\hat{\sigma}}}$ | deviatoric part of the Cauchy (true) stress tensor |
| $\hat{\sigma}_{et}$ | true stress in a equibiaxial extension/tension deformation |
| $\bar{\hat{\sigma}}_{ii}$ | diagonal component of the matrix representation of the deviatoric true stress tensor |
| $\hat{\sigma}_{ij}$ | component of the true stress tensor |
| $\sigma_\parallel$ | component of shear stress in-phase with peak (dynamic) shear strain |
| $\sigma_y$ | yield strength |
| $\hat{\sigma}_\parallel$ | true stress (shear) magnitude parallel to the surface of a section after an oblique cut |
| $\boldsymbol{\hat{\sigma}}_\parallel$ | true stress (shear) tensor parallel to the surface of a section after an oblique cut |
| $\sigma_\perp$ | component of shear stress 90° out-of-phase with peak (dynamic) shear strain |
| $\hat{\sigma}_\perp$ | true stress magnitude perpendicular to the surface of a section after an oblique cut |
| $\boldsymbol{\hat{\sigma}}_\perp$ | true stress tensor perpendicular to the surface of a section after an oblique cut |
| $[\hat{\sigma}]$ | matrix of the components of the Cauchy (true) stress tensor |
| $[\bar{\hat{\sigma}}]$ | matrix representation of the deviatoric part of the Cauchy (true) stress tensor |
| $[\hat{\sigma}]_o$ | matrix representation of the spherical part of the Cauchy (true) stress tensor |
| $\boldsymbol{\tau}$ | Kirchhoff stress tensor |
| $\tau$ | (stress) relaxation or (creep) retardation time |
| $\phi_v$ | filler or solute volume fraction |
| $\boldsymbol{\Omega}$ | spin (or rate of rotation or vorticity) tensor |
| $\omega$ | number of available microstates in an ideal crosslinked molecular chain |
| $\omega$ | angular frequency |
| | |
| °C | degrees Celsius |
| $\emptyset$ | diameter symbol |
| $(\circ)^T$ | transpose operator |
| $\dot{(\circ)}$ | material or spatial time derivative operator |
| $\det(\circ)$ | determinant operator |
| $tr(\circ)$ | trace operator |
| $D(\circ)/Dt$ | material derivative operator |

Grad(∘)     gradient operator in a material (undeformed) reference frame
grad(∘)     gradient operator in a spatial (deformed) reference frame

## Abbreviations:

2D          2-dimensional
3D          3-dimensional
ACN         acrylonitrile
ALLIE       all internal energy in an Abaqus simulation
ALLSD       all viscous dissipation energy in an Abaqus simulation
ANSI        American National Standards Institute
ASTM        American Society for Testing and Materials
ASME        American Society of Mechanical Engineers
BOP         blowout preventer
BR          butadiene rubber
Buna        butadiene rubber
Buna-N      nitrile rubber, acrylonitrile-butadiene rubber
Buna-S      styrene-butadiene rubber
CB          carbon black
CEL         coupled Eulerian-Lagrangian
CoF         coefficient of friction
CR          chloroprene rubber, DuPrene®, Neoprene®
DDT         Davies-De-Thomas (referring to their strain-energy function)
DOF         degree of freedom
DSC         differential scanning calorimetry
DUT         device under test
EPDM        ethylene-propylene rubber with a diene monomer
ET          equibiaxial extension/tension
FE          finite-element
FEA         finite-element analysis
FEPM        tetrafluoroethylene-propylene rubber, TFEP, Aflas®
FFKM        perfluoroelastomer, Chemraz®, Kalrez®
FKM         vinylidene-hexafluoropropylene rubber, Viton®
FMT         Fillers-Moonan-Tschoegl
FPP         fluid pressure penetration
GEMS        Global Engineering Management System
gen-Yeoh    generalised Yeoh strain-energy function
GR-I        butyl rubber, isobutylene-isoprene rubber
GR-M        chloroprene rubber, DuPrene®, Neoprene®
GR-N        nitrile rubber, acrylonitrile-butadiene rubber
GR-S        styrene-butadiene rubber
GR-X        butyl rubber, isobutylene-isoprene rubber
HNBR        hydrogenated nitrile rubber, hydrogenated acrylonitrile-butadiene rubber
IIR         butyl rubber, isobutylene-isoprene rubber
IPPD        *N*-isopropyl-*N'*-*p*-phenylenediamine
IR          *cis*-polyisoprene rubber
ISO         International Organization for Standardization
LEFM        linear elastic fracture mechanics
LM          Levenberg-Marquardt, in reference to the curve fitting algorithm
NBR         nitrile rubber, acrylonitrile-butadiene rubber
NR          natural rubber
O&G         oil and gas
ODR         oscillating disc rheometer
PDF         probability density function
PDMS        polydimethylsiloxane rubber
PP          polypropylene
PS          polystyrene
PT          planar tension/extension
PTFE        polytetrafluoroethylene, Teflon®
RCT         Rubber Chemistry and Technology, referring to the journal
RGD         rapid gas decompression
SBR         styrene-butadiene rubber

| | |
|---|---|
| SEF | strain-energy or stored-energy function |
| SIC | strain-induced crystallisation |
| TFEP | tetrafluoroethylene-propylene rubber, FEPM, Aflas® |
| TPS | time-pressure superposition |
| T&T | Thomson & Tait |
| TTS | time-temperature superposition |
| TTPS | time-temperature-pressure superposition |
| UC | uniaxial compression |
| UT | uniaxial extension/tension |
| UNC | unified coarse pitch thread |
| VDF | vinylidene-hexafluoropropylene |
| VF2 | vinylidene-hexafluoropropylene |
| WLF | Williams-Landel-Ferry |

# 1. Introduction

## 1.1 Terminology: Elastomers, Rubbers, & Compounds

The terms elastomer, rubber, and compound are used interchangeably in practice, though distinct definitions are given in ISO 1382:2012.[1] They all require an initially amorphous assembly of long polymer chains which, after substantial deformation on short timescales, return roughly to their original shape. Over longer timescales, an **elastomer** exhibits permanent deformation due to plastic flow of molecular chains. A **rubber** on the other hand has chemical crosslinks between polymer chains which impose long-term dimensional stability. A **compound** refers to one or more rubbers mixed with all the ingredients necessary to form a finished product. It can be as simple as one base elastomer and one crosslinking agent, but today even the most basic unfilled compounds have at least 5 ingredients, with perhaps 8 to 15 being typical in filled compounds. Arguably, the word "rubber" does not connote the complexity of a modern compound, but the terms are used interchangeably in this work. The term "elastomer" is reserved for "raw rubber", both referring to an uncrosslinked rubber, be it filled or unfilled. Terminology aside, it is important to recognise that modern compounds are highly engineered elastomeric composites.

## 1.2 Rubber Seals and Their Criticality in the Oil & Gas Industry

As Buchter[2] describes, "seals are mechanical devices used to prevent leakage of liquids, solids, or gases." They come in a wide range of materials and configurations, and numerous parameters must be considered for their selection such as: pressure, temperature, fluid compatibility, and dynamic shaft movements. Common sealing materials include metals, thermoplastics, and rubbers.

Rubbers are ideal sealing materials for several reasons. They impose negligible loads on hard countersurfaces, preventing damage and high maintenance costs. They can readily deform into surface imperfections and cut off leak paths. Being nearly incompressible, they efficiently transform applied fluid pressures into sealing contact pressures. Though their operating principles are simple, rubber seals are notoriously difficult to design. They are subject to complex tribological conditions, geometric variations as loads change, and evolution of mechanical properties with time and temperature. Consequently, seal design is a highly empirical and iterative process for custom seals in the oilfield industry.

Rubber seals are widely used in the oil and gas (O&G) industry. Material design and compound selection are critical in these applications because they affect the longevity and efficiency of downhole equipment where costs may exceed £100,000 per tool. Downhole fluids are harsh and diverse, ranging from acids to bases which may be in aqueous or oil

suspensions. Thermal, mechanical, and chemical ageing are present, and these can all contribute to seal leakage or failure that is concomitant with nonproductive time. For example, a leak in completions equipment[3] for a deep water well may take 6 months to redress. At a production rate of 20,000 barrels a day and assuming £50 per barrel, costs exceed £175M (million) of deferred revenue. However, when it comes to protection of life and environment, the costs are even greater.

The most catastrophic loss in the O&G industry was the blowout of the Deepwater Horizon rig in which 11 lives were lost. The resultant lack of well control dumped an estimated 4.9M barrels of oil into the Gulf of Mexico for 87 days (Fig. 1.1) which brought more than a £15B (billion) settlement, the largest in the industry's history.[4,5] Among the factors that contributed to the failure, the blowout preventer (BOP), which includes a large toroidal rubber seal, did not safely direct wellbore fluids through the drilling string. When it works properly, the BOP reduces the severity and likelihood of an explosion or flare up on the drilling rig. The high flow rate of the well eroded a primary seal in the BOP, resulting in leakage of volatile gas. An explosion ensued, and an emergency-actuated rubber seal in a tool called the variable bore ram was able to temporarily isolate wellbore fluids. However, it eventually failed due to excessive thermal loads.[6] Thus, the loss of the Deepwater Horizon highlights the importance of seals in the O&G industry and the potentially catastrophic consequences of seal failure.



**Fig. 1.1:** Showing 2 out of the 411 controlled burns used to consume approximately 250,000 barrels of the Deepwater Horizon oil spill.[4]

## 1.3 Limitations in the Historical Seal Design Process

Historically, industrial seal design has been trial and error. This is a costly and long process that can stretch across multiple years. To circumvent the time and cost, it is customary to reuse old designs, even if they are not optimised for new applications. This results in low reliability and high failure rates, particularly during development but also in operations. Fig.1.2 illustrates this point where seal related failures dominated test failures during the development of a downhole oilfield tool by the project sponsor.[7] In this case, trial-and-error dominated the design process.
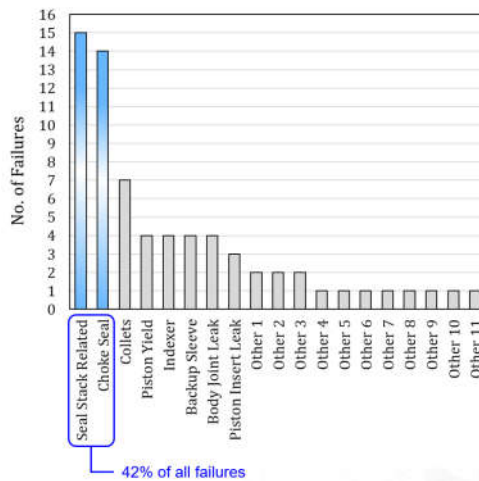
**Fig. 1.2:** Failure modes for a downhole tool used in completions.[7]

## 1.4 The Numerical Simulation of Rubber Seals

To shorten the design lifecycle of seals, finite-element analysis (FEA) is increasingly used during their development. One case study by the project sponsor[8] shortened the development time of packer seals[3] by more than 50% when numerical methods were employed, but knowledge gaps still result in inefficiencies, usually in the form of physical test iterations.

Modules that capture the basic physics of rubber exist in commercially available solvers, and where more advanced physics are essential, user-defined codes can be implemented. One helpful simulation capability, and a focus of this research, is the automation of fluid pressure penetration (FPP) along a sealing interface as leakage occurs. The technique is covered in previous literature where reasonable experimental validations have been achieved. Yet, the author's industrial experience can point to numerous cases where the technique is in gross error. Furthermore, detailed sensitivity analyses on the numerical prediction of seal leakage have not been provided. Thus, it is difficult to determine why results are so varied in industrial and academic literature.

The wide variation in the accuracy of FPP solutions probably arises from too many uncontrolled variables (that is, assumptions) in the models. This makes it impossible to isolate errors due strictly to FPP methods from other parameters. The present thesis strives to close these knowledge gaps by conducting sensitivity analyses on FPP techniques, carefully controlling material and test conditions during leak experiments, and then correlating those physical results to simulated ones. In the end, the goal is to apply the findings of this research to industrial seals, thereby improving seal design methodology and reliability, presumably with benefits to bring efficient use of resources with minimal negative impact on the environment and human life.

As arguments proceed in this work, it is important to highlight a limitation in the scope

of numerical modelling. Many works in rubber research focus on the implementation of non-linear viscoelastic models (see Sections 2.6 and 2.9). These are indeed critical for the general application of seal modelling, but they are difficult to implement in standard engineering practice today. While this point is acknowledged, and modelling errors related to this subject are estimated in later chapters (see Sections 6.5 and 7.4.2), detailed explorations are not pursued here. The idea is to mitigate these effects as much as possible by using unfilled rubber, which minimises viscoelasticity, to isolate and systematically study numerical leak propagation itself. Thus, a simplified sealing material is used to isolate the desired variable. In parallel, a highly filled material is used to understand how much this alters the experimental results which will help focus future research efforts.

## 1.5 Organisation of the Thesis

It is appropriate to begin with a statement of the penultimate finding of this research: experimental leak pressures are bound by numerical predictions that use two different leak criteria commonly employed in the literature, and the measured pressures are far from the limits established by either criteria. Chapter 7 illuminates this finding by comparing experimental leak pressures to numerically simulated ones for bonded rubber face seals that are made from filled and unfilled compounds. The poor correlations could arise from many complexities in rubber mechanics, but efforts are made to systematically rule out the following as primary sources of error:

- the friction model;
- volumetric compressibility;
- numerical discretisation (for instance, the mesh size);
- inelastic effects such as stress relaxation and strain rate sensitivity;
- dynamic effects due to inertia of the deformed seal and elastic instabilities;
- deformation of the test fixture when pressurised;
- asymmetries in the physical test (that is, three-dimensional considerations that are not captured by the two-dimensional analyses).

With these error sources dispelled, it is argued that the discrepancies arise because neither leak propagation criterion is physically correct. Some ideas are proffered that, with further research, could establish a more reliable leak criterion for the numerical simulation of seals.

The arguments in Chapter 7 require some fundamental knowledge of the physics of rubber, and Chapter 2 elucidates this requisite information. A reader skilled in the art of rubber mechanics can skip this early chapter without being lost to the arguments of this thesis. To motivate interest, Chapter 2 often touches on some historical context when it introduces the following technical subjects:

- *The molecular structure of rubber*. This subject accounts for rubber's ability to achieve large elastic deformations and provides the foundation for practically all mathematical models of rubber. The content is not novel, but the presentation is

perhaps unique in its effort to be streamlined and simple without completely sacrificing some important mathematical and thermodynamic concepts.

- *The glass transition*. Building on the molecular structure of rubber, the variation of rubber mechanical properties as a function of temperature is discussed. Using a free volume concept, it is shown that the thermodynamics that underlie the glass transition also result in pressure-dependent mechanical properties, an important consideration for high pressure seals. A summary of how pressure alters the glass transition temperature is provided for several rubbers.

- *The loading mode dependency of rubber*. The stress-strain response of rubber depends on the applied loading mode, and in the general deformation of a component, it is helpful to know which mode is dominant. To this end, biaxiality analysis is introduced, and a novel definition developed by the author and a colleague is shown for a compressible rubber. Additional topics include loading mode equivalencies and some clarifications of planar tension, pure shear, and simple shear loading modes in finite elasticity.

- *Strain-energy functions*. These provide the basis for finite-element modelling of rubbery materials, so they are necessarily introduced.

- *Volumetric compressibility*. Rubber materials are often approximated to be incompressible. This generally accurate assumption leads to significant errors with high pressure seals due to their high level of confinement. Some necessary mathematics are introduced to account for this important effect.

- *Inelasticities and viscoelastic effects in rubber*. To advance some arguments in Chapter 7, it is necessary to introduce how the mechanical properties of rubber change over time and with the load history. Within this context, linear viscoelasticity and reinforcing fillers are presented. A brief section touches on non-linear viscoelastic modelling to illustrate some recent advances in this area.

- *Tensors*. These mathematical objects provide a compact means to express constitutive models for finite elasticity and are used throughout the chapter. Yet, they may be confusing to a novice or casual reader. Therefore, they are introduced with a simple two-dimensional example that is developed by the author. The illustration uses vector and tensor representations of force balance on a bar in uniaxial tension, making it intelligible to students with an elementary understanding of physics. Tensors are also used to present some more advanced topics in non-linear mechanics.

Chapter 3 provides a literature review on the prediction of leakage in elastomeric seals. Analytical, experimental, and numerical techniques are discussed, but emphasis is given to the latter.

Chapter 4 discusses novel contributions to the general research of rubber. These contributions are not explicitly related to the study of seal leakage. Content includes:

- a novel strain-energy function that is suitable to capture both low- and high-strain non-linearities in the stress-strain response of rubber sealing materials that have a high content of reinforcing filler.

- a novel method to accurately predict the stress-strain response of a uniaxial tension specimen when strain cannot be directly measured on the test sample. Although this is somewhat of a tangential topic to the thesis, it is the author's favourite output.

The theory to develop the technique has been available since at least the 1940s, yet it has not been previously proposed.

Chapter 5 studies how different model settings affect leak pressures in the commercially available finite-element solver Abaqus. This thesis appears to be the first publicly disclosed in-depth sensitivity analysis of numerically simulated leak pressures. A two-dimensional axisymmetric bonded face seal is used for all cases. Some topics that are studied include:

- surface interaction models with constant and contact pressure-dependent coefficients of friction. The latter are shown to be more physically realistic and numerically stable.

- different schemes for propagating pressure along a sealing interface. Default schemes in Abaqus are used before presenting two user-defined subroutines with implicit and explicit solvers. This work appears to be the first public disclosure of full codes for pressure penetration in Abaqus. It also provides the first demonstration of automated pressure penetration in Abaqus/Explicit.

- the impact of the finite-element mesh on leak pressures. This includes sensitivities to mesh sizes and shapes. Similar results are found with structured and unstructured quadrilateral meshes. In addition, a small fraction of triangular elements (which are known to be overly stiff for rubbery materials) can be introduced to simplify the generation of a structured mesh without adversely affecting model accuracy.

- the use of biaxiality and strain analyses to ensure appropriate curve fitting of a hyperelastic material model.

- the impact of the seal compression and the extrusion gap on leak pressures. Leak pressures increase as the former increases and the latter decreases.

- the impact of volumetric compressibility on leak pressures. A stiffer volumetric response usually results in higher leak pressures.

Chapter 6 presents an experimental test fixture that is based on the axisymmetric geometry in Chapter 5. Bonded seals made from unfilled and filled rubber formulations are introduced. The former minimises the complications of viscoelasticity, and the latter is more representative of an oilfield sealing material. The materials are characterised in planar tension and uniaxial compression, and stress relaxations are reported. A hyperelastic material model is fit for each material, and the models are validated by comparing experimental compression tests to finite-element studies. Next, experimental tests measure leak pressures for the seals with different compression ratios and extrusion gaps. The results are compared to FPP simulations in Chapter 7, and an alternative leak criterion is proposed for future investigation. Chapter 8 provides guidelines – substantiated by the author's research – for simulating seal leakage with FPP techniques in finite-element analysis. The thesis closes by giving a rational basis for adopting the alternative leak criterion that is suggested in Chapter 7.

## 2. Historical and Theoretical Foundations

### 2.1 Some Historical Notes

In England, unvulcanised rubber originally inherited the French name *caoutchouc*. Likely a derivative of the Amerindian word *cauchu* for "weeping wood", the name befits the trees whose excised bark brings discharge of rubber latex, a viscous liquid (Fig. 2.1). Having origins in the West Indies, the English name evolved to "India rubber" or "rubber", most likely due to the material's ability to remove pencil marks.[9,10,11] Without naming the object, Joseph Priestley briefly pointed to an eraser's utility which he presumably learned from a London shopkeeper in 1770,[12] who may have adopted the idea from France.[13]

Chartered by Spain, Italian chronicler Pietro Martyre d'Anghiera gave the first written account of rubber in 1511,[14] and over the centuries numerous authors have added to this.[9] They indicate that indigenous Mesoamericans made the first practical use of elastomers, and modern evidence dates the use as far back as 1600 B.C.[15] For example, numerous rubber sports balls have been found (Fig. 2.2) as well as stone tools hafted with rubber bands. Hosler and colleagues write that latex from *Castilla elastica* trees was combined with a liquid extract from the morning glory vine *Ipomoea alba*, presumably freeing latex from proteins to promote the formation of small quasi-stabilising crystalline lamellae.[16] Heat used in forming processes may have promoted light crosslinking of sulphur moieties, though gradual cold flow was probably not entirely eliminated.[17]



**Fig. 2.1:** Latex extraction from a tree.[18]



**Fig. 2.2:** Rubber ball artifact from southern Sinaloa; diameter ≈20 cm; mass ≈3 kg.[19]

Raw rubber from trees in the Amazon (*Hevea brasiliensis*) was sent to the French *Académie des Sciences* by Charles Marie de la Condamine in 1736,[11] but plasticity limited its practical use and commercial demand. Regardless, a notable early application was leak-proofing fabric which found its way into clothing and manned balloon flights in the early 1780s. The 1800s brought more profitable developments. In 1821, the English entrepreneur Thomas Hancock developed the world's first masticator, a machine that mechanically

consolidated raw rubber to improve manufacturability and reduce waste (Fig. 2.3). In 1839, Charles Goodyear discovered sulphur vulcanisation (that is, crosslinking), practically eliminating plasticity and low temperature embrittlement. Tangentially, the material's foul odour was also mitigated. By 1844, Hancock had also vulcanised rubber, but his independent conception of the idea is disputed.[9] Regardless of its origin, vulcanisation created innumerable possibilities for new rubber products (Fig. 2.4).



Fig 2.3: One of Thomas Hancock's original masticators. (Adapted from Tunnicliffe.)[20]
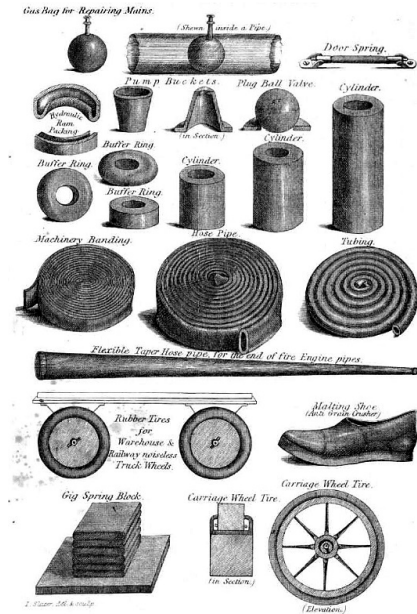


Fig 2.4: A small number of rubber articles. suggested by Hancock.[21]

Rubber manufacturing developed during the Industrial Revolution, but early latex extraction remained pre-industrial for decades, often at catastrophic human and ecological expense. Extraction during the years 1890-1910 was dominated by the British in the Amazon and the Belgians in the Congo. Unsustainable tapping, economic inefficiencies, and growing demand pushed latex harvesting to rubber plantations in Asia. This transition was enabled in 1876 when Henry Wickham smuggled Amazonian seeds to London's Botanical Gardens in Kew.[22] After decades of haphazard depletion coupled with plantation tree disease in the Amazon, Asian rubber became the dominant material by 1914.[9]

One technical improvement and two wars in the 1900s had exceptional impacts on rubber history. In 1904, the Englishman S.C. Mote[23] introduced carbon black (CB) as a reinforcing filler, dramatically improving rubber's mechanical properties. Later, the world wars mandated development of synthetic rubber on both sides of the Atlantic. Germany successfully synthesised rubber in 1909, but it was largely unused until the country lost access to African and Pacific colonies during World War I. However, the material was mechanically inferior to natural rubber and took up to six months to produce. By 1918, shortcomings in rubber supply undoubtedly contributed to Germany's surrender.[9,22]

In the 1930s, Adolf Hitler recognised that rubber was no less critical than oil or steel to a modern military, yet Allied powers controlled more than 90% of the world's rubber supply. Therefore, he incentivised the German chemical company IG Farben to provide his war machine with synthetic rubber, by then a commercially viable but specialty product. Despite their monopoly on natural rubber, the Allies were severely hamstrung in 1942 when Japan's Pacific campaign put a stranglehold on 80% of the world's rubber supply. Germany was unable to capitalise on this Axis windfall because transfer through Russia and the Indian subcontinent was impossible, and an Allied naval blockade held the sea. The U.S. was inexorably forced to produce synthetic rubber, initially finding itself behind its German counterpart. Interestingly, the U.S. company Standard Oil had signed intellectual property agreements with IG Farben as the Nazi regime came to power, gaining access to synthetic rubber technology through a contentious, if not embarrassing, avenue.[24,25] After the war, natural rubber maintained its commercial importance but lost its exclusivity. The post-war demise of direct colonialism also moved control of rubber production to native governance, or in some cases multi-national corporations.[9]

In summary, humans have used rubber for millennia. Mesoamericans successfully extracted and used the raw material, at some point introducing a stabilising agent that mimicked crosslinking. From the mid-19th century, advances in rubber technology have been propelled by ingrained entrepreneurship and extant socioeconomic circumstances in the West. This success was contingent on scientific advancement in the fields of rubber chemistry and physics, subjects to which the remainder of this work is dedicated.

## 2.2 The Molecular Structure and Vulcanisation of Rubber

Hydrocarbons are the building blocks of most common rubbers, so some terminology regarding them is useful. **Aliphatic** hydrocarbons are acyclic (no ring structures) and consist only of carbon ($C$) and hydrogen ($H$) atoms.[26] **Saturated** acyclic hydrocarbons are called **alkanes** and contain no carbon-carbon double or triple bonds ($C=C$ and $C\equiv C$). **Unsaturated** hydrocarbons contain $C=C$ or $C\equiv C$ bonds and are called **alkenes** (or **olefins**) and **alkynes**, respectively. The suffix **-diene** is attached to alkenes with exactly two sets of $C=C$ bonds. A **vinylic** carbon atom is directly involved in a double bond, whereas an **allylic** carbon atom does not directly participate in a double bond but is adjacent to a vinylic carbon.[27] For example, in the molecule $H_2\mathbf{C}=\mathbf{C}H-CH_2-CH_3$, the carbons in bold are vinylic, the carbon in red is allylic, and the last one is neither. The two red hydrogen atoms are also called allylic. Single bonds are called **σ-bonds** (the gray bonds in Fig. 2.5). Double bonds (the red bonds in Fig. 2.5) consist of one σ-bond and one **π-bond**. The latter prevents rotation about the bond axis but is weaker than the σ-bond. (Note: The bond structure is simplified here; see Morrison & Boyd[27] for a more accurate representation of the electron

orbitals.) Finally, **isomers** are molecules with the same molecular formula but different structures.



$$\left\{ \begin{array}{c} \begin{array}{cccc} H & H & H & H \\ | & | & | & | \\ C - C & = C - C \\ | & & & | \\ H & & & H \end{array} \left. \begin{array}{cccc} H & H & H & H \\ | & | & | & | \\ C - C & = C - C \\ | & & & | \\ H & & & H \end{array} \right. \end{array} \right\}$$

**(a)**            **(b)**            **(c)**

**(d)**
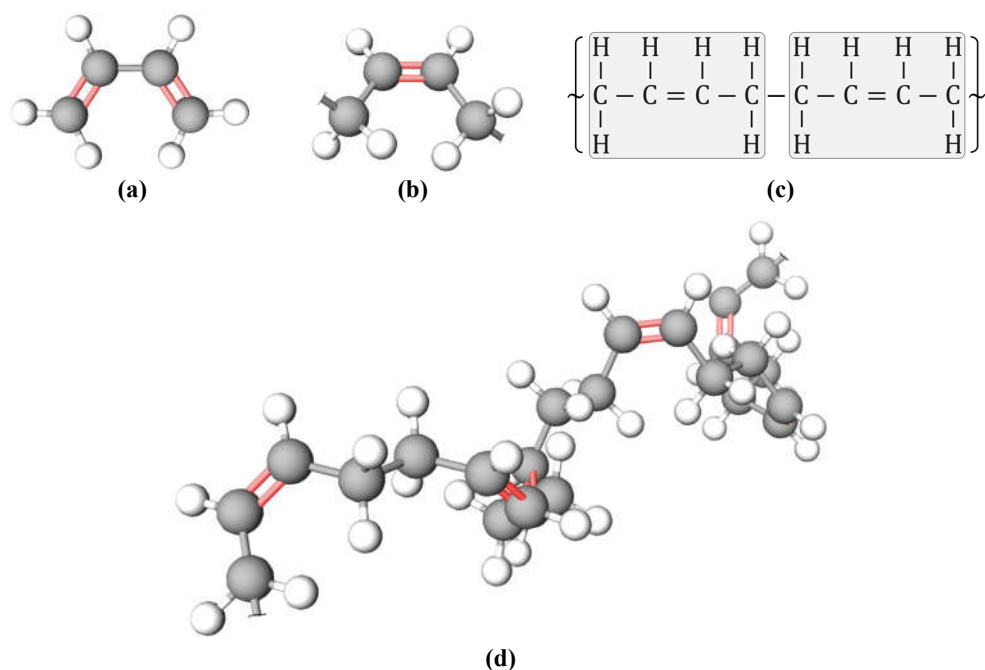
**Fig. 2.5: (a)** Butadiene molecule (an uncommon isomer is used for illustration). **(b)** *cis* - butadiene monomer. **(c)** Molecular formula for *cis* - polybutadiene with 2 monomers shown. **(d)** One possible orientation of 6 butadiene monomers after polymerisation. ● = C , ○ = H.

To illustrate the molecular structure of rubber, consider butadiene rubber (BR). It is synthesised from butadiene molecules ($C_4H_6$) (Fig. 2.5a). A polymerisation reaction converts the base units into butadiene monomers (Fig. 2.5b) and then joins them to form a macromolecule with the formula in Fig. 2.5c. Fig. 2.5d shows one possible arrangement of six polymerised monomers generated with the application Molview.[28] The carbon atoms in the butadiene molecule, butadiene monomer, and all the constituent monomers of the polymer are geometrically planar; however, the structure of the polymer chain backbone is 3-dimensional (3D). Importantly, the C=C bonds in the monomers are preserved in the polymer, and the two ethylene ($CH_2$) groups associated with any single monomer are on the same side of that monomer's C=C bond to give a ***cis***-configuration. The ***trans*** -configuration would occur if the two $CH_2$ groups were on opposite sides of the C=C bond.

A butadiene elastomer is an amorphous assembly of randomly oriented polybutadiene molecules. To illustrate some properties that arise from these arrangements, consider three idealised polybutadiene chains in which each 10-atom monomer is represented by a single sphere with adjacent spheres connected by σ-bonds (Fig. 2.6a). The chains are initially entangled but do not interfere with one another. When an external force is applied, they interfere and resist deformation (Fig. 2.6b). In the presence of interference, it is assumed that the bond length and angle between any sphere and its two adjacent spheres is fixed, a reasonable approximation per energetic considerations of stereochemistry.[29] Finally, also

assume that rotations around the axes of σ-bonds can occur unimpeded. (Note that σ-bond rotations do not alter the bond angles between any three adjacent spheres.) These constraints allow molecular rotations to disentangle the chains when loaded, causing plastic flow in the bulk elastomer.



**(a)**



**(b)**
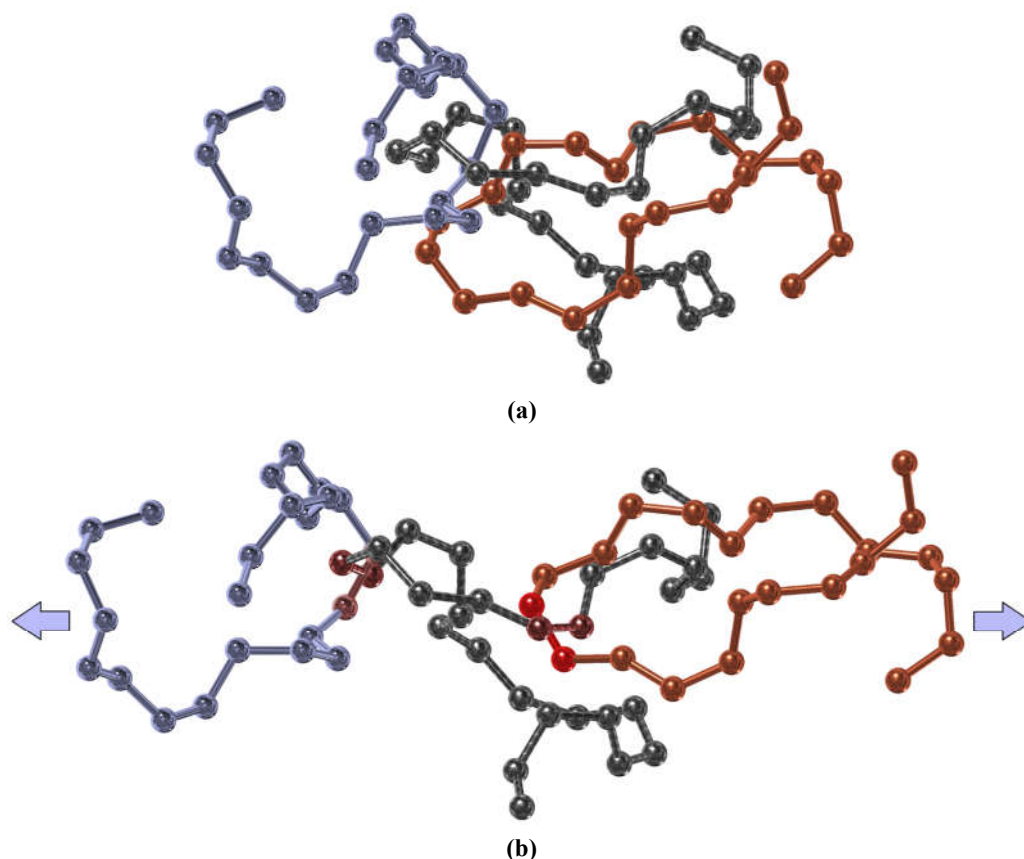
**Fig. 2.6:** Physical entanglement of 3 idealised polybutadiene molecules: **(a)** with no external force applied; **(b)** with an external force applied (a red hue accents the bonds that interfere). (Note: the illustrated molecules are orders of magnitude shorter than actual polymer chains.)

On short timescales, an assembly of chains as shown in Fig. 2.6 can exhibit rubber-like elasticity because they cannot instantaneously disentangle, but to achieve long-term stability they must be crosslinked in a process called **vulcanisation** (or **curing**).[*] To illustrate, consider Fig. 2.7a which shows the exact same chain configuration as Fig. 2.6a with several molecules removed for clarity. The yellow molecules represent the addition of covalently bonded links that join the red and blue chains to the black chain to form a connected network. When deformed, the individual chains can reorient via rotation, but they cannot completely separate unless fracture occurs. For example, consider a tensile load applied to the left-most (blue) and right-most (red) monomers. Fig. 2.7b shows only those monomers along the connected load path. Upon deformation, the bonds rotate to the configuration in Fig. 2.7c. In this deformation, the connected chain exhibits three key

---

[*] Vulcanisation refers specifically to sulphur crosslinking, making it a subset of the more general curing processes. In industrial contexts, the terms are often used informally and interchangeably.

features of rubber elasticity: (i) the length of a vector connecting the ends of the chain along the load path undergoes a large increase in length, here about a factor of two; (ii) the load required to impose the deformation is low because rotation about σ-bonds is relatively unrestricted; and (iii) the crosslinks prevent the chains from completely separating. The first point arises from the imposition of finite (that is, non-infinitesimal) deformations. The second point gives rubber much lower stiffness than most solids of practical interest. The third point prevents complete molecular disentanglement of the rubber, an inevitability in its elastomeric counterpart under a constant load.



**(a)**

**(b)**

**(c)**
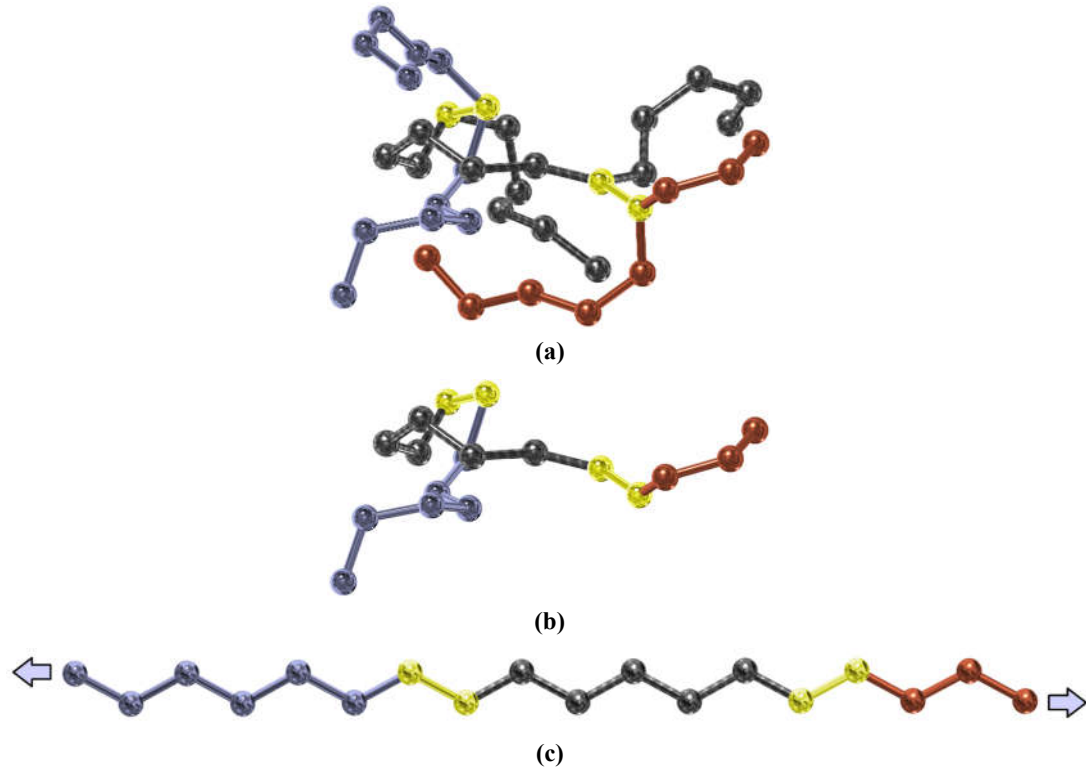
**Fig. 2.7:** Idealised polybutadiene molecules with two crosslinks (yellow) after vulcanisation: **(a)** with no load applied to the network; **(b)** with only the load path monomers shown before deformation; **(c)** with only the load path monomers shown after deformation. (Note: the illustrated molecules are orders of magnitude shorter than actual polymer chains.)

One last feature is essential for the chain in Fig. 2.7c to exhibit rubber-like elasticity. There must be an internal force to restore the network chain to its initial configuration after the load is removed. In most deformed solids, such force arises from an increase in internal energy due to stretching of molecular bonds, but changes in the polymer bond lengths and angles have been proscribed as outlined above. Hence, a different mechanism must drive retraction of the polymer chain. Section 2.5.1 shows in detail that the restoring force arises from entropy. For the moment, a qualitative description ensues.

When the network chain in Fig. 2.7 extends, it changes from a disordered state to an ordered state, and hence its entropy reduces. However, entropic processes naturally seek to maximise disorder. Since stretching moves the polymer away from innate disorder, nature

creates an entropy-based restoring force in the chain. The disposition of polymeric molecules toward maximum disorder is in stark contrast to that of smaller molecules. In the latter, organised (or at least somewhat predictable) atomic arrangements are typical due to nature's tendency toward energy minimisation. On the other hand, unvulcanised and vulcanised polymer chains commonly range from $10^3$-$10^5$ and 75-185 monomers, respectively, which themselves may contain additional degrees of freedom (DOFs) via embedded σ-bonds.[30] This creates a molecular system with practically unlimited DOFs, so entropic principles inescapably drive polymers toward random, disorganised configurations in much the same way that gas molecules randomly distribute in a room. It is important to emphasise that polymer chains do not ignore or violate any energetic principles, but entropic considerations override energetic ones where rubber elasticity is concerned.

Next consider the vulcanisation process in some detail. It commonly involves mixing rhombic sulphur ($S_8$) in an elastomer and exposing it to temperatures of 140-170°C.[30] Initially, the heat reduces the mixture's viscosity to allow forming operations, typically under pressure to fully consolidate the material and eliminate gas voids. Intermediate chemical reactions in vulcanisation are still not fully understood, but the end result is formation of sulphur bridges between carbon atoms. Fig. 2.8 shows two sections of butadiene chains joined with a disulphidic crosslink, though more bridging atoms are possible. The bridges are formed by hydrogen substitution at allylic carbon atoms (dark gray), leaving bonds at vinylic sites (light gray) undisturbed. Replacement of allylic hydrogen instead of vinylic hydrogen is easily understood because the former has a lower bond dissociation energy, 360 kJ/mol versus 430 kJ/mol, respectively.[27,31] More curious is the reaction's preference for substitution of allylic hydrogens instead of addition at C=C bonds. Although the total strength of the C=C bond is 680 kJ/mol, the strength of the π-bond is only 285 kJ/mol. At least two factors probably promote allylic substitution instead of vinylic addition: resonance theory and the conditions of vulcanisation. The former refines the concept of fixed σ- and π-bonds in the carbon-carbon backbone with **hybrid bonds** of intermediate strength that are presumably stronger than allylic hydrogen bonds. Regarding the conditions of vulcanisation, high temperatures favor allylic substitution reactions over vinylic addition.[27]
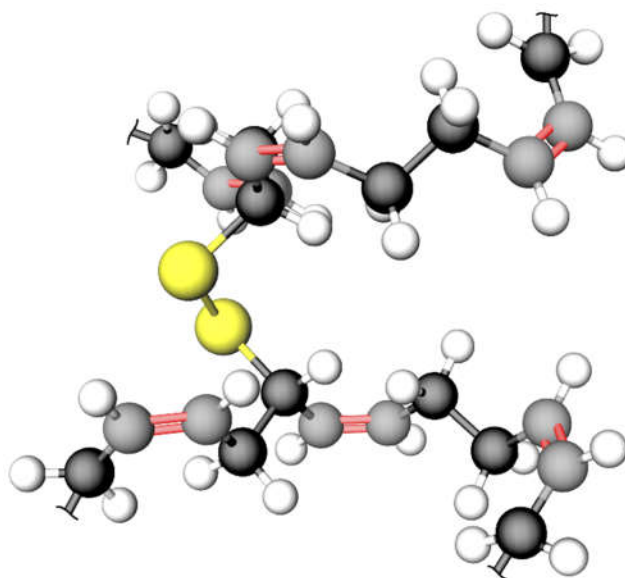
**Fig. 2.8:** Two butadiene chain sections crosslinked by two sulphur atoms at allylic carbons. ● = C (vinylic) , ● = C (allylic) , ○ = H , ● = S.

Sulphur vulcanisation is inefficient and time consuming (5 hrs @ 140°C).[32] The resulting network consists of polysulphidic linkages, dangling fragments, and cyclic sulphides, some of which do not participate in crosslinks at all. The network is also prone to thermal and chemical degradation. To mitigate these problems, all practical compounds use an accelerator, typically an organic base, to impart several benefits: (i) a reduction in curing time by 1-2 orders of magnitude; (ii) higher crosslinking efficiency and hence a reduced quantity of sulphur; and (iii) shorter crosslinks for better network stability. The ratio of accelerator to sulphur controls the character of crosslinks. A high ratio creates shorter crosslinks thereby improving thermal stability and resistance to permanent set. A lower ratio gives longer crosslinks that have more sulphur bonds with the ability to reconfigure across network chains after a deformation. That is, the crosslinks are more labile which enhances fatigue resistance and ultimate strength due to a network repair mechanism.[33]

To reduce the activation energy for crosslinking, zinc oxide (ZnO) and a fatty acid such as stearic acid are often used. These permit curing to take place at lower temperatures which reduces thermal degradation.[31] Activators, the accelerator, and sulphur comprise the curing system of a compound. An anti-degradant is usually incorporated. Ozone readily attacks the C=C bond, and oxidation induces undesired crosslinking at allylic carbons.[33] Both issues are mitigated with *N*-isopropyl-*N*′-*p*-phenylenediamine (IPPD).[32] The elastomer, a curing system, and an environmental anti-degradant make up the five essential ingredients in sulphur vulcanised diene rubbers of practical interest.

Peroxides may be used instead of sulphur to cure elastomers. Crosslinking proceeds by splitting a peroxide (ROOR, where R represents a functional group) at its O-O bond to

generate two free radicals, $ROOR \rightarrow RO\cdot + \cdot OR$, which abstract (remove) hydrogens from polymer chains. The abstraction leaves open bonds at carbon sites that can join to form crosslinks.[34] The benefits of peroxide curing are: (i) the stoichiometric efficiency is at or near one in some rubbers, resulting in negligible non-network material; (ii) $C$-$C$ bonds are more stable than $C$-$S_n$-$C$ bonds which gives better resistance to temperature and permanent set; and (iii) saturated elastomers can be crosslinked because the reaction does not require double bonds. Ultimate strength and fatigue resistance are typically lower in peroxide cured diene rubbers. Refer to Dluzneski[34] for more details on this subject.

## 2.3 The Glass Transition

Before explaining the glass transition in polymers, it is helpful to review the definition of entropy in classical thermodynamics.[35] For simplicity, consider a $1^{st}$-order transition or phase change from gas to liquid. The change in entropy can be written as:

$$\Delta S = \int \frac{dQ}{T} = \frac{\Delta Q}{T} = -\frac{m \Delta H}{T} \qquad (2.1)$$

where $dQ$ is the incremental heat transfer, $T$ is the absolute temperature, assumed constant, during the phase change, $m$ is the mass of the material, and $\Delta H$ is the latent heat of vaporisation. Consistent with the definition of entropy, it is assumed that the integration path is reversible. The negative sign arises because condensation is an exothermic process. Consequently, cooling through a phase change reduces the entropy of a material.

When cooling in the absence of a phase change, Eq. 2.1 can be expressed as:

$$\Delta S = \int \frac{dQ}{T} = \int_{T_1}^{T_2} \frac{mc_p}{T} dT = mc_p \ln\left(\frac{T_2}{T_1}\right) \qquad (2.2)$$

where $c_p$ is the isobaric specific heat capacity (assumed constant) of the material, and $T_1$ and $T_2$ are the initial and final temperatures. Since $\ln(T_2/T_1) < 0$, Eq. 2.2 also gives a negative entropy. From a statistical mechanical perspective, this implies that cooling processes generally reduce the number of microstates available for a material, a fact with significant implications for rubber elasticity which requires accessibility to a large number of microstates. A question arises: can a cooling process reduce sufficiently the number of available microstates in a rubber such that its entropic elasticity is practically eliminated? Theoretical arguments and experimental evidence suggest "yes", and the concept of free volume is helpful to understand this.

**Free volume** ($V_f$) is the empty space between molecules which, when added to the molecular volume, comprises a material's bulk volume ($V$). The actual existence of free volume is inferred from dissolution of polymers in solvents which reduces the total volume of the polymer-solvent system.[36] Sufficient free volume permits a high degree of molecular mobility, enabling the large configurational changes necessary for rubber elasticity. As $V_f$ decreases, macromolecular motion is increasingly hindered which reduces the number of

microstates available to the molecules. Taken to its theoretical limit, the molecular positions relative to one another can be completely constrained to a single microstate leading to $\Delta S \approx 0$. In such a thermodynamic state, entropic elasticity becomes negligible, and large scale elastic deformations are impossible. Elastic behavior then reverts to its more familiar thermodynamic driver, internal energy.

Experimental evidence and theoretical arguments suggest that entropic elasticity is practically eliminated at a free volume well above $V_f = 0$.[36,37,38] This critical free volume is estimated to be between 2.5–12% of the bulk volume. It determines the material's **glass transition** which is the point when the polymer network rapidly (but smoothly) changes from a rubbery to a glassy state. The glass transition is usually determined from bulk properties, for instance, with dilatometry to give isobaric volume–temperature ($V$–$T$) or isothermal volume–pressure ($V$–$P$) plots. Fig. 2.9 shows a $V$–$T$ plot for uncured natural rubber where the **glass transition temperature** ($T_g$) is defined at the intersection of two linear regions. The slopes are the material's thermal expansivities above and below $T_g$. When cooling the rubber through the transition, the free volume reaches a critical limit that severely impedes chain mobility, significantly reducing the rubber's thermal expansivity. In a similar manner, a $V$–$P$ plot reveals the **glass transition pressure** ($P_g$) (Fig. 2.10). Here the slopes are compressibilities which reduce as pressure increases. Although $T_g$ and $P_g$ are both consequences of volumetric constraint, the glass transition is more distinct in the $V$–$T$ plot. The reason for this is not fully clear but is thought to arise because temperature alters molecular energies and free volume, whereas pressure primarily affects only the latter.[39,40,41]
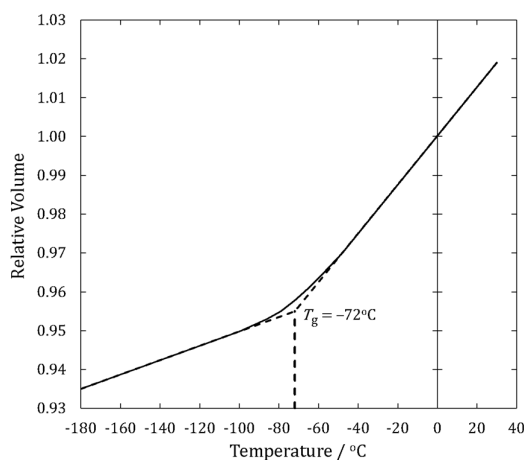


**Fig. 2.9:** Isobaric $V$-$T$ plot to determine $T_g$ for unvulcanised natural rubber. Relative volume is unity at 0°C. (Adapted from Bekkedahl.)[42]
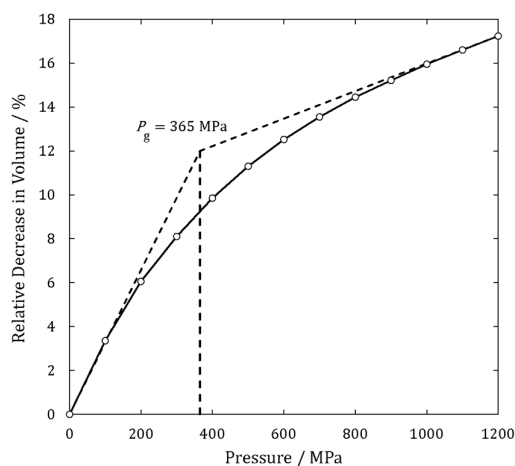
**Fig. 2.10:** Isothermal $V$-$P$ plot to determine $P_g$ for vulcanised natural rubber. The intersection of two linear extrapolations defines $P_g$. (Adapted from Adams & Gibson.)[43]

Other thermodynamic properties such as entropy and enthalpy undergo abrupt changes through the glass transition. In addition, mechanical properties change significantly. For example, the shear modulus of a polymer can increase by a factor of $10^3$ through the glass

transition.[44] Consequently, $T_g$ can be measured with many techniques including thermal analysis,[45] ultrasonic excitation,[46] dielectric measurement,[39] nuclear magnetic resonance imaging,[47] stress-strain measurement,[48] and rebound resilience.[49] Different methods give different $T_g$s, but many agree within $\pm 5°C$ when measurement timescales are properly controlled. Rebound resilience is a notable exception with reported $T_g$s $\approx 30°C$ higher due to the test's inherently high strain rate and a corresponding short timescale.[50] This effect is not exceptional; it is expected as discussed in Section 2.6.3.

Research suggests that the glass transition is a reversible change in thermodynamic phase,[36] but it has several differences from more common state changes such as condensation and solidification. Thermodynamic properties are continuous and smooth through the glass transition, whereas they usually show step changes during phase transitions. Accordingly, there is negligible latent heat associated with the glass transition, and X-ray diffraction reveals that the network structure remains amorphous.[50] Therefore, it is often called a $2^{nd}$-order transition, though this terminology is not strictly accurate. If it were a true $2^{nd}$-order transition, the glass transition would satisfy the relation:[51]

$$\Pi = \frac{\Delta c_p \Delta \kappa_t}{T_g (\Delta \alpha_p)^2} = 1 \tag{2.3}$$

where $\Pi$ is the Prigogine-Defay ratio. $\Delta c_p$, $\Delta \kappa_t$, and $\Delta \alpha_p$ are the changes in isobaric specific heat, isothermal compressibility, and isobaric thermal expansivity, respectively, through the glass transition. Eq. 2.3 expresses a relationship between entropy (through $\Delta c_p$, see Eq. 2.2), internal energy (through $T_g$), and volume (through $\Delta \kappa_t$ and $\Delta \alpha_p$). When $\Pi = 1$, fluctuations in entropy and volume are coupled which allows the thermodynamic state to be completely defined by a single parameter. However, measurements on polymers through the glass transition show $1 < \Pi < 5$.

A rubber (and a polymer in general) that is cooled through its glass transition is not actually in thermodynamic equilibrium. Consequently, the glass transition is best determined with cooling experiments because heating can prematurely convert a glassy polymer to rubber, giving a fictive indication of the state change.[52] In addition, measurements of $T_g$ and $P_g$ depend on the measurement timescale. For example, increasing the interval between measurement times when constructing a $V-T$ plot shifts $T_g$ lower because the longer timescale allows more reconfiguration of molecular chains, a phenomenon called **physical ageing** or **relaxation**.[53] This relaxation occurs well below glass transition temperatures that are based on practical timescales. In fact, some research postulates that experimentally determined $T_g$s are 50–55°C higher than the true $T_g$ where thermodynamic equilibrium is achieved.[36,37,38] These theories suggest that the entropy of a molecular network becomes zero far above absolute zero which violates the third law of thermodynamics, an unresolved issue known as the Kauzmann paradox.[51] Testing these

theories has proven intractable because the timescales to achieve thermodynamic equilibrium in glassy macromolecular networks are on the order of decades, if not longer.[44,51,53]

Although glass transition temperatures and pressures do not represent true thermo-dynamic transitions, they are critical for practical purposes because they define the threshold at which rubbery behaviour ceases. For sealing applications, they establish a material's low temperature and high pressure limits. This is especially critical in arctic and deepwater oilfield applications where high pressure at sub-zero temperatures may be simultaneously encountered. To best assess seal functionality, one must know how pressure alters the glass transition temperature ($dP/dT_g$) (Fig. 2.11). There is limited data on the combined effects of pressure and temperature on the glass transition, but Table 2.1 shows several $T_g$s and some $dP/dT_g$s for rubbery materials. (See the List of Symbols and Abbreviations section for full material names and Section 2.4 for more details on each rubber.) For most materials, $T_g$s are averaged from multiple sources with no differentiation between cured and raw rubber. Differences in measurement technique are also ignored. Consequently, the $T_g$s are accurate to perhaps $\pm 3°C$, with some notable exceptions captured in the notes below the table. References for pressure-glass transition temperature ($P-T_g$) gradients are sparse and sometimes have large discrepancies. Furthermore, the gradients are only accurate for the initial slope of the $P-T_g$ relationship, but even so they appear to be accurate to at least 125 MPa. Finally, Table 2.2 shows $T_g$s and $dP/dT_g$s for some of the thermoplastics used in copolymer rubbers. $T_g$s of copolymers typically lie between those of the constituent monomers.
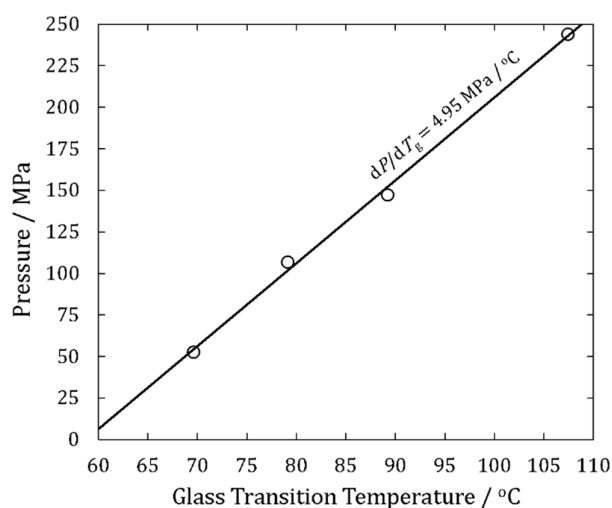


**Fig. 2.11:** Relationship between pressure and glass transition temperature for polyvinyl acetate (wood glue) using dynamic measurements of the dielectric loss coefficient. Note that $dP/dT_g$ remains linear to a remarkably high pressure. (Adapted from O'Reilly.)[39]

**Table 2.1:** Glass transition temperatures at atmospheric pressure and initial pressure-glass transition temperature gradients for several elastomers and rubbers.

| Material | $T_g$ (°C) | $dP/dT_g$ ($\frac{MPa}{°C}$) | Oilfield Service | Oilfield Trade Name | Comment | Refs. |
|---|---|---|---|---|---|---|
| PDMS | -124 | 5.9 | Yes | – | Low pressures only | 36,40,51,54 |
| BR [i] | -93 | 4.2 | No | – | Poor oil resistance | 36,51,54-57 |
| IIR | -70 | 4.1 | No | – | Poor resilience | 45,46,51,54-57 |
| NR / *cis*-IR [ii] | -69 | 5.2 | Rarely | – | Poor oil resistance | 40,45,54,55,57,58 |
| SBR (23.5% PS) | -56 | – | No | – | Poor oil resistance | 45,55,57 |
| EPDM | -48 | – | Specialty | – | For swell packers | 55,57,59 |
| CR | -45 | – | Limited | Neoprene® | Obsolete by NBR | 45,54-57 |
| NBR (20% ACN) [iii] | -36 | 6.7 | Yes | Nitrile | Good oil resistance | 40,55,45,60-63 |
| HNBR (20% ACN) [iv] | -33 | – | Yes | – | Good oil resistance | 62,63 |
| FKM [v] | -19 | 3.1 | Yes | Viton® | High temperature | 55,59,64,65 |
| FFKM [vi] | -19 | – | Yes | Chemraz® | Extreme high temp. | – |
| HNBR (50% ACN) [iv] | -17 | – | Yes | – | Better oil resistance | 62,63 |
| NBR (50% ACN) [iii] | -12 | – | Yes | Nitrile | Better oil resistance | 40,45,55,60,61-63 |
| TFEP, FEPM [vii] | -3 | [vii] | Yes | Aflas® | High temperature | 59,66,68 |

[i] $dP/dT_g$ for BR is taken from Roland[51] for 1,2-polybutadiene which is not the same as the configuration used for rubber, 1,4-*cis*-polybutadiene.

[ii] Natural rubber and *cis*-polyisoprene are entered in the same row because they are chemically identical. In the oil industry, there is a rule-of-thumb that $dP/dT_g$ is 750 psi/°C for all rubbers, but its origin is unclear. Perhaps coincidentally, this rule of thumb is identical to $dP/dT_g$ reported here for natural rubber (750 psi = 5.17 MPa). However, it is important to recognise that the average value reported in the table is based on a range of approximately 600–900 psi/°C (4.14 – 6.21 MPa/°C). In addition, the reported $dP/dT_g$s for oilfield copolymers are much different than the rule-of-thumb which makes its general adoption a dubious practice. Finally, James Walker[67] has published a report that recommends a slightly lower rule-of-thumb for $dP/dT_g$ of rubbers: 725 psi/°C (5.00 MPa/°C). Nielsen[44] suggests using a larger gradient of 853 psi/°C (5.88 MPa/°C).

[iii] NBR with less than 37% ACN has two $T_g$s due to the different monomers.[60] The higher of the two $T_g$s is reported in the table. To determine $T_g$, a linear trendline was fit to the data from Brazier,[45] Gent,[55] Ambler,[60] Sircar & Lamond,[61] Bhattacharjee *et al.*,[62] and Hayashi *et al.*[63] The two lowest points from Hayashi and Sircar were neglected because it appears the authors reported the lower of the two $T_g$s for their NBRs with the lowest ACN content. The linear trend calculates $T_g$s for NBRs with different ACN content according to: $T_g = (0.83(ACN_\%) - 52.9)$°C. Only one reference was found for $dP/dT_g$, so there is limited confidence in the value (which seems rather high).

[iv] HNBR with low (high) ACN content has a higher (lower) $T_g$ than NBR with an equivalent ACN content. Increasing the degree of hydrogenation appears to monotonically reduce $T_g$. The reported temperatures are based on a linear fit to the data of Bhattacharjee *et al.*[62] and Hayashi *et al*:[63] $T_g = (0.525(ACN_\%) - 43.3)$°C.

[v] There are 5 different classes of FKM, so the range of $T_g$ is closer to ±10°C instead of ±3°C. Only one reference was found for $dP/dT_g$, but the relatively low value here seems consistent with fluoroelastomers tested by the project sponsor.

[vi] There is very limited scholarly data for FFKMs. The reported $T_g$ has been inferred from product literature by industrial suppliers. Some suppliers claim special blends of FFKM can function below −40°C.

[vii] Refer to Schlumberger GEMS report 101692827 for $dP/dT_g$ of an Aflas compound.[68]

**Table 2.2:** Thermoplastics used in copolymer rubbers.

| Material | $T_g$ (°C) | $dP/dT_g$ (MPa/°C) | Comment | Refs. |
|---|---|---|---|---|
| PTFE [i] | -85 | 7.8 | Used in TFEP | 56,57 |
| VDF | -38 | – | Used in FKM | 54,56,57 |
| PP [ii] | -10 | 6.3 | Used in TFEP | 36,51,56,57 |
| PS | 100 | 3.1 | Used in SBR | 36,51,54,56 |
| ACN [iii] | 100 | – | Used in NBR & HNBR | 36,54,56,57 |

[i] Brandrup[57] reports many transitions in polytetrafluoroethylene (PTFE), and PTFE properties depend on the level of crystallinity, so it $T_g$s have wide variation.

[ii] $dP/dT_g$ for polypropylene (PP) is for the atactic configuration.[51] The glass transition temperature is for the isotactic configuration and has large variation, −30°C to 10°C.[57]

[iii] The $T_g$ of ACN ranges from 85°C to 105°C.

## 2.4  Types of Rubber
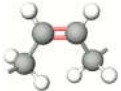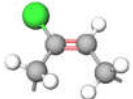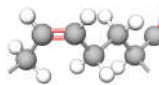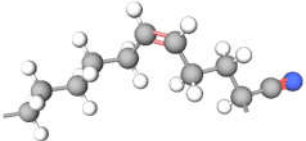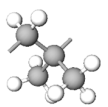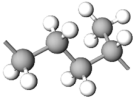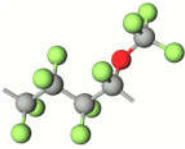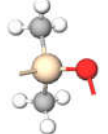
In this section, natural and synthetic rubbers are introduced with some attention given to those that are used in oilfield seals. A wider account of rubbers in oilfield seals, as well as a materials selection guideline, has been given by Mody *et al.*[3] The reported service temperature limits are based on guidelines from James Walker,[69] but oilfield rubber compounds often push the upper limit 15–30℃ higher, particularly for service lifetimes that are of the order of weeks. Table 2.3 shows the names, acronyms, chemical formulas, and molecular structures for all rubbers in this section. The 3D representations were generated with Molview.[28]

### 2.4.1  Natural Rubber and *cis – Polyisoprene* Rubber

The elemental composition of natural rubber (NR), $C_5H_8$, was first deduced by Himly in 1838 and its name "isoprene" was coined by Williams in 1860.[23] *cis*–polyisoprene rubber (IR) is the synthetic twin of NR. Despite its name it has a lower *cis-* content than NR giving it slightly inferior mechanical properties, often negligibly so.[32] NR's molecular structure was correctly proposed by Pickles in 1910,[23] though he imagined each molecular chain formed a ring with low molecular weight. The macromolecular nature of rubber was discounted until Staudinger[29] advocated for it in 1919, yet it remained a contentious proposition until receiving sound experimental support from others in the mid-to-late 1920s.[23] In 1932, Meyer, von Susich, & Valko[50] refined these ideas into an early form of the kinetic theory of elasticity which underpins most models of rubber mechanics.

Natural rubber must be in the *cis-* configuration to have rubbery behavior at room temperature. In the *trans-* configuration, it is a largely obsolete thermoplastic called "gutta percha", though it retains specialty use in biomedical-applications. An important property of NR is that when stretched a fraction of its molecules become aligned and form crystals, a phenomenon called **strain-induced crystallisation**. The result is exceptional tensile strength and fatigue resistance. It also has good resilience and, by corollary, low hysteresis. However, NR is prone to oxidation, ozone cracking, and degradation by light. The material is rarely used for oilfield seals because it swells in hydrocarbons and has a low upper temperature limit of 105℃, whereas 120℃ is required for low-tier oilfield seals.

**Table 2.3:** Names and formulas for different rubbers.

| Name | Acronym | Formula | Monomer(s) |
|---|---|---|---|
| butadiene [i] | BR (Buna) | | |
| natural rubber *cis*-polyisoprene | NR IR | | |
| chloroprene [ii] Neoprene® | CR (GR-M) | | |
| styrene-butadiene | SBR (Buna-S) (GR-S) | | |
| acrylonitrile-butadiene nitrile | NBR (Buna-N) (GR-N) | | |
| hydrogenated nitrile | HNBR | | |
| isobutylene-isoprene butyl [iii] | IIR (GR-I) (GR-X) | | |
| ethylene-propylene [iv] (w/ -diene monomer) | EPDM | | |
| tetrafluoroethylene-propylene Aflas® | TFEP FEPM | | |
| vinylidene-hexafluoropropylene Viton® [v] | FKM VDF VF2 | | |
| perfluoroelastomer [vi] Kalrez® Chemraz® | FFKM | | |
| polydimethylsiloxane silicone | PDMS | | |

[i] The use of the acronyms in parenthesis are deprecated.

[ii] Only 10% of CR is in the *cis-* configuration. The balance is mostly in the *trans-* configuration.[32]

[iii] The isoprene monomer is not shown in the image because it only comprises ≈2% of the rubber.

[iv] The diene monomer is not shown as it is only used in small quantities for crosslinking.

[v] A class 1 FKM is shown (Viton A). Class 2 adds tetrafluoroethylene (Viton B). These are 95% of the market.[32]

[vi] FFKM formulations are generally proprietary. The structure shown is a simple one given by James Walker.[69]

### 2.4.2 Synthetic Rubbers

The first attempts at rubber synthesis were with IR, but chemists were unable to impart the *cis-* configuration until the advent of Ziegler-Natta catalysis in the 1950s.[32] In 1910, the Germans found it easier to polymerise isoprene molecules with an additional methyl ($CH_3$) group resulting in methyl isoprene rubber (or dimethyl-butadiene). Germany used the material in World War I, but thereafter it was obsolesced due to inferior properties and prohibitively long times for polymerisation.[22]

Butadiene rubber (BR) was first synthesised by the Russian chemist Lebedev in 1910, with process improvements continuing through the 1920s. In the lead-up to World War II, Germany heavily invested in economic development of BR with some success,[9] though its mechanical properties were (and still are) inferior to NR. They called the material "Buna", a conjunction of butadiene and the polymerisation catalyst *natrium* (Na, sodium). To improve mechanical properties and reduce cost, the Germans introduced $\approx$25% poly-styrene (PS) to produce styrene-butadiene rubber (SBR) which they called "Buna-S". BR replaces the $CH_3$ groups in NR with hydrogen atoms making the rubber structurally simpler and less reactive. Its low steric hinderance gives it low hysteresis. BR can strain-crystallise,[52] but SBR does not.[70] BR is rarely used by itself in demanding applications, so its service temperature range is difficult to locate. SBR can be used up to 115℃ and is predominant in tyres for light vehicles due to its excellent abrasion resistance in filled compounds.[71] The cost of SBR is similar to that of NR. BR and SBR are not used in oilfield seals because they readily swell in hydrocarbons.

Germany developed the oil-resistant rubber acrylonitrile-butadiene rubber (NBR or nitrile) in the 1930s which they labeled "Buna-N". The acrylonitrile (ACN) side group comprises 15–50% of the material. Its polarity gives good resistance to swelling in hydrocarbons, making NBR a workhorse sealing material in the oilfield. However, it embrittles in hydrogen sulfide ($H_2S$) and amines. The former is produced in some oil wells, and the latter is used as a corrosion inhibitor in completions fluids.[72] NBR's service temperature range is -30℃ to 130℃. Early work suggested NBR did not strain crystallise,[70] but Shaw's[73] recent work on the fracture of NBR challenges this finding. NBR is about 50% more expensive than NR.

Building on academic research from 1903 to 1925, the DuPont company began commercialisation of chloroprene rubber (CR, DuPrene®, or Neoprene®) in 1930. At the time, the material polymerised 700 times faster than IR. It replaces the methyl groups in NR with chlorine (Cl) atoms which improves resistance to oxidation, ozone, and thermo-chemical attacks. The Cl atoms disrupt diene bond energies, so it is crosslinked with metal oxides (MgO and ZnO) instead of sulphur.[30] CR strain crystallises,[70] and it has moderate resistance to swelling in hydrocarbons. It also has a service temperature range of -40℃ to

125℃, so it is an acceptable material for low-tier oilfield seals. However, oilfield usage is largely obsolete due the adoption of NBR. Its cost is also about 50% higher than NR.[†]

Butyl rubber was developed in the US alongside SBR and NBR.[25] It is primarily iso-butylene with a small quantity of a diene rubber, usually isoprene, added for vulcanisation which gives the acronym IIR (formerly GR-I or GR-X). The material is more resistant than NR to heat, oxidation, ozone, and chemical attack. Compared to diene rubbers, it has unrivaled resistance to gas permeation, so it is often used in pneumatic applications. Its poor resilience at room temperature makes it an excellent damping material but a poor choice for dynamic sealing applications. Due to this drawback and its propensity to swell, the material is not used for oilfield sealing. Its service temperature range is -50℃ to 135℃. It costs four times more than NR and does not strain crystallise.[70]

Developed in the 1950s and '60s, ethylene-propylene rubber with a diene monomer (EPDM) is a copolymer ($\approx$60% ethylene) of two thermoplastics that together create a rubbery material. The diene monomer attaches as a side group to provide a crosslinking site. Since the $C=C$ bonds are not part of the main chain, EPDM has good resistance to thermal and chemical degradation, and its service temperature range is -50℃ to 150℃. EPDM readily swells in hydrocarbons, so its use in oilfield seals is generally limited to specialty products, for instance swellable seals. Some formulations can strain crystallise, particularly at low temperatures, and its cost is comparable to NBR.

NBR can be processed to remove nearly all of its residual double bonds resulting in hydrogenated nitrile rubber (HNBR).[74] The material was developed in the 1980s to bridge a cost and performance gap between NBR and fluoroelastomers. It costs 10-15 times more than NBR but is $\approx$30% cheaper than entry-level fluoroelastomers. The hydrogenation improves thermal and chemical resistance, including in amines and $H_2S$.[72] It extends the upper temperature limit of NBR to $\approx$180℃. HNBR is a tough, stiff material, so it can be compounded to give a high shear modulus that is well-suited to resist rapid gas decompression. Crystallisation effects in HNBR are not straightforward. Windslow's PhD thesis[75] reviews this subject in detail. To summarise, HNBR with low ACN content strain-crystallises under certain conditions because it has long ethylene units ($CH_2$) that align when stretched. HNBR with high ACN content can exhibit features of semi-crystalline thermoplastics, including yielding behaviour, due to the regularity of $CH_2$ and ACN units along the polymer chain. It can also strain-crystallise, though typically at strains well above those experienced in seals.

Developed in the 1940s as an insulating material for electrical applications, polydi-

---

[†] As a side note, the US was not constrained to use CR for applications with oil exposure during World War II. Standard Oil had gained rights to Germany's Buna technology, and the US went on to rebrand SBR and NBR as government rubbers GR-S and GR-N.[24]

methylsiloxane (PDMS) rubber is unique in that its backbone consists of silicone-oxygen units instead of carbon. It is a largely inert material, but its strength and stiffness are typically orders of magnitude lower than those of other rubbers which prevents its use in high pressure seals. However, it is stable over a large temperature range of -60℃ to 300℃.

### 2.4.3 Fluoroelastomers

The first commercially successful partially fluorinated fluoroelastomers were developed in the 1950s. These are called FKMs and consist of 2 to 5 different monomers but always have vinylidene-hexafluoropropylene (VDF or VF2, trade name Viton®). General statements about FKMs usually have exceptions, but some guidelines are given. Compared to non-fluorinated rubber, they are superior against oxidation and most chemical attacks including $H_2S$, so they find frequent service in the oilfield. However, they are prone to embrittlement by amines (and bases in general) which are used as corrosion inhibitors in some oilfield fluids.[65] Some grades have limited resistance to steam and polar fluids such as ketones, esters, and ethers. Resistance to gas permeation is similar to that of butyl rubber. A typical temperature range is -20℃ to 250℃. FKMs are about 25 times more expensive than NBR. A detailed review of FKM chemistry, curing, processing, and properties has been given by Arnold et al.[76]

Developed in the 1960s, perfluoroelastomers are fully fluorinated and designated as FFKMs (trade names Chemraz® and Kalrez®). Removal of all CH bonds gives them unrivaled heat resistance, and they are inert to practically all chemical attacks. Like FKMs, the materials are resistant to gas permeation. However, they require specialty manu-facturing and cost 20–25 times more than FKMs ($\approx$£3,500/kg) which means their usage is very limited.[32] In the oilfield, cost tends to restrict usage to small parts such as O-rings. FFKM's temperature range is wide with some suppliers claiming low and high temperature limits around -40℃ and 325℃, though not with the same compound. These limits may not be appropriate for high pressure oilfield seals, especially because mechanical properties deteriorate at the highest temperatures.[3] FFKMs always require anti-extrusion devices such as thermoplastic back-up rings. Academic publications on FFKMs are exceedingly rare, an exception being the review by Arnold et al.[76]

To bridge the performance and cost gaps between FKMs and FFKMs, tetrafluoro-ethylene-propylene rubber (TFEP or FEPM, trade name Aflas®) was developed in the 1970s. Its price is more aligned with FKMs than FFKMs. TFEP has better resistance to amines and steam than FKMs. Its resistance to gas permeation matches that of other fluoroelastomers. Its primary drawback is a high glass transition temperature. A typical service temperature range is 0– 200℃, but in the oilfield a range of 23– 218℃ is often applied. The material can be pushed to 232℃. Like FFKMs, the material has poor extrusion

resistance,[‡] so it requires anti-extrusion devices such as thermoplastic back-up rings. It is also a difficult material to process during manufacturing.[65]

## 2.5 Hyperelasticity

### 2.5.1 The Thermodynamic Foundation of Rubber Thermoelasticity

This section formalises the entropy of a single chain to build an expression for the total entropy of a rubber network. The entropy is then related to external work on the system, revealing the thermoelastic origin of rubber elasticity. This coupling between deformation and heat was observed at least as early as 1805 by Gough who noted that a stretched rubber contracted when heated.[77] However, a correct thermodynamic formalism for arbitrary deformation was not achieved until the early 1940s, perhaps explained most clearly in Treloar's work.[78,79,80]

To develop a micromechanical model for the deformation of rubber, first consider the absolute entropy of the randomly oriented idealised molecular chain in Fig. 2.12a:

$$s_1 = k_B \ln \omega_1 \tag{2.4}$$

where $\omega_1$ is the number of microstates available to the chain. One end of the chain is fixed at origin, $O$, and the other end is at point $B$ with coordinates $(x_1, y_1, z_1)$. Point $B$ is enclosed in differential volume, $dV_1 = dx_1\,dy_1\,dz_1$, and the chain ends are joined by vector $\boldsymbol{r}_1$. Both ends are assumed to coincide with crosslinks in the rubber network.
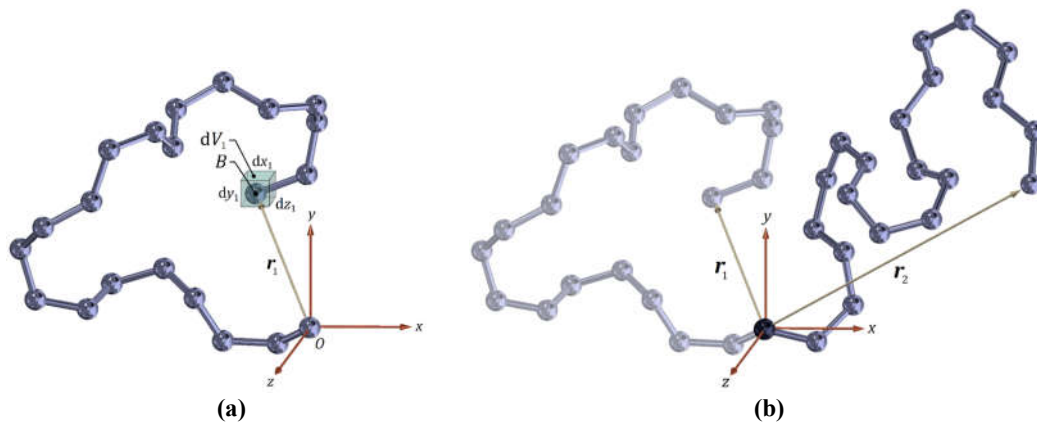


**Fig. 2.12:** A randomly oriented idealised molecular chain in a rubber network: **(a)** before deformation with ends at origin $O$ and point $B$; **(b)** before deformation (light molecules) and after deformation (dark molecules). Both ends are assumed to terminate at crosslinks.

There are numerous microstates that permit the chain end to coincide with point $B$.[50] The probability of finding the end of the chain at an arbitrary point $(x, y, z)$ in space is:

$$P(x, y, z) = p(x, y, z)\,dV \tag{2.5}$$

where $p(x, y, z)$ is a probability density function (PDF, probability per unit volume). The

---

[‡] A reader unfamiliar with this term can refer to Fig. 3.6 for an illustration of extrusion.

PDF for a single chain with a Gaussian distribution of end-to-end chain lengths is given by:[50]

$$p(x, y, z) = \frac{b^3}{\pi^{1.5}} e^{-b^2(x^2+y^2+z^2)} \tag{2.6}$$

where $b = l_{\mathrm{m}}^{-2}\sqrt{3/2n_{\mathrm{m}}}$, and $n_{\mathrm{m}}$ and $l_{\mathrm{m}}$ are the number and length of idealised molecules in the network chain, respectively. Qualitatively, $b$ is a scaling factor that is associated with parameters that affect the total length (**contour length**) of the network chain. From Eqs. 2.5 and 2.6, the probability of finding a chain end in differential volume $dV_1$ at point $B$ is:

$$P(x_1, y_1, z_1) = \frac{b^3}{\pi^{1.5}} e^{-b^2(x_1^2+y_1^2+z_1^2)} dV_1 \tag{2.7}$$

Expressing the absolute entropy of the chain in terms of probability:

$$s_1 = k_B \ln\big(P(x_1, y_1, z_1)\big)$$
$$= c - k_B b^2 (x_1^2 + y_1^2 + z_1^2) \tag{2.8}$$

where all constant terms in the simplified expression have been grouped into $c$.

Next, consider the deformation of the single chain within the rubber network as shown in Fig. 2.12b. Following the logic of Eq. 2.8, the absolute entropy of the deformed chain is:

$$s_2 = c - k_B b^2 (x_2^2 + y_2^2 + z_2^2) \tag{2.9}$$

where $c$ is the same in both equations when $dV_1 = dV_2$, which is the case for an incompressible material. The change in entropy for the network chain is thus:

$$\Delta s = -k_B b^2 [(x_2^2 - x_1^2) + (y_2^2 - y_1^2) + (z_2^2 - z_1^2)] \tag{2.10}$$

Eq. 2.10 can be further simplified by invoking a relationship between the macro-deformation of the rubber and the micro-deformation of the polymer chain within it. One simple relationship invokes the **affine deformation assumption** which requires all crosslinks to translate in exact proportion with the bulk deformation. In terms of the principal axes of deformation which have principal stretches $(\lambda_1, \lambda_2, \lambda_3)$, the following substitutions apply: $(x_2, y_2, z_2) = (\lambda_1 x_1, \lambda_2 y_1, \lambda_3 z_1)$. Eq. 2.10 becomes:

$$\Delta s = -k_B b^2 [(\lambda_1^2 - 1)x_1^2 + (\lambda_2^2 - 1)y_1^2 + (\lambda_3^2 - 1)z_1^2] \tag{2.11}$$

Assuming the change in entropy of the entire rubber network, $\Delta S$, is the sum of the change in entropy of all network chains:

$$\Delta S = \sum_i \Delta s_i = -k_B b^2 \big[(\lambda_1^2 - 1)\sum_i x_{o,i}^2 + (\lambda_2^2 - 1)\sum_i y_{o,i}^2 + (\lambda_3^2 - 1)\sum_i z_{o,i}^2\big] \tag{2.12}$$

where $(x_{o,i}, y_{o,i}, z_{o,i})$ are the undeformed coordinates of the $i^{\mathrm{th}}$ chain. For an isotropic network, the average undeformed end-to-end chain dimensions in each coordinate direction are the same which requires $\sum_i x_{o,i}^2 = \sum_i y_{o,i}^2 = \sum_i z_{o,i}^2 = 3^{-1}\sum_i |r_{o,i}|^2$. The last summation can be expressed as the average end-to-end squared chain distance, $\overline{r_o^2}$, times the total number of chains in the network, $N_c$, such that $\sum_i |r_{o,i}|^2 = N_c \overline{r_o^2}$, and Eq. 2.12 simplifies to:

26

$$\Delta S = -\frac{1}{3}N_c k_B b^2 \overline{r_o^2}(\lambda_1^2 + \lambda_2^2 + \lambda_3^2 - 3) \tag{2.13}$$

It can be shown that $\overline{r_o^2} = 3/(2b^2)$,[50] so Eq. 2.13 further simplifies:

$$\Delta S = -\frac{1}{2}N_c k_B(\lambda_1^2 + \lambda_2^2 + \lambda_3^2 - 3) \tag{2.14}$$

Interestingly, the network's change in entropy is completely independent of any chain contour lengths. This result is accurate only when the end-to-end chain distances are much shorter than contour lengths. To relate $\Delta S$ to macroscopic deformation, classical forms of the 1$^{st}$ and 2$^{nd}$ laws of thermodynamics are required:

$$\Delta U = \Delta W + \Delta Q \tag{2.15}$$

$$\Delta Q = T\Delta S \tag{2.16}$$

where $\Delta U$ is the change in internal energy and $\Delta W$ is external work that deforms the rubber. As previously suggested, let $\Delta U = 0$. The rubber is initially undeformed ($W_1 = 0$), which requires $\Delta W = W_2 = W$. Combining these simplifications with Eqs. 2.14–2.16, it follows that:

$$W = \frac{1}{2}N_c k_B T(\lambda_1^2 + \lambda_2^2 + \lambda_3^2 - 3) \tag{2.17}$$

Eq. 2.17 is the basis for most practical hyperelastic models for rubbery materials. It is usually expressed per unit volume to give **strain-energy density**, and the function is called a **strain-energy function** (SEF) or **stored-energy function**. For an ideal network, the number of chains per unit volume is the same as the number of crosslinks per unit volume (**crosslink density**).[50] An SEF can be differentiated to compute stresses. For an incompressible material, conservation of volume requires $\lambda_1\lambda_2\lambda_3 = 1$.[50] With this expression and Eq. 2.17, the **nominal stress** (or synonymously, **engineering stress**) in a rubber that is stretched an amount, $\lambda$, in uniaxial extension is:

$$\sigma_{ut} = N_c k_B T\left(\lambda - \frac{1}{\lambda^2}\right) \tag{2.18}$$

Therefore, stress is proportional to the crosslink density and the absolute temperature.

Eq. 2.18 readily accounts for Gough's observation in 1805 that a stretched rubber under a constant load contracts when heated. When heat increases $T$ and $\sigma_{ut}$ is constant, then $\lambda$ must decrease to balance the equation. From another perspective, heating the stretched rubber increases its entropy, and hence, the rubber network and its individual chains seek a larger number of microstates. Consequently, the rubber seeks a macroscopic configuration in which it is easier to access more microstates, and that occurs if the chain ends are closer to one another (review Fig. 2.7b,c to verify that reducing $|r|$ increases the available microstates). Therefore, the rubber network contracts.

### 2.5.2 Modes of Deformation & Biaxiality

The stress-strain response of rubber depends on the applied loading mode. As a way of

illustration, the simplest modes are pure and homogeneous. A **pure** deformation occurs when the principal axes do not rotate during the deformation. A **homogeneous** deformation occurs when the state of strain at all points in a body is the same. Fig. 2.13 illustrates three pure, homogeneous deformations for an incompressible unit cube stretched by an amount, $\lambda$. The amount of energy required for each deformation increases from left to right; therefore, $\sigma_{ut} < \sigma_{pt} < \sigma_{et}$ (UT = uniaxial tension; PT = planar tension; ET = equibiaxial tension). In the PT mode, constraint is required to prevent contraction along the unstrained side, but the reaction force to maintain this constraint is not illustrated.
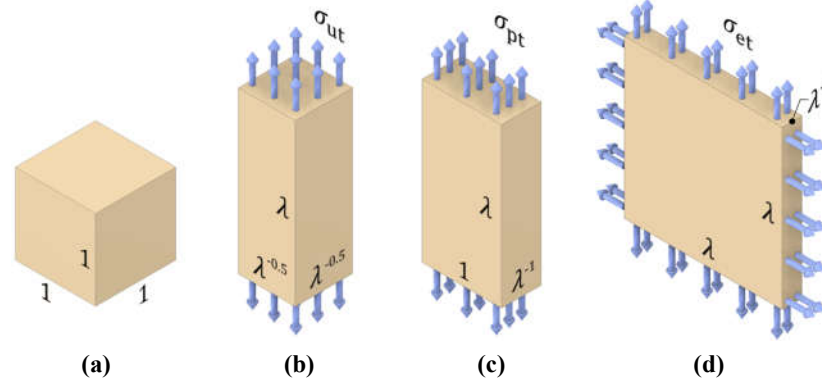


**Fig. 2.13:** An incompressible rubber block of unit volume: **(a)** before deformation; **(b)** after a uniaxial extension; **(c)** after a planar extension; **(d)** after an equibiaxial extension.

The deformations in Fig. 2.13 can be achieved by different loads, resulting in loading mode equivalencies. For instance, an equibiaxial extension is equivalent to a uniaxial compression (UC) (Fig. 2.14). Nominal stresses, $\sigma_{et}$ and $\sigma_{uc}$, are applied to achieve identical deformations, but $\sigma_{et} \neq \sigma_{uc}$. However, true stresses, $\hat{\sigma}_{et}$ and $\hat{\sigma}_{uc}$, are the same. To prove this, superimpose a hydrostatic pressure on the button in Fig. 2.14b such that $P = -\hat{\sigma}_{et}$. Since the body is incompressible, $P$ cannot deform it, but it does cancel the radial stress, leaving a compressive stress of magnitude $\hat{\sigma}_{et}$ on the axial surfaces. The net compressive force is thus $F'_{uc} = \hat{\sigma}_{et} A_2$. The axial force on the button in Fig. 2.14c in terms of true stress is $F_{uc} = \hat{\sigma}_{uc} A_2$. To achieve the same deformations from geometrically identical buttons, $F_{uc}$ must equal $F'_{uc}$, and it follows that true stresses are equivalent, $\hat{\sigma}_{et} = \hat{\sigma}_{uc}$.
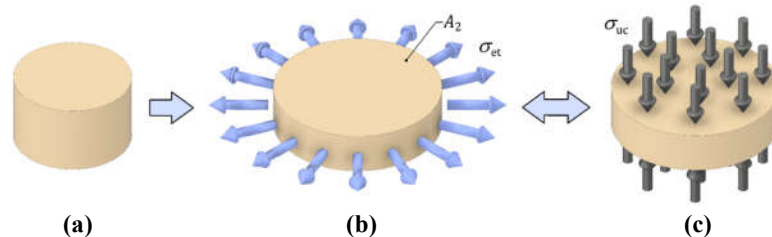


**Fig. 2.14:** Loading mode equivalency in a cylindrical button: **(a)** before deformation; **(b)** after an equibiaxial extension; **(c)** after an equivalent uniaxial compression.

For an incompressible material, a known equibiaxial stretch can be converted to an equivalent uniaxial compression (see Appendix E), and vice versa, with the relation:

$$\lambda_{\text{uc}} = \lambda_{\text{et}}^{-2} \tag{2.19}$$

Using this result and the equivalency of true stresses, any known nominal stress in ET may be converted to an equivalent nominal stress in UC, and vice versa:

$$\sigma_{\text{uc}} = \lambda_{\text{et}}^{3}\sigma_{\text{et}} \tag{2.20}$$

Another common loading mode is simple shear (Fig. 2.15). By definition, simple shear is a constant volume deformation that only captures angular distortions. The deformation imposes $x$-displacements, $u$, that are linear functions of $y$, yielding $u(y) = cy$ where $c$ is a constant such that:

- Lines initially parallel to the $x$-axis remain parallel to that axis;
- Lines initially parallel to the $y$-axis rotate but remain parallel to one another;
- Points along any line parallel to the $x$-axis remain equidistant;
- Planes initially parallel to the $xz$-plane remain parallel to that plane.

To maintain volume constancy, these constraints require $\lambda_z = 1$.
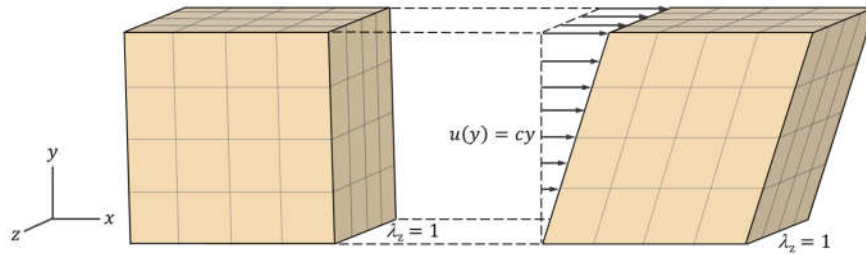


**Fig. 2.15:** Illustration of a simple shear deformation.

In finite strain, simple shear is not a pure deformation because shearing rotates the principal axes. However, it is a homogeneous deformation because the state of strain is uniform throughout the body, a fact illustrated in Fig. 2.15 where the superposed grid shows all deformed sub-units have the same shape.

A planar tension deformation is often called a **pure shear**. To illustrate why, Fig. 2.16 shows a unit cube in planar tension stretched to an extension ratio of 2. Conservation of volume requires the thickness in the unconstrained direction to halve. A diamond is superposed on the block before ($V_1$) and after ($V_2$) deformation to show an element that has undergone a shear. Since $\lambda_z = 1$, careful inspection of the geometry reveals that these two volumes must be equal. In addition, the principal axes do not rotate during this deformation, hence the name pure shear.

To be clear, the sub-element given by $V_2$ does not represent a simple shear of $V_1$. To illustrate why, consider Fig. 2.17a. A face of each sub-element is coincident with the $x'z$-plane in a rotated coordinate system, clearly illustrating that the element has stretched in the $x'$-direction; hence, the $x'$-displacement is given by $u' = u'(x', y')$ which violates simple shear's requirement that $u' = u'(y')$. Specifically, lines that were initially parallel to the $x'$-axis have stretched. Fig. 2.17b illustrates a simple shear element with the same volume and

angular distortion as $V_2$. From observation of Fig. 2.17b, it is not difficult to deduce that a tensile stress is required in the $y'$-direction to maintain the simple shear; hence, a shear stress alone cannot sustain a finite simple shear. Treloar[50] has provided a mathematical proof of this fact. Another complication with finite shear is that there is no simple geometric relationship between the pure shear and simple shear modes. This is in contrast to the infinitesimal strain case in which one mode may be recovered from the other with a 45° rotation of the principal axes.[81]
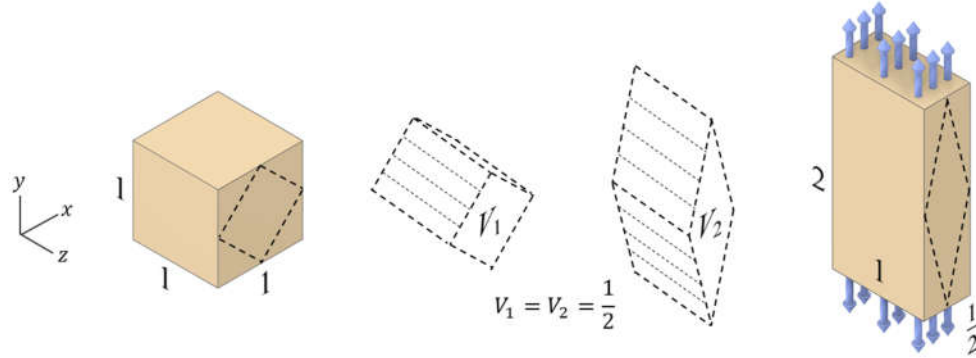


**Fig. 2.16:** Equivalence of planar tension and pure shear deformation modes.
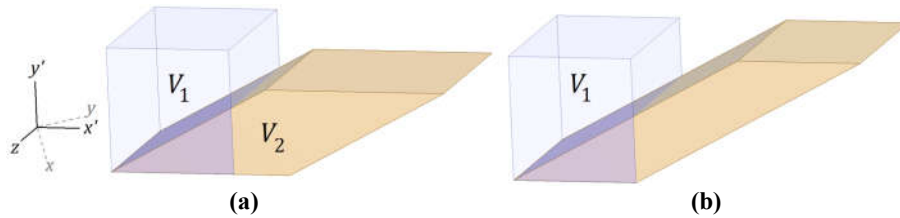


**Fig. 2.17: (a)** The $V_2$ sub-element from Fig. 2.16 aligned with an $(x', y', z)$ coordinate system to illustrate that the pure shear element of $V_2$ is not a simple shear. **(b)** A simple shear element with volume $V_2$ and the same shear angle as that in Fig. 2.17a.

Strains in a deformed body are generally inhomogeneous, and even when homogeneous, they may fall somewhere between the three states illustrated in Fig. 2.13. When this occurs, it is useful to know which mode best characterises the deformation. This is revealed by computing the biaxiality of the deformed body (or a point in the body if the strain is inhomogeneous). Wadham-Gagnon *et al.*[82] and Mars[83] offer two definitions of biaxiality. Windslow *et al.*[84] recently reported a useful one as given below in Eq. 2.21. To compute biaxiality, principal strains are ordered from high to low with $\lambda_3 \geq \lambda_2 \geq \lambda_1$. The biaxiality is then given by:

$$\alpha = \frac{\log(\lambda_1)}{\log(\lambda_3)} \tag{2.21}$$

For an incompressible material, $(\alpha_{et}, \alpha_{pt}, \alpha_{ut}) = (-2, -1, -0.5)$.[84] Any incompressible deformation, even an inhomogeneous one, has a biaxiality bounded by this range. As shown in Appendix D, Windslow and Hohenberger have provided a modification of Eq. 2.21 for use with a compressible material. The practical use of biaxiality is discussed further in Section 5.4.7.

### 2.5.3 Strain-Energy Functions

A major benefit of a strain-energy function is that it captures an isotropic rubber's loading mode dependencies in a single function. For example, the SEF of Eq. 2.17 can be differentiated for the deformations in Fig. 2.13 to yield three stress equations, one of which is shown in Eq. 2.18. The nominal stresses in planar and equibiaxial tension are given by:

$$\sigma_{\text{pt}} = N_c k_B T \left( \lambda - \frac{1}{\lambda^3} \right) \tag{2.22}$$

$$\sigma_{\text{et}} = N_c k_B T \left( \lambda - \frac{1}{\lambda^5} \right) \tag{2.23}$$

Having all deformation modes captured by one function provides an efficient way to model hyperelastic behaviour in finite-element solvers.

The strain-energy function of Eq. 2.17 is often called the statistical or Gaussian SEF. Assuming an incompressible, isotropic material, Rivlin adapted Hooke's law for finite deformations and, through symmetry conditions, derived the Neo-Hookean SEF:

$$W = \frac{1}{2} G (\lambda_1^2 + \lambda_2^2 + \lambda_3^2 - 3) \tag{2.24}$$

which essentially substitutes the shear modulus, $G = N_c k_B T$, into the Gaussian SEF. Although the forms are practically identical, Eq. 2.17 is derived using a statistical thermodynamic approach, whereas Eq. 2.24 is phenomenological in nature. There are a large number of SEFs in both categories. Several authors have provided reviews,[85,86,87] so a detailed account does not ensue here. Brief attention is given to some modelling features of two particular SEFs that will be discussed in a Chapter 4.

Fig. 2.18a shows stress-strain data in uniaxial tension data for an unfilled natural rubber that is fitted with a Neo-Hookean SEF. The shear modulus is chosen to match the initial modulus of the stress-strain data, but two problems are evident. The SEF moderately overpredicts the stress for $1.5 < \lambda < 5.5$ and grossly underpredicts the stress for $\lambda > 6$.
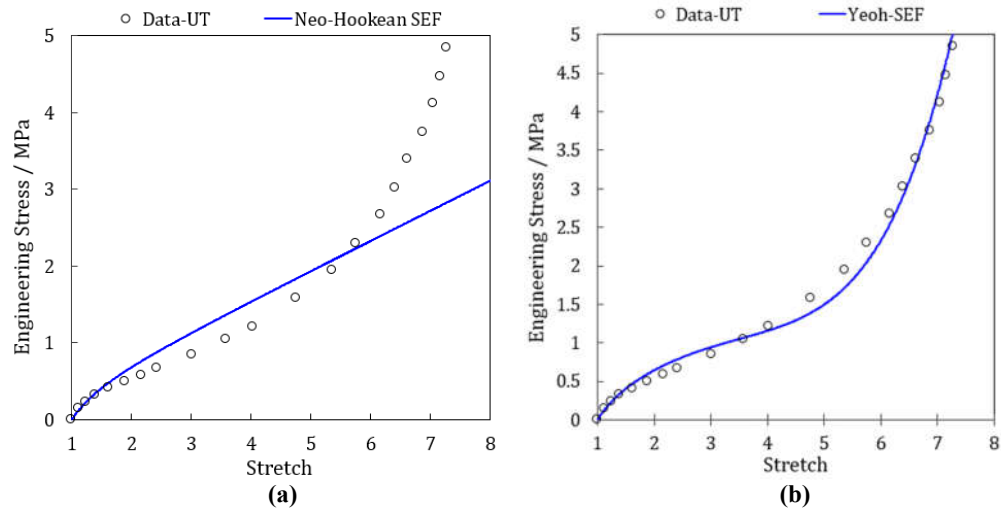


**Fig. 2.18: (a)** Treloar's canonical data set for unfilled natural rubber with his curve fit using the Neo-Hookean SEF; ($G = 0.39$ MPa).[50] **(b)** Yeoh's SEF fit to Treloar's data; $(C_{10}, C_{20}, C_{30}) = (0.195, -0.003, 0.00006)$ MPa.

Between 1948 and 1956, Rivlin[88,89] proposed a general SEF that may be employed to overcome some problems associated with the Neo-Hookean SEF. He gave a general phenomenological form for hyperelastic SEFs in terms of a series expansion:

$$W = \sum_{i,j,k=0}^{n} C_{ijk}(I_1 - 3)^i (I_2 - 3)^j (I_3 - 1)^k \tag{2.25}$$

where $C_{ijk}$ are fitting parameters, $C_{000} = 0$, n is the model order, and $(i, j, k)$ are positive integers. $I_1$, $I_2$, and $I_3$ are called invariants and are given by:

$$\begin{aligned} I_1 &= \lambda_1^2 + \lambda_2^2 + \lambda_3^2 \\ I_2 &= \lambda_1^2 \lambda_2^2 + \lambda_2^2 \lambda_3^2 + \lambda_1^2 \lambda_3^2 \\ I_3 &= \lambda_1^2 \lambda_2^2 \lambda_3^2 \end{aligned} \tag{2.26}$$

For an incompressible material, $I_3 = 1$ so Eq. 2.25 simplifies to:

$$W = \sum_{i,j=0}^{n} C_{ij}(I_1 - 3)^i (I_2 - 3)^j \tag{2.27}$$

The Neo-Hookean form is recovered when n = 1, $C_{10} = G/2$, and $C_{00} = C_{01} = C_{11} = 0$. In general, it is recommended to include both $I_1$ and $I_2$ terms when shear strains exceed 100%.[90] However, expansions strictly in terms of $I_1$ can be appropriate, particularly when strain magnitudes do not exceed 100%.[91] Many industrial applications meet this criterion. Such SEFs are called **reduced invariant forms**, and one popular version was proposed by Yeoh in 1990:[92]

$$W = C_{10}(I_1 - 3) + C_{20}(I_1 - 3)^2 + C_{30}(I_1 - 3)^3 \tag{2.28}$$

Compared to the Neo-Hookean SEF, the Yeoh model significantly improves curve fits at moderate and high strains usually by choosing $C_{20} < 0$ and $C_{30} > 0$ and satisfying the constraint $C_{10} > |C_{20}| > C_{30}$. The improvement is illustrated in Fig. 2.18b where the quadratic term shifts the stresses downward at moderate strains, and the cubic term captures the stiffening effect at high strains. The Neo-Hookean and Yeoh SEFs will be revisited in Chapter 4 where both are found deficient for modelling the behaviour of highly filled sealing rubbers.

### 2.5.4 Tensors, Finite Elasticity, and Their Link to Thermodynamics

Tensors are mathematical objects that allow a compact, general representation of relationships between physical quantities such as stress and strain in finite elasticity. They are implicitly or superficially introduced for stress transformations in elementary solid mechanics,[93] but their underlying concept is generally omitted. More advanced treatments tend to start with a 3D generalisation that carries an undue risk of masking some important attributes of tensors in mechanics.[94] The simple two-dimensional (2D) example below shows some salient aspects of tensors relevant to this work.

Fig. 2.19 illustrates a block with cross-sectional area, $A$, held in uniaxial tension with a

force, $F$. An oblique cut at angle, $(\theta + \pi/2)$, results in an internal section with area, $A'$. The true stress in the block is homogeneous, and by definition is $\hat{\sigma} = F/A$. For equilibrium, the force on the oblique face must be equal and opposite to the applied force, so the sum of forces in the $x$-direction gives:

$$F = F_\perp \cos\theta + F_\parallel \sin\theta \tag{2.29}$$

Eq. 2.29 is essentially a coordinate transformation (more specifically, a rotation) of the force, $F$, by the angle, $\theta$. In terms of stress, it becomes:

$$\hat{\sigma}A = \hat{\sigma}_\perp A' \cos\theta + \hat{\sigma}_\parallel A' \sin\theta \tag{2.30}$$

and with $A' = A\cos^{-1}\theta$, the equation simplifies to:

$$\hat{\sigma} = \hat{\sigma}_\perp + \hat{\sigma}_\parallel \tan\theta \tag{2.31}$$

Eq. 2.32 is also a coordinate transformation of $\hat{\sigma}$, and interestingly, it is not dependent on the magnitude of the area that the stress acts upon. However, it is dependent on the orientation of that area as defined by the oblique cut. A direct comparison of Eq. 2.29 with Eq. 2.31 shows that the transformation rules for force and stress are different. Here, the force transformation is captured in a single coordinate rotation, $\theta$. Stress includes this transformation, but it adds a second one to capture the area's orientation. The additional transformation makes stress more "complicated" than force, but only insomuch as it requires the consideration of two vector rotations instead of one. For the simple case in Fig. 2.19, the following equations can be proven consistent with the general stress transformation equations from elementary solid mechanics:[93]

$$\hat{\sigma}_\perp = \hat{\sigma}(1 + \tan^2\theta)^{-1} \qquad \hat{\sigma}_\parallel = \hat{\sigma}(\tan\theta + \cot\theta)^{-1} \tag{2.32}$$
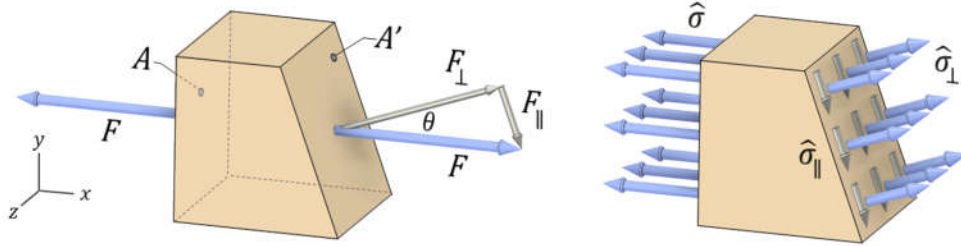


**Fig. 2.19:** Equivalent representations of loads on a body in uniaxial tension; the force description (left) is related to the stress description (right) through the areas on which the force acts.

In Eq. 2.29, it has been implicit that the force values, $(F, F_\perp, F_\parallel)$, are scalar magnitudes of the force vectors, $(\boldsymbol{F}, \boldsymbol{F}_\perp, \boldsymbol{F}_\parallel)$, and in fact, all 6 of these objects are encoded by two objects: the force vector, $\boldsymbol{F}$, and the rotation angle, $\theta$. By analogy, the stress values of $(\hat{\sigma}, \hat{\sigma}_\perp, \hat{\sigma}_\parallel)$ can be interpreted as scalar magnitudes of $(\hat{\boldsymbol{\sigma}}, \hat{\boldsymbol{\sigma}}_\perp, \hat{\boldsymbol{\sigma}}_\parallel)$, and all 6 of these objects are also encoded by two others: $\hat{\boldsymbol{\sigma}}$ and $\theta$. However, $\hat{\boldsymbol{\sigma}}$ is not a vector because it does not follow a vector transformation rule, a fact captured by the different trigonometric dependencies of Eqs. 2.29 and 2.31. Rather, $\hat{\boldsymbol{\sigma}}$ is a **rank-2 tensor**, the number "2" arising from the fact that stress depends on the rotation of two objects, namely area and force vectors. These two vectors are related through the tensor equation:

$$\boldsymbol{F} = \widehat{\boldsymbol{\sigma}}\boldsymbol{n} \tag{2.33}$$

where $\widehat{\boldsymbol{\sigma}}$ is the **Cauchy (true) stress tensor** and $\boldsymbol{n}$ is the unit-normal vector of the area that stress acts upon. In mathematical terms, $\widehat{\boldsymbol{\sigma}}$ is a linear operator that transforms the area vector, $\boldsymbol{n}$, into the force vector, $\boldsymbol{F}$.

Strain is also a rank-2 tensor. There are different options when formulating the strain tensor, but they all encode a relationship between a line element (described by a vector) and its displacement (also a vector quantity) upon deformation. For infinitesimal deformations, stress and strain ($\boldsymbol{\varepsilon}$) are then related through generalised Hooke's law:[95]

$$\widehat{\boldsymbol{\sigma}} = \mathbf{E}\boldsymbol{\varepsilon} \tag{2.34}$$

$\mathbf{E}$ is a rank-4 elasticity tensor that operates on a rank-2 tensor to produce another rank-2 tensor. More generally, a rank-j tensor operating on a rank-k tensor with $j > k$ results in a tensor of rank ($j - k$). For finite deformations, an equation that is analogous to Eq. 2.34 can be constructed by linearising the strain tensor. The mathematics are quite involved and can be found in Holzapfel's text (see in particular Eq. 8.79 in "Linearization and the Principle of Virtual Work").[96] Such linearisations are prevalent in finite-element analysis.

For finite elasticity, strain measures are usually derived from a tensor called the **deformation gradient** (Fig. 2.20) which characterises the local deformation in a body by:

- locating a material point, $B_1$, in the body with position vector $\boldsymbol{r}_1$;
- assigning an arbitrary differential line element, $\mathrm{d}\boldsymbol{s}_1$, emanating from point $B_1$;
- transforming $\mathrm{d}\boldsymbol{s}_1$ to a deformed configuration in the body such that:
  - $\mathrm{d}\boldsymbol{s}_1$ becomes $\mathrm{d}\boldsymbol{s}_2$;
  - material point $B_1$ transforms to $B_2$;
  - the position vector locating $B_2$ is $\boldsymbol{r}_2$.

All this information is concisely captured in the tensor equation:

$$\mathrm{d}\boldsymbol{s}_2 = \frac{\partial r_2}{\partial r_1}\mathrm{d}\boldsymbol{s}_1 = \mathbf{F}\,\mathrm{d}\boldsymbol{s}_1 \tag{2.35}$$

where $\mathbf{F} \equiv \partial r_2/\partial r_1$ is the deformation gradient, a rank-2 tensor. After operating at every material point in a body, it is taken from an undeformed (or reference) configuration to a deformed (or current) configuration. Fig. 2.20 illustrates this concept as well as vectors associated with the transformation of a single material point, $B$, within a larger body.
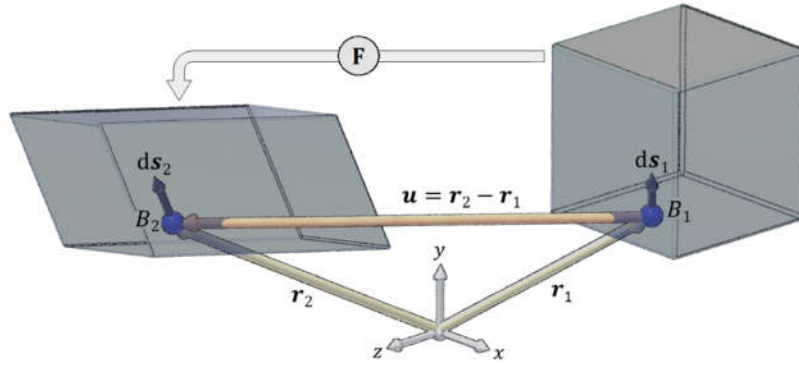
**Fig. 2.20:** Transformation of the line element, $\boldsymbol{s}$, at material point, $B$, from an undeformed to a deformed configuration. The transformation of all material points through the deformation gradient, $\mathbf{F}$, gives the body's updated configuration.

The deformation gradient is the most general descriptor of the kinematics of a body, but it is not the most mathematically convenient for some problems because strains and rotations are coupled in the tensor. When the tensor is referred to a coordinate system, which is required for numerical simulation, this coupling requires 9 independent components in the 3×3 matrix representation of $\mathbf{F}$. However, these can be decoupled with the **polar decomposition** of $\mathbf{F}$ to give:

$$\mathbf{F} = \mathbf{RU} \tag{2.36}$$

where $\mathbf{R}$ is a **rotation tensor** that captures only rigid body rotations, and $\mathbf{U}$ is the **right stretch tensor** which is purely a measure of strain. $\mathbf{R}$ is **orthogonal** which gives it the property, $\mathbf{R}^T\mathbf{R} = \mathbf{R}\mathbf{R}^T = \mathbf{I}$, where $(\circ)^T$ denotes the transpose operator and $\mathbf{I}$ is the **identity tensor**, which itself has the property $\mathbf{AI} = \mathbf{A}$ for any arbitrary rank-2 tensor, $\mathbf{A}$. The **transpose** operation can be interpreted by its matrix counterpart in which rows and columns are swapped, yielding the property, $\left(\mathbf{A}^T\right)^T = \mathbf{A}$. The stretch tensor is symmetric, giving it the useful property, $\mathbf{U}^T = \mathbf{U}$.

There are many other measures of strain aside from the stretch. For instance, the **left Cauchy-Green strain tensor** is given by:

$$\mathbf{B} = \mathbf{FF}^T = \mathbf{RU}^2\mathbf{R}^T \tag{2.37}$$

The second equality follows from the properties, $(\mathbf{RU})^T = \mathbf{U}^T\mathbf{R}^T$ and $\mathbf{U}^T = \mathbf{U}$ due to symmetry. This strain tensor has precisely the same invariants as those in Eq. 2.26 for Rivlin-type SEFs. Thus, there is a clear link between the kinematic formulations of finite elasticity and the strain-energy density of rubber as determined from thermodynamics. For further insight into these connections, the interested reader is referred to Holzapfel's textbook.[96] Bergström[97] provides a good supplement for numerical implementation of finite elasticity, as well as Section 4.2 and Appendices A, B, P, and Q in this thesis.

### 2.5.5 Volumetric Deformation

The volumetric behaviour of rubber, much like thermoelasticity, was a curiosity to early

researchers. In 1805, Gough[77] stated that the volume of rubber decreased when stretched, an incorrect assertion probably arising from inadequate experimental precision. In 1848, Wertheim[98] measured Poisson's ratios, $\nu$, for stretched rubber at finite strains, finding a value of $\approx 0.3$ at 100% strain. This implicitly suggested the volume had increased more than 30%, a vast overprediction. In 1859, Joule[99] found that rubber's volume increased $\approx 0.14\%$ upon stretching 100%, and by 1871 Thomson & Tait[100] deduced (without proof) that rubber's low stiffness should make it, roughly, an incompressible solid. In 1876, Röntgen[101] tested Thomson & Tait's hypothesis, and with a modified definition for Poisson's ratio, he found $\nu \approx 0.5$ at both low and finite strains, thus confirming rubber's low compressibility. Perhaps the most important lesson from Röntgen's study is that the linear elastic definition of Poisson's ratio does not accurately represent a finite volumetric response, a point that was reiterated by Bouasse in 1903.[102] Whitby[103] has given an excellent review of these early articles as most of them are not in English.

Treating rubber as an incompressible material can be useful, but in absolute terms, it is more compressible than metal. Their bulk moduli, $\kappa$, are on the order of 1 GPa and 100 GPa, respectively, but rubber can be approximated as incompressible because its shear modulus, $G$, is $10^2$–$10^3$ times lower than its bulk modulus, whereas $\kappa{:}G \approx 1{:}1$ in metals. However, it is inaccurate to treat rubber as an incompressible material at very high pressures, as Fig. 2.10 makes clear. Even at low pressures, it becomes necessary to consider rubber's compressibility if it is highly constrained – that is, if it has limited free surface area – because the constraint inhibits shear deformation; thus, the majority of any load on the rubber is stored in volumetric deformation. Most seals are highly constrained even prior to the application of differential pressure, so it is essential to consider their volumetric compressibility if a realistic model is required.

Finite elasticity theory addresses volumetric deformation though the **volume ratio** (also called the **Jacobian determinant** and often simplified to the **Jacobian**) which may be expressed by any of the following:

$$J = \frac{dV_2}{dV_1} = \det(\mathbf{F}) = \det(\mathbf{U}) = \sqrt{\det(\mathbf{B})} = \sqrt{I_3} = \lambda_1\lambda_2\lambda_3 \qquad (2.38)$$

where $\det(\circ)$ is the determinant operator and $J > 0$ is a scalar value that maps infinitesimal volumes near a point in an undeformed body to the same point in its deformed configuration. The inequality is required because $J = 0$ and $J < 0$ imply the volume vanishes and is negative, respectively, which are forbidden conditions in continuum mechanics. For an incompressible material, $J = 1$. When volume expands, $J > 1$, and when it contracts, $J < 1$.

Another important concept for addressing volumetric deformation in finite elasticity is the additive decomposition of any tensor into so-called spherical and deviatoric parts. This

is perhaps best introduced by referring to the matrix representation of the true stress tensor, $\hat{\boldsymbol{\sigma}}$, here denoted as $[\hat{\sigma}]$, which is:

$$[\hat{\sigma}] = \begin{bmatrix} \hat{\sigma}_{11} & \hat{\sigma}_{12} & \hat{\sigma}_{13} \\ \hat{\sigma}_{21} & \hat{\sigma}_{22} & \hat{\sigma}_{23} \\ \hat{\sigma}_{31} & \hat{\sigma}_{32} & \hat{\sigma}_{33} \end{bmatrix} \tag{2.39}$$

Letting $P = 3^{-1}(\hat{\sigma}_{11} + \hat{\sigma}_{22} + \hat{\sigma}_{33})$ and $\bar{\hat{\sigma}}_{ii} = \hat{\sigma}_{ii} - P/3$, the decomposition is expressed as:

$$[\hat{\sigma}] = [\hat{\sigma}]_0 + \overline{[\hat{\sigma}]} = \frac{1}{3}P\begin{bmatrix} 1 & 0 & 0 \\ 0 & 1 & 0 \\ 0 & 0 & 1 \end{bmatrix} + \begin{bmatrix} \bar{\hat{\sigma}}_{11} & \hat{\sigma}_{12} & \hat{\sigma}_{13} \\ \hat{\sigma}_{21} & \bar{\hat{\sigma}}_{22} & \hat{\sigma}_{23} \\ \hat{\sigma}_{31} & \hat{\sigma}_{32} & \bar{\hat{\sigma}}_{33} \end{bmatrix} \tag{2.40}$$

where $[\sigma]_0$ and $\overline{[\hat{\sigma}]}$ are the **spherical** and **deviatoric** parts of the decomposition, respectively. The spherical part characterises **dilatational** (volumetric) deformations that are strictly a function of hydrostatic pressure, $P$, on the body. The deviatoric part captures shear stresses that, by definition, cause **distortional** or **isometric** (volume-preserving) deformations. Converting to tensor notation, Eq. 2.40 is expressed as:

$$\hat{\boldsymbol{\sigma}} = \hat{\boldsymbol{\sigma}}_0 + \bar{\hat{\boldsymbol{\sigma}}} = \frac{1}{3}P\mathbf{I} + \bar{\hat{\boldsymbol{\sigma}}} \tag{2.41}$$

This decomposition allows volumetric and shear responses to be decoupled in constitutive models of rubber. One such model can be illustrated by invoking a multiplicative decomposition of the deformation gradient into dilatational and distortional parts:

$$\mathbf{F} = \left(J^{1/3}\mathbf{I}\right)\bar{\mathbf{F}} = J^{1/3}\bar{\mathbf{F}} \tag{2.42}$$

where $\left(J^{1/3}\mathbf{I}\right)$ and $\bar{\mathbf{F}}$ are dilatational and distortional contributions to $\mathbf{F}$, respectively. The dilatational nature of $\left(J^{1/3}\mathbf{I}\right)$ is revealed by noting that it has a form similar to $\hat{\boldsymbol{\sigma}}_0$ in Eq. 2.41. Because $\bar{\mathbf{F}}$, by definition, conserves volume, its determinant must be 1, so by analogy with Eq. 2.38 and comments thereafter, $\det(\bar{\mathbf{F}}) = 1$. Bearing in mind that, generally, $\det(\mathbf{F}) \neq 1$, it becomes necessary to define the so-called **modified principal stretches**, $\bar{\lambda}_i$s, that satisfy this modified incompressibility condition, $\det(\bar{\mathbf{F}}) = 1$. Thus:

$$\det(\bar{\mathbf{F}}) = \bar{\lambda}_1\bar{\lambda}_2\bar{\lambda}_3 = 1 \tag{2.43}$$

These are conveniently computed with the volume ratio as:

$$\bar{\lambda}_i = J^{-1/3}\lambda_i \tag{2.44}$$

From these definitions, it is possible to define the **modified left Cauchy-Green strain tensor** which strictly characterises the distortional strains in a body:

$$\bar{\mathbf{B}} = J^{-2/3}\mathbf{B} \tag{2.45}$$

By analogy with Eq. 2.26, which defines the invariants of $\mathbf{B}$ (which is itself defined in Eq. 2.37), the so-called **modified invariants** of $\bar{\mathbf{B}}$ are:

$$\begin{aligned} \bar{I}_1 &= \bar{\lambda}_1^2 + \bar{\lambda}_2^2 + \bar{\lambda}_3^2 \\ \bar{I}_2 &= \bar{\lambda}_1^2\bar{\lambda}_2^2 + \bar{\lambda}_2^2\bar{\lambda}_3^2 + \bar{\lambda}_1^2\bar{\lambda}_3^2 \\ \bar{I}_3 &= \bar{\lambda}_1^2\bar{\lambda}_2^2\bar{\lambda}_3^2 \end{aligned} \tag{2.46}$$

To exploit the dilatational and distortional decompositions, an SEF of the form:

$$W = W_{\text{vol}}(J) + W_{\text{iso}}(\bar{\mathbf{B}}) \tag{2.47}$$

can be postulated. Each term solely captures dilatational and distortional deformations, respectively. The Cauchy stress can then be expressed as:[97]

$$\hat{\boldsymbol{\sigma}} = \left[\frac{\partial W}{\partial J} - \frac{2\bar{I}_1}{3J}\frac{\partial W}{\partial \bar{I}_1} - \frac{4\bar{I}_2}{3J}\frac{\partial W}{\partial \bar{I}_2}\right]\mathbf{I} + \frac{2}{J}\left[\left(\frac{\partial W}{\partial \bar{I}_1} + \frac{\partial W}{\partial \bar{I}_2}\bar{I}_1\right)\bar{\mathbf{B}} - \frac{\partial W}{\partial \bar{I}_2}\bar{\mathbf{B}}^2\right] \tag{2.48}$$

When a strain-energy function is independent of $\bar{I}_2$, Eq. 2.48 simplifies to:

$$\hat{\boldsymbol{\sigma}} = \frac{\partial W}{\partial J}\mathbf{I} + \frac{2}{J}\frac{\partial W}{\partial \bar{I}_1}\left(\bar{\mathbf{B}} - \frac{1}{3}\text{tr}(\bar{\mathbf{B}})\,\mathbf{I}\right) \tag{2.49}$$

where $\text{tr}(\circ)$ denotes the trace operator, in this case giving $\text{tr}(\bar{\mathbf{B}}) = \bar{B}_{11} + \bar{B}_{22} + \bar{B}_{33}$. By analogy with Eq. 2.40, the term in parenthesis is simply the deviatoric part of $\bar{\mathbf{B}}$, so invoking the definition $\bar{\bar{\mathbf{B}}} \equiv (\bar{\mathbf{B}} - 3^{-1}\text{tr}(\bar{\mathbf{B}})\,\mathbf{I})$, Eq. 2.49 may be expressed by decoupled volumetric and distortional components:

$$\hat{\boldsymbol{\sigma}} = \frac{\partial W}{\partial J}\mathbf{I} + \frac{2}{J}\frac{\partial W}{\partial \bar{I}_1}\bar{\bar{\mathbf{B}}} \tag{2.50}$$

The first term is a scalar value, $\partial W / \partial J$, times the identity tensor, precisely of the same form as the dilatational terms in Eqs. 2.41 and 2.42. The factor of $J^{-1}$, though derived from a consideration of volumetric changes, appears in the deviatoric term strictly to remove volumetric distortions from the strain tensor. Some additional considerations on modelling volumetric compressibility are deferred to Section 4.2.3.

## 2.6 Linear Viscoelasticity

The previous section described the ideal elastic behaviour of rubbery materials in which deformations are fully reversible (that is, mechanical energy is conserved). In reality, all elastomers and rubbers, when deformed, have dissipative effects that are characteristic of viscous fluids. Consequently, these materials are viscoelastic, and their mechanical properties are time-dependent. Viscoelasticity arises from molecular relaxations (for instance, chain disentanglements) of polymer chains,[36,51] but for simplicity, a brief pheno-menological account of some observed behaviours is given here.[104,105]

### 2.6.1 Linear Viscoelasticity with Static Loading

The building blocks for linear viscoelastic models are springs and dashpots. For small simple shear strains, $\gamma$, and strain rates, $\dot{\gamma}$ (Fig. 2.21), these elements can be represented through Hooke's law and Newton's law of viscosity, respectively:[36]

$$\sigma_{\parallel} = G\gamma \tag{2.51}$$

$$\sigma_{\parallel} = \eta\frac{d\gamma}{dt} = \eta\dot{\gamma} \tag{2.52}$$

where $\gamma = \tan(\theta) = u/Y$ and $\eta$ is viscosity. (Strictly speaking, Eq. 2.51 requires a negative sign, but it is often dropped in engineering contexts.) The equations state that stress is

proportional to the strain and the strain rate in a solid and a fluid, respectively, as represented in Fig. 2.22. Stress in the viscous element is also plotted against strain to illustrate that a constant shear stress causes continuous straining (flow) in a fluid.
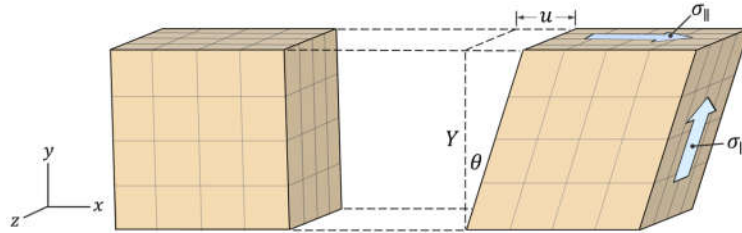


**Fig. 2.21:** Geometry of deformation for a small simple shear of a volume element.



**(a)**          **(b)**
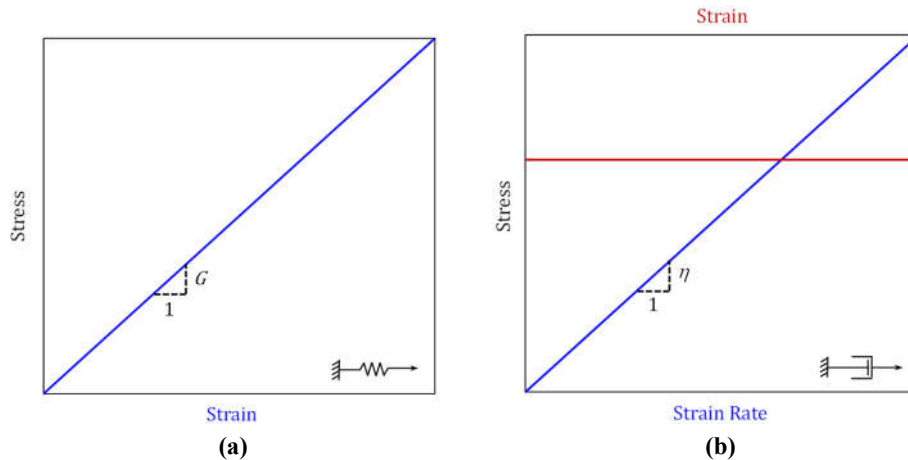
**Fig. 2.22:** Linear elastic and viscous responses according to Eqs. 2.51 and 2.52: **(a)** Hooke's law for a spring element with shear modulus $G$; **(b)** Newton's law for a dashpot with viscosity $\eta$.

A crosslinked rubber with small strains can be modelled reasonably well with Hooke's law, and an uncrosslinked rubber under specific conditions can approach a Newtonian response, at least over a narrow range of strain rates.[106,107] However, elastomers and rubbers generally require more complicated models to describe their rheology. The simplest models that capture some salient features of rubber viscoelasticity combine a spring and a dashpot. In the **Maxwell model**, these are in series, and in the **Voigt** (or **Voigt-Kelvin**) **model**, these are in parallel (see schematic illustrations in Fig. 2.23). Mathematically, these models may be expressed as:[36]

$$\sigma_\parallel(t) = \sigma_o e^{(-t/\tau)} \tag{2.53}$$

$$\gamma(t) = \gamma_\infty \left[ 1 - e^{(-t/\tau)} \right] \tag{2.54}$$

where $\sigma_o$ and $\gamma_\infty$ are an instantaneous shear stress and an equilibrium shear strain, respectively. $\tau = \eta/G$ is a characteristic (stress) **relaxation time** or (creep) **retardation time** that relates the stiffness and viscous behaviours of the model. The utility of these models arises from their exponential functions which, under appropriate loading conditions, cause the stress or strain response to decay over time.
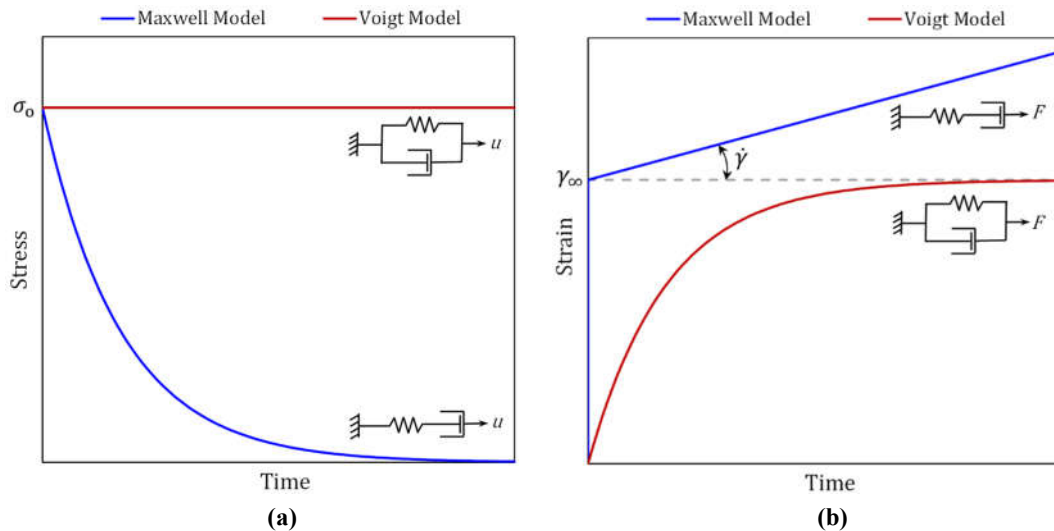
**Fig. 2.23:** Maxwell and Voigt models with: **(a)** a fixed displacement resulting in stress relaxation (note that the Voigt model cannot relax); **(b)** a constant force resulting in creep (note that the Maxwell model creeps indefinitely). (Adapted from Williams.)[108]

Either rheological model can be used to describe **creep** (a continued displacement with a fixed load) or **stress relaxation** (a reduction in force with a fixed displacement) phenomena, but not all models are appropriate for rubber viscoelasticity.[108] Fig. 2.23a shows that a Voigt model with a specified instantaneous displacement is unable to relax stress because the spring cannot unload, rendering the model practically identical to a simple spring. Therefore, the Maxwell model is better suited for modelling stress relaxation in polymers. Fig. 2.23b shows that the Maxwell model predicts continuous creep because, with a constant load, there is no internal mechanism to stop the dashpot's displacement. This may be acceptable for an uncured material, but it is inaccurate for crosslinked rubber; the Voigt model is more suitable since it asymptotically approaches a limiting strain.

Fig. 2.24a compares the Maxwell and Voigt models to rubber test data. The illustration is meant to be qualitative, so the data have been normalised for ease of plotting. The relaxation data are from an HNBR sealing material that has not been previously published, and the creep data is from a filled natural rubber as reported by Tunnicliffe[20] (compound N134 in Fig. 8.11). Neither set of data has reached an equilibrium value, but their changes asymptotically diminish. The figure makes clear that the Maxwell model is entirely inaccurate, needing an additional parameter to define a finite equilibrium stress. The Voigt model performs well although it struggles to capture the rapid changes in strain, a problem that is exacerbated by non-linearities associated with the filler (see Section 2.7).

The Maxwell model can be refined by applying a Prony series expansion to define the normalised relaxation modulus of a material so that:

$$G(t) = 1 - \sum_{i=1}^{n} G_i\left(1 - e^{(-t/\tau_i)}\right) \tag{2.55}$$

where n is the model order of the expansion. The stress can then be assumed to change in exact proportion with the relaxation modulus so that the definition of one determines the

other. This model is illustrated in Fig. 2.24b where it is shown that the stress is bound to a finite equilibrium value, and increasing the model order improves the fit. This same principle can be applied to the creep data in Fig. 2.24a to improve the fit of the Voigt model. The scaling of the shear modulus in Eq. 2.55 can be generalised to multi-parameter hyperelastic material models as discussed by Windslow & Busfield.[109] The authors also demonstrated that, although the Prony series expansion is a linear viscoelastic model, it can successfully model a response with finite strains.
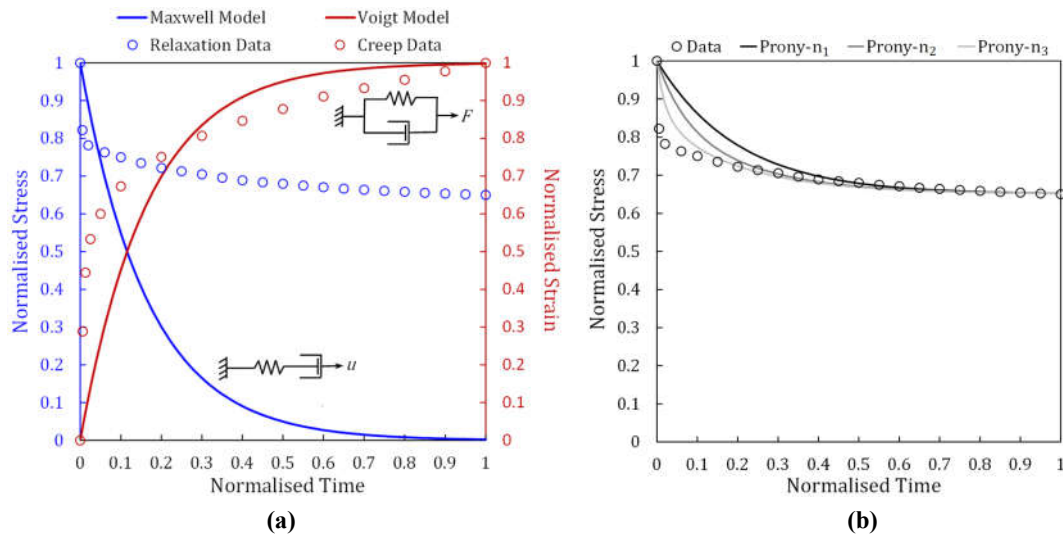


**Fig. 2.24: (a)** Maxwell and Voigt models fit to normalised test data for filled rubbers. **(b)** Prony series model with 3 different model orders fit to the stress relaxation data from Fig. 2.24a.

The Maxwell and Voigt models can be combined to describe more complicated behaviours. One such option, the **Burger model**,[110] is illustrated in Fig. 2.25a, and its response to a static loading and unloading is shown in Fig. 2.25b. The numbers in Fig. 2.25b correspond to the numbered elements that are active in Fig. 2.25a during a specific portion of the strain response. When the load is applied, it generates an instantaneous strain, $\gamma_o$, (1). Next, creep occurs under constant load (2). It is a combination of reversible strain, $\gamma_e$, due to the dashpot in parallel and irreversible strain due to the dashpot in series. Once the reversible strain terminates, completely irreversible creep occurs (3). The total plastic strain, $\gamma_p$, can be deduced by projecting the slope of this linear region to the ordinate. When the load is removed, $\gamma_o$ is completely recovered (4). The elastic portion of the creep is then recovered (5), and residual plastic strain remains in the system. Increasingly complex behaviour that includes multiple relaxation and retardation times can be simulated by adding more elements to the Maxwell, Voigt, and Burger models.[105]
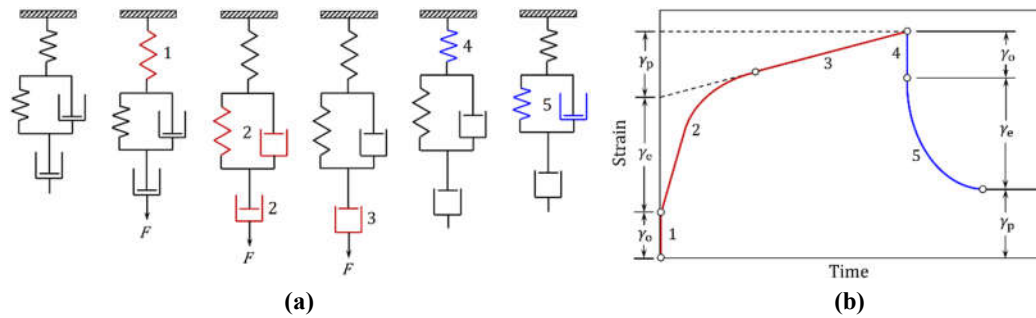
**Fig. 2.25: (a)** A Burger model subjected to loading and unloading with a constant force.
**(b)** Creep response in the model. (Adapted from Cowie & Arrighi.)[36]

**Boltzmann's principle of superposition** is essential for constructing mechanical response curves in linear viscoelasticity. It states that when, for instance, multiple discrete loads are applied to a viscoelastic body, the total strain is the algebraic sum of the individual strains that arise from each load. Thus, the system's total response depends on the load history, but constituent responses are completely decoupled from one another. Fig. 2.26 illustrates this concept with three discrete loads that cause creep. The principle can be extended to loads that vary continuously in time,[104] and Williams[108] illustrates how this is done by introducing a convolution integral to activate and deactivate loads at different time intervals.
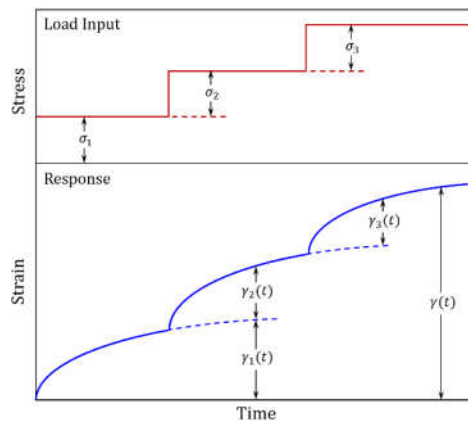


**Fig. 2.26:** Principle of superposition applied to a Voigt element with 3 instantaneous loads.

## 2.6.2  Linear Viscoelasticity with Dynamic Loading

The previous section shows that as time elapses during static loading, rubber becomes more compliant. Conversely, as excitation frequency increases during dynamic loading, rubber becomes stiffer. Both of these behaviours arise from the molecular response time(s) of rubbery materials. Understanding how dynamic loads alter material properties is critical in applications such as shock absorption and vehicle braking where small strain approximations are practically useful even though finite strains may occur. The theory can also be applied to mud motors and progressive cavity pumps in the oilfield.[73] Therefore, this section discusses some aspects of small strain dynamic loading of rubber.

When a dynamic force is applied to an ideal elastic material, the resulting deformation

42

is instantaneous, so the stress and strain curves are in phase with one another. When a dynamic stress is applied to a Newtonian fluid, the strain response is out of phase by $\pi/2$. In a viscoelastic material, the behaviour falls between these two extremes.[105] Because an elastic response conserves energy and a viscous one is purely dissipative, it is possible to determine the elastic and viscous components of a viscoelastic material through the phase difference between an applied stress and the resultant strain, or vice versa.

Fig. 2.27 illustrates load and response curves for a viscoelastic material that is harmonically excited at a frequency, $f = 2\pi\omega$. The strain response lags the applied stress but oscillates with the same frequency, giving the following stress-strain relations:

$$\sigma_{\parallel}(t) = \sigma_0 \sin(\omega t) \tag{2.56a}$$

$$\gamma(t) = \gamma_0 \sin(\omega t - \delta) \tag{2.56b}$$

where $\delta$ is the **loss tangent** (or phase lag) in the strain.

In complex notation, the stress and strain may be related as:[36,105]

$$\gamma(t) = \gamma_0 e^{i\omega t} \tag{2.57a}$$

$$\sigma_{\parallel}(t) = (G' + iG'')\gamma(t) = G^* \gamma(t) \tag{2.57b}$$

where $i = \sqrt{-1}$, and the **complex modulus**, $G^*$, is determined from the **storage modulus**, $G'$, and **loss modulus**, $G''$. $G'$ characterises elastic energy that is stored during a deformation cycle. Although $G''$ is associated with the imaginary part of $G^*$, it characterises a real quantity and is proportional to the energy dissipated during a cycle. The storage and loss moduli are related to the loss tangent by:

$$\tan(\delta) = \frac{G''}{G'} \tag{2.58}$$

The following relations also hold for the complex modulus and its components:[104]

$$G^* = \frac{\sigma_0}{\gamma_0} = G'\sqrt{1 + \tan^2(\delta)} = \sqrt{(G')^2 + (G'')^2} \tag{2.59a}$$

$$G' = \left|\frac{\sigma_{\parallel}}{\gamma_0}\right| = \left|\frac{\sigma_0}{\gamma_0}\right| \cos(\delta) \tag{2.59b}$$

$$G'' = \left|\frac{\sigma_{\perp}}{\gamma_0}\right| = \left|\frac{\sigma_0}{\gamma_0}\right| \sin(\delta) \tag{2.59c}$$

where $\sigma_{\parallel}$ is the stress component in phase with the peak strain and $\sigma_{\perp}$ is the stress component that is 90° out of phase with the peak strain, as illustrated in Fig. 2.27.
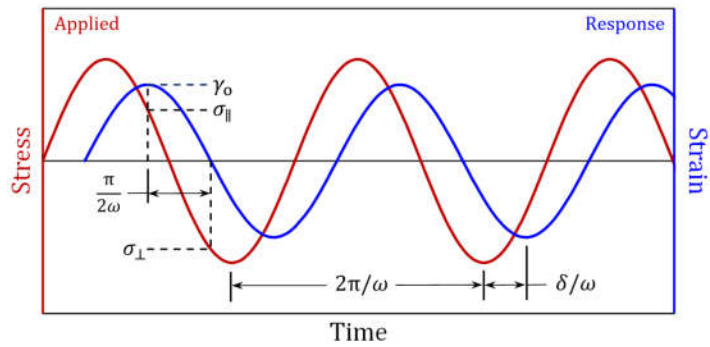
**Fig. 2.27:** A harmonic stress (applied) and strain (response) for a viscoelastic material. The strain has the same frequency as stress, but lags by a factor of $\delta/\omega$.

To summarise, a sinusoidal stress can be applied to a rubber sample (Eq. 2.56a), and the sinusoidal strain response can be measured (Eq. 2.56b) to determine the strain magnitude, $\gamma_o$, and the loss tangent, $\delta$. With Eqs. 2.56a and 2.56b fully determined, the complex modulus can be computed from the first equality in Eq. 2.59a. Finally, the storage and loss moduli can be determined with the second and third equalities in Eq. 2.59a, respectively, thereby characterising energy storage and loss during a deformation cycle. Eqs. 2.58, 2.59b, and 2.59c provide alternate routes for these computations.

Fig. 2.28 graphically shows the relationship between $E'$, $E''$, $\tan(\delta)$, and temperature for an unfilled natural rubber compound, where according to linear elastic theory and assuming incompressibility, $E' \approx 3G'$ and $E'' \approx 3G''$[105] over a range of temperatures through the glass transition. The rubber was excited at a frequency of 1 Hz. Below $T_g$, the material is glassy with $E'$ of the order of GPa, and $\tan(\delta)$ is low. Through the glass transition, $E''$ overtakes $E'$ which indicates significant energy dissipation. Correspondingly, $\tan(\delta)$ peaks through the transition. As the material becomes increasingly rubbery, $E'$ overtakes $E''$ and $\tan(\delta)$ drops significantly, a trend that would continue through the rubbery plateau (see Fig. 2.29) which is not shown in Fig. 2.28.
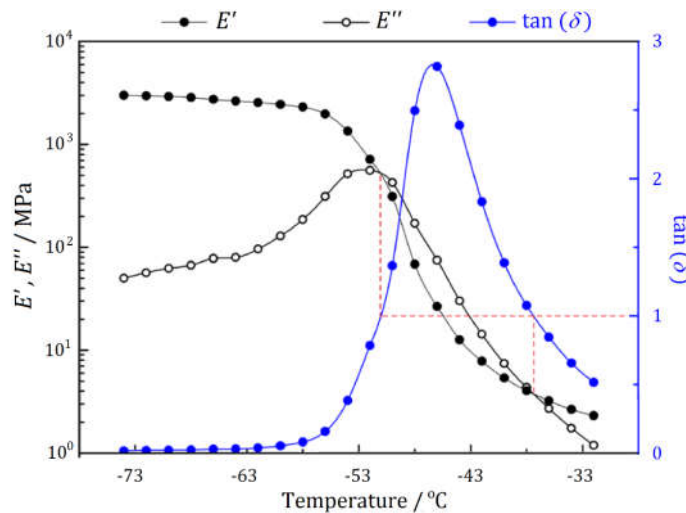


**Fig. 2.28:** Storage modulus, loss modulus, and loss tangent for an unfilled crosslinked natural rubber. Note that $\tan(\delta) = 1$ when $E' = E''$, indicating equal elastic and viscous contributions to the complex modulus. (Adapted from Tunnicliffe.)[20]

44

Below $T_g$, energy loss is low because the rubber molecules are essentially frozen in place, and the rubber, though still amorphous, has mechanical behaviour that is similar to other elastic solids. In the transition zone, the temperature is sufficiently high to thermodynamically drive molecular motion, but the free volume is insufficient to fully accommodate those motions. Hence, the glass transition is a region of maximal molecular interference and, consequently, maximum energy dissipation. Above $T_g$, the free volume is large enough to allow relatively unrestricted molecular motion.

### 2.6.3 Time-Temperature-Pressure Superposition

The glass transition temperature in Fig. 2.28 can be defined at any of a few different points: (i) at the peak of $E''$ (– 52°C); (ii) where the concavity of $E'$ changes (– 49°C); or (iii) at the peak of $\tan(\delta)$ (– 46°C). Regardless of what is chosen, all these temperatures are significantly higher than $T_g$ = – 69°C reported in Table 2.1. The upward shift is typical for dynamic measurements (unless of course $f \ll 1$ Hz) because the polymer chains have less time to relax during such tests. Consequently, the moduli of rubber materials are a function of excitation frequency. Because the mechanical properties of rubber are temperature- and time-dependent over several orders of magnitude, it quickly becomes a burden to test a full range of independent variables. In some cases, it is also difficult to test rubber parts at their operational timescales. For instance, vehicle tyres experience vibrational frequencies in the kHz – MHz range during braking, but test equipment may be limited well below these orders of magnitude.[20] Another issue arises when testing static creep or stress relaxation because the timescales can grow prohibitively long. Provided a rubber is **thermo-rheologically simple**, which means that it is a single-phase and single transition homopolymer or random copolymer,[64] the principle of **time-temperature superposition** (TTS) provides a method to predict mechanical properties over broader timescales than those physically tested. The premise of TTS is that time and temperature affect molecular motion in the same way, so they can be reduced to a single independent variable.[§] Therefore, test data using an experimentally practical timescale at several temperatures can be shifted by orders of magnitude along the time axis to predict mechanical properties at much lower and higher frequencies (or equivalently, lower and higher relaxation times).

Fig. 2.29 illustrates TTS using the stress relaxation data of Catsiff & Tobolsky[111] for a butyl elastomer. Reviewing the authors' references, the material was presumably unvulcanised although they do not explicitly state this. The experimental data (right) covers

---

[§] An assumption in elementary TTS is that all relaxation times in the material have the same temperature shift factors. This assumption is almost always violated in practical engineering materials due to the complexity of rubber compounds. They are highly engineered composites with complex chemistries, so there are multiple relaxation times due to various molecular interactions. So, TTS and similar theories should be used cautiously for industrial rubber compounds.

a timescale from 60–3,600 s with a temperature range from –79°C to 25°C. In the master curve (left), data at 25°C are fixed in place and act as an arbitrarily chosen reference temperature. Data from the other tests are shifted left by temperature-dependent factors, $a_T$, whose magnitudes increase as $|T - T_{ref}|$ increases. In the master curve, the left portion of the data tends toward glassy behaviour. The glass transition zone is broad which is characteristic of IIR. An indication that the material was unvulcanised is the diminution of the modulus after the rubbery plateau, transitioning to a terminal region that is related to the material's viscosity.[36] The poor alignment of data points through the rubbery region can be smoothed with additional corrections,[111] but shifting data that is relatively flat, like that at –20°C, is subject to large uncertainty. Also note that the time axis in some TTS plots does not include the $a_T$ factor in the axis label, although it still implicitly there.
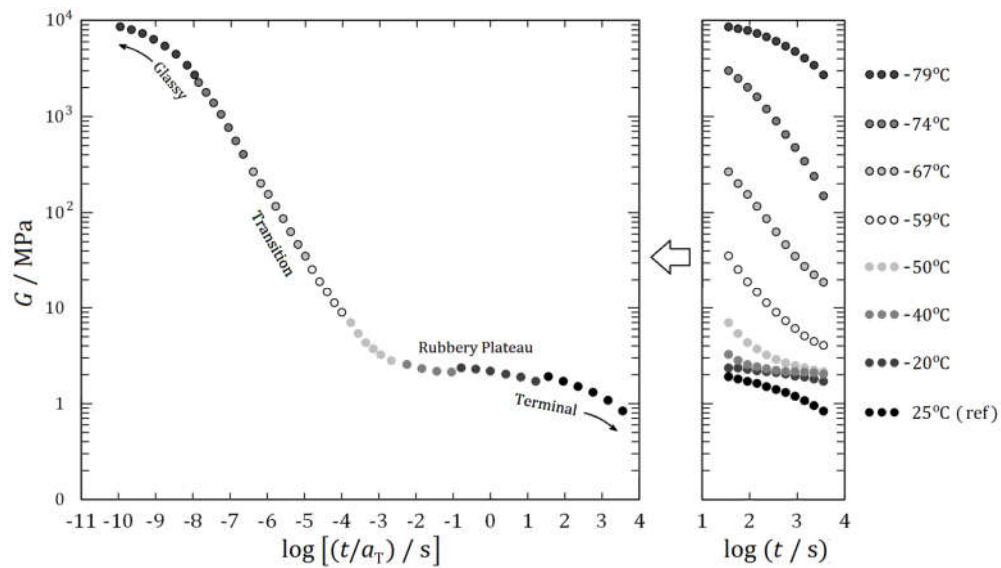


**Fig. 2.29:** TTS master curve (left) for the relaxation modulus of IIR, constructed from the experimental data (right) with a reference temperature of 25°C. For clarity, not all points from the data are retained in the master curve. (Adapted from Catsiff & Tobolsky.)[111]

Different equations have been proposed for TTS shift factors. One of the most common is the **Williams-Landel-Ferry (WLF) model**:[112]

$$\log(a_T) = \frac{C_1(T - T_{ref})}{C_2 + (T - T_{ref})} \tag{2.60}$$

where $C_1$ and $C_2$ are fitting parameters, $T$ is the temperature that is shifted, and $T_{ref}$ is the arbitrary reference temperature for shifting other temperatures (that is, $T_{ref}$ is not shifted). When generating master curves, $C_1 = 40$ and $C_2 = 50$°C are recommended initial guesses, but some rubbers may depart significantly from these values. For instance, butyl rubber has $C_2 = 100$°C.[105] Although the WLF equation originated from phenomenological observations, it can be derived from thermodynamic arguments based on the free volume concept. See, for instance, Moonan & Tschoegl[113] and references therein.

Section 2.3 shows that the glass transition is pressure-dependent. Consequently, **time-**

**pressure superposition** (TPS) can be applied to **piezo-rheologically simple** rubbers which, analogous to thermo-rheologically simple materials, have molecular dynamics whose response times all depend on pressure in the same manner. Although academic literature on TPS is relatively sparse, it has significant implications for oilfield applications where dynamically loaded rubber components (for instance, in mud motors) experience high hydrostatic pressures.[73] A recent summary of the subject, including a recommended experimental apparatus, is given by Aulova *et al.*[41] Some data from their work with natural rubber is shown in Fig. 2.30. The reference pressure is at atmospheric conditions, and as pressure increases, the modulus increases which indicates longer relaxation times. The inset in this figure shows the shift factors, $a_P$, and in this case, they are linear on a logarithmic scale. This linearity is not generally present when superposing data. A comparison of Figs. 2.29 and 2.30 shows that molecular response times are much more sensitive to temperature changes than pressure. The transition in the former occurs over $\Delta T$ on the order of $10^2$, whereas in the latter $\Delta P$ is on the order of $10^4$. As mentioned in Section 2.3, this difference probably occurs because temperature affects both thermal excitations and free volume while pressure primarily affects only the latter.
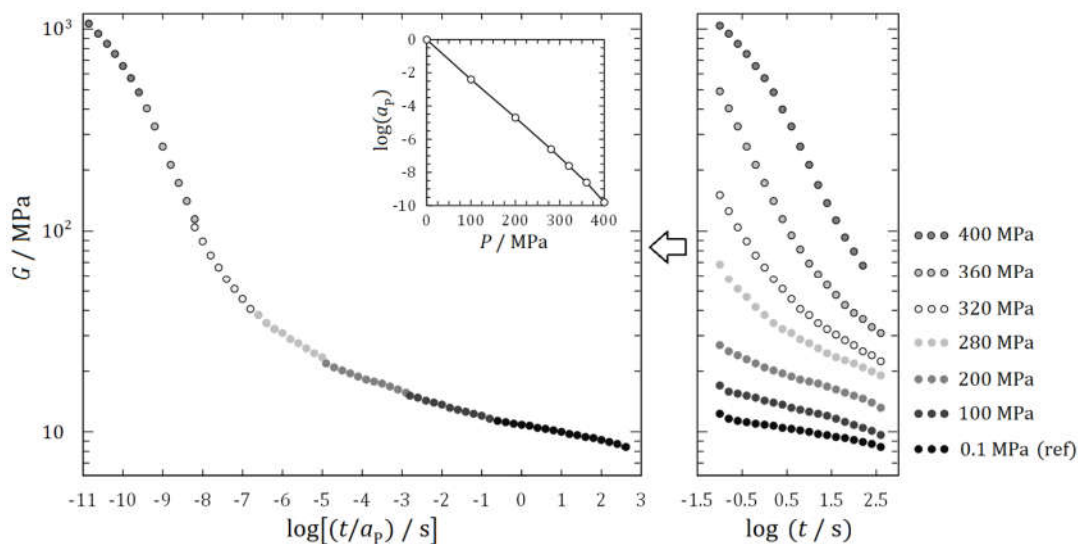


**Fig. 2.30:** TPS master curve (left) for the relaxation modulus of NR, constructed from the experimental data (right) with a reference pressure of 0.1 MPa. For clarity, not all points from the data are retained in the master curve. (Adapted from Aulova *et al.*)[41]

Different models have been proposed to extend the WLF equation for time-temperature-pressure superposition (TTPS). For example, the **Fillers-Moonan-Tschoegl (FMT) model** has the form:[41]

$$\log(a_{T,P}) = \frac{C_1[(T-T_{ref})-f(P)]}{C_2(P)+(T-T_{ref})-f(P)} \tag{2.61}$$

The equation adds a pressure functional, $f(P)$, to the WLF equation, and $C_2$ becomes a function of pressure as well. The model has six fitting parameters which are not detailed here but may be found in Aulova *et al.*[41] Some of these parameters are not entirely

empirical, but arise from thermodynamic relations such as thermal expansivity and bulk modulus.

## 2.7 Fillers in Rubber Compounds

Fillers are materials that are compounded with rubber to reduce cost, give pigment, improve processing, enhance ageing performance, or enhance (reinforce) mechanical properties. Today, the term "filler" can refer to any of these functions, but through the early 20th century, it usually referred to inert, non-reinforcing materials that reduced cost. The consolidation of terms may have arisen because some fillers serve multiple purposes simultaneously.

Filled rubber was common at least by the mid-1870s. Oenslager[114] indicated that the earliest non-reinforcing and reinforcing fillers were, respectively: (i) calcium carbonate (whiting) and barium sulphate; and (ii) zinc oxide, light magnesium carbonate (hydromagnesite, a hydrated mineral containing $MgCO_3$), and white lead (lead carbonate). Technically, carbon black in the form of lamp black was among these earliest fillers, but it was used as a colouring agent. Its particle size, which is about 1 μm, precludes its use as a quality reinforcing agent.[115,116] Mote[23,116] is credited with the first studies on genuine rubber reinforcement with carbon black in 1904, but his work was not popularised until 1912 when Oenslager[9] of B.F. Goodrich incorporated carbon black in vehicle tyres. Today, it is the dominant reinforcing filler. Zinc oxide is still used, albeit usually in small quantities as an activator, not a reinforcing agent. White lead is no longer used due to its toxicity, and hydromagnesite, despite showing some early promise as a reinforcing agent,[117,118] is largely obsolete.

Fig. 2.31 shows some mechanical properties for natural rubber with different fillers. Fig. 2.31a displays stress-strain curves for rubber with a reinforcing filler volume content of 17%. A curve for the unfilled rubber is shown to illustrate that the filled rubber is stiffer in each case, and the upward inflection in the response occurs at a lower strain in filled rubbers. In natural rubber, this upward inflection is due to a combination of strain-induced crystallisation (SIC) and finite-extensibility of the polymer chains. During SIC, some portion of the stretched polymer chains, say 10–20%,[119] crystallise and significantly increase stiffness. Finite-extensibility also has a stiffening effect because fewer chain conformations are available as the molecules stretch. These stiffening effects occur at lower strains in filled rubbers due to strain amplification (see Section 2.7.1). The increases in strength and stiffness, as well as the decrease in elongation, for the filled rubbers are typical. Because of this tradeoff between stress and strain, it is not straightforward to directly compare how well different fillers reinforce rubber from stress-strain curves, so other metrics are useful, with proof resilience and abrasion resistance being common.[120]
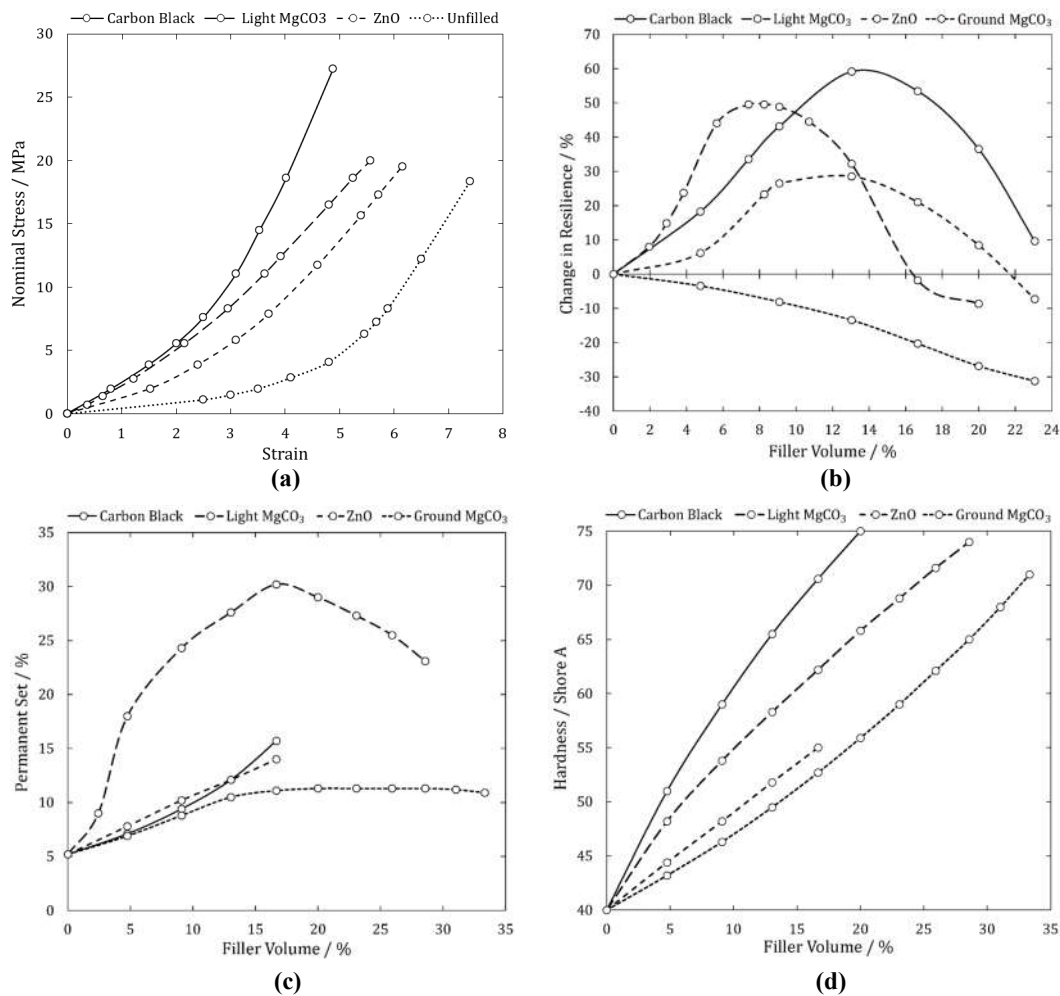
**Fig. 2.31:** Effect of different fillers on some mechanical properties of natural rubber: **(a)** uniaxial stress-strain curves with a filler volume content of 17%; **(b)** resilience at fracture (area under the stress-strain curves); **(c)** permanent set; **(d)** hardness. (Adapted from Greider.)[117],[118]

**Proof resilience**, or the total energy required to fracture a test specimen, is a good gauge to determine reinforcing capability. The resilience with some different fillers and volumes is shown in Fig. 2.31b. Hydromagnesite approaches the reinforcing capability of carbon black, but its use as a reinforcing filler is generally discouraged because its **permanent set** (residual, plastic deformation after the load is removed) is at least 2.3 times higher than that of carbon black if one subtracts the 5% offset that is inherent in the unfilled rubber (Fig. 2.31c). The resilience with a non-reinforcing filler, ground magnesite ($MgCO_3$), is also shown. It monotonically reduces the energy required to fracture the sample, and therefore, it cannot be used for mechanical reinforcement.

Although different mechanical properties can be chosen to assess reinforcing capability, some are poor choices. For example, Fig. 2.31c shows that permanent set is lowest with ground $MgCO_3$, but it has no reinforcing capability at all. Fig. 2.31d makes clear that hardness is also a poor choice because both reinforcing and non-reinforcing materials affect hardness in a similar manner. Despite this, the mechanical behaviour of rubber is often reduced to its hardness in the oilfield, a poor practice that has been slow to change.

49

### 2.7.1 Reinforcing Mechanisms in Filled Rubber

In the 1920s, researchers began debating the reinforcing mechanisms in filled rubber.[121-124] Despite sustained and continuing research this area, definitive answers remain elusive because of the practical difficulty of isolating different mechanisms that occur simultaneously. In this section, a brief account of the topic is given, and the interested reader is referred to Tunnicliffe[20] for more details.

Fig. 2.32 illustrates the generally accepted notion that at least four different factors contribute to the bulk mechanical properties (in this case, shear modulus is chosen) of a rubber compound.[125] The baseline rigidity is due to the rubber itself. For small filler volume fractions, $\phi_v$, stiffness increases through a **hydrodynamic** reinforcement mechanism. The simplest mathematical model of this effect was given by Einstein[126] in 1906 who was studying the increase in viscosity when solute is added to a solvent:

$$\eta = \eta_o(1 + 2.5\phi_v) \tag{2.62}$$

where $\eta$ is the viscosity of the solution and $\eta_o$ is the viscosity of the solvent. Smallwood[127] adapted this equation for elastic solids to give an entirely analogous form:

$$G = G_o(1 + 2.5\phi_v) \tag{2.63}$$

where $G$ is the shear modulus of the filled rubber and $G_o$ is the shear modulus of the unfilled, crosslinked elastomer. Some of the simplifying assumptions in this model are: (i) the fillers are rigid spheres; (ii) a no-slip boundary condition exists between the rubber and filler particles; and (iii) there are no filler-filler interactions (that is, the particles are well-spaced). None of these are practical in an industrial sense because: (i) filler morphology is generally complex; (ii) the rubber-filler boundary condition is open to debate; and (iii) $\phi_v$ is often sufficiently large that filler-filler interactions are guaranteed. To address some of these limitations, the Guth-Gold equation and its modified form were proposed:[128]

$$G = G_o(1 + 2.5\phi_v + 14.1\phi_v^2) \tag{2.64}$$

$$G = G_o(1 + 0.67f_s\phi_v + 1.62f_s^2\phi_v^2) \tag{2.65}$$

where the first equation is for spherical particles and the second equation includes a morphology-dependent shape factor, $f_s$, for the filler.
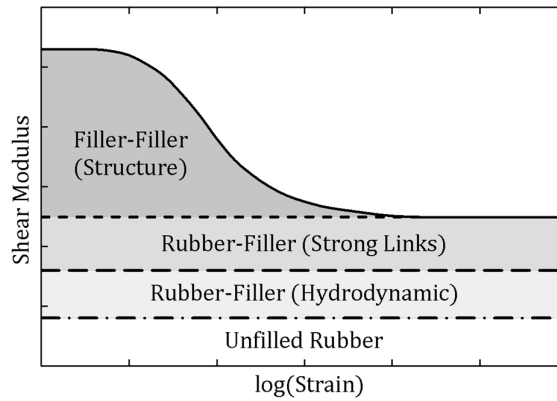
**Fig. 2.32:** Contributions to a rubber's shear modulus. (Adapted from Payne.)[125]
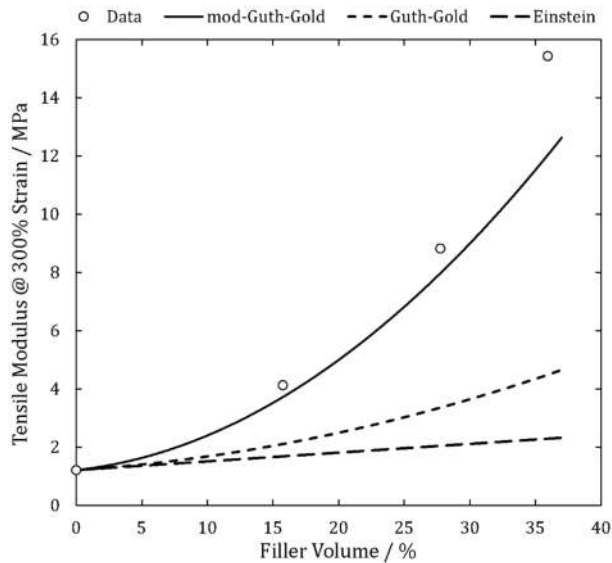


**Fig. 2.33:** Comparison of different models for hydrodynamic reinforcement of filled SBR. $f_s = 6$ for the modified Guth-Gold equation. (Adapted from Cohan.)[129]

Fig. 2.33 shows the increasing accuracy of Eqs. 2.63–2.65, but even the modified Guth-Gold equation systematically under-predicts the rubber's stiffness as $\phi_v$ increases. Presumably, some of this error occurs because the models do not account for bound and occluded rubber. **Bound rubber** is physically restrained or chemically adsorbed, perhaps even bonded, to filler **aggregates** (clusters of filler particles), while **occluded rubber** is trapped by tightly packed filler **agglomerates** (clusters of aggregates). Both are shielded from global strains as illustrated in Fig. 2.34. Their presence is deduced from the fact that a fraction of rubber cannot be recovered from a filled compound upon dissolution in a solvent.[130] Bound and occluded rubber effectively increase the volume fraction of the filler which leads to a systematic underprediction of stiffness with Eq. 2.65. The final form of this equation is subject to some uncertain assumptions, so different forms have been proposed.[131] It should be noted that there is no clear delineation between the hydrodynamic reinforcement and rubber-filler interactions (strong links) in Fig. 2.32; therefore, interpretation remains qualitative.
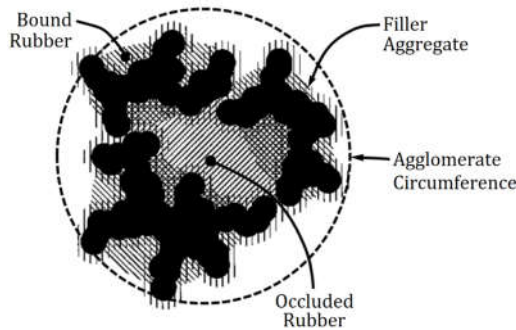
**Fig. 2.34:** Bound and occluded rubber. (Adapted from Tunnicliffe.)[20]



**Fig. 2.35:** Carbon black mixed with low viscosity paraffin oil. (Adapted from Warasitthinon *et al*.)[132]

Fig. 2.32 shows that the final level of reinforcement comes from filler-filler interactions. To achieve this, the filler must be fully dispersed and have a sufficient volume to reach the **percolation threshold** which is the point at which the filler forms a fully permeating network in the rubber matrix. The importance of such structures in determining the stiffness of rubber compounds has been demonstrated by Warasitthinon and coworkers.[132] They mixed carbon black with low-viscosity paraffin oil and showed that the behaviour and magnitude of the composite structure's shear modulus resembled that of a similarly loaded SBR compound. The structural integrity of the oil and carbon black mixture is illustrated in Fig. 2.35 where a ball of the material showed no signs of creep after sitting for 140 days. Generally, filler-filler reinforcement is less stable than the other reinforcing mechanisms, as discussed in the next section.

### 2.7.2 The Payne Effect

Fig. 2.32 shows that the reinforcement due to filler-filler interactions reduces as the strain amplitude increases, a non-linear viscoelastic phenomenon known as the **Payne effect** (synonymously called the **Fletcher-Gent effect**).[133] This results from a microstructural breakdown of the filler network which causes the storage modulus to decrease as strain increases (Fig. 2.36a), and this is concomitant with an energy loss that manifests as a higher loss modulus in filled rubber (Fig. 2.36b). The Payne effect reduces as temperature increases (Fig. 2.37), presumably because thermal energy reduces the strength of the percolated filler network.
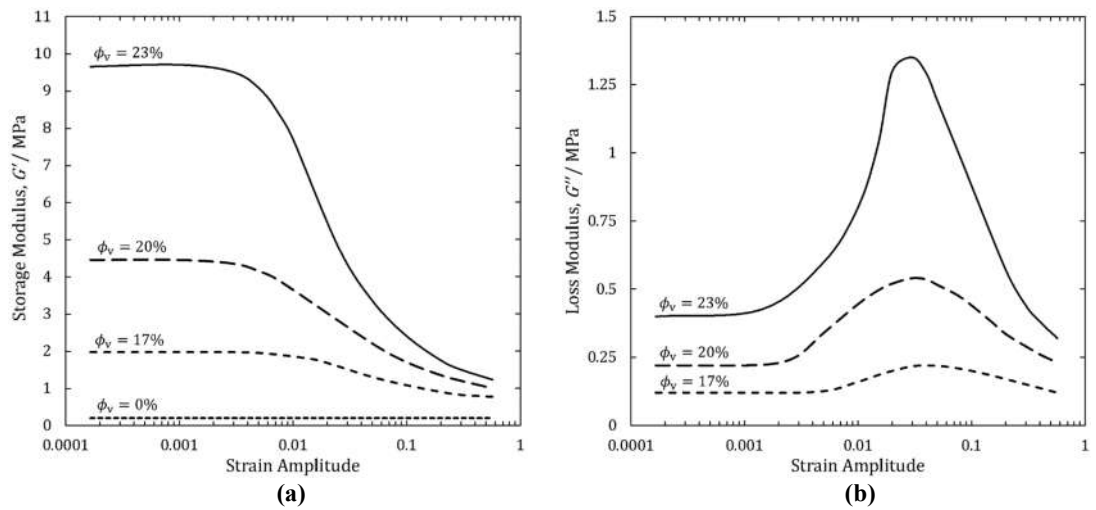
**Fig. 2.36:** The Payne effect in butyl rubber with harmonic loading and different volume fractions of carbon black: **(a)** storage modulus in shear; **(b)** loss modulus in shear. Strain amplitudes are measured from peak-to-peak. (Adapted from Payne & Whittaker.)[134]
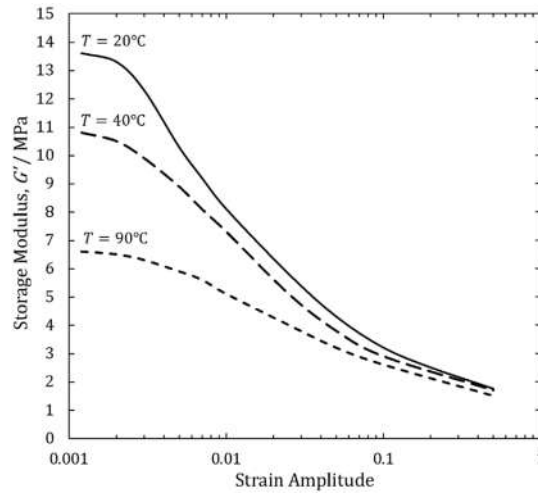


**Fig. 2.37:** Reduction in the Payne effect as temperature increases for natural rubber filled with carbon black and $\phi_v = 32\%$. Strain amplitude is measured from peak-to-peak. (Adapted from Payne & Whittaker.)[134]

### 2.7.3 Hysteresis, The Mullins Effect, & Cyclic Stress Softening

During a loading-unloading cycle, rubber exhibits a hysteretic energy loss as illustrated by the red and blue paths in Fig. 2.38. The difference in area between the solid and dashed lines gives mechanical energy loss. This effect was perhaps first described by Bouasse & Carriere in 1903,[135] and it is an inherent feature of rubber viscoelasticity. It is amplified by strain-induced crystallisation and the presence of reinforcing fillers, manifesting as heat which can be detrimental in rubber components that are dynamically loaded.

In the 1940s and 1950s, Mullins[106,136] published numerous papers studying hysteresis in rubber, and he observed what has become known as the **Mullins effect**. This is illustrated in Fig. 2.38. The red trend shows initial loading (1) and unloading (2) curves. On a subsequent strain cycle, the loading curve follows curve (2) until it reaches the maximum

strain from the previous cycle, and then it follows curve (3) to a higher strain limit. The final unloading path is given by curve (4). The path defined by the union of curves (1) and (3) is identical to the stress-strain curve that would have been achieved if the sample had been loaded to the maximum strain limit (defined by the apex of curve (3)) during the first deformation cycle.

The behaviour in Fig. 2.38 is ideal. In practice, there is a smooth transition zone between curves (2) and (3), and curve (3) does not precisely follow the illustrated path, instead showing slightly softer behaviour. In addition, the load path on the second cycle usually lies between curves (1) and (2), and the unloading paths do not return to the origin due to permanent deformation. This plastic behaviour is illustrated for an oilfield sealing material in uniaxial compression in Fig. 2.39. Because the strain magnitude in Fig. 2.39 is constant, the Mullins effect is not fully illustrated in the figure, but the cyclic softening behaviour is apparent. The figure also makes clear that cyclic stress softening attenuates as the cycle count increases. Consequently, rubber can be preconditioned with deformation to reach a more stable response before testing or operational deployment.
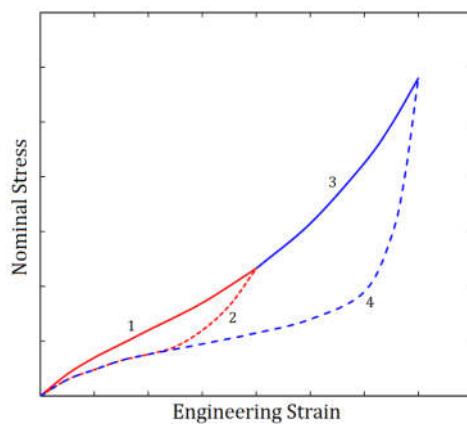


**Fig. 2.38:** An ideal Mullins effect: solid = loading; dashed = unloading.
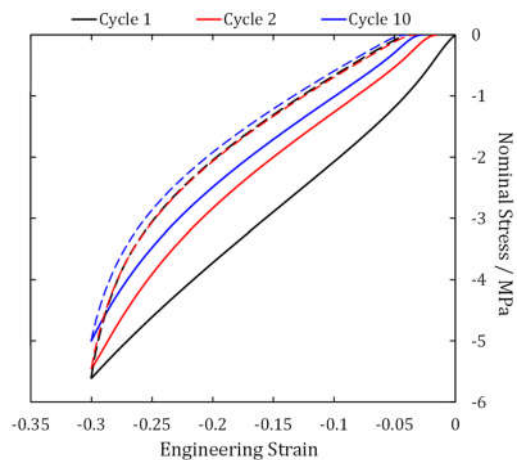
**Fig. 2.39:** Cyclic stress softening with permanent set in uniaxial compression for a filled HNBR compound: solid = loading; dashed = unloading.

### 2.7.4 Effects of Filler on the Glass Transition, Entropic Elasticity, and TTS

As a filler's volume fraction and reinforcing capability increase in a rubber compound, characterisation of the mechanical properties becomes increasingly complicated. For example, Fig. 2.40a shows that in the region of rubbery behaviour, say from 0–80°C, the stiffness of the unfilled rubber increases linearly with temperature (note that the upward trend is barely discernable due to the logarithmic ordinate). However, the stiffnesses of the filled rubbers decrease in this range which is in accord with the inverse relationship between the filler network strength and temperature from Fig. 2.37. The filler also broadens the glass transition zone because it retards molecular relaxation due to physical constraint on the polymer chains. Fig. 2.40b shows TTS master curves for filled and unfilled

compounds. The curve for the unfilled compound is smooth, but there is a breakdown in superposition with the filled material because two relaxation times are associated with the filled rubber: that of the polymer and that of the filler structure. Klüppel[137] demonstrated how to correct the master curve for this effect. The point to emphasise is that additional processing is required when analysing filled rubbers even when restricted to characterising small strains.
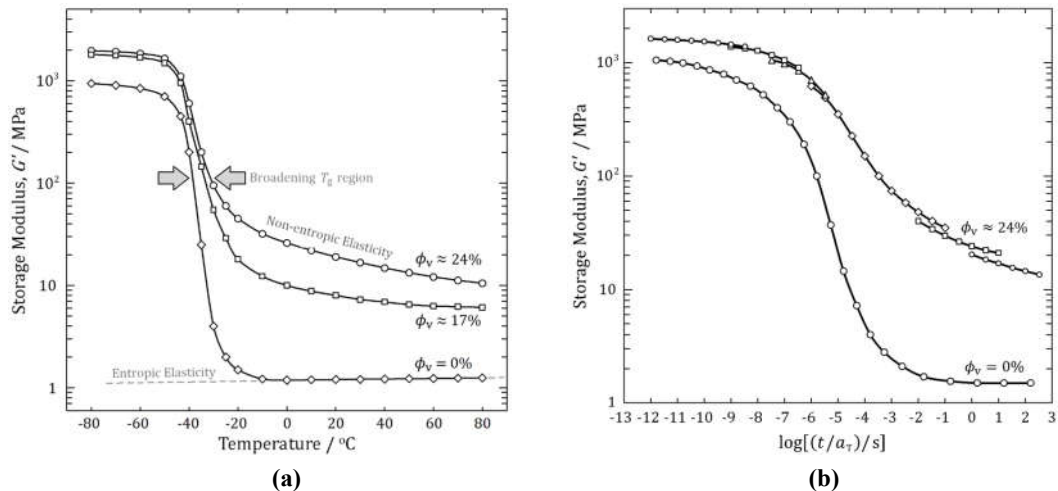


**Fig. 2.40:** Effect of carbon black filler on the small strain storage modulus of an SBR-vinyl rubber: **(a)** as a function of temperature, the glass transition broadens and entropic elasticity is increasingly masked as $\phi_v$ increases; **(b)** as a function of time, TTS breaks down and requires a vertical shift. (Adapted from Klüppel[137] and Fritzsche & Klüppel.)[138]

## 2.7.5 Carbon Black and Precipitated Silica

Carbon black is the most common reinforcing filler used in rubbers. Individual particles are spherical, but they form aggregates that create different morphologies called **structure**. Fig. 2.41. illustrates three aggregates with structure increasing from left to right. Higher structure tends to correlate with an increasingly anisotropic aggregate shape and reinforcing capability. Individual particle size (and correspondingly specific surface area) and surface reactivity also affect reinforcing capability, with smaller carbon black offering superior reinforcement. Table 2.4 lists several grades of carbon black, average particle (not aggregate) diameters, and specific surface areas. The "N" in the grades indicates a "normal" carbon black which does not affect sulphur curing kinetics. The first number roughly correlates with the average particle diameter in tens of nanometres, with N990 being a clear exception to this rule. The last two numbers often characterise structure.



**Fig. 2.41:** Carbon black aggregates with structure increasing from left to right. (Adapted from Hallet & Tunnicliffe.)[139]

**Table 2.4:** Properties of some commercial carbon black grades.
(Adapted from Donnet *et al.*)[140]

| Grade | Mean particle diameter / nm | Specific surface area / $(m^2/gm)$ |
|-------|------------------------------|-------------------------------------|
| N110  | 18  | 138 |
| N220  | 21  | 116 |
| N330  | 30  | 83  |
| N550  | 56  | 41  |
| N660  | 67  | 36  |
| N762  | 107 | 26  |
| N990  | 285 | 9   |

Fig. 2.42 shows that there is a tradeoff between reinforcing capability and viscoelastic energy dissipation. As the carbon black particle size reduces, the difference in maximum and minimum rheometer torques, $M_h - M_l$, increases which indicates a stiffer material (see Section 2.8), but $\tan(\delta)$ also increases. This may be important for dynamic applications because the additional heat generation can adversely affect fatigue life.
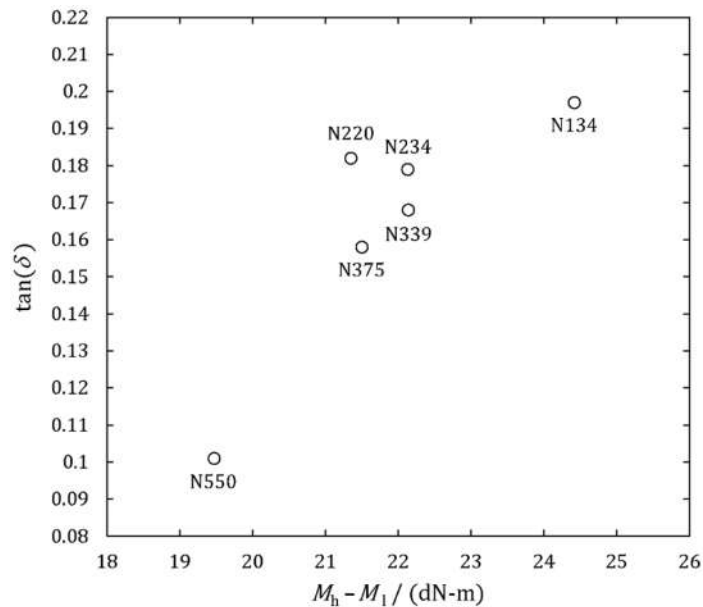


**Fig. 2.42:** Increase in maximum viscoelastic energy dissipation as reinforcing capability increases, as indicated by rheometer torque. (Adapted from Hallet & Tunnicliffe.)[139]

Precipitated silica (silicon dioxide) is the second most common reinforcing filler.[20] It is commonly employed in the tread of vehicle tyres because it reduces rolling resistance when compared to carbon black filled compounds.[141] In such applications, it consists of silica aggregates on the order of 50 nm. Due to surface polarity, it is difficult to disperse in nonpolar diene rubbers, and once dispersed it is prone to agglomeration (clumping into large structures) during curing processes. To mitigate these issues, the silica is often modified with a coupling agent such as silane. This alters the polarity of the aggregates and facilitates interaction between the filler and polymer.[142]

## 2.8 Differential Scanning Calorimetry to Assess the State-of-Cure

Curing of rubber is time- and temperature-dependent, so for manufacturing, it is important to understand how the process proceeds as a function of both parameters. This is initially determined by compressing an elastomer between two small, ribbed platens, one of which is shown in Fig. 2.43a. These are held at a temperature high enough to activate curing, a small oscillating torque is applied to the rubber, and the stiffness is recorded as it evolves over time. A typical output from this rheometer test is shown in Fig. 2.43b. The solid line shows the following trends in the torque: (i) a very brief increase as the discs compress the rubber; (ii) a decrease as the heat lowers the material's viscosity; (iii) an increase as crosslinks form; and (iv) a stable, asymptotic value once fully cured.
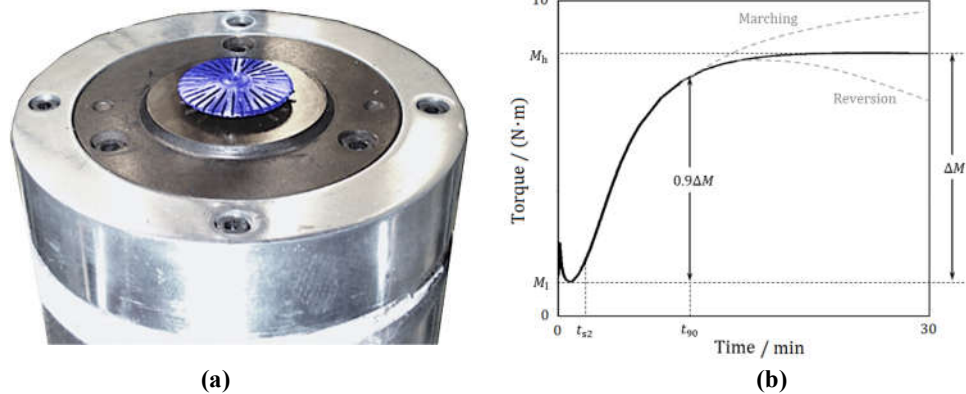


**Fig. 2.43: (a)** The bottom platen of an oscillating disc rheometer (ODR) with the test platen highlighted in blue. (Adapted from Hiwa Engineering Company.)[143] **(b)** The output from a rheometer test. (Adapted from Dluzneski.)[34]

Two measurement times from the rheometer test are used to guide curing processes during manufacturing of rubber components. The scorch time, $t_{s2}$, is the time at which torque increases by $0.23 \, \text{N} \cdot \text{m}$ ($2 \, \text{in} \cdot \text{lbf}$) from the minimum, $M_l$. It is used to determine the time allowed for forming operations such as compression moulding. The time to achieve 90% cure is defined as $\Delta M = 0.9(M_h - M_l)$ and denoted as $t_{90}$. It establishes the minimum time to achieve a sufficient cure for practical applications. Curing processes for rubber components often stop precisely at $t_{90}$ for four reasons: (i) curing continues as the components cool; (ii) to prevent reversion; (iii) to minimise manufacturing time; and (iv) mechanical properties at 90% cure are broadly indistinguishable from those at 100% cure.

**Marching cure** and **reversion** are two problems that may be encountered in rubber compounds. In the former, the stiffness monotonically increases throughout a rheometer test and may not stabilise even over a timescale of the order of several hours. In such cases, it is not simple to determine when the crosslink density is sufficient for practical purposes. Reversion occurs when the cure curve has a local maximum. It indicates that, given sufficient time, the combination of heat and stress reduce the effective crosslink density, an adverse effect that should be controlled.

Cure times for thick rubber components, which must be longer than $t_{90}$ to ensure adequate heat transfer, are often determined by experience-based rules-of-thumb, though specialty thermal modelling software also exists. In any case, it is important to validate curing processes. Hardness measurements can detect gross under-cure on component surfaces, but for critical applications such as high pressure sealing, differential scanning calorimetry (DSC) provides a more reliable technique. Small samples are cut from different portions of the component, including interior regions, and heated through a temperature ramp. If a sample is fully cured, it evolves no heat through the curing temperature (see the lower trend in Fig. 2.44). If it is partially cured, it evolves some heat as it passes through the curing region (see the middle trend in Fig. 2.44). The area under a partially cured trend can be compared to that under a reference trend for the uncured rubber, and the state-of-cure can be estimated as Cure $\% = (1 - A_2/A_1) \cdot 100$. Finally, there are other methods to assess the state-of-cure, and swelling is commonly used as a proxy to assess crosslink density.[50] Schlumberger data provided by Xiaohong Ren[144] reveals that the DSC method is fast and sufficiently accurate for industrial practice.
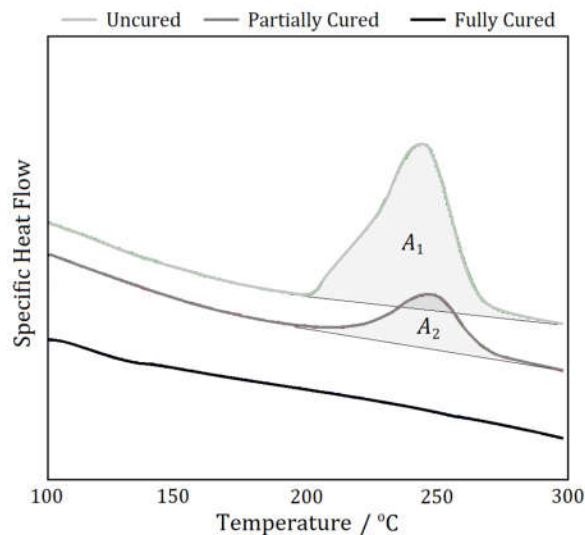


**Fig. 2.44:** Trends from a DSC test for uncured, partially cured, and fully cured rubber samples.

## 2.9 Non-linear Viscoelasticity

Generally, non-linear viscoelastic models are not restricted to small strains, nor do they respect Boltzmann's principle of superposition.[**] They are particularly relevant when modelling filled rubber due to the strain amplitude and history dependencies outlined in Section 2.7. In addition, they can address damage, fracture, and fatigue life. The primary drawbacks of these models are that they require many model parameters which may be difficult to ascertain, and they often require user-defined coding or specialty software to

---

[**] As a sidenote, linear viscoelasticity can address some aspects of large strains by replacing Hooke's law for elasticity with a hyperelastic material model.[97,109]

execute. The load cases in which they have been validated may also be restricted, hindering their general adoption. A review of some non-linear viscoelastic models was given by Carleo *et al.*[145] Predictions from two such models are illustrated in Figs. 2.45–2.48.

Carleo[146] provided a good illustration of some difficulties that arise when developing novel non-linear viscoelastic models. She developed a 9-parameter viscoelastic material model based on fractional derivatives. It was successfully implemented for uniaxial extension of a rubber block in MATLAB, but when converted to a subroutine for implementation in Abaqus, the model became unstable, therefore limiting its generalisation. Figs. 2.45 and 2.46 show some of her results from the simulations in Abaqus. The model successfully captured cyclic stress softening during the first 3 loading cycles, but thereafter the block showed unrealistic extension in a direction that was not loaded.
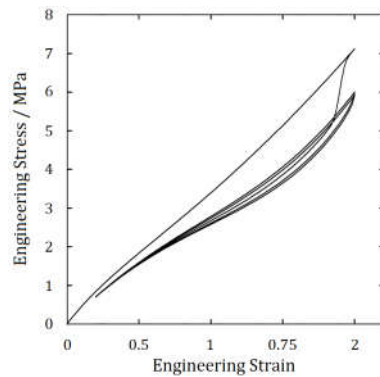


**Fig. 2.45:** Cyclic stress softening with a fractional derivative model in Abaqus. (Adapted from Carleo.)[146]



**(a)**            **(b)**
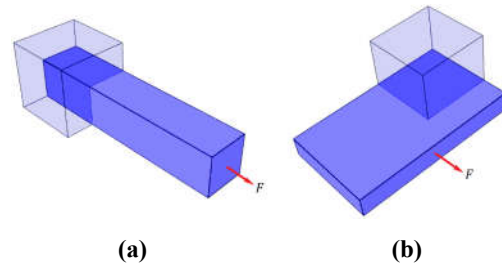
**Fig. 2.46: (a)** Realistic deformation during a uniaxial extension. **(b)** Unrealistic deformation during a uniaxial extension. (Adapted from Carleo.)[146]

Carleo and coauthors[147] achieved better success with a 10-parameter model based on a stress decomposition into elastic and hysteretic (viscous) components, the former including a strain-dependent continuum damage parameter to soften the material. Fig. 2.47 shows cyclic stress-strain response for the model in uniaxial extension. It successfully captures hysteresis, cyclic softening, the Mullins effect, large strain non-linearity, and permanent set. The model was implemented in Abaqus for a 3D bushing component, and the results of a radial deformation are shown in Fig. 2.48.

59
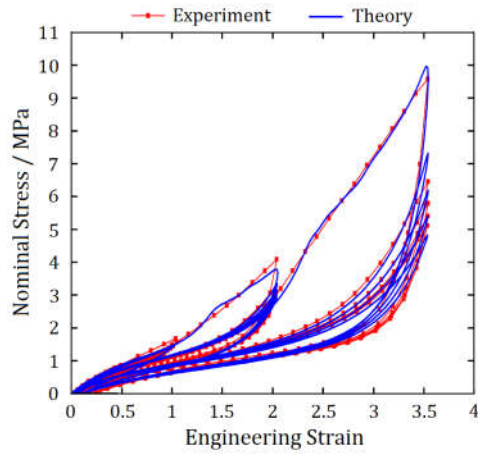
**Fig. 2.47:** Successful simulation of multiple visco-elastic non-linearities in uniaxial extension with a continuum damage model. (Adapted from Carleo et al.)[147]
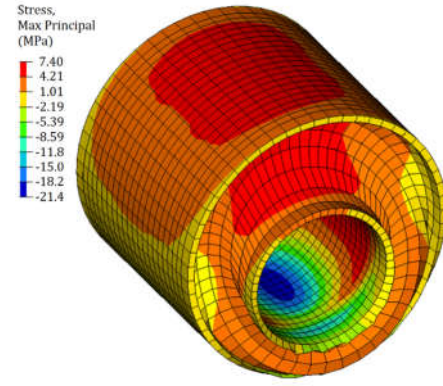


**Fig. 2.48:** Successful simulation of a 3D component in Abaqus with a continuum damage model. (Adapted from Carleo et al.)[147]

## 2.10 Rate-Dependent Tensors & Objectivity

In Section 2.5.4, the left Cauchy-Green strain tensor was introduced and shown to be a function of the deformation gradient, $\mathbf{B} = \mathbf{FF}^{\mathrm{T}}$. These tensors are only functions of deformed and undeformed coordinates, and hence independent of time. This fact is more apparent by letting $\boldsymbol{r}_1 = (x, y, z)$ and $\boldsymbol{r}_2 = (x', y', z')$ and expressing $\mathbf{F}$ in matrix form:

$$\mathbf{F} = \begin{bmatrix} \dfrac{\partial x'}{\partial x} & \dfrac{\partial x'}{\partial y} & \dfrac{\partial x'}{\partial z} \\ \dfrac{\partial y'}{\partial x} & \dfrac{\partial y'}{\partial y} & \dfrac{\partial y'}{\partial z} \\ \dfrac{\partial z'}{\partial x} & \dfrac{\partial z'}{\partial y} & \dfrac{\partial z'}{\partial z} \end{bmatrix} \tag{2.66}$$

In time-dependent analyses, it is necessary to account for not just positions as given by $\boldsymbol{r}_1$ and $\boldsymbol{r}_2$, but also velocities and accelerations which may be derived from tensor calculus. Holzapfel[96] and Bergström[97] provide details on this subject, and a few illustrative results are given below.

Fig. 2.20 shows undeformed and deformed representations of a body. In continuum mechanics, these are called **material** and **spatial** representations, respectively. The kinematics of a body can be expressed in either configuration, and it is possible to transform between them. For example, the **material time derivative** of a smooth field, $\mathcal{F}$, (which could be scalar-, vector-, or tensor-valued) in the undeformed configuration is:

$$\frac{\mathrm{D}\mathcal{F}}{\mathrm{D}t} \equiv \left.\frac{\partial \mathcal{F}}{\partial t}\right|_{\boldsymbol{r}_1} = \dot{\mathcal{F}} \tag{2.67}$$

in which the partial derivative, by definition, holds the position vector constant. To account for directional changes, the **material gradient** of $\mathcal{F}$ is defined as:

$$\mathrm{Grad}(\mathcal{F}) = \left.\frac{\partial \mathcal{F}}{\partial \boldsymbol{r}_1}\right|_t \tag{2.68}$$

60

in which $t$ is fixed during the partial differentiation. (Take note of the similarity between Eq. 2.68 and the definition of $\mathbf{F}$ in Eq. 2.35). The gradient describes how a field is changing with respect coordinate directions in that field. The analogs of these equations in the spatial configuration are:

$$\left.\frac{\partial f}{\partial t}\right|_{r_2} = \dot{f} \tag{2.69}$$

$$\text{grad}(f) = \left.\frac{\partial f}{\partial r_2}\right|_t \tag{2.70}$$

The use of upper and lowercase letters or variables in the material and spatial frames, respectively, are common in continuum mechanics, but the convention is not followed in this work. The material time derivative of a field expressed in the spatial frame is computed with the **material time derivative operator**:

$$\frac{D(\circ)}{Dt} = \frac{\partial(\circ)}{\partial t} + \text{grad}(\circ)\mathbf{v}_2 \tag{2.71}$$

where $(\circ)$ is a scalar-, vector-, or tensor-valued field expressed in the spatial frame. Eq. 2.71 shows that the derivative of a spatial field with respect to the material frame is the sum of time and position partial derivatives, the position derivatives being multiplied by the **spatial velocity field** which is given by:

$$\mathbf{v}_2 = \frac{\partial r_2}{\partial t} = \dot{\mathbf{r}}_2 \tag{2.72}$$

The **material** and **spatial velocity gradients** are readily computed with the gradient operators as $\text{Grad}(\mathbf{v}_1) = \partial \mathbf{v}_1 / \partial r_1$ and $\text{grad}(\mathbf{v}_2) = \partial \mathbf{v}_2 / \partial r_2$, respectively. It can be shown that the material and spatial velocity gradients require:[96]

$$\text{Grad}(\mathbf{v}_1) = \frac{D\mathbf{F}}{Dt} = \dot{\mathbf{F}} \tag{2.73}$$

$$\mathbf{L} \equiv \text{grad}(\mathbf{v}_2) = \dot{\mathbf{F}}\mathbf{F}^{-1} \tag{2.74}$$

Eqs. 2.73 and 2.74 make clear that the material and spatial velocity gradients are 2nd-order tensors. The spatial velocity gradient can be additively decomposed into symmetric and skew components such that:

$$\mathbf{D} = \frac{1}{2}(\mathbf{L} + \mathbf{L}^{\mathrm{T}}) = \mathbf{D}^{\mathrm{T}} \tag{2.75}$$

$$\mathbf{\Omega} = \frac{1}{2}(\mathbf{L} - \mathbf{L}^{\mathrm{T}}) = -\mathbf{\Omega}^{\mathrm{T}} \tag{2.76}$$

where the last equalities in each equation follow from the definitions of **symmetric** and **skew (anti-symmetric) tensors**. $\mathbf{D}$ is called the **rate of deformation tensor**, and $\mathbf{\Omega}$ is called the **spin** (or **rate of rotation** or **vorticity**) **tensor**. These are the rate-dependent analogs of the stretch and rotation tensors introduced in Eq. 2.36. Rate-dependent tensors show up in time derivatives of strain tensors. For example, the material time derivative of the left Cauchy-Green strain tensor is:

$$\dot{\mathbf{B}} = \mathbf{L}\mathbf{B} + \mathbf{B}\mathbf{L}^{\mathrm{T}} \tag{2.77}$$

Special care is required when developing rate-dependent constitutive equations. Physical quantities that are described must be independent of any observer who reports them, an axiom called the **principle of material frame-indifference**, or simply **objectivity**. A physical quantity that is independent of an observer is called **objective**. Objectivity requires that the distance between two arbitrary points in space is the same regardless of the reference frame in which that distance is measured. Similarly, time intervals between two arbitrary events being observed must be the same regardless of the reference frame. Let there be two observers in different reference frames, one of which has physical quantities denoted with the prime symbol, $(\circ)'$. The mathematics that describe frame-indifference of an arbitrary scalar ($\phi$), vector ($\mathbf{a}$), and tensor ($\mathbf{A}$) in these frames require that they transform according to:

$$\phi'(\mathbf{r}', t') = \phi(\mathbf{r}, t)$$
$$\mathbf{a}'(\mathbf{r}', t') = \mathbf{Q}\mathbf{a}(\mathbf{r}, t) \tag{2.78}$$
$$\mathbf{A}'(\mathbf{r}', t') = \mathbf{Q}\mathbf{A}(\mathbf{r}, t)\mathbf{Q}^{\mathrm{T}}$$

where $(\mathbf{r}, \mathbf{r}')$ locate a point in space with respect to the different frames, $(t, t')$ are times measured by different clocks in each frame, and $\mathbf{Q} = \mathbf{Q}(t)$ is an orthogonal tensor that is restricted to rigid body rotations. It is self-evident that scalars in each frame are identical. Since $\mathbf{Q}$ only permits rotations, it does not change the length of the vector on which it operates. Furthermore, it does not alter the orientation (that is, the angle between) any two vectors in one frame that are transformed to the other frame. By analogy, $\mathbf{Q}$ and $\mathbf{Q}^{\mathrm{T}}$ do not alter the "length" and "orientation" of a tensor when they operate on it according to Eq. 2.78.

It can be shown that the following quantities which have been introduced are objective:

- volume ratio, $J$;
- deformation gradient, $\mathbf{F}$;
- rotation tensor, $\mathbf{R}$;
- stretch tensor, $\mathbf{U}$;
- left Cauchy-Green strain tensor, $\mathbf{B}$;
- Cauchy stress tensor, $\hat{\boldsymbol{\sigma}}$;
- rate of deformation tensor, $\mathbf{D}$ (and notably, the spin tensor, $\boldsymbol{\Omega}$, is not objective).

However, complications can occur when derivatives of these tensors are required. For example, the velocity gradient in Eq. 2.74 is given by $\mathbf{L} = \dot{\mathbf{F}}\mathbf{F}^{-1}$. It can be shown that a change in observer gives the following transformation rule:

$$\mathbf{L}' = \mathbf{Q}\mathbf{L}\mathbf{Q}^{\mathrm{T}} + \dot{\mathbf{Q}}\mathbf{Q}^{\mathrm{T}} \tag{2.79}$$

Hence, $\mathbf{L}$ is not objective because Eq. 2.79 does not have the same form as Eq. 2.78, and it cannot be directly used when formulating constitutive equations.

Rate-dependent constitutive equations are used for dynamic simulations, for instance

in Abaqus/Explicit. When derivatives of vector or tensor quantities are required, the quantities may need adjustment to cast them into an objective form. This gives rise to **objective stress rates**. There are a variety of rates that may be chosen. For instance, the **Green-Naghdi stress rate** and **Jaumann-Zaremba stress rate** are respectively defined in terms of the Cauchy stress tensor as:

$$\widehat{\boldsymbol{\sigma}}_{\text{gn}} = \dot{\widehat{\boldsymbol{\sigma}}} - \dot{\mathbf{R}}\mathbf{R}^{\mathrm{T}}\widehat{\boldsymbol{\sigma}} + \widehat{\boldsymbol{\sigma}}\dot{\mathbf{R}}\mathbf{R}^{\mathrm{T}} \tag{2.80}$$

$$\widehat{\boldsymbol{\sigma}}_{\text{jz}} = \dot{\widehat{\boldsymbol{\sigma}}} - \boldsymbol{\Omega}\widehat{\boldsymbol{\sigma}} + \widehat{\boldsymbol{\sigma}}\boldsymbol{\Omega} \tag{2.81}$$

These equations satisfy objectivity such that $\widehat{\boldsymbol{\sigma}}_{\text{gn}} = \mathbf{Q}\boldsymbol{\sigma}_{\text{gn}}\mathbf{Q}^{\mathrm{T}}$ and $\widehat{\boldsymbol{\sigma}}_{\text{jz}} = \mathbf{Q}\widehat{\boldsymbol{\sigma}}_{\text{jz}}\mathbf{Q}^{\mathrm{T}}$.

Although different objective stress rates exist, they are not all equally effective at modelling different problems. Ideally, one should use so-called **work conjugate** measures of stress and strain (or rate of deformation). For example, the stress measure $\boldsymbol{\tau} = J\widehat{\boldsymbol{\sigma}}$ (**Kirchhoff stress**) is work conjugate to the rate of deformation tensor, $\mathbf{D}$, so they make a suitable couple to build a constitutive equation. As Vorel & Bažant[148] point out, the Green-Naghdi and Jaumann-Zaremba stress rates are not work conjugate to any finite strain tensors, yet they are used in many commercial finite-element solvers. In addition, Holzapfel states that these rates give undesirable oscillations in simple shear. To avoid such problems, Vorel & Bažant recommend use of the **Truesdell stress rate**:

$$\widehat{\boldsymbol{\sigma}}_{\text{tr}} = \dot{\widehat{\boldsymbol{\sigma}}} - \mathbf{L}\widehat{\boldsymbol{\sigma}} - \widehat{\boldsymbol{\sigma}}\mathbf{L}^{\mathrm{T}} + \widehat{\boldsymbol{\sigma}}\operatorname{tr}(\mathbf{D}) \tag{2.82}$$

Further attention on stress rates is given in .

## 2.11 Summary

This concludes the main theoretical foundations that support the remainder of this work. Some key takeaways are:

- the links between Gough's early observations of thermoelasticity, Treloar's development of a kinetic theory to explain the phenomenon, and tensor mathematics which establish a general framework for finite elasticity;

- a summary of glass transition temperatures from multiple sources as well as the variation in $T_{\text{g}}$ as a function of hydrostatic pressure, the latter being an important consideration for high pressure seals in the oilfield;

- arguments that the glass transition pressure arises from the same source as the glass transition temperature, namely constraints on free volume;

- a clarification of the equivalence of uniaxial compression and equibiaxial extension in terms of true stress, and a proof of their equivalence in terms of engineering stress (also see Appendices E and F);

- force and stress descriptions of a load on a bar that is held in uniaxial extension to conceptualise a tensor;

- an illustration on why a pure shear is not a simple shear;

- the introduction of some common strain-energy functions;

- an introduction to biaxiality and giving reference to the first reported numerical implementation of biaxiality analysis for a compressible material;

- an introduction to viscoelastic effects that arise in rubbery materials, with an emphasis on reinforcing fillers that amplify inelasticities;

- a discussion of objectivity and work conjugate pairs in finite elasticity, two effects that may be introducing errors and discrepancies in finite-element solvers.

# 3. Literature Review on Elastomeric Seals

## 3.1 Overview

Elastomeric seals are commonly used to prevent fluid exchange between regions that share a common boundary. For example, Fig. 3.1a shows a rubber O-ring compressed between a piston and a housing which, upon application of pressure, prevents fluid transfer across the sealing boundaries (Fig. 3.1b). Ideally, seals perfectly impede fluid migration, but in practice, pressure and chemical concentration gradients always lead to some leakage.[149] This implies any sealing system must tolerate some leakage with seal failure being defined by a finite leak threshold. Seal fracture is often a precursor, but not always a prerequisite, for unacceptable leakage (Fig. 3.1c). For instance, **elastic leak** occurs when fluid bypasses a sealing interface without mechanically damaging the seal (Fig. 3.1d).
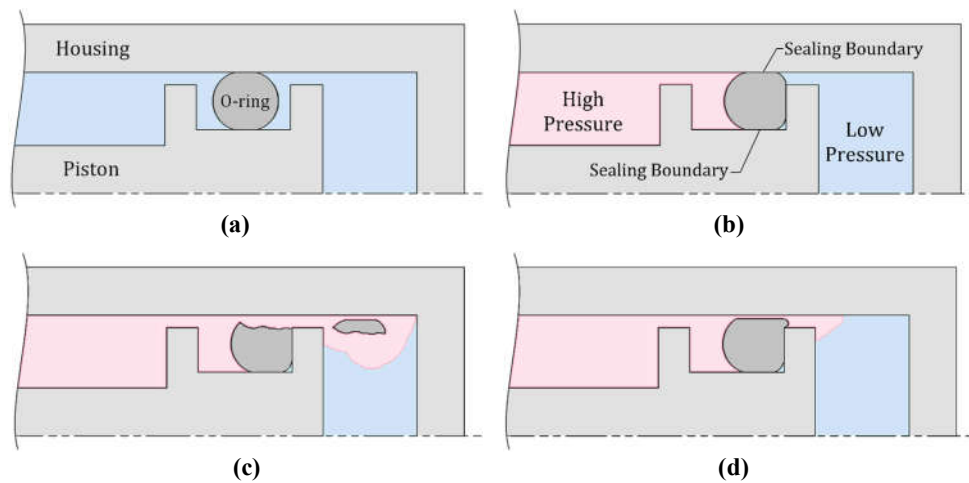


**Fig. 3.1: (a)** O-ring compressed between a piston and housing with no differential pressure. **(b)** O-ring preventing fluid migration from a high pressure zone to a low pressure zone. **(c)** Leakage due to fracture of the seal. **(d)** Leakage due to elastic leak of the seal.

As motivation for the numerical calculations in Chapters 5 through 7, this chapter reviews the literature for elastic leak prediction in seals, with a focus on studies where:

- Fracture does not occur;
- Leakage is strictly pressure-driven. For instance, fluid transfer via chemical concentration gradients is not covered;
- Leakage occurs along sealing interfaces. That is, fluid migration through the seal or surrounding bodies is not considered, thereby omitting fluid diffusion and swelling;
- Mechanical deformations and fluid motions are quasi-static. Consequently, dynamic effects associated with, for instance, boundary layer lubrication are not considered.

A strict focus on elastic leak is not just of theoretical interest. The research sponsor has documented multiple instances of leakage with no apparent damage to sealing components. For some of the topics that are not covered here, refer to Windslow[75] for fracture and gas diffusion, Lou *et al*.[150] for swelling, Müller & Nau[149] and Nau[151,152] for dynamic considerations, and Flitney[153] for a general account of seals and sealing materials.

## 3.2 Techniques for Prediction of Elastic Leak

There are two primary approaches to predict elastic leak at a sealing interface. Classical theories rely on arguments from mechanics, usually considering a macroscopic length scale, to establish a relationship between contact pressure, fluid pressure, and leakage. Alternatively, percolation theories consider the microscopic surface topography of contacting bodies which contain small channels that permit leaks. Fig. 3.2 illustrates these channels with a PDMS button that is compressed against a rough surface. With a light load, dark spots appear at areas highlighting the region of contact. As the load increases, the dark areas coalesce, but some voids are still visible. The unfilled areas allow pressurised fluid to enter the contact interface and, possibly, permeate across the seal.
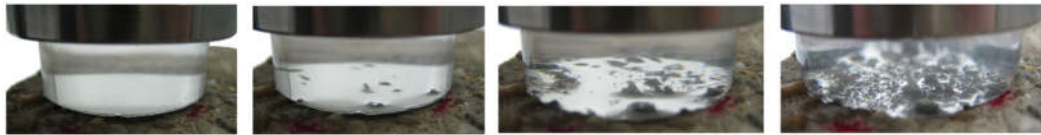


**Fig. 3.2:** A PDMS button with compression load increasing from left to right. Light areas at the contact interface indicate possible leak paths. (Adapted from Lorenz.)[154]

Both of the strategies are valid for certain problems. For oilfield seals, which generally have large initial contact pressures and smooth countersurfaces, it appears most appropriate to explore leak prediction using classical theories. For instance, sealing elements in oilfield completions packers[3] are tested in metal tubulars with arithmetic mean surface roughness and initial contact pressure of the order of 2 μm and 7 MPa, respectively.[155] Considering test fluid volumes of the order of 40 L, leaks at the microscale are negligible if not completely absent during typical hold periods of 15 minutes.[156,157,158] Furthermore, seals often show no apparent leakage until a critical pressure is reached, a fact visually supported by the supplementary online videos of leakage in Lui *et al.*[159] Druecke[160] also recognised that the onset of seal leakage can be sudden, and he gave a classical mechanical description of the problem (see his Appendix D). These works, as well as direct observation of axial buckling in annular seals,[161] indicate that seal leakage is intimately tied to elastic instability.

The review in this subsection consists of three parts. First, a sample of analytical models for leakage is shown, followed by representative studies from percolation theory. Finite-element models for leak prediction are then presented in two categories: those that (a) only assess contact pressures, and (b) those that also simulate fluid pressure penetration (FPP) at the sealing interface. Despite their commercial availability since the 1990s,[162] FPP algorithms have received little research attention, so a comprehensive review of the academic studies is given. Based on the author's anecdotal experience, many industrial studies of FPP exist, but their proprietary nature does not permit a critical assessment of their accuracy.

### 3.2.1 Analytical Models for Leak Prediction

Seal contact pressures, which are assumed to correlate with sealing capability, have been studied analytically. The models require simple geometry and constitutive laws. Müller & Nau[149] gave a basic analytical model for a plane strain rectangular seal installed in a groove (Fig. 3.3). From generalised Hooke's law for a linearly elastic material,[81] they derived an equation for the total contact pressure at a frictionless sealing interface:

$$\sigma_c = \sigma_o + \frac{\nu}{1-\nu}P_f \approx \sigma_o + P_f \tag{3.1}$$

where $\sigma_o$ is the initial contact pressure due to compression and $P_f$ is the applied fluid pressure. The approximation is true for a nearly incompressible material such as rubber because $\nu \approx 0.5$. Eq. 3.1 indicates that the seal is self-energising because the fluid pressure superposes with the contact pressure. This principle holds for O-rings although their initial contact pressure profile, assumed to follow Hertzian contact theory,[163] is more complicated. Of course, Eq. 3.1 cannot hold for arbitrarily high pressures because, as illustrated in Fig. 3.1, the seal (or perhaps a countersurface body) must eventually fail mechanically.
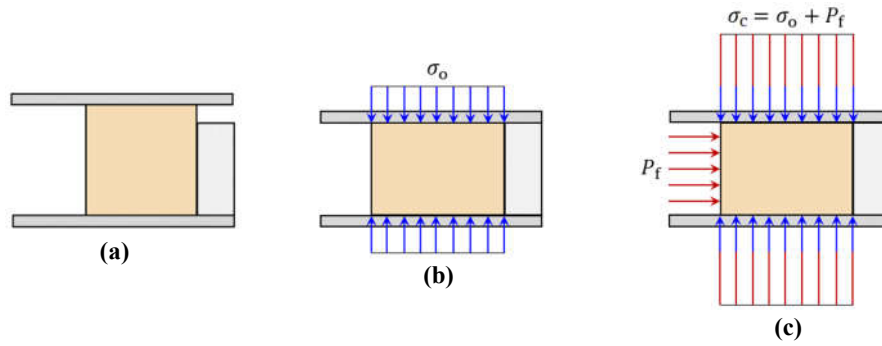


**Fig. 3.3:** Plane strain rectangular seal: **(a)** before compression; **(b)** after compression in a gland; **(c)** with fluid pressure applied. (Adapted from Müller & Nau.)[149]

In 1967, Lindley[164] proposed a load-deflection equation for a laterally unrestrained O-ring (that is, one free to expand in a direction perpendicular to the direction of compression):

$$F_c = 3GdC(1.25\varepsilon^{1.5} + 50\varepsilon^6) \tag{3.2}$$

where $F_c$ is the total compression force, $d$ is the cross-sectional diameter of the O-ring, $C$ is the circumference of the O-ring (see Fig. 3.4), and $\varepsilon = \Delta d/d$ is the average strain due to compression by an amount, $\Delta d$. The first term arises from a plane strain assumption and Hertzian contact theory, and the second term is an empirical correction factor. Lindley gave the peak contact stress as:

$$\sigma_{c.max} = G\sqrt{\frac{24}{\pi}}(1.25\varepsilon^{1.5} + 50\varepsilon^6) \tag{3.3}$$

Lindley's equation follows experimental trends but tends to underestimate stress at low values of compressive strain as shown in Fig. 3.4.

67
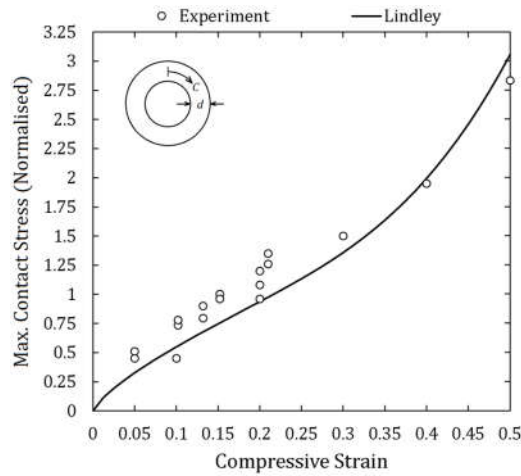
**Fig. 3.4:** Comparison of Lindley's contact stress equation with experimental data. Stress is normalised by the shear modulus. (Adapted from George, Strozzi, & Rich.)[165]

Dragoni & Strozzi[166,167] derived plane strain contact pressures for a laterally constrained O-ring in a rectangular groove. They modified Eq. 3.3 to give the maximum contact pressure as:[166]

$$\sigma_{c.max} = G\sqrt{\frac{24}{\pi}}(1.25\hat{\varepsilon}^{1.5}) \tag{3.4}$$

where $\hat{\varepsilon}$ is an "equivalent" compression that may be derived from the O-ring and gland dimensions. From this, they deduced contact pressures in two orthogonal directions as illustrated in Fig. 3.5b. They validated the model with finite-element studies and experiments on thin photoelastic discs. Their test fixture is shown in Fig. 3.5a. Their solutions worked better than Lindley's equation at 10% compression but became unsuitable at 20% compression. The authors also noted that their model was insensitive to changes in Poisson's ratio, and this is a significant limitation. Because a high pressure seal is well-confined, its volumetric stiffness, which correlates to its Poisson's ratio (see Eq 4.7), significantly alters contact pressure. Although typical rubber compounds have Poisson's ratios in a narrow range of 0.495-0.4995, the corresponding range of bulk modulus to shear modulus ($\kappa : G$) is $10^2$-$10^3$. So, when shear deformations are inhibited, any energy changes to the system are stored in volumetric deformation which is sensitive to $\kappa$.
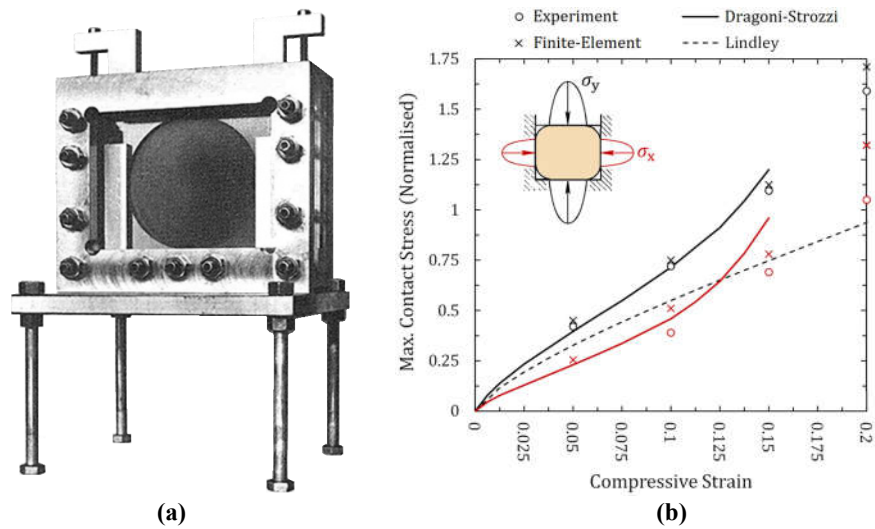
**Fig. 3.5: (a)** Dragoni & Strozzi's [166] test fixture; **(b)** Comparison of contact stress equation (loaded in the *y*-direction) with numerical and experimental results. Stress is normalised by the shear modulus.

Some authors have developed models for O-ring extrusion. Nikas[168] predicted the shape and contact pressure profile for the extruded portion of a Neo-Hookean O-ring with a square cross-section. Also assuming a Neo-Hookean material, Eshel[169] predicted the pressure for elastic extrusion of an O-ring via roll-out through a frictional extrusion gap (see inset in Fig. 3.6). He also considered upper and lower bounds for "plastic" extrusion which would occur if the O-ring exceeded its "yield" strength, admittedly an ill-defined property for rubber. Fig. 3.6 shows that his model was reasonable as the data follow roughly the elastic extrusion theory. The black data points indicate failures in which the O-rings were mechanically damaged, and they generally fall within the theoretical plastic failure limits.
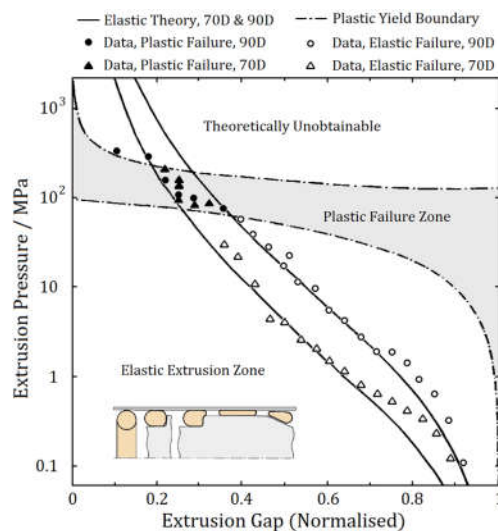


**Fig. 3.6:** Comparison of Eshel's elastic extrusion and plastic yield equations with experimental data. The inset illustrates elastic extrusion roll-out under pressure. (Adapted from Eshel).[169]

Some authors have described superposition models that account for fluid pressure on O-rings. Based on empirical evidence, Karaszkiewicz[170] suggested that Eq. 3.1 should be:

$$\sigma_c = \sigma_o + 0.9P_f \tag{3.5}$$

in order to reduce the significance of the fluid pressure's contribution to the total contact pressure. Other extensions of superposition include: (i) a Hertzian contact model with two correction parameters to account for fluid pressure (Fig. 3.7);[171] (ii) viscoelastic effects;[172] (iii) an X-ring geometry;[173] and (iv) use of Muskhelishvili's complex analysis for structural mechanics[174] to decompose stress into real and imaginary components.[175]
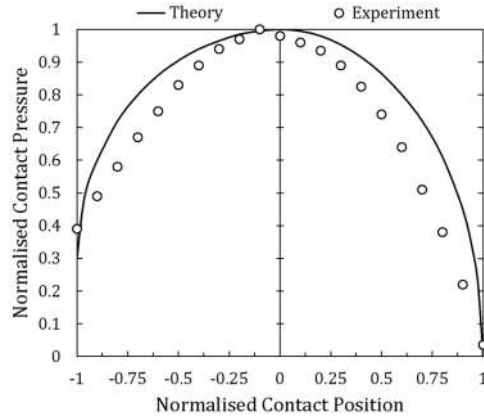


**Fig. 3.7:** Theoretical and experimental contact pressure profiles for an O-ring (20% compression) with fluid pressure. Pressure is normalised by the maximum contact pressure. Position is normalised with respect to the centre of the nominally compressed O-ring. (Adapted from Kim *et al.*)[171]

Fracture mechanics has also been invoked to predict leakage. Beghini *et al.*[176] developed a linear elastic fracture mechanics (LEFM)[177] model to predict fluid penetration in a metal flange with a linear bolt pattern. It was based on the similarity of a flange interface and a partially open planar edge crack. The model considered a bolt preload, which held the crack closed, to be countered by fluid pressure on the adjoined bodies (Fig. 3.8). A stress intensity factor was imposed to predict the critical pressure for leakage. Brighenti & Artoni[178] developed an LEFM model for a planar PDMS seal on a hard surface. The model predicted a critical pressure that would initiate separation (that is, a "crack") at the sealing interface. The authors studied the effect of a lead-in angle between the seal and hard countersurface (Fig. 3.9), finding that shallow lead angles reduced the cracking pressure due to less efficient self-energisation.
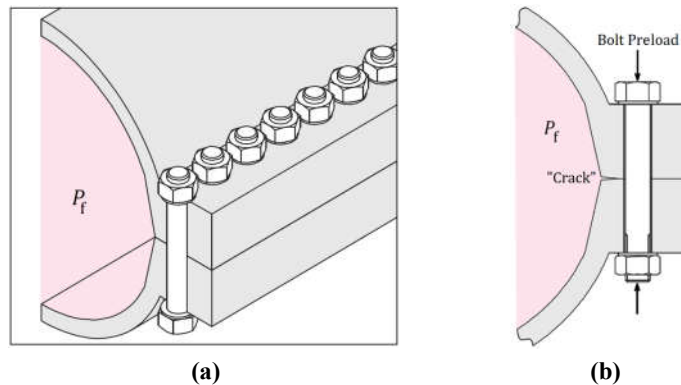


**Fig. 3.8: (a)** A flange with internal pressure and a linear bolt pattern. **(b)** Partial separation of the flange due to the internal pressure. (Adapted from Beghini *et al.*)[176]
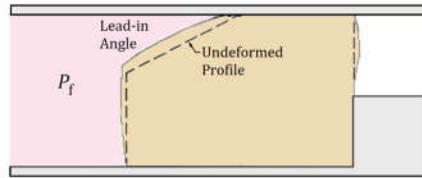
**Fig. 3.9:** Seal with a lead-in angle after compression. (Adapted from Brighenti & Artoni.)[178]

There has been some work on leak prediction of seals with long aspect ratios such as swell packers. As the name implies, these seals absorb fluid, swell, and create an annular seal. Fig. 3.10 shows swell packers in unswollen (left) and swollen (right) states. The swollen packer separates high pressure and low pressure annular regions. Length to cross-sectional thickness ratios may be greater than 100 : 1. Notable work on this subject has been given by Druecke and coauthors.[160,161,179] They did not focus specifically on quantitative prediction of elastic leak, but developed a fracture model and illustrated elastic instabilities with small-scale experimental tests.
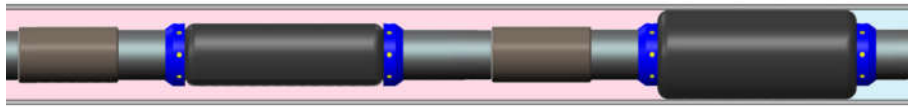


**Fig. 3.10:** Swell packers (the black components) in unswollen (left) and swollen (right) states.

Al-Hiddabi *et al.*[180] focused on long seals that are bonded to a metal tubular which is mechanically expanded, thereby creating an annular seal similar in concept to Fig. 3.10. They developed a model to predict contact pressures as a function of compression and fluid pressure. The model showed good qualitative agreement with an FE model that assumed a Neo-Hookean material. Notably, the authors predicted a critical seal length, after which additional length would not increase sealing capability. Druecke[179] reached a similar conclusion for swell packers. These two works question a well-accepted notion in the oilfield that pressure retention in swell packers directly scales with seal length.

Liu *et al.*[159] studied rectangular plane strain seals with long aspect ratios (Fig. 3.11). The seal assumed bonded and frictionless interfaces at its bottom and top, respectively. Compression by an amount, $\varepsilon = \Delta h / h$ created an initial contact pressure profile which was altered by application of pressure on an exposed seal face. Using analytical arguments, they proposed an equation to predict the pressure required for leakage:

$$P_{\text{leak}} = G \left[ \frac{A}{1-\varepsilon} \left( \frac{L}{h} \right) + \frac{B\varepsilon}{1-\varepsilon} \left( \frac{L}{h} \right)^2 \right] \qquad (3.6)$$

where $L$ and $h$ are defined in Fig. 3.11a, and $A$ and $B$ are fitting parameters that arise from shear strains at the bottom corners of the seal (indicated by the black dots). (Note: Liu's publication of Eq. 3.6 contains typesetting errors.) The fitting parameters are deduced from FE studies, so the model is semi-empirical. Fig. 3.12 shows experimental validation of Eq. 3.6 as given by Liu. The model works well for 10% compression and an aspect ratio near 2, but the fit is poor for larger compression and aspect ratios.

71
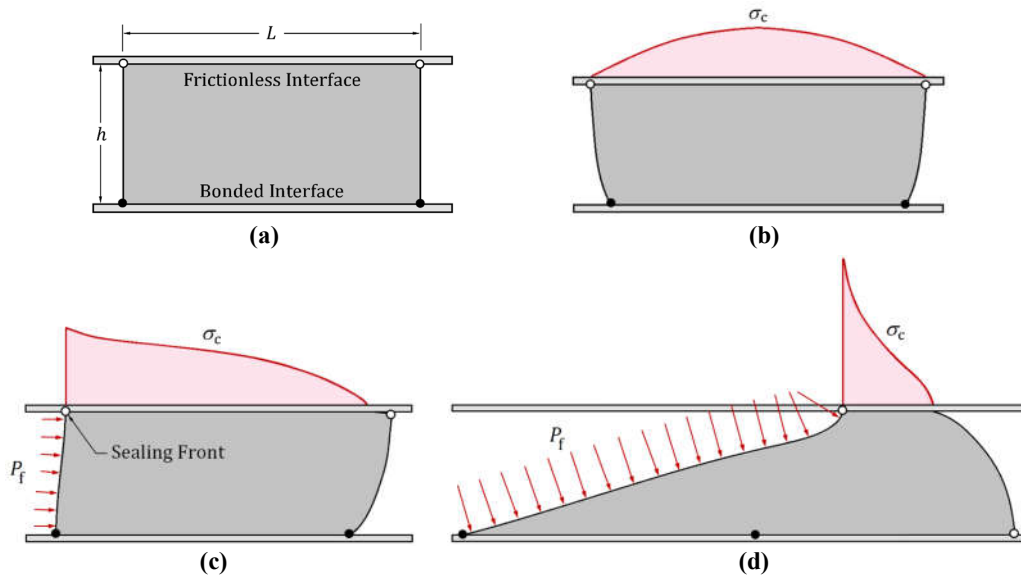
**Fig. 3.11:** Plane strain seal geometry studied by Liu *et al.*:[159] **(a)** before compression; **(b)** after compression; **(c)** after application of pressure; **(d)** at the critical pressure when $P_f = \sigma_{c.max}$. The red line and pink shading indicate the contact pressure profile along the top of the seal.
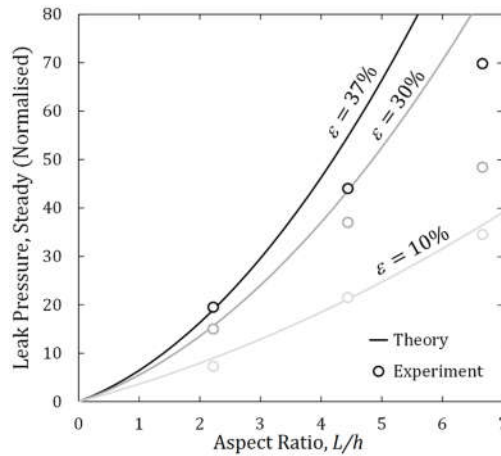


**Fig. 3.12:** Comparison of Eq. 4.6 with experimental results. (Adapted from Liu *et al.*)[159]

In summary, analytical models are qualitatively useful, and for some simple problems, they give reasonable quantitative predictions. Material constitutive models are restricted to linearly elastic or Neo-Hookean behaviour, but this appears reasonable for compressions up to perhaps 20%. Several models include Hertzian contact pressure profiles due to compression. These appear reasonable for O-rings, but Nau[151] notes that Hertzian contact does not apply to rectangular seals. Some models address combined contact and fluid pressures, but they cannot predict critical leak pressures because they are premised on additive superposition. Finally, the frictional behaviour at the sealing interface is usually assumed frictionless or, at best, to follow Coulomb's model. Both models are too simplistic for hyperelastic materials.[181,182,183]

### 3.2.2 Percolation Models for Leak Prediction

Fig. 3.13a illustrates fluid percolation through a sealing interface, with side and top views of the percolating network shown. Leakage across the entire seal occurs when the contact pressure is insufficient to block the flow channels. Typical examples of this modelling approach are given by Bottiglione *et al.*[184] and Lorenz & Persson.[185,186] The authors determined the characteristic size of leak paths by analysing surface topography and then invoked pressure-flow relationships from fluid mechanics (Fig. 3.13b). The technique has been validated for contact pressures of the order of kPa, but it fails at higher contact pressures when flow is completely restricted. This subject is not explored further in this thesis, but it is worth noting that Persson[187] has extended the concept for metal-to-metal seals at differential pressures of the order of 1 MPa.
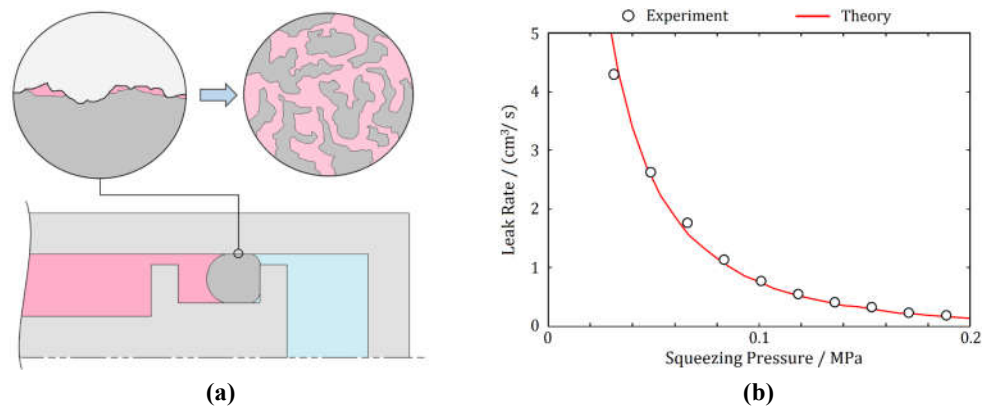


**Fig. 3.13: (a)** Illustration of fluid percolation through surface asperities at a contact interface. **(b)** Comparison of a percolation model with experiment. (Adapted from Lorenz & Persson.)[185]

### 3.2.3 Finite-Element Models for Leak Prediction

Finite-element models for leak prediction can be split into two categories: those that strictly assess deformation and contact pressure due to compression, and those that also account for the effect of pressure. Some examples of the former and a comprehensive review of the latter are given in this subsection.

***Contact Pressure Models***

In 1987, George, Strozzi, & Rich[165] constructed a plane strain finite-element model (FEMALES, for Finite-Element Mechanical Analysis of Large Elastic Strain) for a laterally unconstrained O-Ring with Neo-Hookean behaviour. Fig. 3.14a shows one of their deformed meshes superposed on an O-ring that was compressed in an experiment, and the correlation is nearly exact. Fig. 3.14b is a repeat of Fig. 3.4, but with the addition of solutions from FEMALES to illustrate its improvement over Lindley's analytical equation. One year later, Dragoni & Strozzi[166] developed a plane strain FE model for a laterally constrained O-ring, and their results are illustrated in Fig. 3.5.

|                          |                          |
| :----------------------: | :----------------------: |
|          **(a)**         |          **(b)**         |
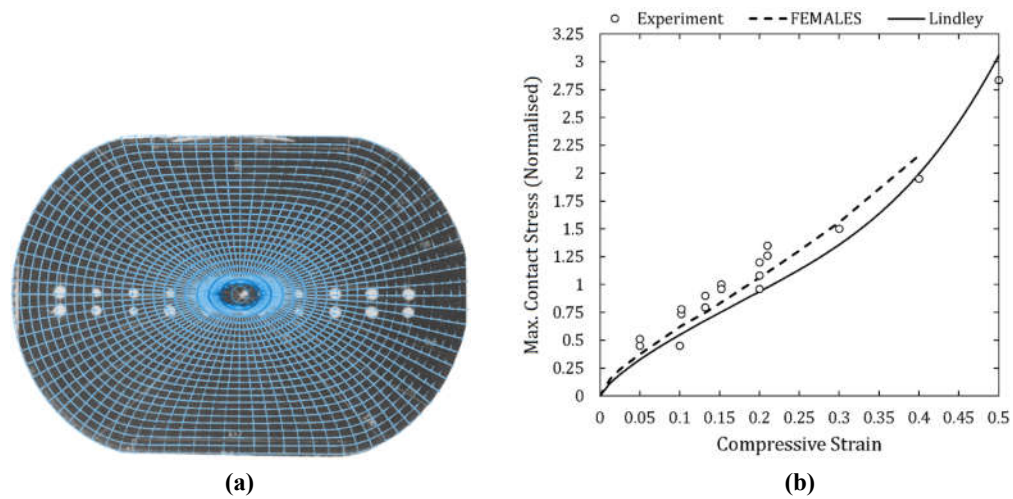
**Fig. 3.14: (a)** FE mesh overlay on a compressed O-ring. **(b)** Comparison of FEMALES, Lindley, and experimental contact pressures, with stress normalised by shear modulus.
(Adapted from George, Strozzi, & Rich.)[165]

In 1992, Green & English[188] conducted axisymmetric FE simulations on O-rings using the commercial software Ansys. They showed that axisymmetric and plane strain models differed significantly as compression and constraint increased (Fig. 3.15), even for large O-rings with small curvature. They found the Neo-Hookean material model was accurate up to 30% compression and demonstrated frictional sensitivities using a Coulomb model. An important implication of their work is that plane strain experimental studies of O-rings, which are common,[165] may not accurately represent axisymmetric O-ring behaviour.
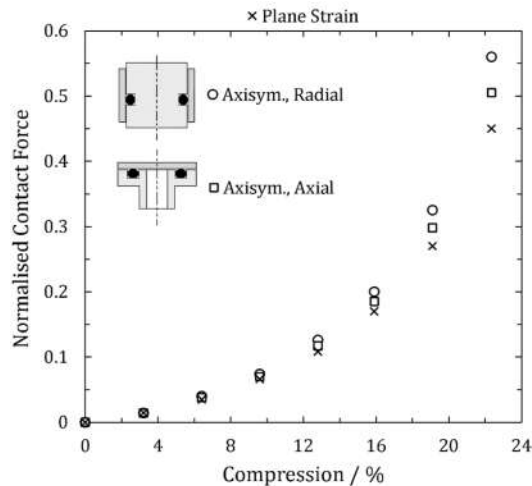


**Fig. 3.15:** Maximum contact forces for different FE models of O-rings.
(Adapted from Green & English.)[188]

There are numerous other studies on contact pressures in seals, such as:

- optimisation of seal length for oilfield expansion mandrels;[189]
- determining an empirical leak equation for underground shielding tunnels;[190]
- 3D simulation of an O-ring compressed by a flange;[191]
- pinching damage of a seal in a ball valve;[192]
- analysis of O-rings with D-shaped[193] and U-shaped[194] cross-sections;

74

- analysis of Chevron seals (also called Vee-packing);[195]
- analysis of metal-to-metal seals.[196]

Some of these studies used a Mooney-Rivlin material model which is discouraged for problems involving uniaxial compression (or equivalently, equibiaxial tension).[50]

### *Pressure Penetration Models*

Consider further the analytical/semi-empirical model of Liu *et al.*[159] The experimental leak pressures from Fig. 3.12, repeated in Fig. 3.16a, are for steady-state leakage which occurs at a constant flow rate across the entire seal. Fig. 3.16b shows these are much lower than experimental leak initiation pressures. The leak equation was fit to the steady pressures because they were repeatable and, presumably, the frictionless interface was approximated well during steady leak. In some cases, accurate prediction of the leak initiation pressure is of greater interest, and as will be shown, an accurate model for friction becomes critical.



(a)



(b)
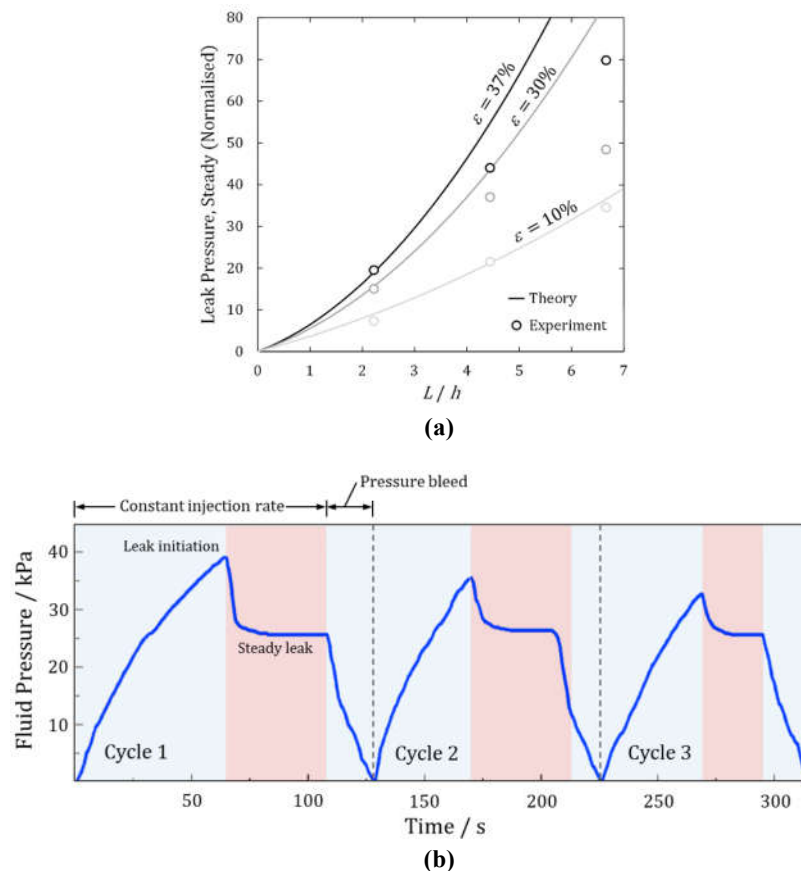
**Fig. 3.16: (a)** Steady leak pressures vs. aspect ratio. **(b)** Test data for 3 pressure cycles showing differences between leak initiation and steady leak pressures. (Adapted from Liu *et al.*)[159]

Fig. 3.17 compares contact pressure profiles for rectangular plane strain seals with frictionless and (Coulomb) frictional interfaces, with $\mu$ indicating the coefficient of friction. The models were generated in Abaqus and assume a Neo-Hookean material. The graphics on the left show the seals with a low pressure applied, and the maximum contact pressure

in both seals exceeds the fluid pressure. Higher fluid pressures are applied on the right. In the frictionless seal, the applied pressure equals the maximum contact pressure, so leak is imminent. This same pressure is applied to the frictional seal, but friction causes the peak contact pressure to exceed the fluid pressure because a small portion of the pressure is directed upward near the **sealing front** which is defined in Fig. 3.17a, better energising the seal. According to this cursory analysis, the frictional model seals better than the frictionless model.
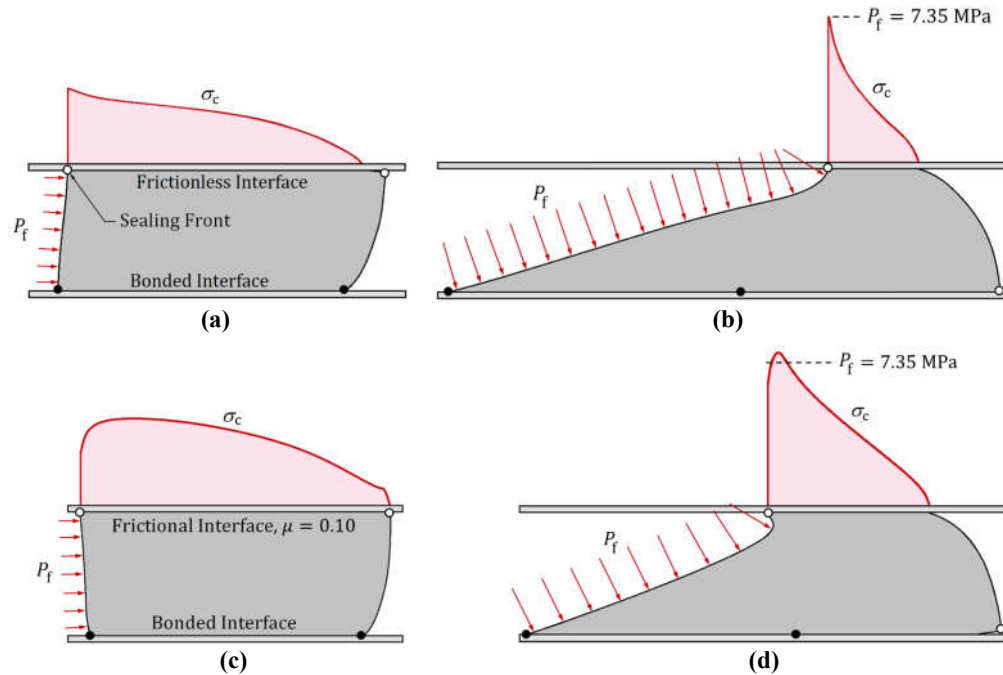


**Fig. 3.17:** Rectangular plane strain seals with: **(a)** low pressure and a frictionless interface; **(b)** the critical leak pressure applied to the frictionless seal; **(c)** low pressure and a frictional interface; **(d)** the same pressure as applied in Fig. 3.17b to illustrate that the peak contact pressure in the frictional case exceeds the fluid pressure.

Examination of the contact pressure profile in Fig. 3.17d reveals an important consideration that is irrelevant in the frictionless case. With friction, a portion of the contact pressure profile near the sealing front is less than the fluid pressure, so presumably, fluid can leak through this region and alter the pressure profile, possibly inducing leakage. Fig. 3.18 illustrates this by plotting a frictional contact pressure profile near the sealing front. The contact pressure profile is normalised by its maximum, and it is greater than the applied fluid pressure. However, the model does not account for leakage through the initial 6% of the sealing interface. A better model would account for this possibility, and several techniques to account for this have been addressed in the literature.
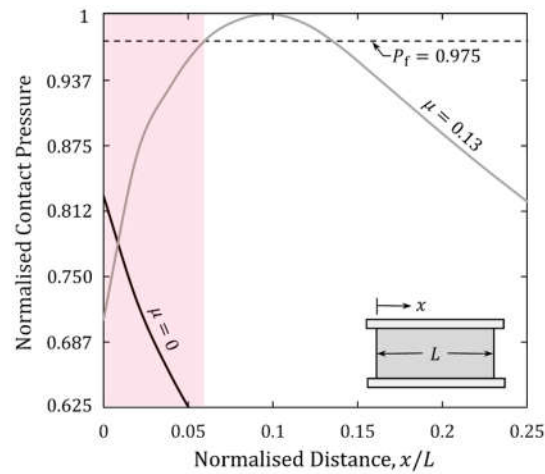
**Fig. 3.18:** Normalised contact pressure profiles near the sealing front with frictional and frictionless interfaces. The frictionless seal clearly leaks. It is unclear if the frictional seal will leak because fluid penetration through the shaded portion of the profile is not simulated.

In 1999, Estrada & Parsons[162] conducted 3D and axisymmetric FE simulations of a tubular flange joint with a Neoprene gasket using an incompressible Mooney-Rivlin material model. Their coarse FE mesh and its boundary conditions are illustrated in Fig. 3.19. For the 2D analysis, they used Abaqus' automated fluid pressure penetration algorithm to predict leakage, making this perhaps the earliest demonstration of such capability in the literature. The authors found their 2D and 3D FE results in accord with industrial design guidelines.
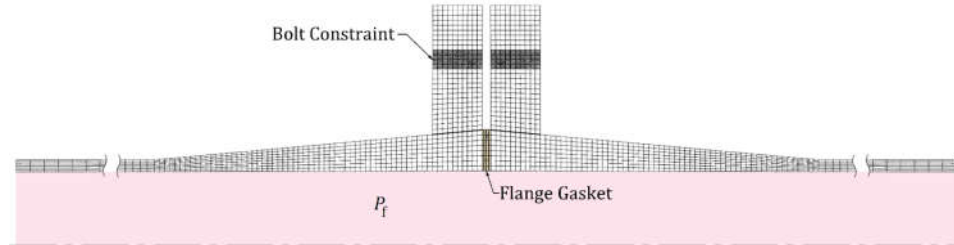


**Fig. 3.19:** The FE mesh of the radial flange gasket from Estrada & Parsons.[162]

Estrada & Parsons stated that Abaqus' FPP algorithm propagates pressure when contact and fluid pressures are equal, but this appears to be a misunderstanding. Abaqus' default setting propagates pressure when the contact pressure falls to zero.[197] Importantly, this leak criterion, $\sigma_c = 0$, is much different than the traditional criterion, $\sigma_c = P_f$. In Abaqus, leakage can be set to occur at any user-specified contact stress, but there is no built-in capability to update the leak criterion to match fluid pressure as the simulation progresses. To impose leakage when $\sigma_c = P_f$, pressure must be manually propagated step-by-step, or a user-defined subroutine could possibly impose the criterion, though such a routine has not been publicly demonstrated. This topic is given more thorough attention in Chapter 7.

In 2004, Möller & Stey[198] developed an Abaqus subroutine to implement FPP in a 3D analysis of an elastomeric seal. They benchmarked the algorithm against the built-in 2D FPP capability, finding some small differences between the solutions. Regardless, the

algorithm successfully ran their 3D problem. Fig. 3.20 shows some of their results. In 2014, Slee et al.[199] studied FPP in a metal-to-metal seal, recognising that once Abaqus propagates fluid pressure to a node with open contact, it cannot remove pressure from that node in later steps if the contact closes up again. They wrote a subroutine to remove fluid pressure from nodes when this occurred. Today, Abaqus has a built-in FPP algorithm for 3D analyses, but a subroutine is still required to remove fluid pressure from nodes that change from open to closed contact. New subroutines to handle closing contact were developed for this thesis and are presented in Chapter 5.
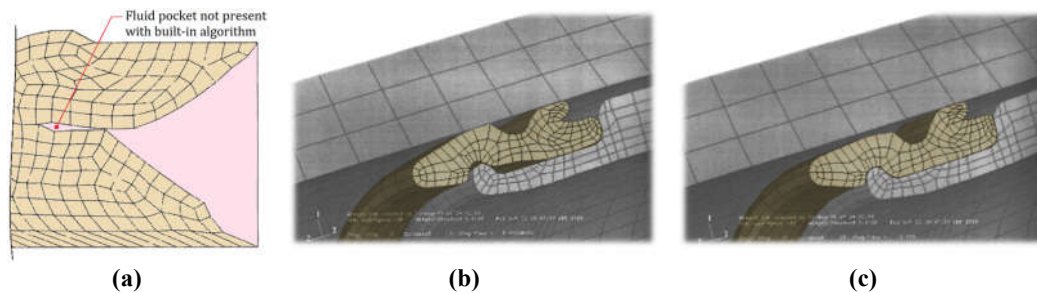


**Fig. 3.20:** Pressure penetration solutions in Abaqus: **(a)** fluid pocket in a 2D model of a Vee-seal using a user-defined FPP subroutine; **(b)** 3D radial seal before pressure application; **(c)** 3D radial seal after pressure application. (Adapted from Möller & Stey.)[198]

Several authors have studied pressure penetration through flexible pipe couplings used in offshore applications for the oilfield. These tools feature a metal seal ring that is swaged into a polymeric barrier on its inner surface and a metal body on its outer surface. Fig. 3.21 schematically illustrates the critical seal in the tool. Li et al.[200] conducted an FE study on the assembly, but it is unclear how they applied the pressure load. Fernando & Karabelas[201] also studied the seal ring with an axisymmetric FE model. They defined what appears to be a novel leak equation:

$$\sigma_c = \alpha P_f + (1 - \alpha)\sigma_y \tag{3.7}$$

where $\sigma_c$ and $P_f$ are contact and fluid pressures at a node, $\sigma_y$ is the yield strength of the weakest material at a sealing interface, and $\alpha$ is a material- and geometry-dependent parameter. As shown in Fig. 3.22, a plot of normalised contact pressure versus normalised fluid pressure defines the threshold at which leakage occurs. The authors manually implemented their leak criterion by iterating 2D solutions with increasing pressure increments, extracting contact stress results, and then moving the pressure load when the leak criterion was satisfied at nodes along the sealing front. The simulations were validated against experimental tests with an ultrasonic technique to measure contact stress, and good agreement was found. It is not clear if Eq. 3.7 can be adopted for elastomeric seals because they do not have a well-defined yield strength. In addition, the authors do not explain how they determined $\alpha$. Tang et al.[202,203] provided two more examples of pressure penetration on seal rings using Abaqus' built-in FPP algorithm.
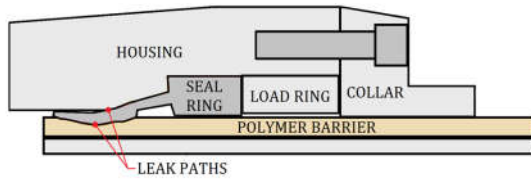
**Fig. 3.21:** Flexible hose coupling for offshore oilfield applications. (Adapted from Fernando & Karabelas.)[201]
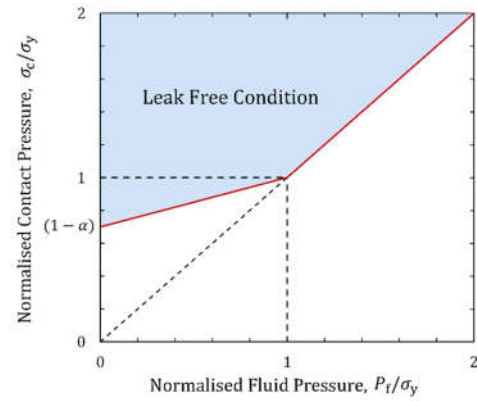


**Fig. 3.22:** Leak failure map based on Eq. 4.7. (Adapted from Fernando & Karabelas.)[201]

Hu *et al.*[204] conducted experimental and FE studies on a simplified version of an oilfield packer seal,[3] illustrated schematically in Fig. 3.23. They used Abaqus' built-in FPP with a 2D axisymmetric model. They conducted friction characterisation tests and used a Coulomb model with $\mu = 0.045$ for rubber-on-steel and $\mu = 0.024$ for rubber-on-polymethyl methacrylate, commonly called plexiglass. The plexiglass allowed visualisation of the seal during experimental testing (Fig. 3.24). As shown in Fig 3.25, they achieved remarkable consistency between simulation and experimental results.



| (a) | (b) |
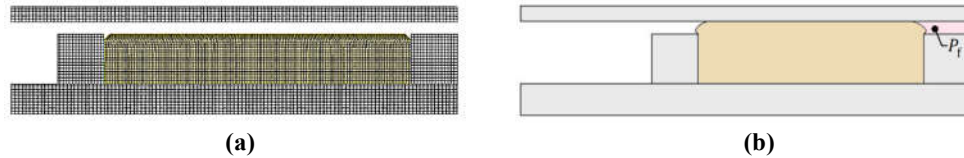
**Fig. 3.23:** Schematic illustration of a 2D axisymmetric oilfield packer seal: **(a)** FE mesh; **(b)** after setting and with a small amount of pressure applied. (Adapted from Hu *et al.*)[204]
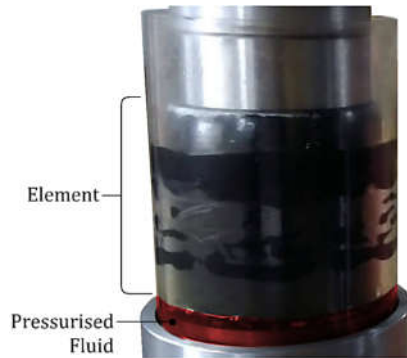


**Fig. 3.24:** Packer seal test fixture with transparent tubular. (Adapted from Hu *et al.*)[204]
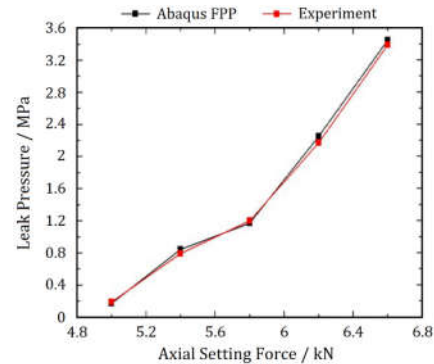


**Fig. 3.25:** Experimental and numerical results for a packer seal. (Adapted from Hu *et al.*)[204]

Zhao *et al.*[205] conducted a 3D FE analysis of a linear section of a cabin seal for an aircraft. They used Abaqus' built-in FPP capability. The seal, a fabric-rubber composite, was vertically compressed, and then cabin pressure was applied (Fig. 3.26). Unique to this study, the authors knew *a priori* that the critical contact pressure for leakage was 42.4 kPa, so this was specified in the FPP settings.
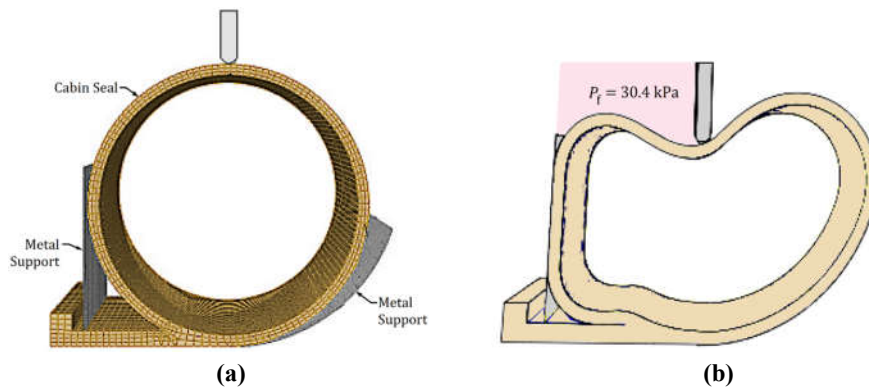
**Fig. 3.26: (a)** 3D FE mesh of an aircraft cabin pressure seal before compression. **(b)** The seal after compression and with pressure along one surface. (Adapted from Zhao *et al.*)[205]

Gong and coauthors[206,207,208] conducted a series of studies in Abaqus for gasket seals in underground shield tunnels (Fig. 3.27). The seal geometry in different configurations is shown in Fig. 3.28. They used Abaqus' 2D FPP algorithm with default settings, finding predicted leak pressures were generally lower than experimental results, but accurate within ±20%. They conducted a mesh-sensitivity study for the seal compression step, but not the pressure penetration loading. A Mooney-Rivlin model and Coulomb friction (usually with $\mu \approx 0.5$) were used. They also used adaptive re-meshing to correct mesh distortion that occurred when pre-manufactured voids in the seal collapsed.



**Fig. 3.27:** Underground shield tunnel constructed from curved sections that are sealed by compression gaskets. (Photo from the Institution of Civil Engineers.)[209]
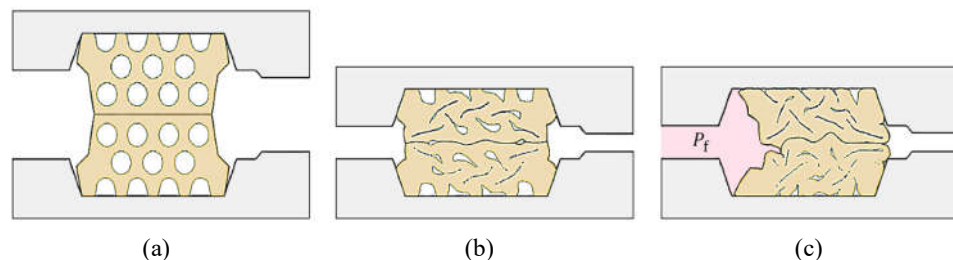


**Fig. 3.28:** Shield tunnel gasket seals: **(a)** before compression; **(b)** after compression; **(c)** with fluid pressure applied. (Adapted from Gong *et al.*)[190]

Gorash and coauthors have published a series of papers that explore fluid pressure penetration. In 2016, they conducted 2D metal-to-metal FPP studies in Ansys using a multi-scale model approach to address roughness at the microscale.[210] A year later, they

80

attempted 2D FPP in Abaqus/Standard (which uses an implicit solution scheme) for an oilfield swell packer,[211] but convergence was not achieved due to contact issues. They achieved a converged solution in Abaqus/Explicit which has no built-in FPP algorithm, so pressure was not propagated. Nevertheless, the seal suddenly extruded at a critical pressure, indicative of elastic instability.

In 2018, Gorash *et al.*[212] successfully extruded a swell packer with Abaqus' built-in FPP algorithm (Fig. 3.29). Important to note, a material model for unfilled rubber was used which is not realistic for practical swell packer materials. Contact convergence was facilitated with a bi-linear Coulomb-Orowan frictional law.[213] This law applies a Coulomb friction model until a critical shear force threshold, above which the frictional force is constant regardless of any increase in the normal load. If the frictional force drops below the shear threshold, the Coulomb model resumes. Wriggers[214] noted that this mitigates nodal locking and has a smoothing effect on the contact behaviour. Convergence was also helped with Abaqus' global automatic stabilisation control which adds non-physical viscous damping to the model at the expense of some modelling error. Turning their attention back to Abaqus/Explicit, the authors implemented a coupled Euler-Lagrange (CEL) approach to solve the swell packer extrusion problem (see the next paragraph for details on CEL), but the simulation did not converge (Fig. 3.30). However, convergence was achieved on a seal with a low aspect ratio, $L/h = 0.2$.
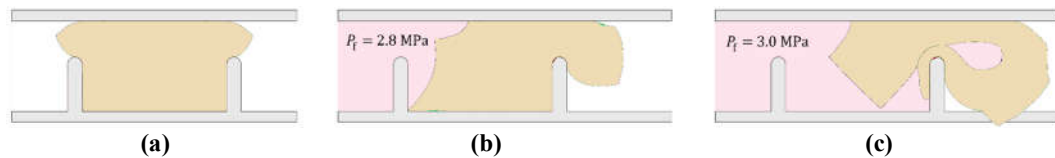


**Fig. 3.29:** An unbonded swell packer: **(a)** before application of FPP; **(b)** with pressure applied but prior to blowout; **(c)** with FPP at blowout. Note that a contact definition was not assigned at the interference on the bottom right. (Adapted from Gorash *et al.*)[212]
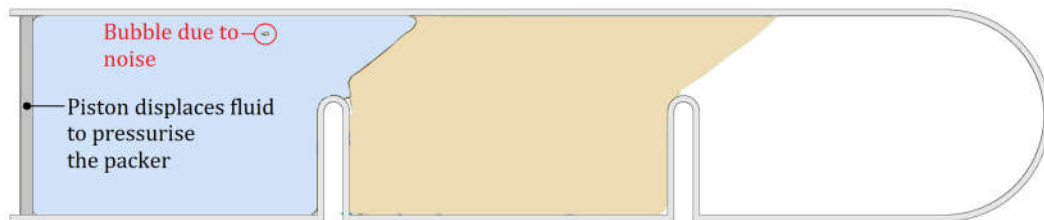


**Fig. 3.30:** A swell packer loaded with pressure by a fluid using the CEL approach. Bubbles appear and disappear in the fluid domain due to computational noise. Compared to Fig. 3.29b, the deformation appears unrealistic because fluid does not penetrate between the gauge ring and swell packer. The simulation failed to converge at the point shown. (Adapted from Gorash *et al.*)[212]

Morrison, Gorash, & Hamilton[215] used Abaqus' built-in FPP and CEL capabilities to study leakage across the axisymmetric seal shown in Fig. 3.31. The CEL approach assigns a Lagrangian mesh to solid bodies and an Eulerian mesh to fluid domains. Referring to Fig. 3.31, the seal uses a Lagrangian mesh. The fluid domain permeates the whole interior of the bounding walls, and a working fluid is initially assigned in the left domain. In Fig.

3.31b, a piston has pushed the fluid across the seal to cause leakage. Distinct from Abaqus' FPP algorithm, CEL accounts for contact nodes opening and closing during the simulation. However, it has drawbacks. It is computationally expensive, requires significant post-processing, and is subject to computational noise in the fluid domain (Fig. 3.32a). Nevertheless, once the authors fully processed their data, they achieved good correlation between Abaqus' FPP and CEL solutions (Fig. 3.32b). For a more detailed review of CEL, see Foucard et al.[216] and references therein.

As a final note, Abaqus has some online tutorials that are relevant to the topics in this section. See Parraga[217] and Morlacchi[218] for demonstrations of FPP on a threaded joint and the CEL technique with a boat hull, respectively.



(a)                                                      (b)

**Fig. 3.31:** 1° segment of the axisymmetric seal studied by Morrison et al.:[215] **(a)** with a pressurised fluid prior to leakage; **(b)** as fluid breaches the sealing interface. (Images adapted from Gorash.)[219]



(a)                                                      (b)
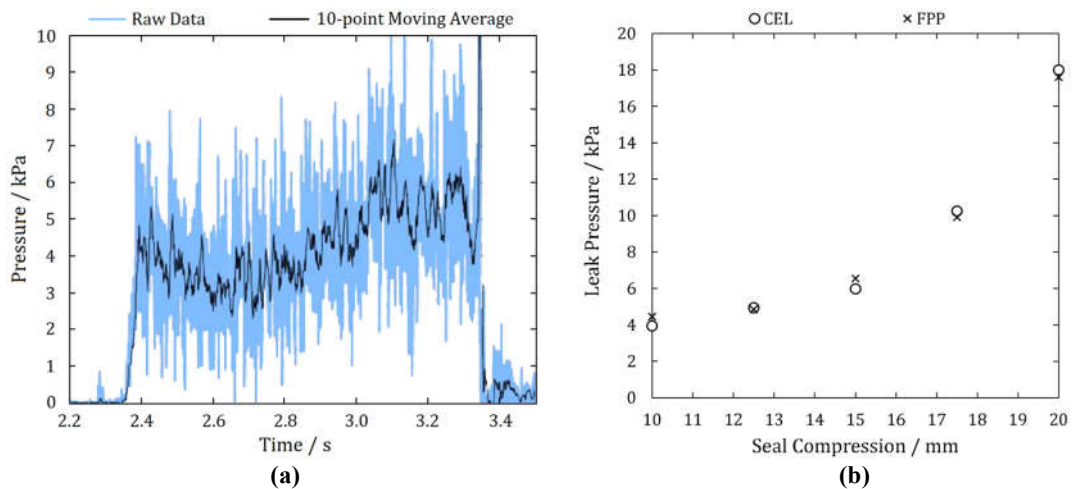
**Fig. 3.32: (a)** Noise in the fluid pressure time history when using the CEL approach. **(b)** Comparison of CEL and FPP leakage pressures. (Adapted from Morrison et al.)[215]

82

## 3.3 Summary

Several analytical models have been developed to predict contact pressures for simple seal geometries and in particular for O-rings. Some of these account for the application of fluid pressure, but they are generally unable to predict critical leakage pressures because they assume fluid and contact pressures superpose. One exception to this is the semi-empirical model of Liu *et al.*,[159] but it does not account for friction. Based on FE studies that have extended Liu's work, friction is a critical parameter when modelling seal leakage because it alters the contact pressure profile near the sealing front, potentially allowing fluid to penetrate the sealing interface. Due to the coupling of frictional behaviour, which itself is complicated for elastomers, and the evolution of contact stress with fluid pressure, numerical simulation appears to be the only recourse to develop accurate models for leak prediction.

As summarised in Table 3.1, there are several methods to simulate pressure penetration at a contact interface, the most common being automated FPP in Abaqus or Ansys. Several authors have achieved good correlation between experimental and numerically simulated leak pressures. However, studies in Chapter 5 reveal that predicted leakage pressures are sensitive to many factors including: (i) the frictional model; (ii) mesh size; (iii) how pressure (a surface load) is discretised to nodes (a concentrated load); (iv) the leak criterion (such as $\sigma_c = 0$ or $\sigma_c = P_f$); and (v) changes in nodal contact status. Collectively, these factors can change leak predictions by more than 50%, but they have not been systematically addressed in the literature. Some other concerns or gaps in the existing literature are: (i) the use of a Mooney-Rivlin model without showing that uniaxial compression is a negligible loading mode, for instance through the use of a biaxiality analysis; (ii) simulated pressures for rubber seals are much lower than those encountered in the oilfield where 35 to 70 MPa is common; and (iii) material compressibility, which can become important for highly constrained seals, is usually not modelled. Given the uncertainties in the published models, some of the reported accuracies may simply be fortuitous. Chapter 5 addresses some of these knowledge gaps in the literature with an in-depth assessment of numerical FPP techniques in Abaqus.

**Table 3.1:** Summary of FE studies that simulate fluid pressure penetration in seals.

| Year | Authors | Analysis | | Rubber SEF | Poisson's Ratio, $\nu$ | Rubber Friction, $\mu$ | Max. $\Delta P$ / MPa | Propagation Technique[i] | | | |
|------|---------|----|----|------------|------------------------|------------------------|----------------------|------|------|------|------|
| | | 3D | 2D | | | | | FPP | Man. | Sub. | CEL |
| 1999 | Estrada & Parsons[179] | X | X | Mooney-Rivlin? | 0.5 | 0.8 | 0.35 | X | - | - | - |
| 2004 | Möller & Stey[215] | X | X | ? | ? | ? | ? | - | - | X | - |
| 2014 | Liu *et al*.[176] | - | X | Neo-Hookean | 0.5 | 0 | 0.08 | Not Attempted | | | |
| 2018 | Gorash *et al*.[230] | - | X | van der Waals | 0.5 | 0.3[ii] | 3 | X | - | - | X |
| 2018 | Morrison *et al*.[233] | - | X | Ogden-$n_3$ | 0.499995 | 0.3 | 0.018 | X | - | - | X |
| 2018 | Hu *et al*.[221] | - | X | Yeoh | 0.5 | 0.024, 0.045 | 2.3 | X | - | - | - |
| 2018 | Zhao *et al*.[222] | X | - | Mooney-Rivlin | 0.5 | 0.21 | 0.04 | X | - | - | - |
| 2018 | Gong & Ding[223] | - | X | Mooney-Rivlin | 0.5 | 0.5, 0.57 | 2.3 | X | - | - | - |
| 2019 | Gong *et al*.[224] | - | X | Mooney-Rivlin | 0.5 | 0.5, 0.57 | 1.7 | X | - | - | - |
| 2020 | Gong, Ding, & Xie[225] | - | X | Mooney-Rivlin | 0.4999 | 0.2-0.8 | 1.3 | X | - | - | - |
| 2014 | Slee *et al*.[216] | X? | - | N/A | N/A | N/A | 450 | X | - | X | - |
| 2014 | Fernando & Karabelas[218] | - | X | N/A | N/A | N/A | 200 | - | X | - | - |
| 2016 | Gorash *et al*.[228] | - | X | N/A | N/A | N/A | 23 | X | X | - | - |
| 2019 | Tang *et al*.[219] | - | X | N/A | N/A | N/A | 40 | X | - | - | - |
| 2020 | Tang *et al*.[220] | - | X | N/A | N/A | N/A | 30 | X | - | - | - |

[i] FPP: a built-in algorithm for fluid pressure penetration in Abacus or Ansys.
Man.: pressure was manually propagated, step-by-step, by the user.
Sub.: a user-defined subroutine-controlled the pressure penetration.
CEL: automated pressure penetration via the coupled Euler-Lagrange scheme.

[ii] 0.3 was specified for the Coulomb part of Coulomb-Orowan frictional behaviour.

# 4. Novel Constitutive & Characterisation Models for Hyperelasticity

## 4.1 Overview

This chapter presents two novel contributions to the literature that are not related specifically to the problem of seal leakage. A strain-energy function is proposed that models large non-linearities in the stress-strain curves of highly filled sealing materials. Focus is given to the SEF's behaviour at low strains (say, ≤ 10%) which have less attention in the modeling literature than the characteristic stiffening response that occurs at larger strains. The SEF has six model parameters, yet its mathematical structure is simple enough to allow curve fitting by inspection. This technique is demonstrated and shown to give results that are comparable to parameters that are algorithmically determined. Validation of subroutines to implement the SEF in Abaqus are also demonstrated.

The second new contribution relates to the uniaxial tension test. In some cases, it may be necessary to approximate strain from the grip displacement, but this can introduce large errors when the rubber specimen is not prismatic. Hence, a method to correct stress-strain data when strain is measured from grip displacement is proposed. Numerical and experimental studies are used to validate the technique.

## 4.2  A Novel Strain-Energy Function for Highly Filled Elastomers[††]

Strain-energy functions have received exhaustive attention in the literature,[87] and particular attention has been given to the characteristic stiffening phenomenon at large strains (see Fig. 2.18). In Section 2.7, some complications due to reinforcing filler were introduced. For example, Fig. 4.1 shows Treloar's unfilled data for NR[220] compared to a filled industrial material from Yeoh.[92] Yeoh's material data is much stiffer, and the strain stiffening effect occurs at much lower strains due to molecular constraint that is imposed by the reinforcing filler. It is for this latter reason that Yeoh could not reasonably use the Neo-Hookean SEF, leading him to propose a new SEF that fit well to the data for his filled material. Yet, a key limitation remains in the Yeoh SEF and almost all other SEFs that have been proposed in the literature. To understand this limitation, one characteristic of high pressure oilfield seals must be discussed.

Sealing materials in the oilfield often have extraordinary amounts of reinforcing filler to counter two types of failure: extrusion and rapid gas decompression (RGD, or synonymously, explosive decompression). The former failure mode has already been illustrated in Fig. 3.1c where a portion of a seal fractures through an extrusion gap. The latter mode is a consequence of gas diffusing into the rubber at a high pressure over a

---

[††] The work in this section is published in *Rubber Chemistry & Technology*, **92** (4), 653-686.

relatively long time. When pressure reduces quickly, the gas undergoes a volumetric expansion. Without sufficient time to diffuse out of the rubber matrix, the gas creates internal fractures that can cause complete failure of the seal. Both failure modes are mitigated by introducing large amounts of filler to increase the shear modulus, and this stiffness inherently resists deformation and fracture.[75] Fig. 4.1b illustrates the exceptional stiffness of an oilfield sealing material by comparing a 90D (Shore A) HNBR to more conventional industrial elastomers. The strain stiffening response of the HNBR material is not exceptional, but the rapid reduction in the tangent modulus at low strains is. It is this characteristic that most SEFs model poorly.
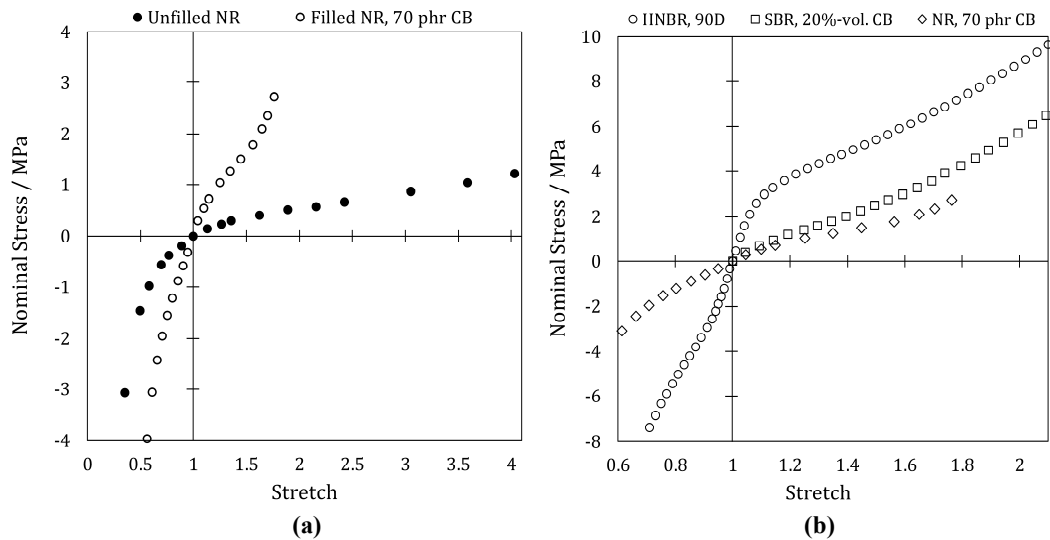


**Fig. 4.1:** Stress-stretch response of: **(a)** a filled industrial material from Yeoh[92] compared to Treloar's uniaxial data[220] for unfilled NR; **(b)** a highly filled oilfield sealing material (HNBR, 90D) and two filled industrial materials from Yeoh[92] and Fujikawa *et al.*[221]

To demonstrate how most SEFs are ill-suited for modelling oilfield seals, Fig. 4.2a shows the Neo-Hookean SEF with two different shear moduli when fit to the 90D HNBR material. If the shear modulus is chosen to fit the initial slope of the stress-strain curve, the model grossly overpredicts the stress magnitudes at all strains above 10%. If the shear modulus is reduced to better fit the overall profile, there are large underpredictions in stress magnitudes at low strains. The source of these mismatches lies in the fact that the mathematical form of the Neo-Hookean SEF precludes it from tracking the curvature of the stress-strain data at low strains. Turning to the Yeoh SEF in Fig. 4.2b, there is improvement in the curve fit with parameters determined by inspection or with a Levenberg-Marquardt (LM) algorithm[222] (see Appendix G). However, even the Yeoh model poorly tracks the stress-strain data at low strains. The problem with both of these SEFs is that the low-strain behaviour is controlled by the $(I_1 - 3)^1$ term. In fact, almost all particular SEFs that have been proposed in the literature adopt this term or one similar, and it is why they poorly fit the low strain behaviour of sealing materials in the oilfield.
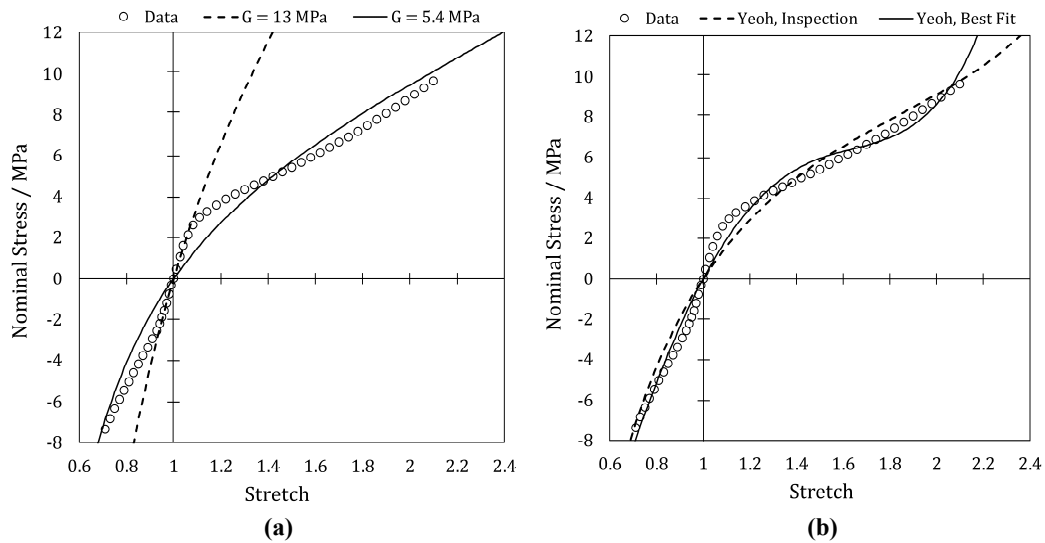
**Fig. 4.2:** SEFs fit to data for HNBR seal material; **(a)** Neo-Hookean; **(b)** Yeoh: coefficients by inspection, $(C_{10}, C_{20}, C_{30}) = (2.9, -0.15, 0.025)$ MPa, and by LM algorithm, $(C_{10}, C_{20}, C_{30}) = (3.6, -0.84, 0.185)$ MPa.

To address the fitting problem at low strains, Davies *et al.*[91] proposed the so-called Davies-De-Thomas (DDT) SEF which may be cast as:

$$W = K_1(I_1 - 3 + D^2)^m + K_3(I_1 - 3)^2 \tag{4.1}$$

where $0 < m \leq 1$ acts on the leading term and $0 \leq D \ll 1$ is introduced as a low strain correction parameter. In fact, this parameter is not necessary to correct low strain behaviour for many problems, so let $D = 0$. The real strength of the DDT SEF is the freedom of its parameter $m$. When $m < 1$, stresses at the lowest strains are amplified and a rapid diminution in the tangent modulus can be modelled accurately. This is illustrated in Fig. 4.3 where $(K_1, K_3) = (2.78, 0)$ MPa are fixed and $m$ is incrementally reduced from 1 to 0.8. Of course, the upward inflection can be captured by setting $K_3 > 0$. Using the LM fitting algorithm, a curve fit using the DDT model is shown in Fig. 4.4, and it tracks the data remarkably well.
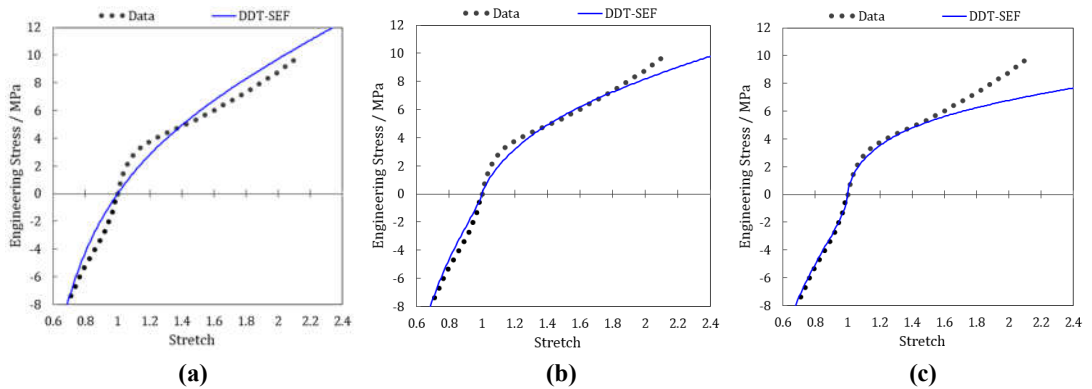


**Fig. 4.3:** Improvement in fitting the low strain behaviour of a 90D HNBR material by varying the parameter $m$ in the DDT SEF: **(a)** $m = 1$ which returns the Neo-Hookean SEF; **(b)** $m = 0.9$; **(c)** $m = 0.8$.
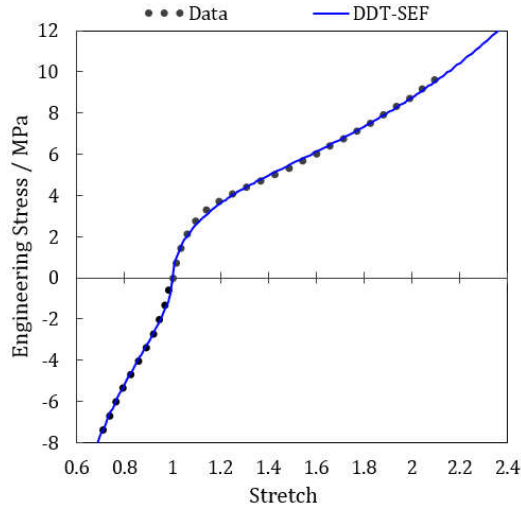
**Fig. 4.4:** A curve fit using the LM algorithm; $(K_1, K_2) = (2.78, 0.16)$ MPa and $(m, D) = (0.78, 0)$.

The DDT SEF does introduce a problem during numerical implementation when a rubber is in an unstrained state. To illustrate, consider the uniaxial stress equation for the DDT SEF which may be derived by using the chain rule to differentiate Eq. 4.1 with respect to $\lambda$:[50]

$$\sigma_u = 2(\lambda - \lambda^{-2})[mK_1(I_1 - 3 + D^2)^{m-1} + 2K_3(I_1 - 3)] \tag{4.2}$$

where $\sigma_u$ can denote uniaxial tension or compression stress. In the unstrained state, $\lambda = 1$ and $I_1 = 3$, and restricting to $m < 1$ (to address the low strain diminution of modulus as illustrated in Fig. 4.4) with $D = 0$, algebraic manipulation of Eq. 4.2 results in an indeterminate fraction of $0/0$. Setting $D > 0$ alleviates this problem, but it leaves a finite energy in Eq. 4.1 even in the unstrained state. That is, strain-energy is positive with no load on the system. Both of these problems are avoided by enforcing $D = 0$, and then imposing logic (for instance, an IF-THEN statement) to assign zero stress to any rubber in an unstrained state.

Building on concepts from the Yeoh and DDT SEFs that have been outlined, this thesis proposes and implements a novel SEF of the form:

$$W = K_1(I_1 - 3)^m + K_2(I_1 - 3)^n + K_3(I_1 - 3)^p \tag{4.3}$$

where $(K_1, K_2, K_3)$ and $(m, p, q)$ are real numbered fitting parameters. Typical constraints on the parameters are: $K_1 > 0$ ; $K_2 \leq 0$ ; $K_3 \geq 0$ ; $K_1 > |K_2| > K_3$ ; $0.7 \leq m < 1$ ; and $m < p < q$. These give a form that is well-aligned with Yeoh's model, so the model is designated the generalised Yeoh (gen-Yeoh) SEF. The flexibility in the exponents allows the function to accurately capture low and high strain non-linearities for highly filled sealing rubbers.

### 4.2.1  Curve Fitting the gen-Yeoh SEF by Inspection

Due to a simple mathematical structure, and using the constraints that have been suggested, the parameters of the gen-Yeoh SEF can be determined to a good degree of

88

accuracy by inspection. To illustrate, consider Fig. 4.5a which plots data from the HNBR sealing material on log axes. The $x$-axis is expressed in terms of the first invariant, and the $y$-axis uses a measure of stiffness called reduced stress which for uniaxial tension and compression is given by:[‡‡]

$$\hat{\sigma} = \frac{\sigma_{\mathrm{u}}}{2(\lambda - \lambda^{-2})} \tag{4.4}$$

For reference, the figure includes stretch values, $\lambda_{\mathrm{ut}}$, in uniaxial tension that correspond to $\log(I_1 - 3)$. The UT and UC data overlay one another fairly well, indicating that they are well conditioned for fitting with $I_1$-based SEFs.[91] This condition does not always occur (see Appendix K for further comment), so it is ideal to have data from more than one loading mode to confirm the approach.
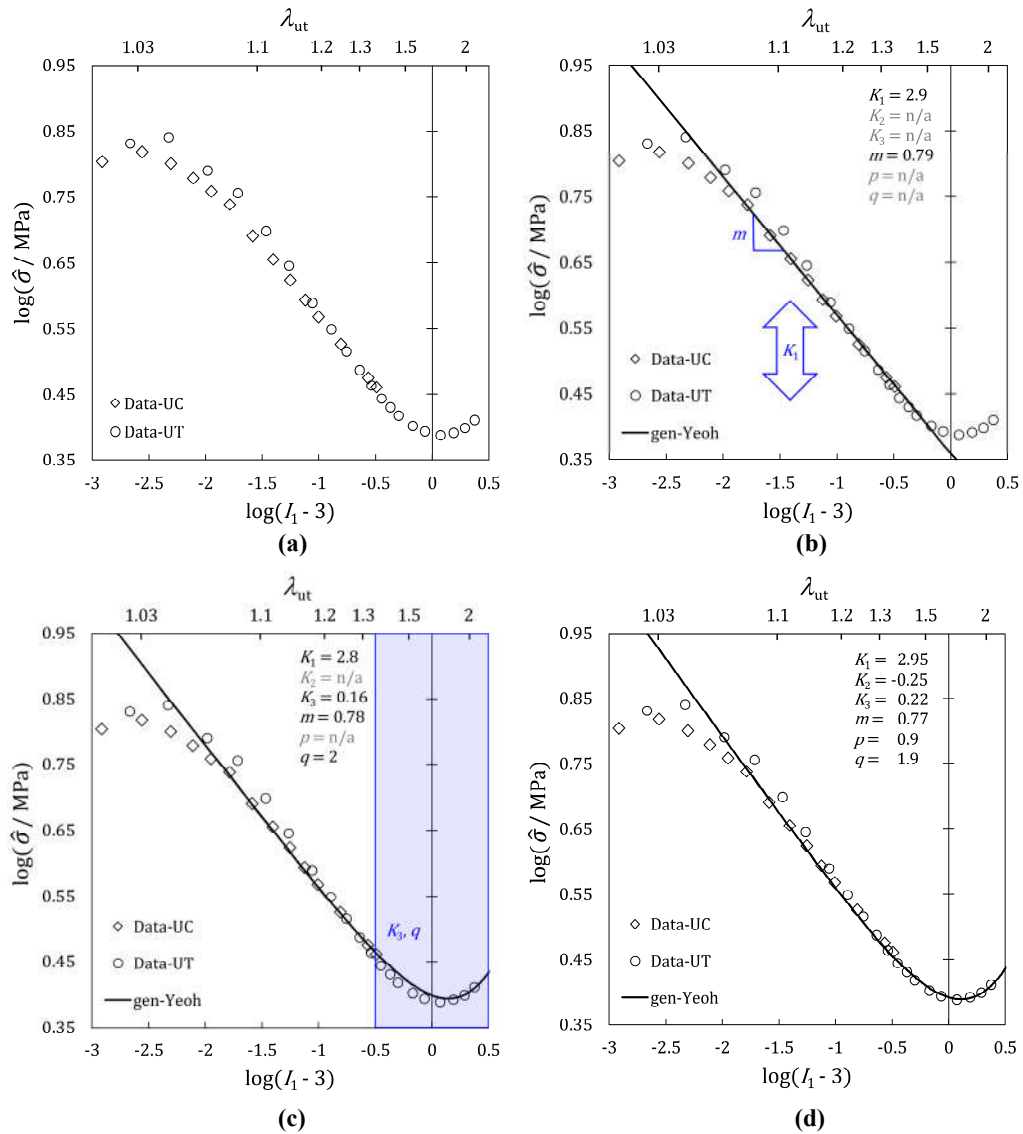


**Fig. 4.5:** Fitting the gen-Yeoh SEF by inspection for a 90D HNBR sealing material: **(a)** uniaxial data; **(b)** setting $K_1$ and $m$; **(c)** setting $K_3$ and $q$; **(d)** setting $K_2$ and $p$.

---

[‡‡] The factor of 2 in the denominator of Eq. 4.4 is missing in early versions of the RCT publication.

To fit the gen-Yeoh SEF to the data, first adjust the vertical position with $K_1$ and set the slope of the linear region with $m$ (Fig. 4.5b). Next assign a guess value $q = 2$ and adjust $K_3$ to capture finite-extensibility. Slight adjustments to $K_1$ and $m$ may also improve the fit (Fig. 4.5c). Finally, adjust $K_2$ and $p$ to better tune the overall fit and adjust other parameters as necessary (Fig. 4.5d). Bear in mind that the data points less than $\log(I_1 - 3) = $ -2.5 are subject to large measurement error, and the errors are amplified in the log plot. This becomes apparent when the data is converted back to linear axes as shown in Fig. 4.6a where the low strain fit looks good.

For comparison with the method of fitting by inspection, the LM algorithm was also used to determine model parameters. Fig. 4.6b shows a seemingly trivial improvement in the curve fit, giving credence to fitting the model by inspection. Fig. 4.6b also shows a proper ordering of the predicted stress responses in planar and equibiaxial loading modes, and there are no intersections of the different loading mode curves that could cause problems with numerical stability.
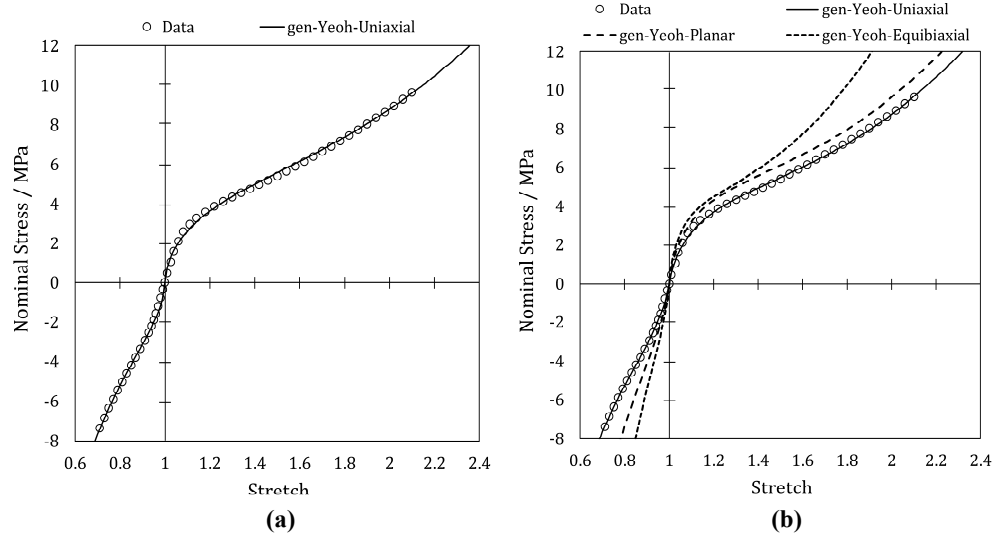


**Fig. 4.6:** Stress-stretch plots with the gen-Yeoh SEF for HNBR sealing material on linear axes: **(a)** same parameters as Fig. 4.5d; (b) parameters from LM algorithm, $(K_1, K_2, K_3) = (5.38, -2.85, 0.4)$ MPa, $(m, p, q) = (0.89, 1.08, 1.85)$.

### 4.2.2 A Summary of Errors with the Different Strain-Energy Functions

Table 4.1 shows relative errors of various curve fits in this section using the following equation:

$$e_R = \frac{1}{N_p} \sum_i^{N_p} \sqrt{\frac{(\sigma_{i,SEF} - \sigma_{i,data})^2}{\sigma_{i,data}^2}} \qquad (4.5)$$

where $N_p$ is the total number of measurement points, $\sigma_{i,data}$ are stress data points, and $\sigma_{i,SEF}$ are stresses predicted by the SEF. The DDT and gen-Yeoh SEFs have the lowest errors, and using the LM algorithm reduces fitting errors as expected.

**Table 4.1:** Errors from Eq. 4.5 for different SEFs when fit to the HNBR sealing material data

| Model | Fitting Method | Comment | Error |
|---|---|---|---|
| Neo-Hookean | Inspection | $G = 13$ MPa | 1.103 |
| Neo-Hookean | Inspection | $G = 5.4$ MPa | 0.282 |
| Yeoh | Inspection | Fig. 4.2b | 0.228 |
| Yeoh | LM algorithm | Fig. 4.2b | 0.151 |
| DDT | LM algorithm | Fig. 4.4 | 0.061 |
| gen-Yeoh | Inspection | Fig. 4.5 | 0.074 |
| gen-Yeoh | LM algorithm | Fig. 4.6b | 0.035 |

### 4.2.3 Validation of the gen-Yeoh SEF Subroutines

The UHYPER and VUMAT subroutines for the gen-Yeoh SEF were validated in Abaqus/Standard and Abaqus/Explicit, respectively, and the codes are in Appendices A and B. Some notes on using the routines are in Appendices P and Q. Abaqus/Explicit does not have a fully incompressible quadrilateral finite-element, so following the proposed deviatoric and volumetric decomposition of Eq. 2.47, a term to model slight compressibility is added to the gen-Yeoh SEF to give:

$$W = K_1(\bar{I}_1 - 3)^m + K_2(\bar{I}_1 - 3)^p + K_3(\bar{I}_1 - 3)^q + \kappa(J - 1)^2 \tag{4.6}$$

where $\kappa$ is the material's bulk modulus. In the absence of a volumetric compression test to determine the bulk modulus, it may be estimated from linear elastic theory as:

$$\kappa = \frac{2G(1+\nu)}{3(1-2\nu)} \tag{4.7}$$

by assuming a Poisson's ratio with $0.495 \leq \nu \leq 0.4995$ typical.

Eq. 4.6 assumes that the compressibility is a linear function of pressure (or stress), but as Fig. 2.10 indicates, the linearity is lost at high pressures. Thus, there are cases where it is appropriate to include an additional term for volumetric deformation:

$$W = K_1(\bar{I}_1 - 3)^m + K_2(\bar{I}_1 - 3)^p + K_3(\bar{I}_1 - 3)^q + \kappa_1(J - 1)^2 + \kappa_2(J - 1)^4 \tag{4.8}$$

where $\kappa_1$ describes the low-pressure (linear) volumetric response, and $\kappa_2$ is a quadratic correction for higher pressures. It is perhaps confusing to describe $\kappa_1(J - 1)^2$ as a linear term since it raised to the power of two, but this occurs only because it is expressed with $J$ instead of $I_3$. When the latter is used, $(J - 1)^{2i}$ terms are replaced by $(I_3 - 1)^i$, and the peculiarity of describing a quadratic term as linear is avoided. For the validation exercises that follow, the simpler form of Eq. 4.6 has been assumed.

The UHYPER subroutine for the gen-Yeoh SEF was initially tested with the Yeoh parameters from Fig. 4.2b and compared to Abaqus' built-in Yeoh model. A Poisson's ratio of 0.495 was assumed, and it was converted to compressibility parameter $D_1$ according to:[223]

$$D_1 = \frac{2}{\kappa} = \frac{3(1-2\nu)}{G(1+\nu)} = 2.78707 * 10^{-3} \text{ MPa}^{-1} \tag{4.9}$$

where $G = 2C_{10}$ in the Yeoh model and $G \approx 2K_1$ in the gen-Yeoh model.

Homogeneous modes of deformation, including simple shear, were tested on a unit cube with one linear, hybrid, reduced integration brick element (C3D8RH in Abaqus nomenclature). With only one exception, stresses, strains, energy density, and element volume matched to 9 decimal places, the maximum precision in Abaqus' visualisation module. In the pure deformation modes (for instance uniaxial tension), finite stresses were computed in principal directions in which no load was applied. These were an artefact of the numerical solution and only amounted to 0.001% of the stress values in the directions of applied deformation. The artificial stresses also arose in tests with a fully incompressible element, so the issue did not arise solely from volumetric deformation.

To test inhomogeneous deformations, a unit cube ($1\,\text{mm}^3$) was meshed with $20^3$ elements. The cube was fixed on its bottom surface and twisted through 60° on its top surface. Fig. 4.7 shows maximum principal nominal strains in the cube. All maximum and minimum principal stresses and strains matched to 9 decimal places. Element volumes and energy densities also matched to 9 decimal places.
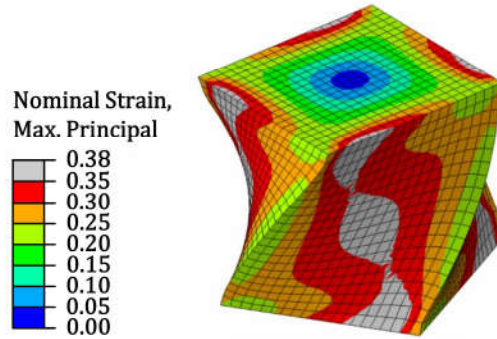


**Fig. 4.7:** Maximum principal nominal strain contours in cube when twisted 60°.

The gen-Yeoh model was then run using the algorithmically-determined parameters in Fig. 4.6b and $D_1 = 1.86495 * 10^{-3}\,\text{MPa}^{-1}$. Simulation times with the built-in Yeoh model, UHYPER Yeoh model, and UHYPER gen-Yeoh model were 161 s, 163 s, and 165 s, respectively, using full nodal precision and 8 processors on a 12 core Intel Xeon E5-2620 CPU.

In Abaqus/Explicit, inertia effects must be considered, so a density of $1\,\text{g/cm}^3$ was assigned to the material. Mass scaling[224] was required to prevent the stable time increment from becoming too small for the computer's numerical precision. Scaling factors up to $10^7$ affected stress, strain, volume, and strain-energy density less than 1%. A factor of $10^3$ was used for final validation of the VUMAT subroutine.

When comparing the built-in and VUMAT Yeoh models in homogeneous modes of deformation, artificial stresses again occurred in the directions in which no loads were applied. However, they were two orders of magnitude lower than their Abaqus/Standard counterparts. Consequently, some small but negligible differences between the built-in and VUMAT solutions were found with homogeneous deformations.

92

Small discrepancies were found in the twisted cube solutions when using the built-in and VUMAT Yeoh models, though they were negligible in terms of practical engineering design. Table 4.2 summarises the percent differences for some selected field outputs with the different material solution techniques.

**Table 4.2:** Percent difference in selected field output values using built-in and VUMAT Yeoh models.

| Field Output | | Built-In Yeoh | VUMAT Yeoh | Difference |
|---|---|---|---|---|
| Principal stress / MPa | Max. | 8.7532 | 8.7839 | 0.35% |
| | Min. | 1.3431 | 1.3477 | 0.34% |
| Principal strain | Max. | 0.38557 | 0.38581 | 0.06% |
| | Min. | $-0.018584$ | $-0.018599$ | 0.08% |
| Volume / mm³ | Max. | $1.2580 * 10^{-4}$ | $1.2582 * 10^{-4}$ | 0.02% |
| | Min. | $1.2458 * 10^{-4}$ | $1.2459 * 10^{-4}$ | 0.01% |
| Energy density / $\frac{mJ}{mm^3}$ | Max. | 1.3919 | 1.3913 | 0.04% |
| | Min. | $5.6965 * 10^{-3}$ | $5.7079 * 10^{-3}$ | 0.20% |

Discrepancies were expected when testing inhomogeneous deformations because Abaqus/Explicit uses the Jaumann objective stress rate with built-in material models and the Green-Naghdi objective stress rate with VUMAT models. These have differences when finite rotations and shear occur simultaneously.[225] Furthermore, Vorel & Bažant[148] argue that both of these stress rates are not generally accurate in numerical simulations. They recommend converting to the Truesdell stress rate, but this has not been pursued here. Nevertheless, it is a topic worth further exploration as it may reconcile the discrepancies between the solutions of the built-in and VUMAT Yeoh models. This could become particularly important for problems with larger shear and rigid body rotation.

The gen-Yeoh model ran without issue using the VUMAT and the same material parameters as the gen-Yeoh UHYPER subroutine. Using double precision with eight solution domains, simulation times with the built-in Yeoh, VUMAT Yeoh, and VUMAT gen-Yeoh models were 33.15 min, 31.35 min, and 39.32 min, respectively. The VUMAT Yeoh model ran faster than the built-in Yeoh model. This result was repeatable and indicates that the VUMAT code may be simpler than the built-in routine, perhaps because the VUMAT is written specifically for the 3D case. The gen-Yeoh model takes significantly longer because computations are more complex with non-integer exponents in the SEF.

## 4.3 A Novel Model to Correct Uniaxial Tension Test Data[§§]

Section 2.5.2 introduced several loading modes that are used to characterise the mechanical response of rubbery materials. The mode that is most commonly used is the uniaxial tension test. This test specimen is often a flat or cylindrical dumbbell clamped at its ends and extended until fracture in its gauge section (Fig. 4.8a).[226] Stress-strain response is determined from the axial force and displacement. A load cell measures force, and ideally

---

a mechanical or non-contact displacement transducer permits calculation of strain in the gauge section. Alternatively, strain can be approximated from grip displacement. The error in this approximation is minimised when the dumbbell is gripped at its gauge section (Fig. 4.8b), but constraint at the narrow section usually causes premature fracture at the grip, a problem often encountered with rubbery materials.



<div align="center">(a)          (b)</div>
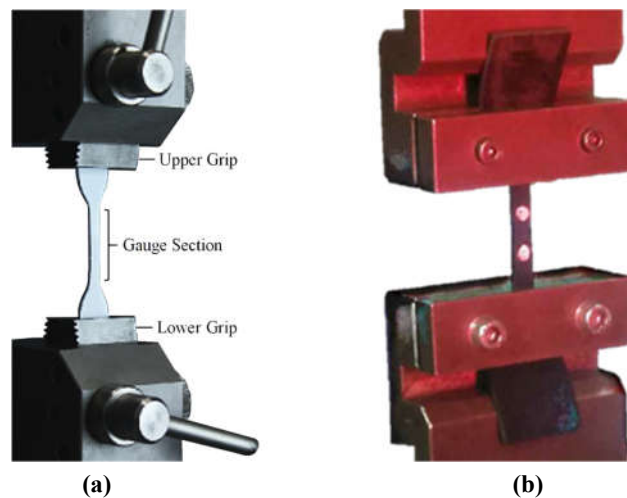
**Fig. 4.8:** Tensile test specimens: **(a)** gripped at wide section (adapted from Veryst Engineering);[226] **(b)** gripped at gauge section.

Even if displacement in the gauge section is directly measured, strain calculations can still introduce large error, for instance with metal plasticity.[227] When necking (a local reduction in the cross-sectional area of the gauge section) occurs, axial strains in the necked region are much larger than those in the gauge section. In addition, the location of necking in the gauge section is not known *a priori*, complicating isolation of strain measurements to the necked region. Different authors have proposed modified specimen geometries,[228] analytical models,[229] and finite-element methods[230] to address these complications when used for measurements of metal plasticity.

Techniques for correction of stress-strain data of polymers are scarce. Some studies on thermoplastics exist,[231] but information on elastomers is generally restricted to mechanical testing itself, particularly the difficulties of equi-biaxial tension testing.[232,233,234] Uniaxial tension testing has received little attention perhaps because it is relatively simple and standardised.[235] Nevertheless, Brown[236] described some pitfalls when testing rubber in uniaxial tension. Importantly, he noted that grip displacement is a poor choice for strain measurement because it has no "simple exact relationship to the elongation of rubber [in the gauge section]."

One solution to the issue raised by Brown is to directly measure strain. There are techniques to do so, but these introduce different challenges. Extensometers with mechanical probes must translate large distances without imposing constraint at the attachment points. Non-contact equipment eliminates this problem, but the hardware and

processing software costs are of the order of £10,000. Optical measurement systems, such as those that track two dots in the gauge section or speckle interferometry which permits strain measurements in multiple directions, also require an unobstructed view of the test specimen. This poses a problem if a thermal or pressure test chamber is required. Sight glass mitigates the problem (Fig. 4.9), but strain data may still be noisy due to inadequate lighting or reflections (Fig. 4.10). High temperatures can also degrade or evaporate marks for optically tracking displacement in a test specimen. In summary, equipment to accurately measure strain in elastomeric dumbbells exists, but cost or experimental setup may preclude its use, and significant measurement errors are still possible.



**Fig. 4.9:** Thermal test chamber with sight glass.
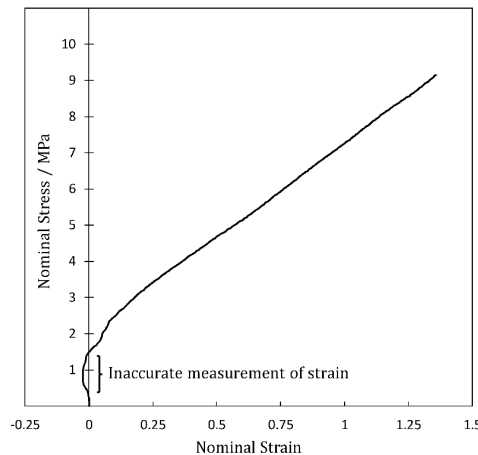


**Fig. 4.10:** Inaccurate optical measurement of strain through the sight glass of a thermal test chamber.

One can eliminate cost and equipment problems by solving the issue raised by Brown: establish an accurate relationship between grip displacement and elongation in the gauge section. To the author's knowledge, the only work that describes a systematic handling of this problem is the PhD thesis of De Focatiis.[237] He described a technique that discretises a dumbbell with variable cross-sectional areas into short pieces, and then uses an iterative

technique to adjust the modulus of the sections such that a measured stress-strain response is reproduced. In this thesis, an alternative to De Focatiis' approach is developed. The model applies to any strain-energy function for incompressible isotropic rubbery materials in which nominal uniaxial stress has the form $\sigma = \sigma(\lambda)$ where $\lambda$ is stretch computed from grip displacement. The model works for filled and unfilled elastomers, uses an iterative solution scheme, and is validated with finite-element simulations and experimental testing.

### 4.3.1 A Two-Block Model for a Dumbbell

Consider two bonded rubber blocks with dimensions as shown in Fig. 4.11a. The body is a rough representation of a half-dumbbell with no radii transitions between the gauge and gripping sections. Let uniaxial force $F$ stretch the body into a deformed configuration such that:

$$\lambda_T L_T = \lambda_1 L_1 + \lambda_2 L_2 \tag{4.10}$$

as required for displacement compatibility and $\lambda$'s are the uniaxial stretches (Fig. 4.11b). Compatibility can also be expressed in terms of displacement, $\delta$, or nominal strain, $\varepsilon$:

$$\delta_T = \delta_1 + \delta_2$$
$$\downarrow \tag{4.11}$$
$$\varepsilon_T L_T = \varepsilon_1 L_1 + \varepsilon_2 L_2$$

where strain and stretch are related by definition, $\varepsilon = \lambda - 1$. Assuming incompressibility and no shear strains develop so that all block faces remain orthogonal, the deformed block widths and thicknesses may be computed from the axial stretch in each block. For simplicity, assume the material is Neo-Hookean with axial force:[50]

$$F = G t w_1 (\lambda_1 - \lambda_1^{-2})$$
$$\tag{4.12}$$
$$F = G t w_2 (\lambda_2 - \lambda_2^{-2})$$

where $G$ is the material's shear modulus, also assumed to be known.
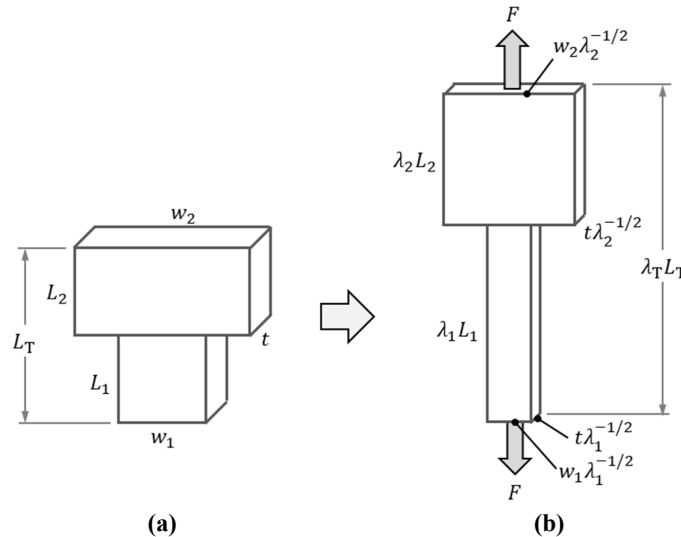


**Fig. 4.11:** Two-block representation of a dumbbell: **(a)** before stretching; **(b)** after stretching.

96

In Eqs. 4.10 and 4.12, $\lambda_1$ and $\lambda_2$ are unknown, and $\lambda_1$ is of particular interest because it gives stretch in the narrow (gauge) section of the dumbbell. The equations can be solved by specifying either $\lambda_T$ or $F$. Since displacement control is common in uniaxial tension testing, the procedure below assumes $\lambda_T$ is known, assigns a guess value for $F$, and solves for $\lambda_1$ and $\lambda_2$. The force equations (Eqs. 4.12) can each rearrange to a cubic function:

$$\lambda_i^3 - \frac{F}{Gtw_i}\lambda_i^2 - 1 = 0 \quad , \quad i = 1, 2 \tag{4.13}$$

Since $F$, $G$, $t$, and $w_i$ are always positive, the polynomials' discriminants following the method of Zwillinger[238] are always positive, so $\lambda_i$ has one real root. In addition to Zwillinger's solution, there are a variety of methods online to solve the cubic polynomial.

Closed-form solutions for $\lambda_i$s are not possible for most strain-energy functions, but Eq. 4.12 can be solved numerically for more complicated hyperelastic models. After $\lambda_1$ and $\lambda_2$ are solved, Eq. 4.10 checks displacement compatibility. If it is not satisfied to a desired accuracy, $F$ is assigned an updated value and the procedure repeats. Fig. 4.12 illustrates the procedure; however, the following two sections show that some additional steps are required to render it more practically useful.
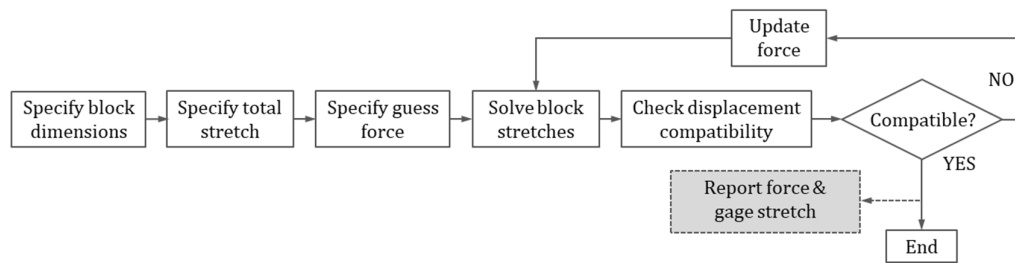


**Fig. 4.12:** Solution procedure for solving force and displacement compatibility with a two-block model of a Neo-Hookean dumbbell with a known shear modulus.

### 4.3.2 Geometric Considerations: An *n*-Block Model for a Dumbbell

To address more complicated dumbbell geometry, the two-block model of Fig. 4.11 can be generalised to an arbitrary number of blocks, $n$, with accuracy improving as $n$ increases. For instance, Fig. 4.13 shows a six-block model superimposed on top of a half-dumbbell. It must be noted that the test specimen geometry need not be a dumbbell, but such form is used in this paper. The principles underlying decomposition into an *n*-block model may be applied to any test specimen geometry that is fully determined, which is generally the case in a uniaxial tension test specimen.
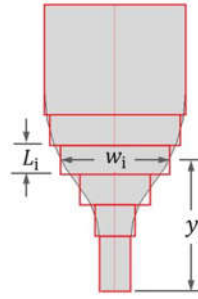
**Fig. 4.13:** Half-dumbbell (black outline) decomposed into six blocks (red rectangles).

To proceed, the dumbbell dimensioning scheme from ASTM D412[235] is assumed (Fig. 4.14a). The detailed calculations here may be applied to the different die sizes described in the specification. To construct the full $n$-block geometry, the widths of blocks in the curved sections must be solved, and this becomes possible after constructing Fig. 4.14b where half-widths are indicated with prime superscripts. The dimensioning scheme in Fig. 4.14a implies that all ends of the radii in the curved sections are tangent, and hence the line joining the centers of $R_1$ and $R_2$ is perpendicular at the intersection of their arcs at $(x_\perp, y_\perp)$ in Fig. 4.14b. The angle joining the centers is derived to be:

$$\alpha = \text{acos} \left( \frac{R_1 + R_2 + w_1' - w_2'}{R_1 + R_2} \right) \tag{4.14}$$

The half-widths of the dumbbell in the curved regions are thus:

$$x = R_1 + w_1' - \sqrt{R_1^2 - (y - L_1)^2} \qquad L_1 \le y \le y_\perp \tag{4.15}$$

$$x = w_2' - R_2 + \sqrt{R_2^2 - (y - (L_1 + (R_1 + R_2) \sin \alpha))^2} \qquad y_\perp \le y \le y_2 \tag{4.16}$$

where $y_\perp$ and $y_2$ are given by:

$$y_\perp = L_1 + R_1 \sin \alpha \tag{4.17}$$

$$y_2 = L_1 + (R_1 + R_2) \sin \alpha \tag{4.18}$$



(a)　　　　(b)
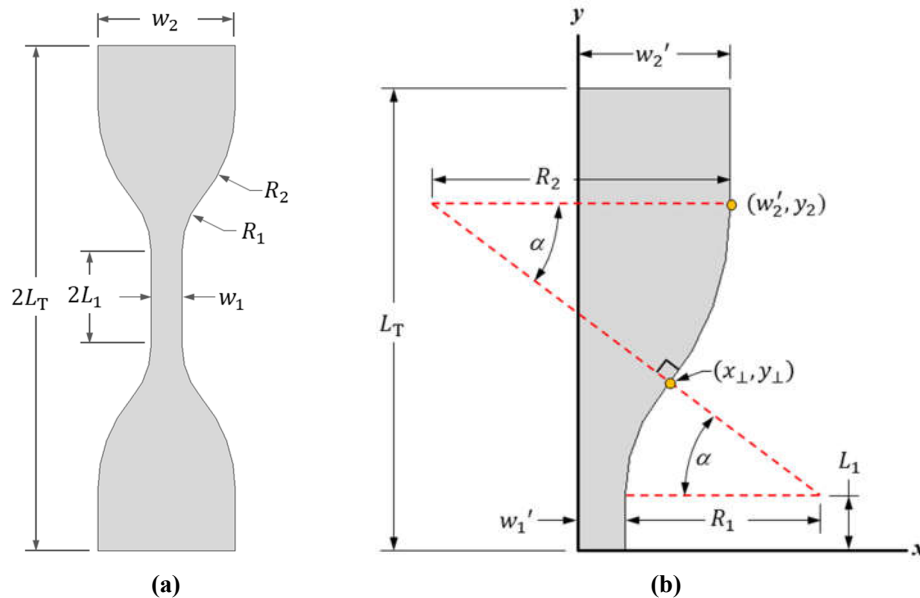
**Fig. 4.14: (a)** ASTM D412 dumbbell dimensioning scheme; **(b)** geometry for determining $n$-block locations ($y_i$) and widths ($w_i$) in the curved regions of the dumbbell.

98

After discretising a dumbbell into $L_i$'s as shown in Fig. 4.13, Eqs. 4.15–4.18 solve $w_i = 2x_i$ at $y_i$ for each block. Thus, the $n$-block geometry is fully determined for the entire dumbbell. Generalising Eqs. 4.10 and 4.12 to $n$ blocks, the system equations become:

$$L_T \lambda_T = L_1 \lambda_1 + L_2 \lambda_2 + \cdots + L_i \lambda_i + \cdots + L_n \lambda_n \tag{4.19}$$

$$F = Gtw_1(\lambda_1 - \lambda_1^{-2}) = Gtw_2(\lambda_2 - \lambda_2^{-2}) = \cdots = Gtw_i(\lambda_i - \lambda_i^{-2}) = \cdots = Gtw_n(\lambda_n - \lambda_n^{-2}) \tag{4.20}$$

These can be solved using the procedure in Fig. 4.12. Cylindrical dumbbells can be addressed with substitutions, $w_i' \rightarrow r_i$ and $tw_i \rightarrow \pi r_i^2$, where $r_i$ is the radius of each cylindrical partition.

### 4.3.3 Incorporating the Hyperelastic Model

In the preceding analysis, a Neo-Hookean material with a known shear modulus has been assumed. However, the purpose of mechanical testing is typically to determine material model parameters (such as the shear modulus) which are not known *a priori*. Of course, this determination is more complicated as the number of model parameters increases. In any case, the preceding analysis requires a fully determined material model to initiate a solution with the procedure in Fig. 4.12. To address this need, this section describes how reasonably accurate material model data can be generated from stress-strain data based on grip displacement while gripping at a wide section of the dumbbell, and then algorithmically processing that material model to create an accurate representation of the stress-strain profile in the gauge section of a dumbbell.

Fig. 4.15 illustrates the complete $n$-block model solution procedure when a hyperelastic material model is initially unknown. The first step is to collect force versus displacement data from a mechanical test. This is converted into stress versus strain data of the dumbbell with strain taken simply from the grip displacement. A suitable hyperelastic model is selected to fit to this data to provide a realistic representation of all the observed phenomena. The solution then proceeds through the upper loop of Fig. 4.15 until displacement compatibility is satisfied.

Since the hyperelastic model is initially fitted to the stress-strain data based on grip displacement, the initial solution from the upper loop simply replicates this stress-strain profile; therefore, it too under predicts stretch in the gauge section. To correct the stretch in the gauge section, the total stretch in a second iteration of the upper loop is set equal to the gauge stretch from the initial solution, which naturally shifts the stress-strain curve in the direction of positive strain. To ensure a purely horizontal shift, the force from the initial solution must be recorded before restarting iterations in the upper loop. Once the entire routine is complete, the gauge stretch from the updated solution properly maps to the force from the initial solution. For this mapping to be accurate, the coefficients of the hyperelastic

model that were initially determined must reasonably represent the "average" stress-strain profile along the entire dumbbell and the actual stress-strain profile in the gauge section. That is, if an inappropriate material model or parameters are selected for the initial curve fit in the second block of Fig. 4.15, the material model output from the full solution procedure will be inaccurate. Examples of how to use this procedure with an accurate initial material model are shown in the next two sections.
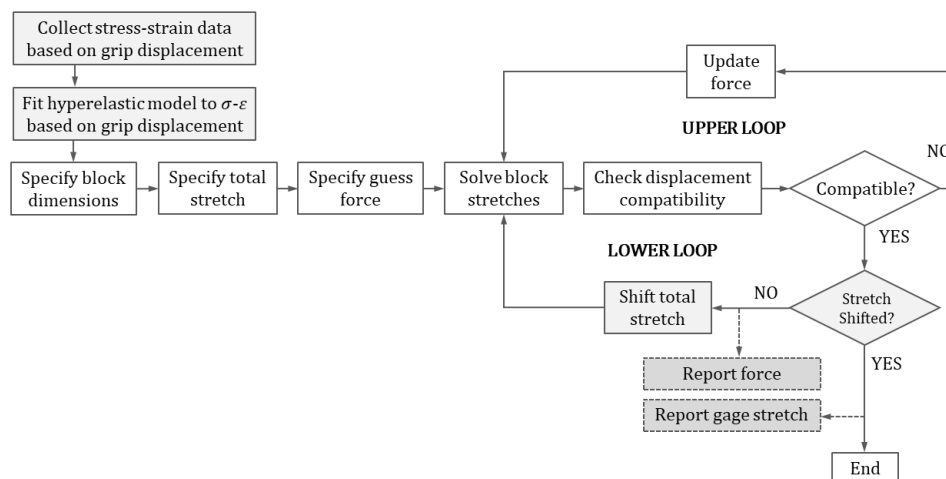


**Fig. 4.15:** Solution procedure for solving force and displacement compatibility with corrected stretch in the gauge section for an *n*-block model.

### 4.3.4 Validation of the *n*-Block Model with Finite-Element Analysis

A virtual experiment was conducted with the finite-element method in Abaqus/Standard R2017 to assess the accuracy of the *n*-block model. Treloar's uniaxial tension data[220] as reported by Steinmann *et al.*[85] was used. A third-order Ogden strain-energy function[239] was used with coefficients as reported by Steinmann. Table 4.3 captures input information for an incompressible, isotropic model of a quarter-dumbbell fixed at its bottom plane of symmetry and stretched at its top (Fig. 4.16). The dumbbell for the FE model was truncated at the location of the grip, which importantly contains curved geometry defined by the transition radii, $R_1$ and $R_2$. It was assumed that no deformation occurred above the grip, and that the grip imposed no horizontal constraint. Although neglect of the constraint was not physically realistic, it provided a better virtual test for the *n*-block model which itself does not consider horizontal constraint. Nevertheless, the error in this approximation is shown to be small in subsequent sections. Mesh-independence within 1% was confirmed by altering element sizes by factors of two. This required an element seed size of 0.1 mm. For reference, the Ogden strain-energy function and uniaxial pulling forces are given by:

$$W = \Sigma_{j=1}^3 \left[ \frac{\mu_j}{\beta_j} \left( \lambda_1^{\beta_j} + \lambda_2^{\beta_j} + \lambda_3^{\beta_j} - 3 \right) \right] \tag{21}$$

$$F_i = w_i t \sum_{j=1}^{3} \left[ \mu_j \left( \lambda_i^{(\beta_j - 1)} - \lambda_i^{-\left(1 + \frac{\beta_j}{2}\right)} \right) \right] \tag{22}$$

where $\mu_j$'s and $\beta_j$'s are fitting parameters, $(\lambda_1, \lambda_2, \lambda_3)$ are principal stretches, $\lambda$ is stretch in the direction of uniaxial extension, and i's represent individual $n$-blocks as shown in Fig. 4.13.

**Table 4.3:** Inputs for the finite-element model when testing an $n$-block model.

| Parameter | Value |
|---|---|
| $\left(L_1, L_{grip}, w_1', w_2', R_1, R_2, t\right)$ – see Fig. 4.14 | $(16.5, 42.01, 3, 12.5, 14, 25, 2)$ mm |
| Material model | Ogden, 3rd-order |
| Model parameters, $(\mu_1, \mu_2, \mu_3)$ | $(0.5649, 3.856 \times 10^{-3}, 7 \times 10^{-13})$ MPa |
| $(\beta_1, \beta_2, \beta_3)$ | $(1.297, 4.342, 15.13)$ |
| Displacement (half-value) | 185 mm |
| Number of horizontal elements | 30 |
| Number of vertical elements | 421 |
| Element type | Plane stress<br>Linear quadrilateral<br>Reduced integration<br>Enhanced hourglass control |
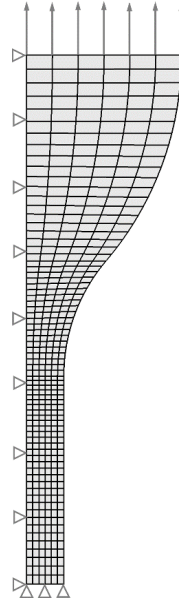


**Fig. 4.16:** Finite-element mesh for a quarter-model dumbbell (mesh size enlarged for clarity).

Fig. 4.17a shows the Ogden strain-energy function with Steinmann's model coefficients fitted to Treloar's data. Using Eq. 4.5 to compute errors, the average error of the fit is 3.06%. The stress-strain curve predicted by FEA in the gauge section precisely follows the strain-energy function because the FE material model is defined by the Ogden SEF parameters. The error of $1.95 \times 10^{-4}\%$ can be attributed to numerical discretisation.

In an experiment when strain is calculated from grip displacement, one typically does not know hyperelastic model parameters or strain in the gauge section. Therefore, one would not have access to any information in Fig. 4.17a. Instead, stress-strain data based only on grip displacement (that is, 'FEA-grip' in Fig. 4.17b), which artificially shifts the stress-strain response to the left (or alternatively, upward), would be available. However,

the generated 'FEA-Grip' curve can be used with the $n$-block model to recalculate back the original source Treloar data.
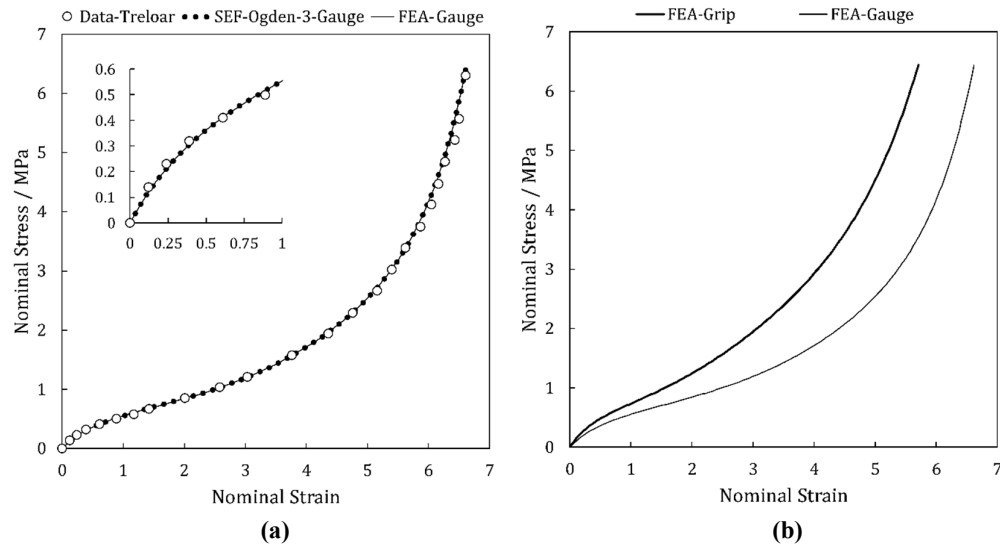


**Fig. 4.17:** Stress-strain response of a dumbbell: **(a)** in the gauge section with Treloar's data, Ogden strain-energy function, and FEA (inset magnifies lower strain response); **(b)** shift in the response when strain is based on grip displacement.

Fig. 4.18 shows a third-order Ogden model fit to the stress-strain curve based on grip displacement as defined by the 'FEA-Grip' curve in Fig. 4.17b. The fitting error from Eq. 4.5 is 0.16%. It is important to note that the material parameters for this model (which are noted in the figure caption) are not the same as those that define the original hyperelastic model in Table 4.3. This is not surprising since the parameters in Table 4.3 are determined directly from the stress-strain profile in the gauge section, while those in Fig. 4.18 are determined directly from the grip displacement. After processing the 'SEF-Ogden-3-Grip' model through the $n$-block calculator, the corrected data points shift right along the strain axis as shown in Fig. 4.18. The points map well onto the 'FEA-Gauge' stress-strain curve to give a composite error of 2.38%. Clearly the $n$-block model accurately reproduces the desired stress-strain response in the gauge section, and the corrected data points can be used to curve fit an accurate hyperelastic model.
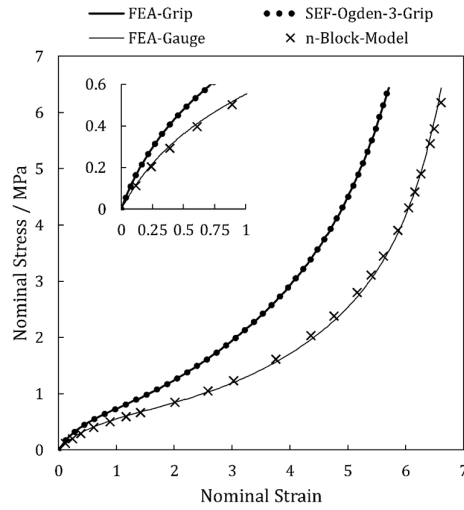
**Fig. 4.18:** $3^{rd}$-order Ogden strain-energy function fit to an FEA stress-strain curve based on grip displacement, $(\mu_1, \mu_2, \mu_3) = (0.08545, -1.275, 8.979 \times 10^{-9})$ MPa , $(\beta_1, \beta_2, \beta_3) = (3.102, -0.6306, 10.95)$. The $n$-block model shifts points in the 'SEF-Ogden-3-Grip' curve toward the 'FEA-Gauge' curve. The inset magnifies lower strain response.

### 4.3.5  Validation of the $n$-Block Model with a Non-contact Video Extensometer

An unfilled natural rubber dumbbell was tested with a non-contact video extensometer in uniaxial extension. The narrow section of the dumbbell was 33 mm long, and initial grip separation was 55.7 mm. Fig. 4.19 shows the stress-strain response with strains based on the grip-displacement strain and the video extensometer strain. The gen-Yeoh SEF from Eq. 4.3 was fit to the curve based on grip displacement. The LM algorithm[222] was used to give $(K_1, K_2, K_3) = (0.1687, -0.00305, 0.000106)$ MPa and $(m, p, q) = (0.967, 1.699, 2.854)$ with a fitting error of 1.15%. The strain-energy function is not plotted in Fig. 4.19 because it is indistinguishable from the grip displacement curve.

Fig. 4.19 also shows $n$-block model corrected data points which match the video extensometer curve well. The errors of the $n$-block model and grip displacement curve with respect to the video extensometer are 2.24% and 12.6%, respectively. The error of the $n$-block model is well within uncertainties inherent in the material (batch variation) and experimental setup.

The maximum strain in Fig. 4.19 is limited to about 300% due to the video extensometer's range. However, the accuracy of the $n$-block model in this and the preceding example in Section 4.3.4 gives confidence that, if necessary, one could accurately predict response at larger strains using the grip displacement alone.
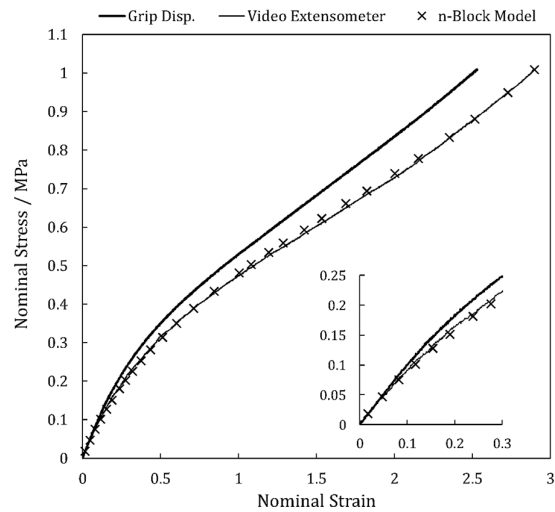
**Fig. 4.19:** Stress-strain response of unfilled natural rubber with strain based on grip displacement, video extensometer, and $n$-block model correction. The inset magnifies lower strain response.

## 4.4 Summary

Building on the benefits of the Yeoh and DDT SEFS, the gen-Yeoh SEF has been introduced. It is well suited to capture both low and high strain nonlinearities in highly filled elastomeric materials such as those in oilfield seals. In particular, the SEF accurately models materials that have a rapid reduction in modulus at low strains. The gen-Yeoh SEF has been fit to stress-strain data with a good degree of accuracy by inspection, and a methodical approach for this fitting exercise has been shown. The manual curve fits have been found comparable to those that are algorithmically determined. Subroutines that implement the function with slight volumetric compressibility have been validated in Abaqus. Detailed codes and notes for their use are provided in Appendices A, B, P, and Q.

An analytical model that correlates grip displacement to displacement in the gauge section of a dumbbell during uniaxial extension has been developed. This novel model is well-suited for correcting stress-strain data in elastomeric dumbbells when strain cannot be directly measured in the gauge section. An iterative scheme solves a user-specified constitutive equation to satisfy displacement compatibility. The procedure maps stress-strain data based on grip displacement to stress-strain response in the gauge section. The model provides an inexpensive, viable alternative to equipment that directly measures strain. Furthermore, the model can be used when experimental setup complicates or precludes direct measurement of strain, such as when a thermal or pressure test chamber is required. The model is also useful for large displacement testing where strains can exceed the physical limits of optical measurement equipment. A Fortran implementation of the model is in Appendix C.

# 5. Prediction of Elastic Leak with Fluid Pressure Penetration in Abaqus

## 5.1 Overview

This chapter lays some groundwork for experimental validation of fluid pressure penetration (FPP) algorithms in later chapters. Although commercial solvers package FPP capability in the context of seal leakage, these modules fundamentally address a contact problem: they determine the threshold at which forces change nodal contacts from opened-to-closed, and vice versa.

To proceed, a 2D finite-element model and applicable settings in Abaqus/CAE (a pre-processor) are introduced before turning to some detailed studies of fluid pressure penetration at a contact interface in Abaqus/Standard and Abaqus/Explicit, both of which are FE solvers. The fluid is simulated only with a mechanical pressure; other details of the fluid are ignored. The primary objective is to identify leak pressure sensitivities to several parameters that are not well addressed in the literature, including the effects of the FE mesh, friction model, volumetric compressibility, and seal compression. Manual and automated FPP techniques are described. The automated techniques include algorithms that are native in Abaqus as well as novel user-defined subroutines. Importantly, a DLOAD subroutine for Abaqus/Standard is developed to remove pressure from nodes that change from open to closed contact as a seal deforms. This chapter also develops a VDLOAD subroutine to simulate FPP in Abaqus/Explicit, thereby overcoming contact convergence problems encountered when using the implicit solver. This latter subroutine appears to be the first publicly disclosed demonstration of such capability.

## 5.2 Geometry

The geometry for the finite-element model is shown in Fig. 5.1. It is a 2D axisymmetric seal between upper and lower plates. The seal is bonded to the lower plate and has a contact interface at the top; hence there is only one potential leak path. A gauge ring with height, $h_g$, provides another contact interface to control the **extrusion gap** which is the region where the seal displaces when pressure is applied on the left side of the seal. The round on the gauge ring mitigates the risk of fracture when the seal deforms into the extrusion gap.
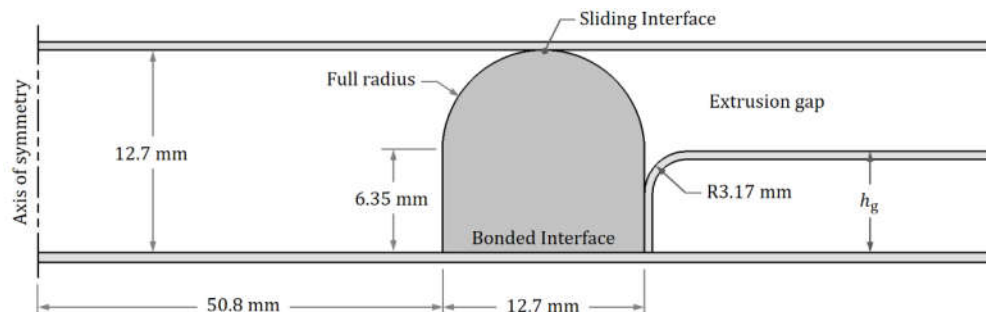


**Fig. 5.1:** Geometry for the finite-element model; $h_g = 6.35$ mm.

## 5.3 Hyperelastic Material Model

Uniaxial tension data for a 70D (Shore A) HNBR compound was provided by the project sponsor and used to generate the hyperelastic material model for the studies in this chapter. The Yeoh strain-energy function (Eq. 2.28) was used and matched the test data well up to strains of 150% (that is, $\lambda = 2.5$), which was a reasonable upper limit for strains in the simulations (see Section 5.4.7 for confirmation of this statement). Model parameters were determined with a Levenberg-Marquardt algorithm adapted from Press *et al.*[222] as shown in Appendix G. Volumetric compressibility was simulated with a Poisson's ratio of 0.495 which was converted to a compressibility parameter with Eq. 4.9. To simplify the analysis, viscoelastic and hysteretic effects were neglected. Fig. 5.2 shows the model fit to the uniaxial test data and the predicted responses in pure shear (that is, planar tension/compression) and equibiaxial loading modes. The ordering of the responses is physically realistic with $|\sigma_{ut}| < |\sigma_{pt}| < |\sigma_{et}|$ for any given stretch.
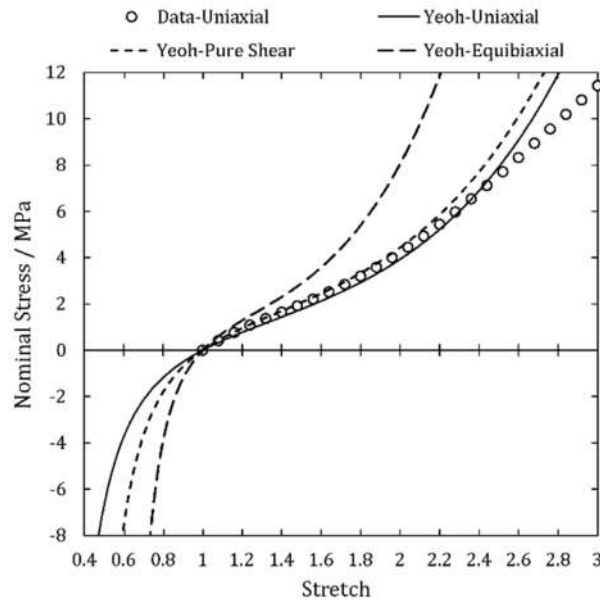


**Fig. 5.2:** Yeoh SEF fit to uniaxial tension data for a 70D (Shore A) HNBR material; $(C_{10}, C_{20}, C_{30}) = (0.75, 0.071, 0.0075)$ MPa.

## 5.4 Initial Finite-Element Studies with Fluid Pressure Penetration

### 5.4.1 Steps

The main steps for all simulations in this work consisted of a vertical compression followed by a pressure on the left side of a seal. Fig. 5.3 shows the seal before compression, after compression by $\varepsilon = 15\%$ of the nominal seal height (specifically, 1.905 mm), and after the application of pressure but before any leakage has occurred.
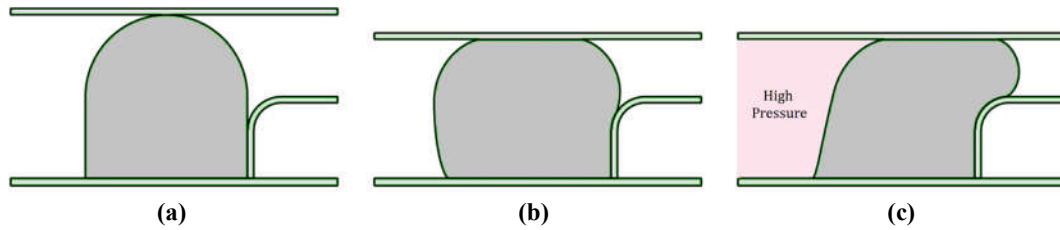
**Fig. 5.3:** Axisymmetric seal with $h_g = 6.35$ mm: **(a)** before compression; **(b)** after 15% compression; **(c)** after compression and with 2.8 MPa applied to the left side of the seal.

Unless otherwise specified, Abaqus/Standard was used with automatic incrementation in the implicit solver, and all inertial effects were neglected. The minimum allowable load increment was reduced from a default value of $10^{-5}$ to $10^{-8}$ because contact convergence often required smaller load increments. To achieve such small increments during automated load bifurcations, the number of iteration attempts was increased from the default value of 5 to 10. This setting was found critical for simulating seal leakage, but the location of the controlling parameter is not intuitive (see Fig. 5.4). From the Step module, the path is Other → General Solution Controls → Manager… → [Select step, P-01 in this example] → Edit… → Continue… [this loads the General Solution Controls Editor] → Specify: → Time Incrementation [the 2$^{nd}$ tab] → More [select the top one] → $I_A = 10$. Different methods of pressure application were explored in this work and will be explained in other sections.
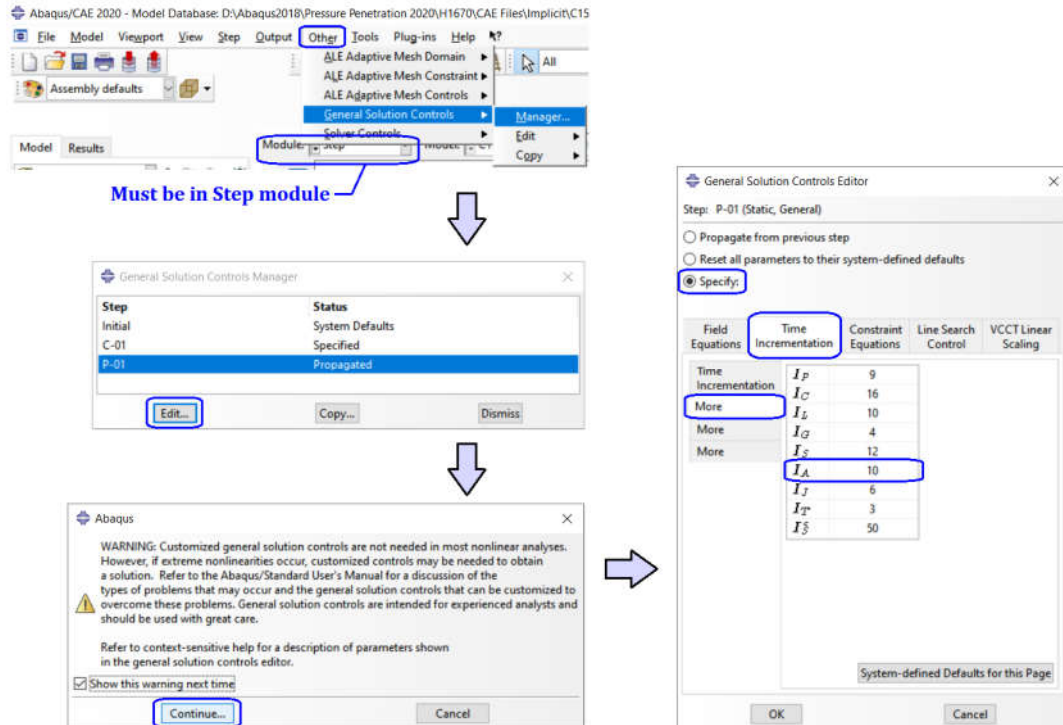


**Fig. 5.4:** Path to change the maximum number of iteration attempts for an Abaqus implicit step.

### 5.4.2 Interactions

At least two contact definitions were required for all simulations in this work. Fig. 5.5 shows the master-slave contact surfaces. Following common conventions for surface-to-surface contact definitions,[240] slave surfaces were assigned to the seal because it used a smaller mesh and was a more compliant material than all countersurfaces. In simulations with large compression (say, 30%) or when the gauge ring was removed, additional contact definitions were required to prevent the sides of the seal from penetrating the bottom plate.
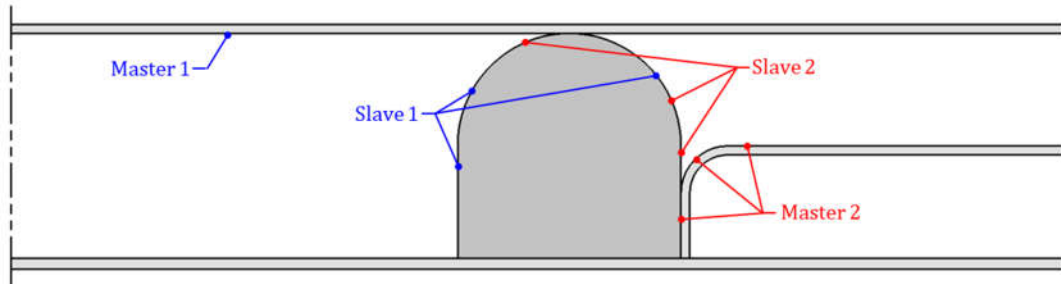


**Fig. 5.5:** Master-slave surfaces for contact definitions.

Fig. 5.6 shows some additional contact settings. For most pressure application steps, the default contact control was changed to allow automatic stabilisation which improved contact convergence. The technique introduces viscous energy dissipation in a system when contact instabilities occur,[241] for instance when contact status changes rapidly. Because this viscous damping is artificial, it must be kept as small as possible, so exhaustive attention was given to this control before settling on a stabilisation factor of 0.01 between Master-1/Slave-1 and 0.10 between Master-2/Slave-2 (note: lower values reduce damping but also converge more slowly, if at all). It was found that overdamping a sliding contact interface inhibited movement and gave unrealistic deformations. The damping parameters "Tangent fraction" and "Fraction of damping at end of step" were usually left at their default values of 1 and 0, respectively. The former scales damping in the tangential direction relative to the normal direction, and the latter determines the fraction of damping that remains at the end of a load step.

When contact stabilisation is used, Obbink-Huizer[242] suggests that the energy output ALLSD (all viscous dissipation in a static implicit analysis) be low compared to ALLIE (all internal energy). For the simulations in this work, ALLSD was of the order $10^3$-$10^4$ lower than ALLIE. In a limited number of cases, simulations converged with no stabilisation applied, and these were compared to leak pressures when stabilisation was applied. The results were the same within approximately 0.01 MPa, with the order of leak pressures being 10 MPa, so the impact of this artificial viscous dissipation is deemed negligible in this work.
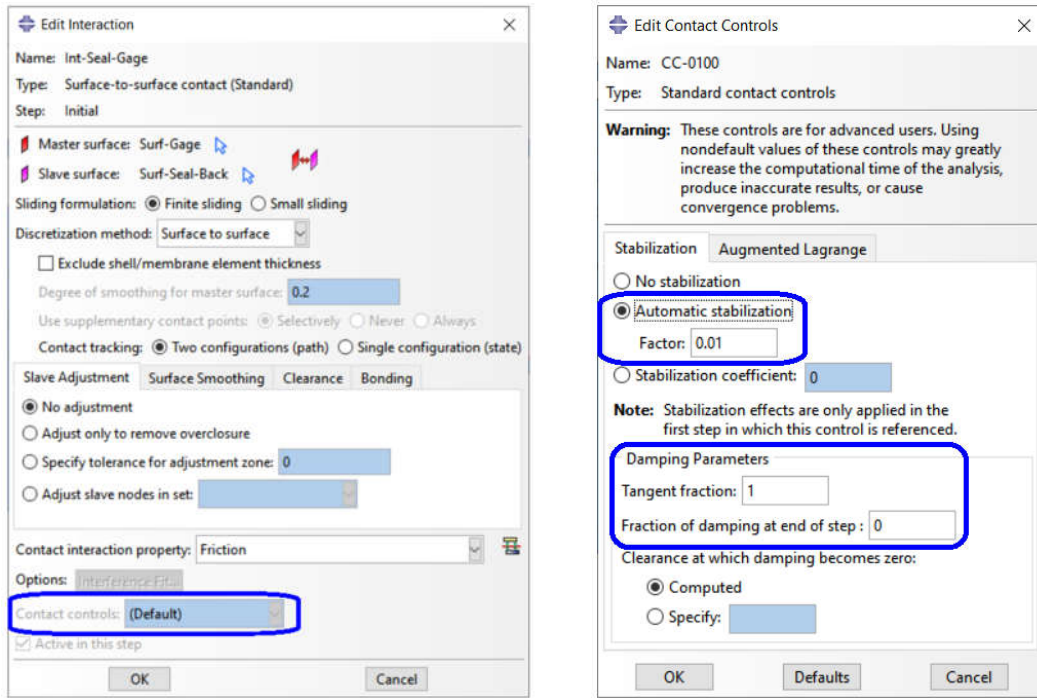
**Fig. 5.6:** Contact settings and contact controls.

Some alternative techniques[242] to address contact convergence issues were attempted. Contact controls apply local damping at interaction surfaces, but alternatively Abaqus can apply global damping[243] to the seal during a load step (Fig. 5.7). This sets a magnitude for energy dissipation to a user-specified fraction of the system energy. The default fraction is $2 * 10^{-4}$, but results in this work were unrealistic even with a value as low as $10^{-5}$. For example, Fig. 5.8 shows a local minimum in the predicted leak pressures as the coefficient of friction increases with a Coulomb (constant coefficient) friction model. The trend is as expected for $\mu \geq 0.2$ because an increasing coefficient of friction is expected to better resist seal deflection into the extrusion gap and, hence, require a higher pressure for leakage. However, for $\mu \leq 0.15$, the problem becomes increasingly unstable. The instability arises because friction itself dissipates energy which tends to stabilise the movement of the seal. When friction is insufficient to stabilise the sliding contact, the solver imposes a larger amount of viscous damping. To overcome the artificial dissipation, more total energy must be applied to displace the seal and cause leakage. Even at the lowest coefficients of friction (CoFs) in Fig. 5.8, ALLSD is of the order 0.1% of ALLIE, yet the unrealistic behaviour is still observed. So clearly, great care is required when applying global stabilisation. Section 5.7.1 gives further evidence that the minimum in Fig. 5.8 is indeed artificial and not due to some other effect.

Regardless of the damping technique employed (local or global), viscous stabilisation imposes a computational disadvantage. To converge, it may require such small load steps that solution times exceed those that can be achieved in Abaqus/Explicit, a solver that is otherwise less efficient than the implicit solver in Abaqus/Standard.

109
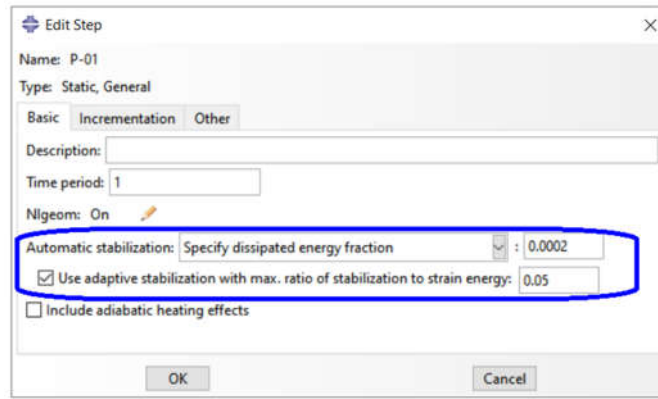
**Fig. 5.7:** Adding global stabilisation to a load step.
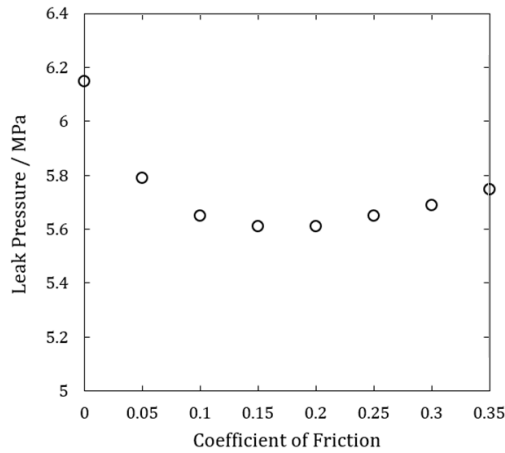


**Fig. 5.8:** A physically unrealistic local minimum in the leak pressure as a function of the coefficient of friction with a Coulomb friction model. $\varepsilon = 5\%$; $h_\text{g} = 6.35$ mm.

Augmented Lagrange and penalty formulations were studied for the normal component of contact. The latter was found to converge more easily, but this finding should not be generalised.[244] With the penalty formulation, Abaqus allows the user to reduce contact stiffness which can help convergence, but the reductions required to help convergence in this work resulted in unrealistic contact penetrations. Of the options explored to facilitate contact convergence, only local contact control was deemed acceptable for the problem studied.

### 5.4.3 Friction Modelling

It is well-known that the coefficient of friction for elastomeric materials is contact pressure-dependent,[181,182,183] yet it is rare to see pressure-dependent contact models in seal simulations. In fact, Gorash *et al.*[212] are the only authors in Table 3.1 that used a formulation more sophisticated than the Coulomb model. The dominance of the model is probably for two reasons. First, the rubber seal simulations in Table 3.1 have at most 2.3 MPa of applied pressure, and the variation in the coefficient of friction in this range is limited. Second, coefficients of friction depend on many parameters such as the lubricating medium, rubber

compound ingredients, sliding velocity, temperature, and surface characteristics. This makes the characterisation of rubber friction behaviour taxing. Nevertheless, recent work by Yanes *et al.*[245] indicates the criticality of using a contact pressure-dependent friction model for high pressure seals. Fortunately, their work also indicates that above, say 10 MPa, the coefficient of friction becomes nearly constant, and the variation across different materials and variables is diminished. Internal data from the project sponsor is consistent with this finding.

The contact pressure-dependent friction model in this work (Fig. 5.9) is derived from correspondence[246] with Yanes for a 75D (Shore A) HNBR material. The model assumes a slow sliding speed (of the order 0.1 mm/s) and a lubricated condition. It is worth noting that even with no contact pressure, the coefficient of friction in the present work is significantly lower than that used by most authors in Table 3.1. Possibly, some authors have adopted excessively high CoFs due to a lack of publicly available data.
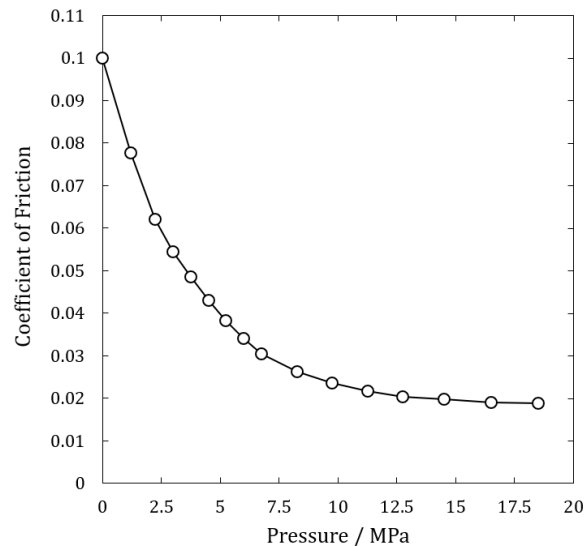


**Fig. 5.9:** Contact pressure-dependent coefficients of friction used for the frictional model.

### 5.4.4 Application of Pressure

When pressure is applied to elastomeric seals, it is common for the contact status of nodes at contacting surfaces to change. For example, Fig. 5.10a shows a seal after compression. The node indicated by the red dot initially has an open contact status, so it experiences pressure when the fluid pressure is initially applied. As the seal deforms, the node is pushed into the contact interface (Fig. 5.10b), and ideally pressure is removed from the node and all others where contact has closed. As more pressure is applied, contact at the highlighted node eventually opens as pressure propagates through the sealing interface (Fig. 5.10c).

111
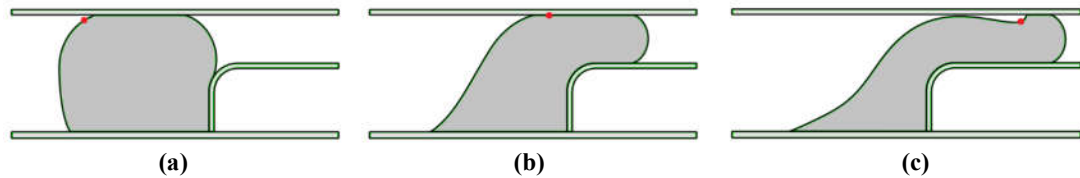
**Fig. 5.10:** The changing contact status of a node in a seal: **(a)** after compression, contact is open near the sealing front indicated by the red dot; **(b)** as pressure increases, the contact at the same node closes; **(c)** at an even higher pressure, the contact status at the node opens again.

In Abaqus, pressure loads may be applied to surfaces in the Load module, but pressure does not automatically update at nodes with a changing (that is, opening or closing) contact condition. It is possible to manually remove or add pressure to nodes step-by-step, but the process is iterative and time-consuming. To overcome this problem, Abaqus/Standard has fluid pressure penetration algorithms that automatically propagate pressure; however, they are unable to remove pressure from nodes that change from open contact to closed contact (for instance, when changing from Fig. 5.10a to Fig. 5.10b). For simplicity, this section ignores this limitation in Abaqus' native algorithms. Later sections will address the removal of pressure when contact closes.

Before creating a fluid pressure penetration load, the surface interaction where pressure will be applied and monitored is first defined. Pressure penetration is then defined as a separate interaction (Fig. 5.11a) that calls the previously defined contact interaction. In this case, the contact definition "Int-Seal-Top" corresponds to the Master-1/Slave-1 definition in Fig. 5.5. The "Region on Master" and "Region on Slave" options determine the points where pressure initiates, and pressures at these locations immediately propagate to adjacent nodes with open contact. These regions are shown in Fig. 5.11b. The "Critical Contact Pressure" determines the threshold at which pressure propagates into a contact surface. The default value of zero is most frequently adopted in the literature, and it is also used in this work. This is at odds with the classical definition in which fluid pressure propagates when it is equal to contact pressure, but the generally adopted FE leak criterion (that is, when $P_{\text{contact}} = 0$) appears necessary to achieve simulated leak pressures that align with most experimental results such as those in Table 3.1. This latter convention is adopted for most numerical studies in this thesis, but its use is challenged in Section 7.4.5.

The last setting to mention is "Penetration time" (Fig. 5.11a). It defines how rapidly pressure increases to full scale when a node changes from closed to open contact during a load step. The default setting of 0.001 s was found to be acceptable for most studies in this work, but on occasion it was increased to facilitate convergence. Larger values smoothed the load transition and had negligible impact on final leak pressures reported in this work.

112
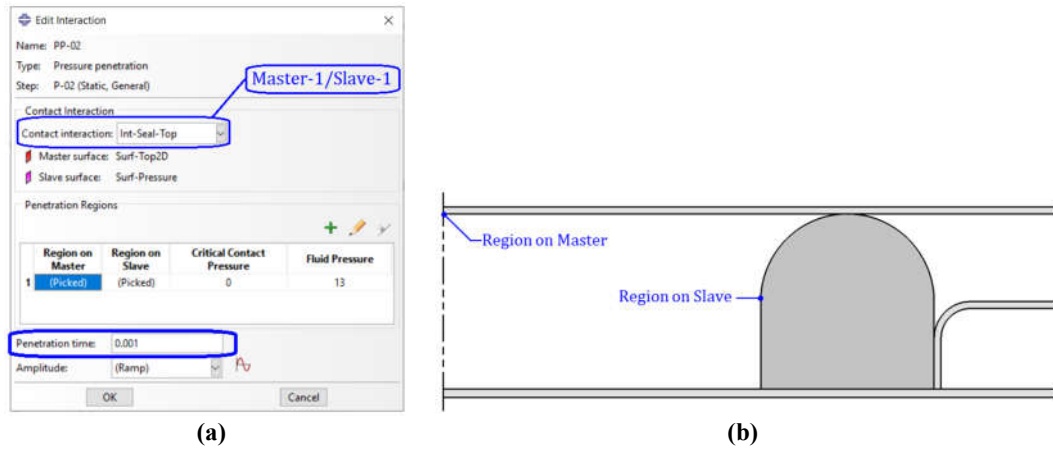
**Fig. 5.11: (a)** Options with a pressure penetration interaction/load; **(b)** pressure initialisation locations on the master and slave surfaces.

Abaqus/Standard has two options for converting pressure (a surface load) to nodal forces when computing a numerical solution. The default behaviour in Abaqus R2018 and later versions is to truncate the pressure at the last element that is exposed to fluid pressure (Fig. 5.12a). Alternatively, the fluid pressure can be linearly ramped down across the last element that is exposed to fluid pressure (Fig. 5.12b). This latter option is the default and the only behaviour available in Abaqus R2017 and earlier versions. In Abaqus R2018 and later versions, the R2017 scheme is not accessible via Abaqus/CAE; it must be specified in the input file with the text "`wetted front=mid element`" as shown in Fig. 5.13. The R2018 scheme results in a higher total force at the sealing interface and therefore predicts lower leakage pressures than the R2017 scheme. Some quantitative differences between the schemes are highlighted in Sections 5.5 and 5.6.
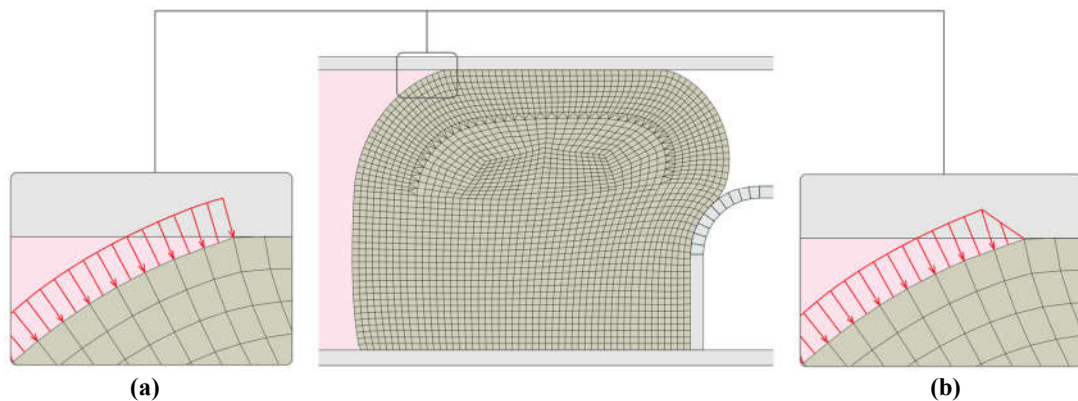


**Fig. 5.12:** Different pressure integration schemes in Abaqus: **(a)** R2018 scheme; **(b)** R2017 scheme.

```
** INTERACTIONS
**
** Interaction: PP
*Pressure Penetration, master=Surf-Top2D, slave=Surf-Pressure, penetration time=.001, wetted front=mid element
_PickedSet1452, _PickedSet1451, 13., 0.
**
```

**Fig. 5.13:** Keyword to implement the R2017 integration scheme in R2018 and later versions of Abaqus.

113

### 5.4.5 Constraints and Boundary Conditions

The bottom plate and gauge ring were modelled as rigid bodies and fixed in position for all steps. The top plate was modelled as rigid and displaced vertically to compress the seal before pressure was applied. The bottom surface of the rubber seal was fixed in position. All other seal surfaces were free or subjected to interactions and loads previously discussed.

### 5.4.6 Meshing and Element Types

A coarse mesh with global size $\approx 0.6$ mm was used for some initial studies. The partitioned seal geometry and mesh are shown in Fig. 5.14. Local refinement of 0.06 mm was applied to a portion of the top of the seal where pressure would break through the contact interface. The free mesh regions were quad-dominant and had 367 quadrilateral and 3 triangular elements. The structured regions used 484 quadrilaterals.
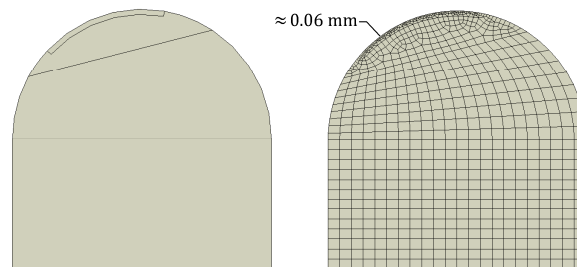


**Fig. 5.14:** Partitioned seal (left) and FE mesh (right). The global seed size of 0.6 mm transitions to a maximum refinement that is one order of magnitude smaller.

When modelling incompressible or nearly incompressible hyperelastic materials in Abaqus/Standard, the Abaqus theory manual[247] recommends reduced integration hybrid elements with enhanced hourglassing control. Hybrid elements split deviatoric and volumetric element deformations into an additive decomposition. The split improves computational stability, but it comes at the expense of an extra internal constraint on the element. A fully integrated quadrilateral element has four integration points that, combined with the volumetric internal constraint, yield an overly stiff behaviour. However, the four integration points can be collapsed into one which relaxes stiffness at the expense of accuracy of integrated quantities such as stress. The inaccuracy can be partially corrected by imposing fictitious forces in the element with a feature called hourglassing control, but these forces generate artificial energy. The tradeoff is acceptable if artificial energy remains low compared to the total energy in the system. In summary, rubber incompressibility necessitates a hybrid element, and practice shows that this element performs well with a reduced integration element, which in turn necessitates hourglassing control. For more details on these effects, refer to Windslow.[75] Abaqus/Explicit does not have hybrid quadrilateral elements, so it can encounter numerical instabilities when modelling nearly incompressible materials.[247]

### 5.4.7 Strain and Biaxiality Analyses

Strain magnitudes and finite-element biaxialities (see Section 2.5.2) were analysed to understand the seal deformations during compression and pressure applications. Biaxiality was assessed with a UVARM subroutine[248] that implements a modified version of Eq. 2.21. The code can be found in Appendix D. Fig. 5.15 shows contour plots of biaxialities in the seal after compression and with two differential pressures. Most finite-elements in the seal were not in perfect uniaxial tension ($\alpha_{ut}$ = -0.5), planar tension ($\alpha_{pt}$ = -1), or equibiaxial tension ($\alpha_{et}$ = -2), so a decision was made to classify each element into one of the three loading modes. A natural choice is to bisect the range between each loading mode and assign each element into one of three bins. This is reflected in the contour scale in Fig. 5.15. Visually, it is apparent that the seal deformations are dominated by planar tension (green) followed by equibiaxial tension (blue). The uniaxial tension loading mode (red) is negligible during pressure application. Hence, when curve fitting a hyperelastic material model for this problem, the fit should be biased to the planar and equibiaxial loading modes. From a practical perspective, a contour plot will usually suffice to determine the dominant loading modes, but if desired, element biaxialities can be computed from principal strains. For the case of Fig. 5.15c, the percentages of biaxialities are $\left(\%_{ut}, \%_{pt}, \%_{et}\right) =$ (3%, 76%, 21%). Similar numbers were computed for compression ratios from 5-30% and gauge ring heights from 0-9.5 mm (this height range covers 0-75% of the nominal seal height).
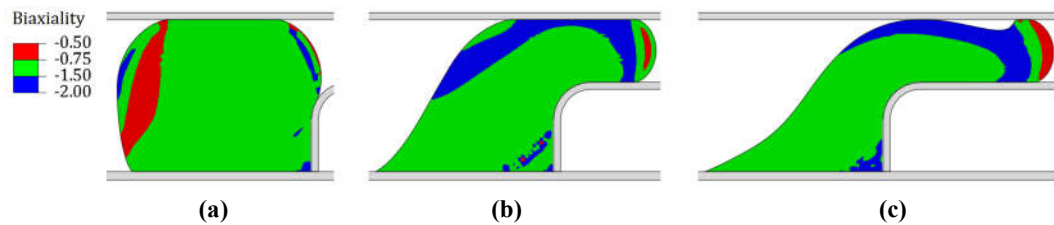


**Fig. 5.15:** Element biaxiality at different stages of deformation with Abaqus' R2017 pressure penetration scheme: **(a)** after 15% compression; **(b)** with $\Delta P = 5$ MPa; **(c)** near the leak pressure with $\Delta P \approx 10$ MPa.

The risk of fracture in the seal was assessed through maximum principal stretches. Fig. 5.16 shows that the maximum stretch is about 2.75 and occurs at the bottom left corner of the seal when leak is imminent. Fig. 5.15 shows that the loading mode at this location is planar tension, and direct computation gives $\alpha = $ -1.01. It is not surprising that an element at this bonded boundary is in near-perfect planar tension because tangential (that is, out-of-plane) deformation is fully constrained at the bond interface. The magnitude of stretch raises some concern as it is near the fracture limit in uniaxial tension (see data in Fig. 5.2 where $\lambda_{ut.max} = 3$), and the fracture limit in planar tension is usually lower than that in uniaxial tension. This location must be inspected for fracture in any physical testing based on this seal configuration. The principal stretch is an imperfect gauge to assess the risk of

fracture in rubber, but more elaborate methods were not employed here. For further discussion of rubber fracture, refer to Windslow's PhD thesis[75] and subsequent work by Windslow et al.[84]
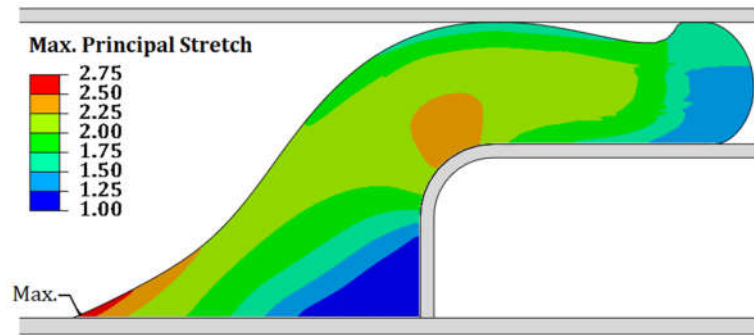


**Fig. 5.16:** Maximum principal stretch in the seal when leakage is imminent. $\varepsilon = 15\%$, $h_g = 6.35$ mm.

When curve fitting a hyperelastic material model, it may be necessary to bias the fit to a particular region of strain, especially when dealing with highly filled rubbers that exhibit imperfect hyperelasticity. Therefore, it is necessary to understand the most typical strains encountered in a problem. To this end, Table 5.1 reports stretches in the seal for different loading modes (as determined from biaxiality analyses) in the finite-elements when leakage was imminent. Several compression ratios ($\varepsilon$) and gauge ring heights ($h_g$) are shown. Stretch values are reported with an average, one standard deviation ($\sigma_1$), and a maximum. The last row reports average strains across several different compressions and gauge ring heights. Given that planar tension is the dominant loading mode for this problem, Table 5.1 indicates that the most critical region of stretch for an accurate hyperelastic model when leakage is imminent is around $\lambda = 1.84$. Referring to Fig. 5.2, the uniaxial tension data fits nicely at this stretch, but this does not guarantee that the predicted planar tension response is accurate. However, the use of a Yeoh material model mitigates this problem because $I_1$ only strain-energy functions generally have realistic responses even when fit to a single loading mode.[223] In addition, the fit to the uniaxial tension data is good over a wide stretch range from 1-2.4. According to Table 5.1, average stretches are within this range, so the Yeoh strain-energy function in Fig. 5.2 is an appropriate material model for the problem.

**Table 5.1:** Average, one standard deviation ($\sigma_1$), and maximum stretches for different loading modes in the seal when leak is imminent. $\varepsilon$ is the compression ratio and $h_g$ is the gauge ring height.

| $\varepsilon$ / | $h_g$ / | $\lambda$ (avg $\pm$ $\sigma_1$) | | | $\lambda_{max}$ | | |
|---|---|---|---|---|---|---|---|
| % | mm | UT | PT | ET | UT | PT | ET |
| 5 | 9.53 | 1.38 ± 0.02 | 1.91 ± 0.44 | 1.38 ± 0.16 | 1.40 | 2.73 | 1.75 |
| 10 | 4.76 | 1.39 ± 0.04 | 1.63 ± 0.24 | 1.39 ± 0.07 | 1.44 | 2.27 | 1.55 |
| 15 | 6.35 | 1.49 ± 0.06 | 1.98 ± 0.32 | 1.52 ± 0.20 | 1.59 | 2.73 | 1.78 |
| 27.5 | 6.35 | 1.65 ± 0.04 | 2.23 ± 0.46 | 1.72 ± 0.24 | 1.70 | 2.89 | 2.14 |
| 30 | 0 | 1.29 ± 0.05 | 1.44 ± 0.14 | 1.26 ± 0.05 | 1.39 | 2.07 | 1.34 |
| Average | | 1.44 ± 0.04 | 1.84 ± 0.32 | 1.45 ± 0.14 | - | - | - |

### 5.4.8 Effects of Compression Ratio and Gauge Ring Height

Fig. 5.17a shows simulated leak pressures versus seal compression with no gauge ring. A curve fit based on Liu's work[159] (Eq. 3.6, repeated below) for rectangular plane strain seals is also shown. For the curve fit, $G$ is estimated to be 1.5 MPa from Fig. 5.2. ($G \approx 2C_{10}$) From the seal geometry, $L/h = 1$. The curve fitting parameters are $A = 0.16$ and $B = 3.6$ which are significantly different than those reported by Liu (3 and 2.9, respectively). This discrepancy probably arises from the different loading conditions (axisymmetric vs. plane strain) and geometries (curved seal vs. rectangular). Nevertheless, it appears that the modelling work done by Liu maps to the present work well when no gauge ring is used.

$$P_{\text{leak}} = G \left[ \frac{A}{1-\varepsilon} \left(\frac{L}{h}\right) + \frac{B\varepsilon}{1-\varepsilon} \left(\frac{L}{h}\right)^2 \right] \qquad (3.6, \text{ repeated})$$

Fig. 5.17b shows that Eq. 3.6 ($A = -0.1$, $B = 20$) is not a good model when the gauge ring height is appreciable (4.76 mm) and compression is too high ($> 25\%$). One reason for this could be the relatively higher strains in the seal when a gauge ring is used (see Table 5.1). The seal material stiffens at these higher strains due to finite-extensibility, and this effect is not captured by Eq. 3.6 because the material is described solely by its shear modulus. However, inaccuracy due to the material model is probably small because, as Fig. 5.2 indicates, there is not a great deal of stiffening in the range of strain that is encountered in this problem. The significant deviation at larger compressive strains primarily comes from the constraint of the gauge ring. Specifically, the leak pressure is a function of the extrusion gap, and the extrusion gap is a function of the compression (which Eq. 4.6 addresses) and the gauge ring height (which Eq. 3.6 does not address). Presumably, Eq. 3.6 can be modified to include an extrusion gap parameter. Such modification is not pursued here, but it is noted that the leak pressure transitions from an approximately linear form to a highly quadratic one. For instance, a $2^{\text{nd}}$-order polynomial fit to the data in Fig. 5.17b over the range of strain from 0.25-0.40 has a correlation coefficient of $R^2 = 0.998$.
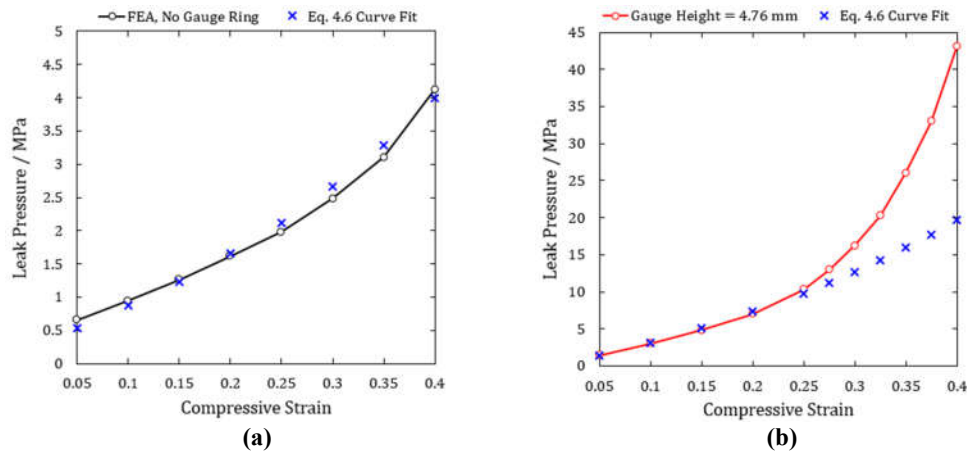


**Fig. 5.17:** Leak pressures in FEA (R2017 scheme) vs. compressive strain and with a curve fit from Eq. 3.6: **(a)** with no gauge ring, $(A, B) = (0.16, 3.6)$; **(b)** with a 4.76 mm gauge ring, $(A, B) = (-0.1, 20)$. Fitting parameters are determined by visual inspection.

Fig. 5.18a shows leak pressures at different levels of compression for a variety of gauge ring heights. A linear-to-quadratic transition is evident with gauge ring heights from 3.18-6.35 mm, but the curve for a 7.92 mm height is strictly quadratic with $R^2 = 0.999$. This reiterates that Eq. 3.6 is not a good model when the extrusion gap is sufficiently small, an observation that is not surprising. Eq. 3.6 was constructed based on analytical arguments that relate shear strains at the bottom corners of the seal to a critical leak pressure. When a gauge ring has sufficient height, the shear strains at these corners are drastically altered. In such case, it appears that a quadratic equation could replace the relatively complicated rational form of Eq. 3.6. However, it seems probable that a quadratic form must also break down when considering extrusion gaps in most industrial seals. The gaps become so small that local fracture at the extrusion gap leads to a coupled fracture-leakage problem. The present work is focused strictly on elastic leak, so numerical and experimental studies attempt to avoid any fracture regime. For further discussion and modelling of seal fracture, refer to the work of Wang et al.[249] and Windslow.[75] Fig. 5.18b shows the same data as Fig. 5.18a but changes the abscissa from compressive strain to gauge ring height.
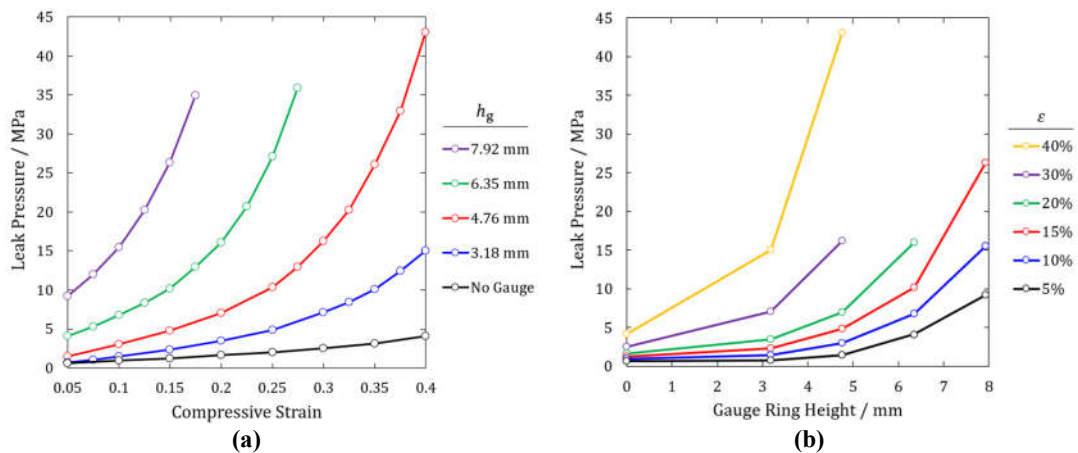


**Fig. 5.18:** Leak pressures for different compression ratios and gauge ring heights with Abaqus' R2017 pressure penetration scheme. The data in each plot are the same but expressed differently by changing the abscissa from **(a)** compressive strain to **(b)** gauge ring height. Compressions of 25% and 35% are omitted from **(b)** for clarity.

## 5.5 Mesh Sensitivity Studies

To the author's knowledge, the criticality of mesh-size on the prediction of elastic leak was not addressed in the literature until this thesis. It will be shown that achieving mesh-independent solutions is difficult and time-consuming because of the level of refinement required at the sealing interface. In this section, a single configuration with $h_g= 6.35$ mm and $\varepsilon = 15\%$ is used to demonstrate a systematic approach that achieves a mesh-independent solution within 1% accuracy.

Mesh-independent solutions were initially attempted with a structured-to-free mesh transition as shown in Fig. 5.19. This required four free mesh transition zones and often

resulted in poorly shaped elements due to the rapid growth across the partitions. To overcome this problem, structured transition zones were required.
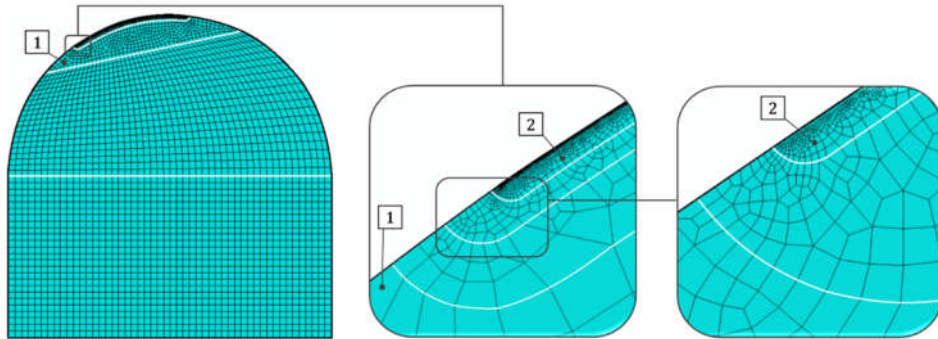


**Fig. 5.19:** An example of a free mesh transition to the sealing interface.

Fig. 5.20 shows quadrilateral transitions to the sealing interface with a $3:1$ ratio between each level. This transition technique was found satisfactory for solution accuracy, but it has a notable disadvantage. When studying mesh independence, a common practice is to refine a mesh in factors of two and then check convergence of the desired output, in this case leak pressure. It is possible but extremely time consuming to refine a mesh with $3:1$ transitions by a factor of two when a high level of refinement is required because a completely new mesh is required for each refinement. Alternatively, a $3:1$ refinement ratio can be maintained while increasing the convergence criterion from 1% (which is typically used) to something slightly larger, say 1.5%. Another option is to use a transition technique that has a $2:1$ ratio with triangular elements, a shape that is usually avoided when simulating rubbery materials. Fig. 5.21 illustrates this technique with single-stage and two-stage triangular transitions. Regardless of the transition technique (quadrilateral or triangular) that was used, the predicted leak pressures were practically identical in the mesh studies. For instance, with a 0.041 mm sealing interface mesh size, the leak pressure with the quadrilateral transition mesh was only 0.6% lower than the triangular transition mesh. The same difference was also found when the mesh size was reduced to 0.014 mm. One artefact to be aware of is the relatively poor continuity of contours through triangular mesh regions. Fig. 5.22 illustrates that the quadrilateral transitions have better continuity than the triangular transitions. These irregularities were found to have negligible impact on the pertinent leak results, so the triangular transition technique was used for most studies. A global seed size of 0.25 mm was sufficient to give mesh independence within 1% for strain contours through the body of the seal. As a final note on mesh transitions, Dragoni and Strozzi[166] illustrated a technique that achieves a $2:1$ ratio with quadrilateral transitions, but this was not tested in this thesis.
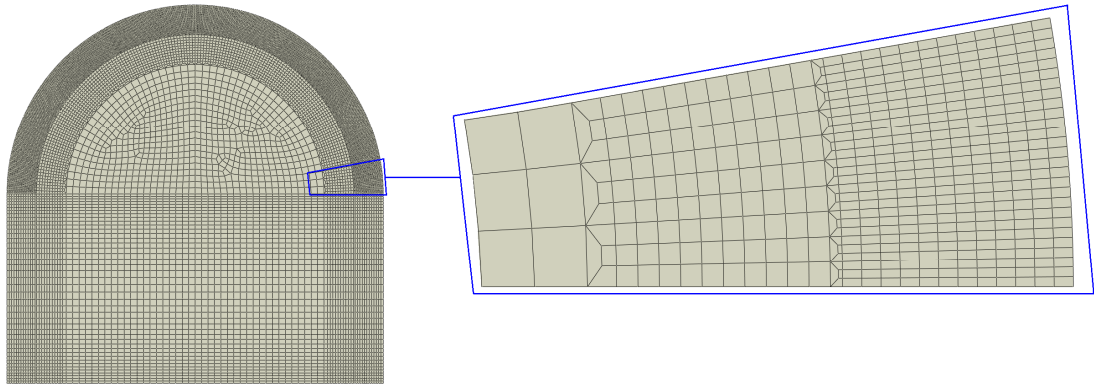
**Fig. 5.20:** An example of a structured quadrilateral mesh transition to the sealing interface.



| (a) | (b) |
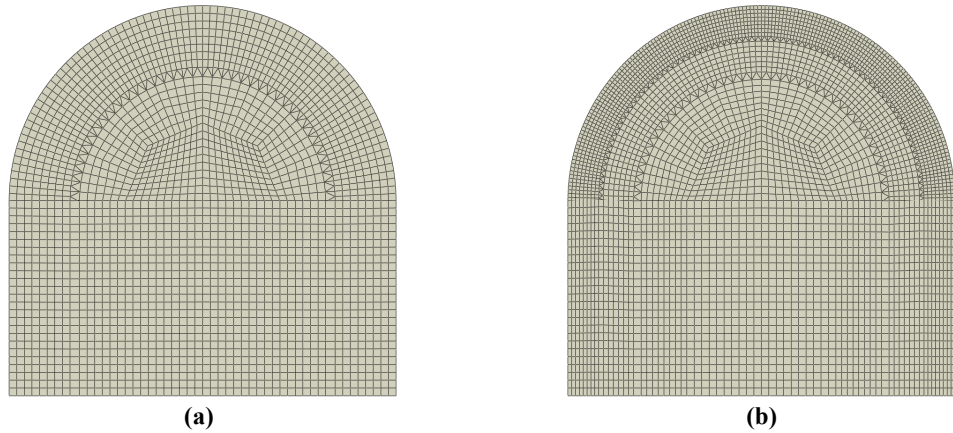
**Fig. 5.21:** Examples of structured triangular mesh transitions: **(a)** single-stage; **(b)** dual-stage.



| (a) | (b) |
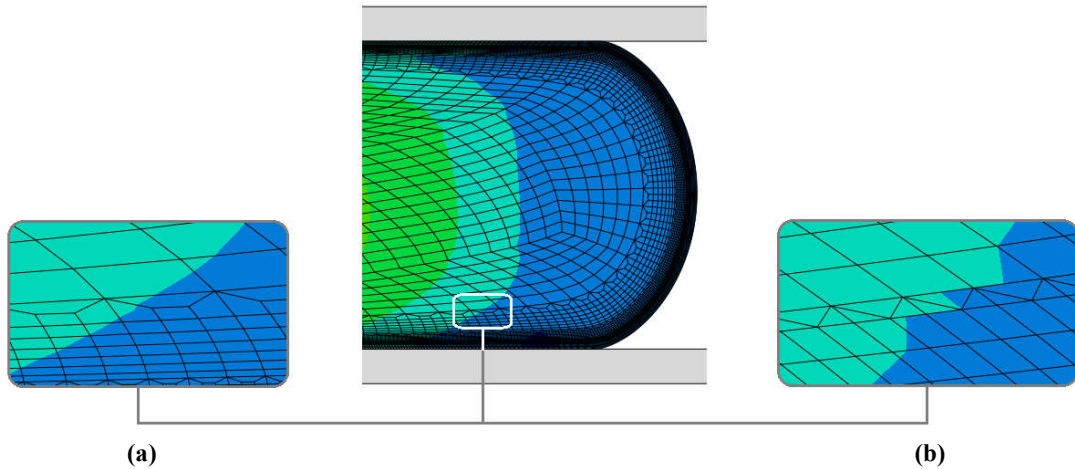
**Fig. 5.22:** Differences in nominal strain contour continuity across the mesh transitions: **(a)** quadrilateral transitions; **(b)** triangular transitions.

Fig. 5.23 shows the convergence of leak pressures as a function of the mesh size at the sealing interface with the R2017 and R2018 pressure integration schemes. Due to the slow convergence, a logarithmic scale is used for the mesh size which is normalised by the seal height (12.7 mm). The smallest and largest sizes in the plot are 0.005 mm and 0.25 mm, respectively. The difference between the R2018 and R2017 solutions differ by 21% for the largest size, reducing to 0.9% at the smallest size. The R2017 scheme achieves a solution

that is mesh-converged within 1%, but the R2018 solution is slightly higher at 1.3%. An attempt to partition one more level to 0.0025 mm was not attempted and, based on the difficulty in constructing the mesh with size 0.005 mm, may not have been possible due to limitations with graphics and precision in Abaqus/CAE. Fig. 5.23 makes clear that achieving a mesh-independent solution based on leak pressures is difficult. In these 2D simulations, a mesh-converged solution was possible, but the computational costs in 3D could preclude mesh-independent solutions in practical contexts. A reasonable compromise may be to study the rate of convergence for larger mesh sizes and then extrapolate to estimate a mesh-independent solution. Yet, even this could be a time-consuming exercise due to noise in the convergence trends. Fig. 5.24 shows the mesh transitions required to achieve the 0.005 mm mesh size at the sealing interface. It requires six 2:1 transitions, yielding 7 regions with significantly different element sizes.
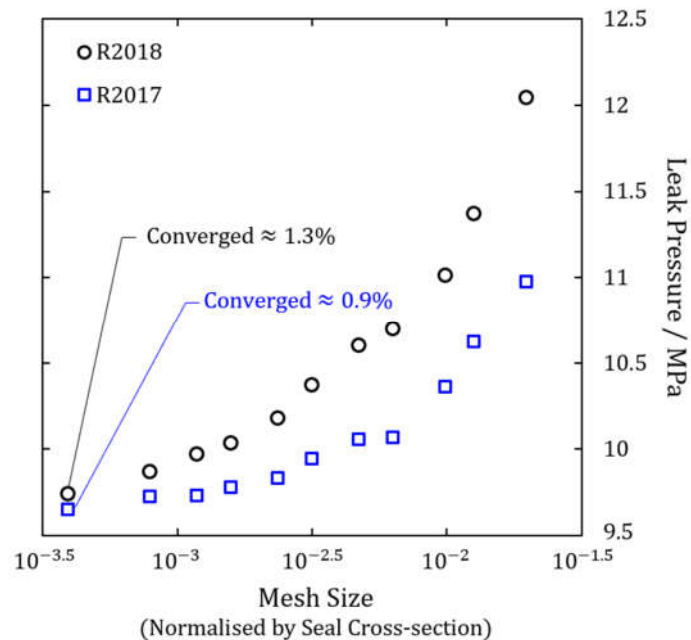


**Fig. 5.23:** Convergence of leak pressures as mesh size reduces. The convergence values listed for each scheme are computed with mesh sizes that differ by a factor of 2. The mesh size is normalised by the seal cross-section height of 12.7 mm.
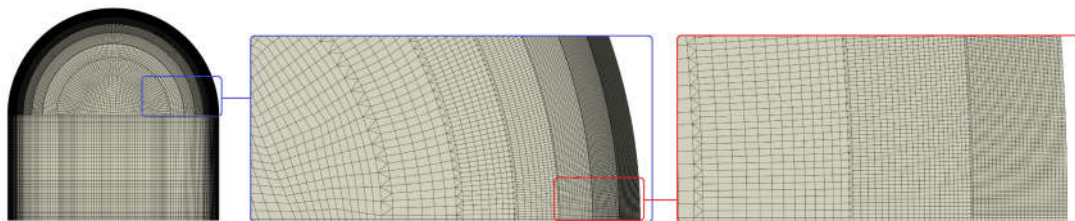


**Fig. 5.24:** Mesh transitions to achieve a 0.005 mm size at the sealing interface. There are 168,294 quadrilateral and 11,812 triangular elements.

## 5.6 Fluid Pressure Penetration with Closing Contact

### 5.6.1 Manually Closing Contact in Abaqus/Standard

Section 5.4.4 shows that Abaqus' FPP algorithms do not close contact if a node that initially has pressure is pushed into a contact interface. One solution to this problem is to manually update pressure surfaces step-by-step as contact status changes. This is an iterative, labour-intensive process.

To proceed, it is important to understand how Abaqus decides when to propagate pressure in Abaqus/Standard. Fig. 5.25 shows a seal that is subjected to pressure when propagation from one node to the next is imminent. At $P_{\text{apply}}$ = 7.24 MPa, the contact pressure at the node just to the left of a node that is in physical contact has a finite contact pressure (that is, $P_{\text{contact}} > 0$, Fig. 5.25a). It may seem odd for a node that is not in physical contact with the sealing interface to have a finite contact pressure, but this occurs because Abaqus distributes the nodal contact force due to contact pressure across the two adjoining elements. The load distribution to each node is not equivalent; rather, it is weighted by the solver, the details of which are not elucidated in Abaqus' FPP documentation.[197,250] On the next load step (Fig. 5.25b), the pressure increases to $P_{\text{apply}}$ = 7.25 MPa, and this is sufficient to reduce the contact pressure to zero; therefore, on the next load step with $P_{\text{apply}}$ = 7.26 MPa (Fig. 5.25c), the fluid pressure propagates to the next node, thereby breaking its contact. The algorithm proceeds in this manner until full leakage occurs.
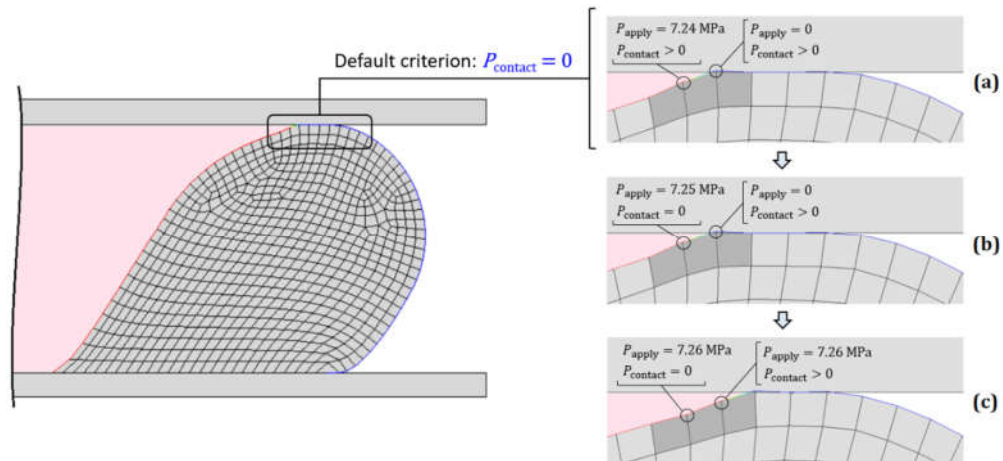


**Fig. 5.25:** Illustration of how Abaqus' default FPP algorithm propagates pressure. A detailed explanation can be found in the text.

To manually close contact, the inverse of the procedure in Fig. 5.25 can be implemented. To demonstrate, a mesh size of 0.03 mm (Fig. 5.26) was used at the sealing interface to achieve a reasonable computation time. The solution was not expected to be mesh-independent within 1%, but from Fig. 5.23 the order of error could be estimated as +4% based on the R2018 integration scheme. The R2018 scheme was chosen because it was easier to implement manually since it did not require a linear ramp-down of the

pressure at the sealing front. A gauge ring with height 6.35 mm and a compression ratio of 15% were used. Two pressures are reported. The **crack pressure** is required to break nodal contact at the sealing front. Stated another way, it is the pressure threshold at which the nodal contact status at the sealing front changes from opening-to-closing to closing-to-opening. The **leak pressure** is the final pressure that fully breaks through the seal. In this case, the crack and leak pressures are 14.87 MPa and 15.08 MPa, respectively (Fig. 5.27). The simulation required 109 pressure steps, and in between each of these, an additional step was required to relieve or propagate pressure across an element which gave a total of 218 manually implemented pressure steps. The pressure propagation loads were not known *a priori*, so convergence errors aside, 109 of these steps required at least one additional iteration to determine where to break a step. Abaqus' restart capability[251] was used to shorten the total simulation time, but even so it required about 2 weeks to complete the solution. For reference, the final setup ran in about 2 hours on a single 2.6 GHz processer in Windows 10. Splitting the problem across multiple processors only increased simulation time. Appendix R provides more images of the seal deformation as a function of pressure.
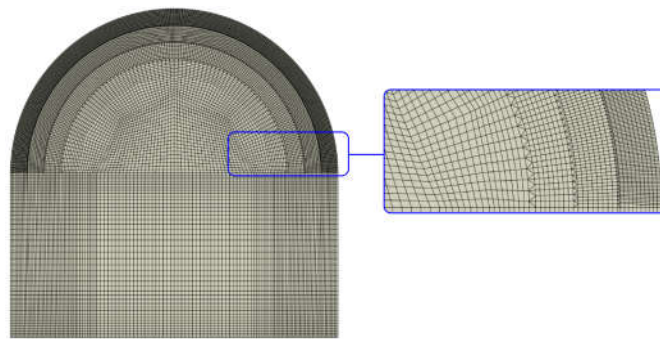


**Fig. 5.26:** Mesh transitions to achieve a 0.030 mm size at the sealing interface. There are 18,526 quadrilateral and 1,744 triangular elements.



|        (a)        |        (b)        |
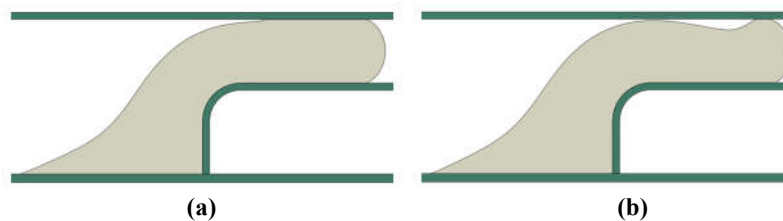
**Fig. 5.27:** Seal deformation at: **(a)** $P_{crack} = 14.87$ MPa; **(b)** $P_{leak} = 15.08$ MPa. The simulation fails to converge before pressure fully breaks through the seal due to rapid changes in contact status, but the reported leak pressure is, for practical purposes, fully converged at this last point.

### 5.6.2 Automating Contact Closure in Abaqus/Standard with a DLOAD Subroutine

The iterative process in the preceding section was required because the native FPP algorithms in Abaqus do not address closing contact. However, it is possible to write a DLOAD subroutine[252] that removes pressure from nodes with closing contacts, and when the sealing interface later transitions to opening contacts, the DLOAD can be swapped to Abaqus' native FPP algorithm in a new load step. In the present example, nodal contacts

stopped closing when $P_{\text{apply}} = 11.80$ MPa, and the node at the sealing front was stable until $P_{\text{crack}} = 14.87$ MPa. Therefore, at any pressure between these two limits, the DLOAD subroutine could be swapped to Abaqus' FPP algorithm to complete the leak simulation.

Two DLOAD subroutines for pressure penetration have been used in the literature,[198,201] but detailed codes were not disclosed. To the author's knowledge, this thesis presents the first publicly disclosed DLOAD subroutine that closes contact with pressure loads in Abaqus. The subroutine differs from Abaqus' native algorithm in that it uses kinematic conditions instead of contact pressures to define where pressure is applied. This choice is made because it is difficult to extract nodal forces, and hence calculate contact pressures, in a DLOAD subroutine. The challenge occurs because the DLOAD subroutine does not call the necessary variables to directly compute contact pressures, but according to Moller & Stey,[198] there is a complicated workaround for this. This was not pursued in this work, but it will be shown that the subroutine that is based on a kinematic definition has good agreement with Abaqus' native FPP algorithms.

More details on the DLOAD subroutine are given in Appendix H. Here, a conceptual explanation is sufficient. After the compression step, pressure application on the seal is split into 3 distinct load steps:

1.  Pressure is applied to the seal with the DLOAD subroutine until the nodal contact transitions from closing to opening contacts.

    a.  The nodes that receive pressure are determined by their position with respect to the rigid (top) sealing interface. For a compression of 15%, any node below 10.795 mm (that is, $(12.7 - 0.15 * 12.7)$ mm) receives pressure. This value is stored in "$y\_lim$" in the subroutine.

    b.  In this example, the transition can be assigned anywhere between 11.80-14.87 MPa because the nodal contact is stable through this range. The transition point in Appendix H is arbitrarily set at 13.5 MPa and stored in the "$F\_lim$" variable.

2.  An intermediate step swaps the DLOAD subroutine to Abaqus' native FPP algorithm. In doing so, the DLOAD linearly ramps down pressure from 13.5 MPa to 0 MPa while the FPP interaction linearly ramps up from 0 MPa to 13.5 MPa.

3.  The solution progresses to completion with Abaqus' FPP algorithm.

With this technique and the R2018 integration scheme, $P_{\text{crack}} = 14.92$ MPa, but convergence was not achieved for $P_{\text{leak}}$. This highlights a common problem in Abaqus/Standard: achieving converged solutions is difficult, and even seemingly trivial changes to the model affect convergence. The source of non-convergence is almost always a consequence of problems with contact forces and penetrations. Nevertheless, the crack pressure with this method only differed from the fully manual solution in the previous section by 0.3%. The slight discrepancy arises because the node at the sealing front shifted by one element when swapping from the DLOAD subroutine to Abaqus' FPP algorithm.

124

With the DLOAD subroutine and the R2017 integration scheme, $P_{\text{crack}} = 13.62$ MPa and $P_{\text{leak}} = 14.01$ MPa. These were lower than the fully manual solution by 8.4% and 7.1%, respectively, and the differences can probably be attributed to the different integration schemes; that is, the R2018 scheme truncates pressure at the sealing front, whereas R2017 uses a linear ramp-down.

Finally, the DLOAD subroutine was run until full leakage instead of swapping to Abaqus' native FPP algorithm. In this case, the simulation terminated before full leakage occurred, but $P_{\text{crack}} = 14.04$ MPa which was 5.6% lower than the fully manual case. The lower crack pressure occurred because Abaqus assigns a finite contact pressure to nodes that are not in physical contact with the sealing interface (see Fig. 5.25), so it can more readily resist pressure penetration when compared to the kinematic definition in the DLOAD subroutine. In any case, all solutions fell within 10% of one another and would probably be in closer agreement with smaller mesh sizes according to trends in Fig. 5.23.

### 5.6.3 Automating FPP in Abaqus/Explicit with a VDLOAD Subroutine

Abaqus/Explicit does not have a built-in capability to propagate pressure, but such ability is highly desirable to overcome difficulties with contact convergence in Abaqus/Standard. Therefore, a VDLOAD subroutine[253] was written to simulate pressure penetration with the explicit solver. To the author's knowledge, this is the first publicly available demonstration of such capability. Like its DLOAD counterpart, the VDLOAD subroutine determines which nodes receive pressure based on their position relative to the sealing interface. The detailed code and notes on implementation are given in Appendix J, but there is one important point to make in this section. In both Abaqus/Standard and Abaqus/Explicit, default contact behaviours are assigned. The former uses a penalty method which allows nodes to penetrate a contact surface. The latter uses a kinematic method that practically eliminates nodal contact penetration.[254] The differences in contact algorithms are visually evident in Fig. 5.28. As a result, nodes are more easily pulled away from the contact interface in Abaqus/Explicit, so leak pressures are systematically lower than those predicted in Abaqus/Standard. It will be shown that the impact on leak pressures may be minor.



(a)          (b)          (c)
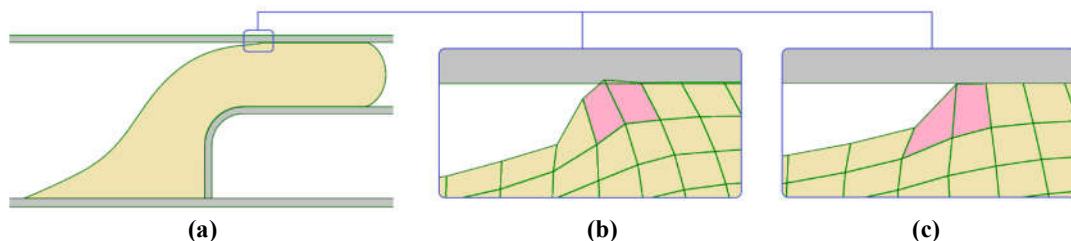
**Fig. 5.28:** Illustration of the difference in contact formulations: **(a)** the deformed seal; **(b)** with penalty contact in Abaqus/Standard, nodes on the seal can penetrate the countersurface; **(c)** with kinematic contact in Abaqus/Explicit, the nodal penetration is virtually eliminated.

The explicit solver has better contact convergence than the implicit solver, but careful attention must be given to timescales and material masses. Ideally, loading times and densities are set exactly as they occur in a real application, but this often results in impractical simulation times because there is an upper bound on the increment of time that advances the solution from a current state to the next one. The order of this time increment in an undamped system can be estimated as:[255]

$$\Delta t_c \approx \frac{L_e}{c_d} \tag{5.2}$$

where $L_e$ is the length of the smallest edge in a mesh and $c_d$ is the dilational wave speed of the material. For a linearly elastic virtually incompressible material, the wave speed is:

$$c_d = \sqrt{\frac{3G}{\rho}} \tag{5.3}$$

where $G$ is the shear modulus and $\rho$ is the mass density. For example, consider a typical rubber finite-element model with $G = 1$ MPa, $\rho = 1$ g/cm$^3$, and $L_e = 0.01$ mm. The critical time according to Eq. 5.2 is $10^{-7}$ s. If pressure is ramped to 10 MPa at a rate of 1 MPa/s, then approximately $10^8$ iterations are required to solve the problem, and this is a best-case scenario. Damping mechanisms and mesh deformation reduce the time increment further. Therefore, it may be impossible to achieve a solution with the explicit solver in a reasonable time because the solution advances too slowly.

One option to shorten simulation time is to introduce mass scaling which artificially increases mass to increase $\Delta t_c$. For example, Fig. 5.29a shows how increasing the density of the rubber by orders of magnitude reduces simulation time on a single 2.6 GHz processor. For the problem studied with a mesh size of 0.03 mm, mass scaling was required to achieve a solution in a reasonable time, but caution was exercised because mass scaling introduces kinetic energy in the model which can cause unwanted inertia effects. On one hand, higher inertia makes it more difficult to move the seal and can increase leak pressures. On the other hand, the extra mass can amplify inertia-driven elastic waves during deformation, disrupt the sealing front, and cause pressure to propagate prematurely. Such elastic waves in a seal are illustrated in Appendix R. Therefore, it is a good practice to confirm that desired outputs are not altered by mass scaling. For the studies in this work, Fig. 5.29b shows that the leak pressures were quite insensitive to mass scaling.
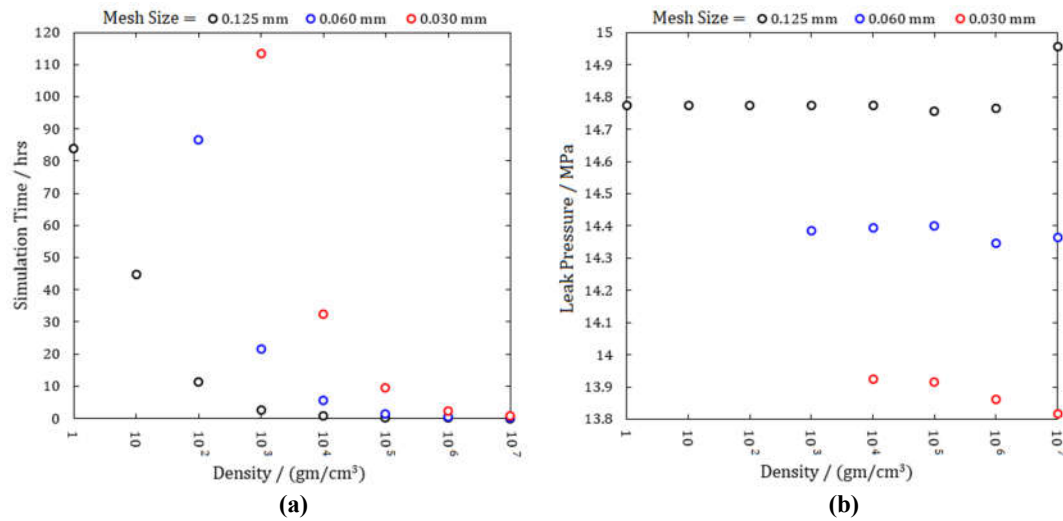
**Fig. 5.29:** Impact of mass scaling with different mesh sizes on: **(a)** simulation time; **(b)** leak pressure.

Table 5.2 summarises several results from this chapter and shows that:

- The FPP method with the R2018 integration scheme and no consideration of closing contact on pressurised nodes gave crack and leak pressures about 30% lower than the techniques that address closing contact. This highlights the importance of using subroutines to address closing contact if it occurs.

- The manual propagation solution was in excellent agreement with the DLOAD + R2018 solution. The slight differences arose from a 1-node offset in the pressurised surface after contacts began to open.

- The R2017 scheme predicted lower pressures than the R2018 scheme which is consistent with trends in Fig. 5.23.

- The crack pressures with the VDLOAD and DLOAD subroutines differed by 0.9%, indicating that the different solvers in Abaqus were in accord. The slightly lower pressure with the explicit solver arose due to the different contact formulations illustrated in Fig. 5.28.

- The crack and leak pressures were nearly identical in the explicit analysis. This seems consistent with Druecke's[160] observation that seal leakage may be related to an elastic instability because pressure rapidly breaks through the seal after initial contact is broken.

**Table 5.2:** Summary of leak pressures with a mesh size of 0.03 mm and a gauge ring height of 6.35 mm.

| Solver | FPP Method | $P_{crack}$ / MPa | $P_{leak}$ / MPa |
|---|---|---|---|
| Implicit | R2018 | 10.03 | 10.18 |
| Implicit | Manual | 14.87 | 15.08 |
| Implicit | DLOAD + R2018 | 14.92 | n/a |
| Implicit | DLOAD + R2017 | 13.62 | 14.01 |
| Implicit | DLOAD | 14.04 | n/a |
| Explicit | VDLOAD | 13.92 | 13.93 |

## 5.7 Further Sensitivity Analyses

This section explores how the friction model, volumetric compressibility, and seal compression affect leak pressures. Some trends with Coulomb friction models are illustrated since, despite being physically unrealistic, they are commonly used in the literature (see Table 3.1). The results with Coulomb friction are compared to contact pressure-dependent friction models. The impact of volumetric compressibility is presented with simulations that vary Poisson's ratio, even to unrealistic (that is, overly compressible) values. This gives insight into the validity of adopting an incompressible material model, another common practice in the literature (Table 3.1). Finally, these model sensitivities are combined with some studies on the effect of seal compressions at 5%, 10%, and 15%. The latter two values are encountered in some O-ring designs of the financial sponsor. The sensitivity analyses are demonstrative and should not be generalised to other sealing systems.

### 5.7.1 Friction Model

When using a constant CoF model and the implicit solver, converged solutions were not consistently achieved at compression levels above 10% due to poor contact convergence. However, the VDLOAD subroutine enabled the study of how a constant CoF model affected leak pressures.

One benefit of the explicit solver was that it did not require contact stabilisation which, as Fig. 5.8 shows, can result in physically unrealistic behaviour when a Coulomb friction model is specified. Fig. 5.30 shows that the leak pressures scale linearly with the CoF until $\mu = 0.2$. Above this value, stick-slip causes erratic movement of the seal, and pressure can suddenly break through the contact interface. The explicit solver gave a more accurate representation of leak pressures at the lower range of CoFs considered here, but results were erratic at the higher CoFs. It must be noted that these results scale mass by $10^6$, but the preceding section suggests that the leak pressures are reasonably converged with this level of scaling. Yet, it is conceivable that a reduction in mass scaling could mitigate the erratic behaviour by reducing inertia effects that disrupt the sealing front. The "Contact Pressure-Dependent" trend uses the friction model from Fig. 5.9. It shows stable behaviour over the entire CoF range and reiterates the benefit of using a contact pressure-dependent friction model when simulating rubber. The trend also shows less variation in leak pressures, a consequence of the diminution of CoFs with increasing contact pressures. This diminution also resulted in lower leak pressures with the contact pressure-dependent friction model.
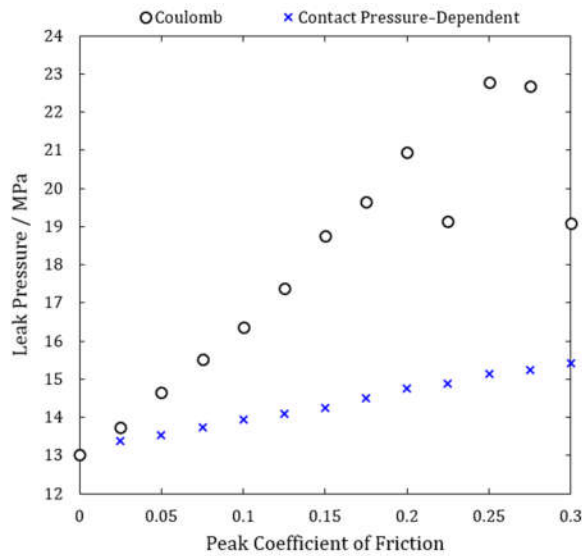
**Fig. 5.30:** Effect of CoFs on leak pressures in Abaqus/Explicit with a mesh size of 0.03 mm, $\varepsilon = 15\%$, and $h_\mathrm{g} = 6.35$ mm. "Coulomb" assumes a constant CoF. "Contact Pressure-Dependent" uses a contact pressure-dependent CoF with the maximum value capped to the value on the $x$-axis. For instance, "Contact Pressure-Dependent" at a CoF of 0.1 uses the model shown in Fig. 5.9. Other CoFs for the "Contact Pressure-Dependent" series linearly scale all data points in Fig. 5.9 by the same value. For example, the "Contact Pressure-Dependent" model with $\mu = 0.2$ scales all data in Fig. 5.9 by a factor of 2.

### 5.7.2 Volumetric Compressibility

The effect of volumetric compressibility on leak pressures is significant when a seal is highly confined, but Fig. 5.31 shows that the effect may be important even when a seal has a large extrusion gap. Leak pressures with 15% compression and a gauge ring height of 6.35 mm scale linearly with Poisson's ratio. Artificially low Poisson's ratios for rubbery materials are also simulated. The bottom of the range is set to $\nu = 0.475$ ($\kappa{:}G = 20{:}1$) which is the default value in Abaqus/Explicit. Realistically, industrial rubber seals should probably be limited to a minimum value of 0.495 ($\kappa{:}G = 100{:}1$),[256] so Fig. 5.31 may give an exaggerated view of the sensitivity of leak pressures to volumetric compressibility.
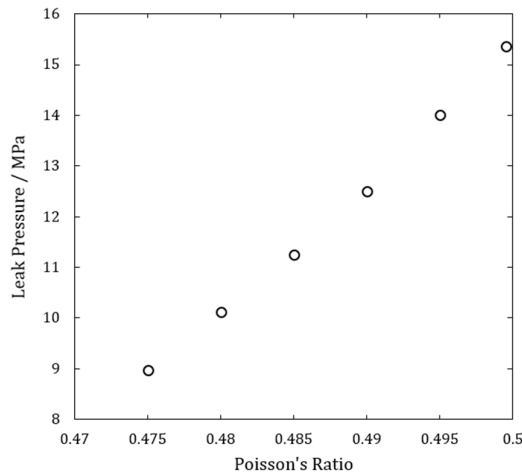


**Fig. 5.31:** Effect of Poisson's ratios on leak pressure in Abaqus/Standard with a DLOAD subroutine and the R2017 FPP algorithm. Mesh size is 0.03 mm, $\varepsilon = 15\%$, and $h_\mathrm{g} = 6.35$ mm.

129

### 5.7.3 Seal Compression

Fig. 5.32 illustrates the effect of seal compression on leak pressures for different Poisson's ratios and contact pressure-dependent CoFs. The numbers in parentheses express the variation in leak pressures with respect to pressures indicated by the ○ symbols. Varying Poisson's ratio from 0.49 to 0.4995 affects the leak pressures by about $\pm10\%$ for the different levels of compression (Fig. 5.32a). The trends on the impact of friction are less straightforward (Fig. 5.32b). There is little difference in the solutions with $\mu_{max} = 0.1$ and $\mu_{max} = 0.05$ for all compression levels because the friction model curves were both low (trending toward a frictionless case), so they gave similar behaviour. With $\varepsilon = 5\%$, all three friction models gave similar leak pressures because the contact interface was small as illustrated in Fig. 5.33. Therefore, friction forces contributed less resistance to the pressure, and the leak pressure was dominated by the stiffness of the seal. At the two larger compression ratios, the friction model with the largest CoFs increased the leak pressures by similar amounts, roughly 10%.
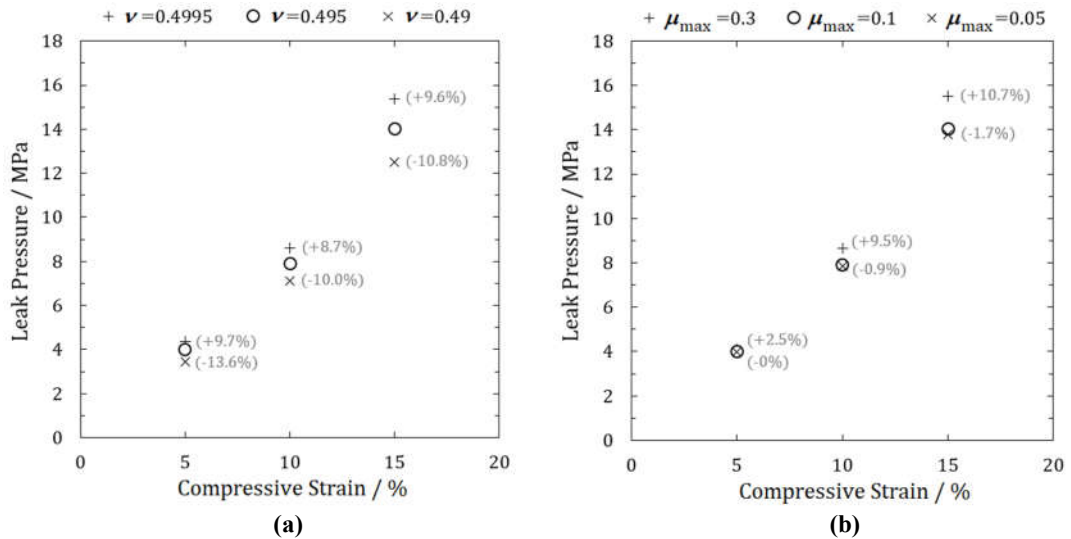


**Fig. 5.32:** Effects of compression ratio on leak pressure with a DLOAD subroutine and the R2017 FPP algorithm: **(a)** with varying Poisson's ratios; **(b)** with varying contact pressure-dependent friction models capped as explained in Fig. 5.30.
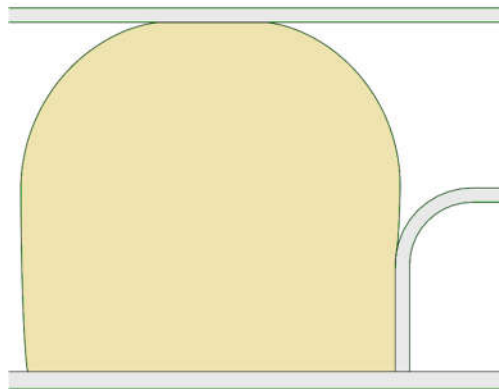


**Fig. 5.33:** Small contact interface at the top of the seal after 5% compression (compare to Fig. 5.3b).

## 5.8 Summary

A 2D axisymmetric finite-element model of a bonded rubber face seal subjected to compression and differential pressure has been presented in this chapter. The seal was treated as a perfectly hyperelastic material. The hyperelastic model was generated from uniaxial tension data for a filled sealing material, and strain and biaxiality analyses were completed. The material model neglected complications that arise from viscoelasticity, plasticity, and cyclic stress softening. Metal sealing surfaces were treated as rigid bodies. These limitations are further assessed in chapters that follow.

To address the problem of contact convergence in Abaqus/Standard, three different controls were studied: local surface-to-surface contact stabilisation, global stabilisation, and contact stiffness. Of these, local contact control gave the most realistic results over a broad range of studies. Global stabilisation resulted in unrealistic trends in leak pressures in models with low friction, and an important finding was that a low ratio of viscous dissipation energy (ALLSD) to internal energy (ALLIE) is necessary but not sufficient to ensure a physically realistic result. Reducing contact stiffness helped convergence, but the reductions were so large that unrealistic contact penetrations occurred. Recently, Abaqus added a general contact algorithm[257] that may improve contact convergence, but this was not studied in the present work.

Different methods of simulating fluid pressure penetration have been presented. In Abaqus/Standard, pressure loads may be specified on a surface in the Load or Interaction modules. The latter option allows the pressurised surface to update when nodes change from closed to open contact, but it does not remove pressure when they change from open to closed contact. To study this problem, pressure removal and propagation were simulated manually across each element, and results showed that removal of pressure from nodes significantly increased the leak pressure.

To overcome the drawbacks of manually adjusting the location of pressure loads, a DLOAD subroutine was created for Abaqus/Standard. The routine can simulate leakage as a standalone code or run as a complement to Abaqus' native FPP algorithms. The predicted leak pressures with and without the subroutine were similar. Small discrepancies were attributed to differences in the pressure integration scheme (truncation vs. linear ramp-down at the sealing front), the mesh size, and the leak criterion (specifically, the use of nodal position or contact pressure to determine when pressure should propagate).

Contact convergence in Abaqus/Standard was not always possible, so Abaqus/Explicit was used as a remedy. This required the development of a VDLOAD subroutine since the explicit solver does not have a native FPP capability. Leak pressures from the VDLOAD subroutine were in accord with those from the DLOAD subroutine, with slight discrepancies explained by different contact formulations (penalty in Abaqus/Standard vs.

kinematic in Abaqus/Explicit). Crack and leak pressures in the explicit solver were nearly identical which suggests a link between seal leakage and elastic instability. Leak pressures were remarkably insensitive to mass scaling which was required to achieve solutions in a reasonable time. Such large scaling was probably acceptable due to the simulation timescales being of order up to 10 s, significantly longer than impact simulations where explicit analysis are often employed. The VDLOAD subroutine for FPP appears to be the first of its kind in publicly available literature.

Leak pressures were found to reduce significantly as mesh size reduced, and convergence to a mesh-independent value was slow. Consequently, element size transitions were required from the bulk of the seal to the sealing interface to achieve solutions within a practical time. With free mesh transitions, element shapes were often unacceptable. Therefore, structured quadrilateral and triangular transitions were explored. Both options took significantly more time to construct than a free mesh but reduced the total number of elements. Across transition zones, quadrilaterals gave smoother field contours than triangles, but the quadrilateral transition was more difficult to systematically adjust when studying mesh-independence. Fortunately, leak pressures were largely unaffected by the transition shape, so triangular transitions were employed in most studies. A surface mesh size of 0.005 mm was required for mesh-independence within 1%, but a size of 0.03 mm was used in most studies to shorten simulation time. For reference, the nominal height and width of the seal were both 12.7 mm.

Coulomb and contact pressure-dependent friction models were studied in detail. Several deficiencies in the Coulomb model must be reiterated. First, the model is physically unrealistic for rubbery materials when contact pressures have large variation. Second, it introduced inaccuracies in the prediction of leak pressures at both low and high CoFs in this work. The problem at the low range was specific to Abaqus/Standard and related to global stabilisation. Abaqus/Explicit performed better with low CoFs. With high CoFs, contact convergence was extremely difficult in Abaqus/Standard, especially for compression ratios above 10%. In some cases, the node at the sealing front would stick on the countersurface, resulting in unrealistic deformations. In Abaqus/Explicit, the contact interface became unstable at high CoFs due to stick-slip, and this caused an unpredictable trend in leak pressures. The contact pressure-dependent friction models converged better than the Coulomb models in both solvers over the entire range of CoFs and compression ratios in this work. Contact pressure-dependent friction models are more physically realistic and numerically stable, so based on the studies in this work, a Coulomb friction model is highly discouraged when simulating rubber seals.

Leak pressures increased linearly as volumetric compressibility decreased. Sensitivity of leakage to bulk modulus is expected for highly constrained seals, but even the relatively

unconstrained seals in this work showed sensitivity. This suggests that careful attention should be given to the volumetric stiffness of seals even when some surfaces are not constrained or loaded.

As expected, leak pressures increased as the compression ratio and gauge ring height increased. When no gauge ring was used, or when a short gauge ring was used at sufficiently low compression, leak pressures were modeled well by Liu's[159] plane strain leak equation; however, his model became inaccurate as the extrusion gap decreased due to extra constraint from the gauge ring. Leak pressures as a function of compression ratio transitioned from an approximately linear to highly quadratic behaviour and depended on the gauge ring height.

In closing this chapter, it is evident that accurately simulating seal leakage with FPP is no trivial task. Leak predictions are sensitive to a litany of model settings, and many parameters have been adopted in the literature without careful thought. When seal performance is critical, a more comprehensive approach is in order, and the lessons herein provide guidance; yet, the sensitivities that have been demonstrated raise questions regarding the accuracy of leak predictions by other researchers. Studies that have validated FE solutions could be merely fortuitous, representing a bias toward publishing only positive results. To better assess the accuracy of the FPP modelling methods, Chapter 6 presents an experimental test fixture that is based on the preceding FE models. Hence, the seal that is physically studied is designed to fail by elastic leak. Leak pressures are measured and then correlated to FE-based leak predictions to further assess the accuracy of FPP techniques.

# 6. Experimental Testing of Bonded Rubber Face Seals

## 6.1 Overview

This chapter develops an experimental basis to assess the accuracy of pressure penetration modelling capabilities in Abaqus in the next chapter. It introduces a test fixture that mirrors the FE geometry of Chapter 5. The fixture is analysed to ensure appropriate safety factors prior to physical testing. An unfilled NR material and a filled EPDM material are introduced. Cure rheology and mechanical characterisations of both materials are presented, and curve fitting of hyperelastic models based on pure, homogeneous deformations is demonstrated. The models are then validated with force-deflection data taken from compression testing of the bonded seals. An experimental test plan for elastic leak of the seals under different compression ratios and extrusion gaps is summarised, and the chapter closes with a presentation of the leak pressure results.

## 6.2 Experimental Test Fixture

The test fixture (Fig. 6.1) replicates the finite-element geometry previously shown in Fig. 5.1. Table 6.1 identifies components in the fixture. When testing, the top plate (Item 1) provided a sealing countersurface for the bonded seal (Item 6). This seal was bonded to a seal carrier (Item 5) that was fixed to the bottom plate (Item 3) with a bolt (Item 12). An O-ring (Item 7) in the seal carrier prevented leakage along the bottom plate. The seal carrier, which was not used in the previous chapter, provided a simple, economical means for redressing bonded seals. The spacer ring (Item 2), which was fixed between the upper and lower plates with bolts (Item 8), controlled compression of the bonded seal. Spacer ring heights were varied to achieve nominal seal compressions of 5%, 10%, and 15%. A single notch was machined on top of the spacer rings to prevent a face seal with the top plate. Without this feature, pressure could have been trapped between the bonded seal and the spacer ring, thereby increasing leak pressures. The gauge ring (Item 4) controlled the extrusion gap. Heights were chosen to achieve gaps equivalent to 50%, 75%, and 100% of the nominal seal height which, referring to Fig. 5.1, correspond to $h_g = (6.35, 3.18, 0)$ mm, respectively. The gauge ring had a 3.17 mm radius to prevent fracture as the seal deformed into the extrusion gap. ANSI/ASME B1.1[258] grade 8 ($\sigma_y = 896$ MPa minimum) screw hardware was used per the project sponsor's internal design standards.
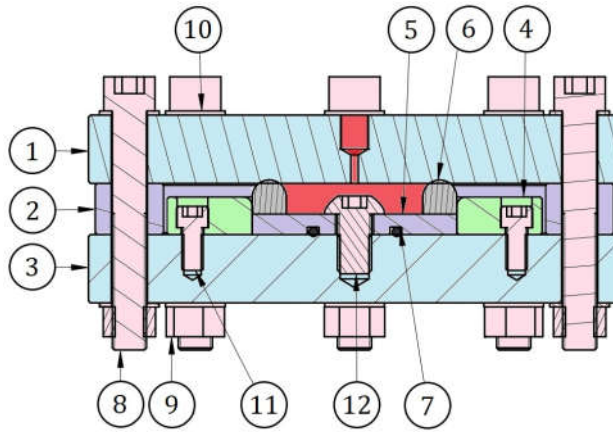
**Fig. 6.1:** Assembly drawing of the experimental test fixture.

**Table 6.1:** Test fixture components.

| Item No. | Qty. | Description |
|---|---|---|
| 1 | 1 | Top Plate |
| 2 | 1 | Spacer Ring |
| 3 | 1 | Bottom Plate |
| 4 | 1 | Gauge Ring |
| 5 | 1 | Seal Carrier |
| 6 | 1 | Bonded Seal |
| 7 | 1 | O-ring #216 |
| 8 | 8 | Bolt, 1/2-13 X 3.75 UNC, Socket Head |
| 9 | 8 | Nut, 1/2-13 UNC |
| 10 | 16 | Washer, 1/2 |
| 11 | 8 | Bolt, 5/16-18 X 5/8 UNC, Low Head Socket |
| 12 | 1 | Bolt, 1/2-13 X 0.75 UNC, Button Head |

The bonded seal was pressurised through a port at the centre of the top plate as illustrated by the red region in Fig. 6.1. This caused the bonded seal to displace into the extrusion gap until leakage occurred. During pressurisation, the seal was required to avoid contact with the counterbore in the gauge ring; otherwise leakage could have occurred prematurely. Prior to building the fixture, simulations determined an appropriate offset between the fixture's centreline and the counterbores. A distance of 54.6 mm (Fig. 6.2) was suitable for all assembly conditions.
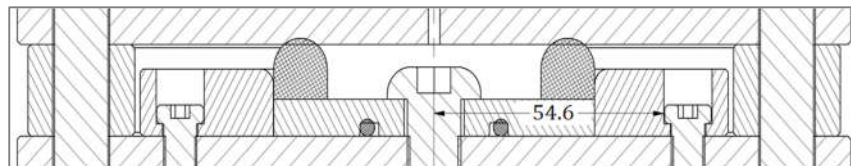


**Fig. 6.2:** Offset between the fixture centerline and the counterbore in the gauge ring. Units are mm.

All metal components in the fixture were 4140 steel with the following properties: $\sigma_y$ = 758 MPa, $E$ = 206.8 GPa, and $v$ = 0.3 where $E$ is Young's modulus. A 3D linear elastic FE half-model was used to determine a maximum working pressure (Fig. 6.3a). For simplicity, only the meshed components were used in the analysis. Partitions permitted the

135

use of quadratic brick elements for all parts. The top plate was subjected to a pressure of 52 MPa over the circular area defined by the radius of 54.6 mm in Fig. 6.2. The bottom plate was fixed along the circular area defined by the seal carrier.



| (a) | (b) |
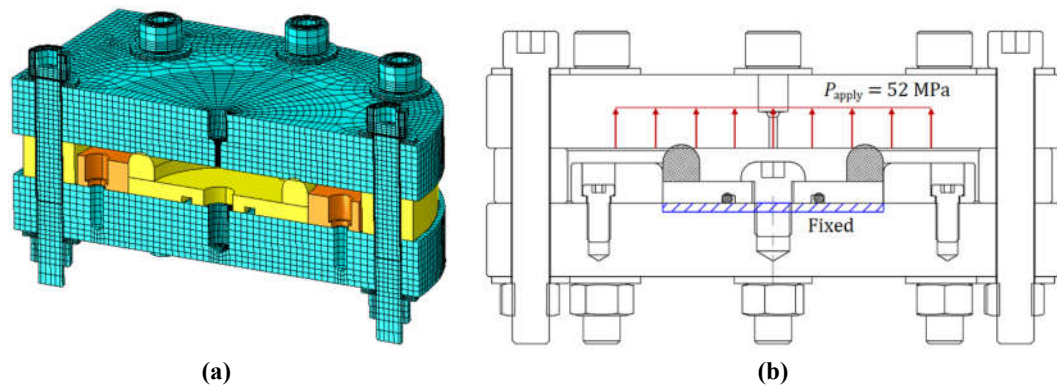
**Fig. 6.3: (a)** Mesh for an FE half-model of the test fixture. Unmeshed parts are illustrated but not included in the analysis. **(b)** Pressure and fixed displacement boundary conditions for the FE model.

Fig. 6.4 shows von Mises stress contours in the fixture with 20X magnification of the displacement. Maximum stress in the top plate is just above 600 MPa at the pressure port, giving a safety factor of approximately 1.26 against yielding. Due to their higher yield strength, the bolts have a slightly higher safety factor despite having larger stresses. With the pressure load, the plates separate approximately 0.9 mm at the pressure port and 0.6 mm at the gauge ring counterbore. The influence of this plate deflection on the seal leakage is discussed in Section 7.4.4.
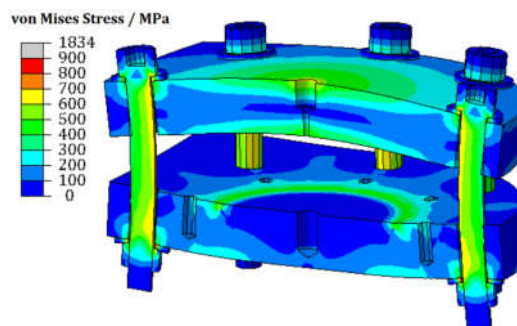


**Fig. 6.4:** von Mises stress contours in the FE model. Contours are capped at 900 MPa which corresponds to the bolt yield strength.

## 6.3  The Bonded Seals

Table 6.2 shows two rubber compound formulations for the elastic leak test fixture. The sulphur cured unfilled natural rubber was designed by Guangzhou JST Seals Technology[259] in China. With a Shore A hardness of 33 durometer, the material would not be well-suited for industrial sealing, but it was used to minimise inelastic effects such as stress relaxation and cyclic stress softening. Fig. 6.5a shows the bonded NR seal.

To provide a better model material for an industrial seal, a filled compound was provided by Cameron Brookshire,[260] a subsidiary of the financial sponsor. The facility had

136

a range of EPDM, NBR, and HNBR elastomers available for use. EPDM (KELTAN 2450) was selected for its relatively low glass transition temperature (see Table 2.1) to mitigate inelastic effects. The ethylene content of this EPDM is about 50% which yields an amorphous material, mitigating potential complications related to crystallinity. The compound was peroxide cured and used a silane-treated silicon dioxide (silica) reinforcing filler. The resultant Shore A hardness was 84 durometer.

The bonded EPDM seal is shown in Fig. 6.5b. An earlier version of this compound was mixed and found lighter in colour than the NR material, so it appears that the batch used for bonded seal manufacturing collected some trace amounts of carbon black from the mixer. This could have implications on the final mechanical properties and is mentioned in case a researcher attempts to reproduce this compound. For the purposes of this work, the batch variation was inconsequential because the same batch was used for mechanical characterisation of coupons and experimental testing of bonded seals.

**Table 6.2:** Bonded seal rubber compound formulations in parts (weight) per hundred rubber.

| Ingredient | Type | NR | EPDM |
|---|---|---|---|
| Natural rubber | Elastomer | 100 | |
| KELTAN 2450 | Elastomer | | 100 |
| Insoluble sulphur | Curing agent | 2 | |
| Vulcup | Curing agent | | 7 |
| TAIC DLC | Curing coagent | | 3 |
| Silane 174 DLC | Silica coupling agent | | 1 |
| Hi-Sil 190 | Reinforcing filler | | 50 |
| Stearic acid | Activator | 1.2 | 1 |
| Zinc oxide | Activator | 5 | |
| Accelerator CZ | Accelerator | 1 | |
| Accelerator NS | Accelerator | 0.5 | |
| N-phenyl-1-naphthylamine | Antioxidant | 1.8 | |
| TMQ / Antioxidant RD | Antioxidant | 2 | |
| IPPD / 4010 NA | Antioxidant | 2 | |
| NAUGARD 500 | Antioxidant | | 2 |
| ZF10 paraffin | Mold release agent | 1.8 | |



(a)                                          (b)

**Fig. 6.5:** Bonded rubber seals: **(a)** the unfilled natural rubber; **(b)** the silica-filled EPDM rubber.

## 6.4 Cure Rheology Characterisation of the Bonded Seal Materials

To generate an accurate material model for FEA, it is essential that the mechanical properties of coupons that are used in characterisation tests be representative of those in the bonded seals. Although well-known in industrial settings, this issue is often not discussed in academic literature (for instance, in the studies of Table 3.1), and not taking it into account can lead to inconsistent mechanical properties that result in undesirable variations in performance. Hence, further discussion is warranted here.

Fig. 6.6a shows a rheometer curve for the NR compound. It was cured at 165℃ and exhibited reversion. That is, the torque during curing reached a local maximum where the mechanical properties were optimal. This phenomenon is a consequence of the instability of sulphur crosslinks and is common in sulphur cured compounds. An ideal manufacturing process achieves a state-of-cure that is at or near the local maximum. For rubber components with small cross-sections, which is the case in this work, it is not difficult to achieve a cure near this maximum by imposing a cure time and temperature that closely follow the rheometer curve, but it will be seen that some adjustments may be required.

Fig. 6.6b shows the rheometer curve for the EPDM compound at 160℃, a temperature that was recommended based on the experience of the manufacturer. The peak torque was much higher than that in the NR compound due to the silica filler, and a marching cure occurred. The illustrated timescale is short, so it is possible that the curve would stabilise over longer times. Reversion is unlikely in this compound since the curing temperature was not aggressive for EPDM and the material was peroxide cured.



**(a)**                                    **(b)**
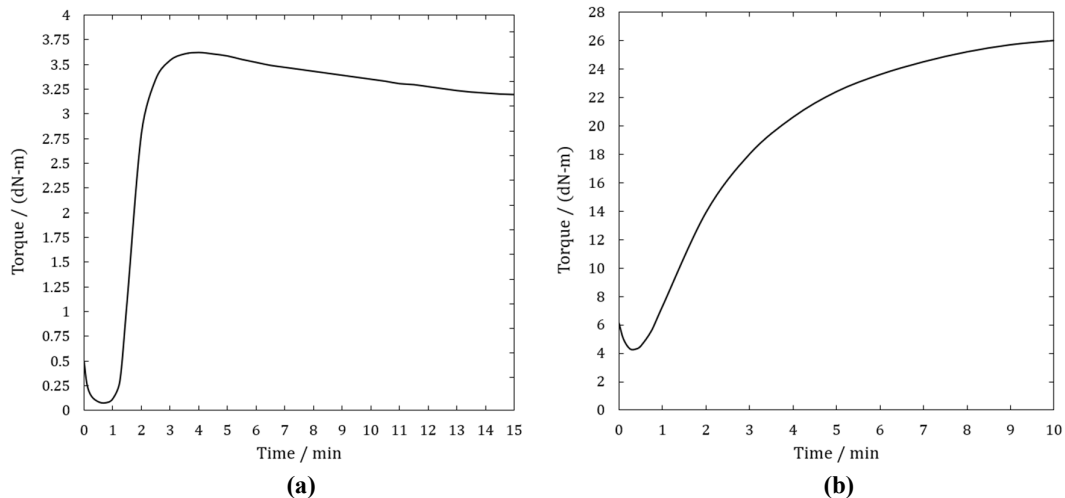
**Fig. 6.6:** Rheometer curves for: **(a)** the unfilled natural rubber; **(b)** the filled EPDM rubber.

After manufacturing first articles with NR and EPDM, JST used DSC to verify that the state-of-cure in the seals was sufficient. Fig. 6.7a shows three heat flow curves for NR with a temperature ramp of 10℃/min up to 300℃. The curing reaction occurred over a temperature range of 150-240℃, and the heat, captured in the area under the reaction curve,

was 14.0 J/gm. To assess the state-of-cure of the bonded seals, a small sample was cut from the centre of their cross-sections. The NR seal was initially cured at 165℃ for 5 min which, based on Fig. 6.6a, was expected to put it into a region with slight reversion. However, the heat of reaction was 3.1 J/gm (78% cured) as indicated by the blue curve in Fig. 6.7a. Such discrepancy between a rheometer test and a physical part are common in manufacturing due to the complex thermal history encountered in real components during curing. This is why it is a good practice to verify the state-of-cure in manufactured components. To achieve an acceptable level of cure, the time was increased to 15 min and the temperature was decreased to 160℃ to mitigate reversion. This resulted in a reaction heat of 0.9 J/gm, or 94% cured which is an acceptable limit for practical purposes.

The curing condition for the EPDM seals was 160℃ for 25 min with a post-cure (that is, after removal from the mold) of 180℃ for 1 hr. This latter stage is common with peroxide cured compounds and mitigates the effects of marching cure. Fig. 6.7b shows that the bonded seal was 100% cured by this process.
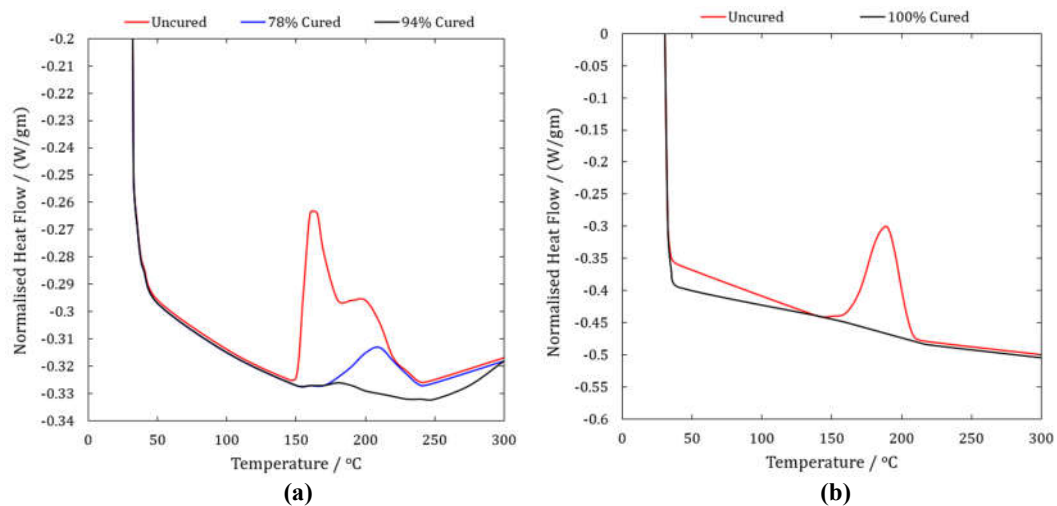


**Fig. 6.7:** Normalised heat flow during a temperature sweep with DSC using a ramp of 10℃/min:
**(a)** the unfilled NR compound; **(b)** the filled EPDM compound.

## 6.5  Mechanical Characterisation of the Bonded Seal Materials

First cycle stress-strain responses were measured for both rubber materials. Little material was available for this exercise due to high consumption when building first articles and verifying sufficient cure, so priority was given to planar tension testing which was the most critical loading mode in the test fixture (for evidence, refer to the biaxiality analysis in Section 5.4.7). Uniaxial compression was also important for the application, so a compression test was done for each material. Fig. 6.8 shows the stress-strain responses with a strain rate of 1%/s.
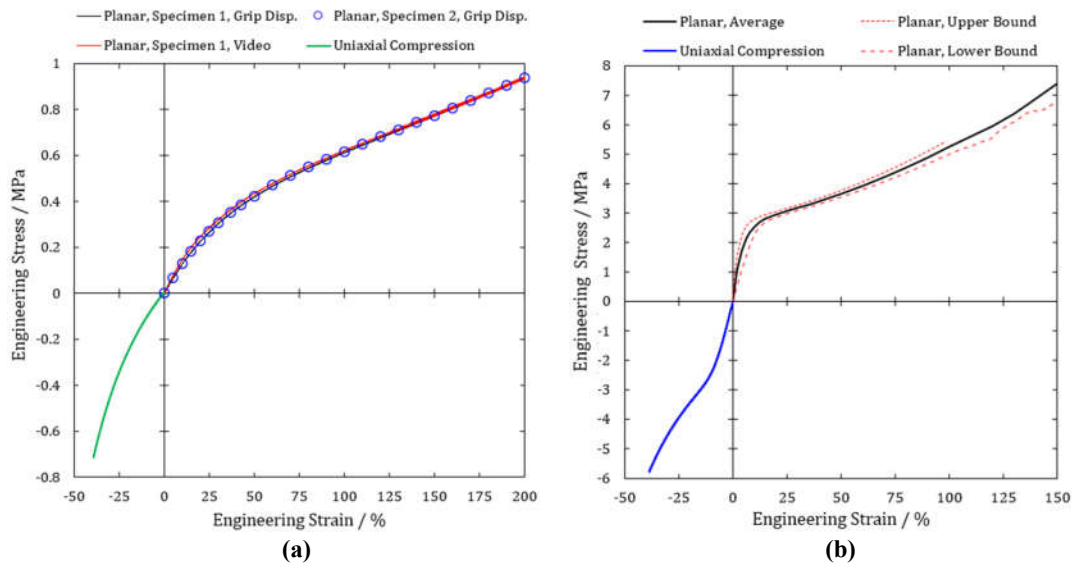
**Fig. 6.8:** Stress-strain responses for planar tension and uniaxial compression loading modes with a strain rate of 1%/s: **(a)** the unfilled NR compound; **(b)** the filled EPDM compound.

Only two samples could be prepared for planar testing of NR. The grip design is shown in Fig. 6.9. To assess the possibility of anisotropy, the samples were cut in two different directions. The first specimen was nominally 150 mm × 2 mm with a gauge height of 15 mm whereas the second was shorter at 120 mm × 2 mm with a gauge height of 12 mm. After clamping in the grips and removing slack due to compression, the actual gauge heights increased slightly to 17.22 mm and 14.35 mm, respectively. To control the clamping force, a bolt torque of 2 N·mm was found sufficient to prevent slippage of the specimen without introducing premature fracture. A video extensometer was used to compute strain in the taller specimen, but it was not able to resolve strain in the shorter specimen. As shown in Fig. 6.8a, this was not a problem because the stress-strain curves generated from the video extensometer matched well with those generated from grip displacement. The stress-strain trends from the two different tensile specimens were nearly indistinguishable, so repeatability was good. In-plane anisotropy was negligible which is not surprising for an unfilled NR compound. Only one uniaxial compression test was conducted, and since the mode was less critical, it was given a smaller bias when generating a hyperelastic material model in the next section. The compression button was 12.5 mm in height and 28 mm in diameter.

Fig. 6.8b shows planar tension and uniaxial compression data for the EPDM compound. One planar curve is computed as the average of upper and lower bounds from three test specimens. The upper bound fractured at a fairly low strain due to the grip constraint. The trend for the lower bound became noisy above 100% strain due to slippage of the specimen. Two 150 mm wide and one 120 mm wide sample were tested with a bolt torque of 4 N·mm. The narrow specimen was cut in a direction transverse to the other two, and it defines the lower bound in Fig. 6.8b. The figure indicates that some anisotropy may have been in the

plaque, though experimental variation cannot be ruled out. As expected, the stiffness of the filled EPDM compound was much higher than that of the NR compound. It also exhibited an inflection in the uniaxial compression data that is common in filled rubber compounds.[261] Presumably, this was due to breakdown of the filler network as the rubber deformed.
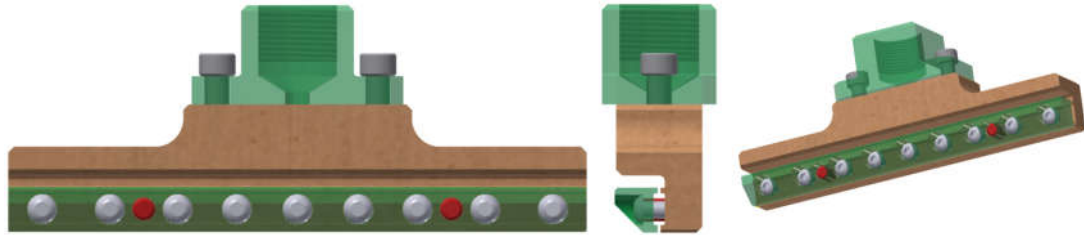


**Fig. 6.9:** Planar tension grip.

In Chapter 7, inelastic effects in the bonded rubber seals are discussed, so some characterisation of these behaviours was necessary. Fig. 6.10a shows a stress-strain curve for the EPDM material after stretching a planar specimen to 10% strain at a rate of 1%/s, holding at a fixed displacement for 1 hr, stretching to 100%, and then holding fixed for another hour. At both hold positions, stress relaxation occurred. When stretching from 10% to 100%, the stress rapidly recovered to track the virgin stress-strain path as if the relaxation step had never occurred. This phenomenon is commonly referred to as the Mullins effect.[106,136] Fig. 6.10b shows stress, normalised by the peak stress at the beginning of each hold period, as a function of time. The relative relaxation with 10% strain was greater than that with 100% strain, a common observation in engineering rubbers even in the absence of any Mullins effect.[262]

The stress at any strain for EPDM in Fig. 6.10a is lower than that at any respective strain in Fig. 6.8b. The difference arises from batch variation or something else uncontrolled during the manufacturing process, not test variability or inelastic effects. The batches were manufactured about 12 months apart, and the latter (which was used for manufacturing bonded seals) clearly picked up carbon black from the mixer. It is also possible that the silane coupling reaction was inadequate in the first batch. Either of these could contribute to the stiffer response in the second batch. Nevertheless, the normalised relaxation curves of the softer batch are deemed suitable for arguments that are developed later in this work.

Fig 6.11 shows normalised stress relaxation in the NR compound when held in planar tension with 10% strain. The relaxation was 5% after 15 min which was much lower than that in the EPDM (>30% at the same time), a consequence of the former being an unfilled rubber. Further comment on inelastic behaviours is deferred to Chapter 7.

141
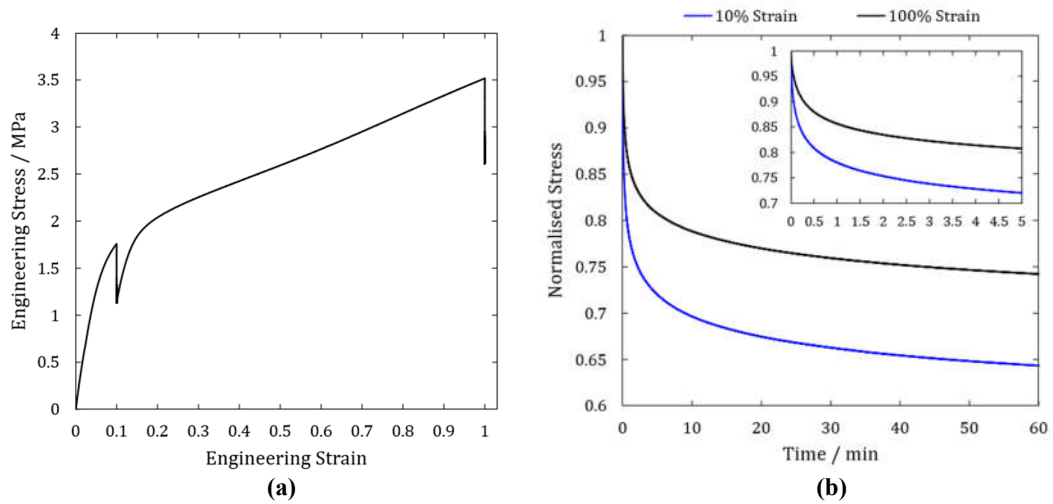
**Fig 6.10:** Stress relaxation in the EPDM compound: **(a)** with 1 hr holds at $\varepsilon = 10\%$ and $\varepsilon = 100\%$ and a Mullins effect present between the displacements; **(b)** normalised by the peak stress at the beginning of each hold period. The inset magnifies the response during the first 5 min.
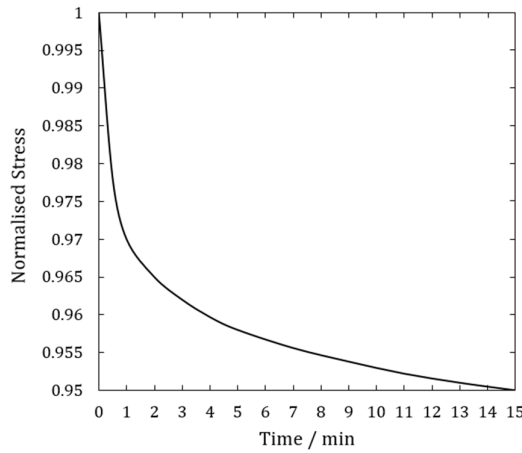


**Fig. 6.11:** Stress relaxation in the NR compound with $\varepsilon = 10\%$.

## 6.6 Hyperelastic Material Models for the Bonded Seal Materials

Fig. 6.12 shows gen-Yeoh SEF curve fits to the stress-strain data from Fig. 6.8. The fits were determined by inspection. The NR material was simple to fit, but the EPDM was more challenging because it exhibited a rapid reduction in modulus at tensile strains below 25%. As described in Section 4.2, this phenomenon is typical for highly filled rubbers, is difficult to model, and was the motivation for development of the gen-Yeoh SEF. In a recent paper by Robertson & Hardman,[263] this characteristic feature is attributed to the Payne effect[125] which is a consequence of the breakdown of polymer-filler or filler-filler interactions as deformation increases. The authors also discussed the well-known upturn in modulus, often attributed to finite chain extensibility, which began around $\varepsilon = 0.5$ in the EPDM compound. The NR compound did not exhibit this upturn until tensile strains above 200% which were beyond the region of interest for the problem.

142
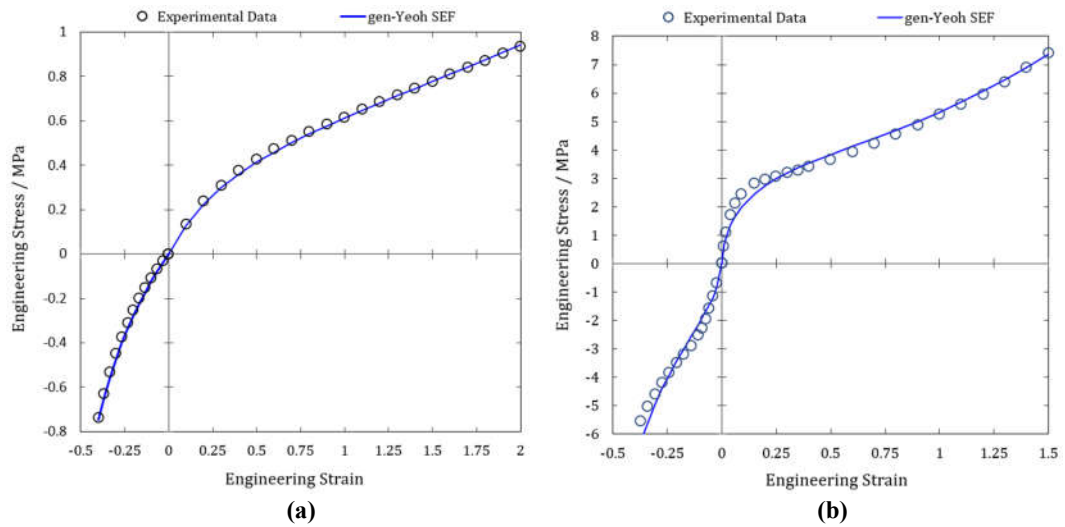
**Fig. 6.12:** gen-Yeoh hyperelastic material models fit to stress-strain data from Fig. 6.8: **(a)** the unfilled NR compound with $(K_1, K_2, K_3) = (0.19, -0.02, 0.005)$ MPa and $(m, p, q) = (1, 1.5, 1.85)$; **(b)** the filled EPDM compound with $(K_1, K_2, K_3) = (1.8, 0, 0.06)$ MPa and $(m, p, q) = (0.77, 0, 2)$. Positive strain is planar tension and negative strain is uniaxial compression.

Table 6.3 shows relative errors of the fits in each loading mode for each material using Eq. 4.5. The composite error of the NR in planar tension is 1.5% which is well within material and experimental variation. The 10% error for NR in uniaxial compression is deceptively large because it is skewed by a few points at the lowest strains where there was large uncertainty in measurements. High relative errors at low strains are common and have been observed by other authors,[264] but they are of little consequence for the current problem since strains at leakage will be shown to be much larger than those at the low strains where uncertainty is high. As discussed in Chapter 5, curve fits should be biased to the dominant loading mode in an application, and it has been established that planar tension is the most important mode in the bonded seal. This bias is evident in the NR composite errors. The bias in EPDM is smaller because it was not possible to improve the fit in planar tension without creating a physically unrealistic material model. Specifically, to capture the rapid reduction in modulus at low strains, the first exponent, $m$, in the gen-Yeoh SEF had to be less than one, but it could not be reduced to an arbitrarily low value without violating the condition of $\sigma_{et} > \sigma_{pt} > \sigma_{ut}$ at any particular strain.*** Fig. 6.13b shows that for the parameter choices in Fig. 6.12b, the planar and equibiaxial curves nearly intersect. Fig. 6.13a shows this was not a problem with the NR compound. For further discussion on parameter restrictions with the gen-Yeoh SEF, refer to Section 4.2 and a recent work by Heczko *et al.*[265] The latter authors show that the gen-Yeoh SEF is unstable with $m < 0.5$.

---

*** To be precise, this ordering must only be satisfied with respect to true stresses, not nominal stresses.

**Table 6.3:** Relative errors of the curve fits in Fig. 6.12.

| Material | Loading Mode | $e_R$ / % |
|---|---|---|
| NR | Planar tension | 1.5 |
| | Uniaxial compression | 10 |
| EPDM | Planar tension | 6.1 |
| | Uniaxial compression | 9.4 |
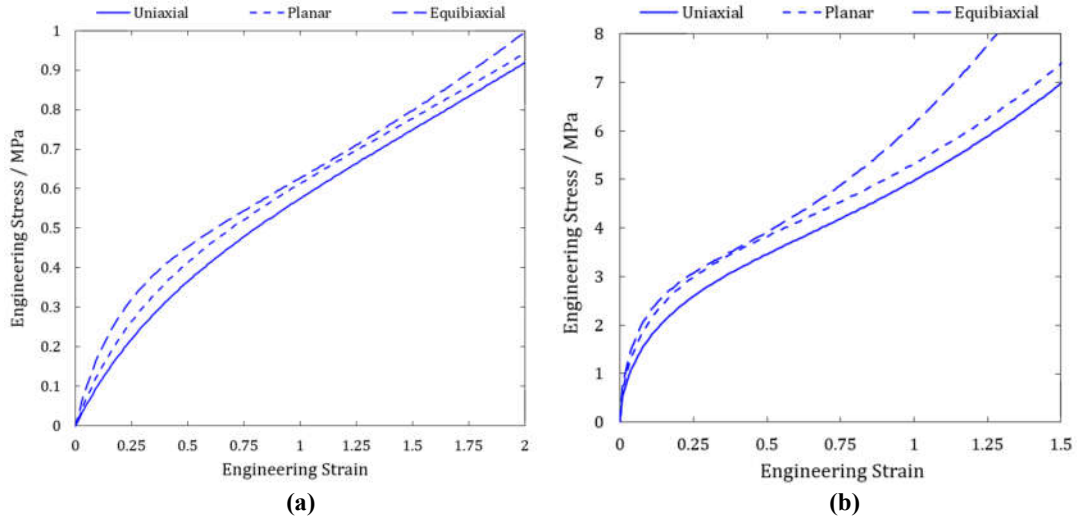


**Fig. 6.13:** Hyperelastic material models with the gen-Yeoh SEF in different tensile loading modes for: **(a)** the unfilled NR compound; **(b)** the filled EPDM compound in which the planar and equibiaxial loading modes nearly intersect.

## 6.7 Validation of the Hyperelastic Material Models

The hyperelastic material models were validated by axially compressing bonded seals to 50% average strain (based on the nominal seal height) at a rate of 1%/s in a uniaxial test machine. WD-40 was used as a lubricant. Both NR and EPDM readily absorb hydrocarbons and soften, so compression was started immediately after applying the lubricant. The tests lasted about 1 minute. Using a swell prediction calculator that was developed by the project sponsor,[266] the maximum dimensional change in the EPDM rubber, a material known for high swelling potential,[179] was calculated to be about 0.063 mm which is 0.5% of the nominal cross-sectional dimensions of the rubber. This is a worst-case scenario because it assumes the rubber is fully immersed in a solvent which was not the case in these tests.

Fig. 6.14a shows experimental compression of the NR seal, and Fig. 6.14b shows the corresponding deformation in FEA using the model parameters from Fig. 6.12a and the contact pressure-dependent friction model from Fig. 5.9. Volumetric compressibility was included in the FE model with a compressibility parameter of $D_1 = 0.006002$ MPa$^{-1}$ which assumed $\nu = 0.4995$. The Poisson's ratio corresponds to $\kappa{:}\,G = 1000$, a reasonable assignment for unfilled NR.[50] The shear modulus (required per Eq. 4.9) was estimated from the initial slope of the UT curve in Fig. 6.13a through the relation $G = E/3 \approx 0.33$ MPa. Two deformed distances of 90.6 mm and 5.33 mm are shown in Fig. 6.14b, and the

corresponding values based on pixels from the photo in Fig. 6.14a are 90.2 mm and 5.21 mm giving differences of 0.4% and 2.3%, respectively. Therefore, experimental and FE correlations based on deformation of the NR seal are excellent. For safety reasons related to large compression loads, a clear photo of the EPDM seal was not possible because this would have required opening the test chamber. Nevertheless, it is noted that the EPDM was visually observed through sight glass and the deformations appeared similar to the NR seal.



**(a)**                 **(b)**
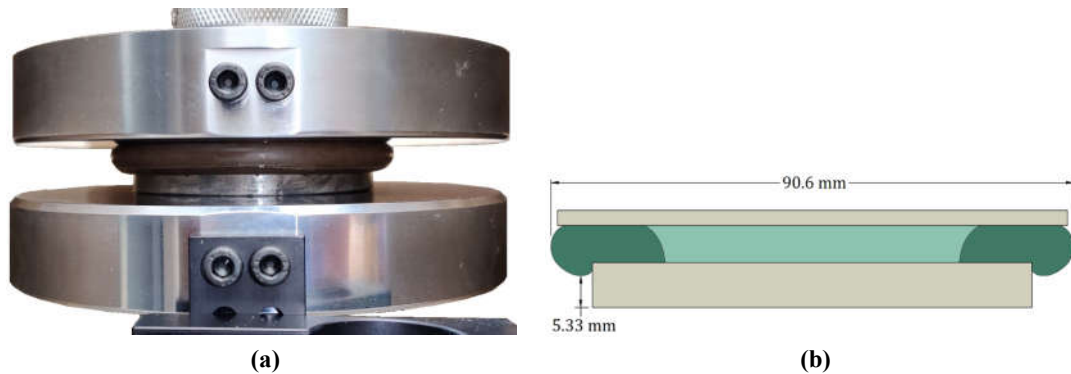
**Fig. 6.14:** A bonded NR seal compressed to $\varepsilon = 0.5$: **(a)** experimental test; **(b)** FE solution.

As further model validation, force-displacement data were analysed for both materials. Fig. 6.15a shows the results for NR with displacement converted to an average axial strain based on the height of the rubber seal. Two experimental data sets are shown. "Data, Run 1" is for a new NR bonded seal, and "Data, Run 2" is for a seal that had been previously compressed 15% and tested to full leakage with a gauge ring height of 6.35 mm. Both trends agree well down to -30% strain and then deviate. From -30% to -50% strain, the force magnitudes are the opposite of expectation because, presumably, the previously tested seal would have undergone stress softening if any were present, which would yield lower forces than the seal that was not previously tested. However, repeated compression cycles on both seals gave results that were bound by the two experimental trends in Fig. 6.15a.

To investigate the unexpected variation in experimental force magnitudes below -30% strain, friction sensitivity studies were conducted with FEA. Referring again to Fig. 6.15a for NR, "FEA, CoF = Baseline" corresponds to the result using the friction model in Fig. 5.9. The other FE results scale the baseline friction model by multiplying all the CoFs by the factor indicated in the legend. The following observations and conclusions are made:

- The baseline FE curve matches the experimental data well down to -37% strain.

- From -37% to -50% strain, the baseline FE curve qualitatively matches the experimental trends. There is a softening behaviour, but the FE trend exaggerates the rate of this effect.

- All the friction models predict a similar force-strain response down to -30% strain. This gives confidence that the hyperelastic model was accurate at least to this strain.

- The force-strain trends are very sensitive to the friction model over a narrow range of CoF scaling factors from 1X-1.2X (refer to the caption of Fig. 5.30 for an

145

explanation of how contact pressure-dependent CoFs were scaled). In addition, the curve with a 1.2X multiplier shows a non-smooth force peak and a rapid diminution around $\varepsilon = $ -0.4. In the FE model, this transition corresponds to a point at which the seal suddenly and rapidly slid in the radial direction, suggesting an instability in the system that was sensitive to the friction model. This instability could also be visually detected during experimental compression of the NR seals. They compressed smoothly in the vertical direction, and then they transitioned to significantly increase their rate of movement in the radial direction beyond -30% strain.

- With sufficiently high friction, the force peak is not observed, and rapid movements in the radial direction do not occur. Moreover, CoF multipliers in the broad range of 2X-5X only slightly change the force-strain curves.

In summary for the NR compound, the deformation and force-strain correlations give high confidence in the hyperelastic material model. They also suggest that inelastic effects such as relaxation and cyclic stress softening were negligible during testing. Deviations between the experimental and FE results at strains below -30% are attributed to a friction-dependent instability in the system.
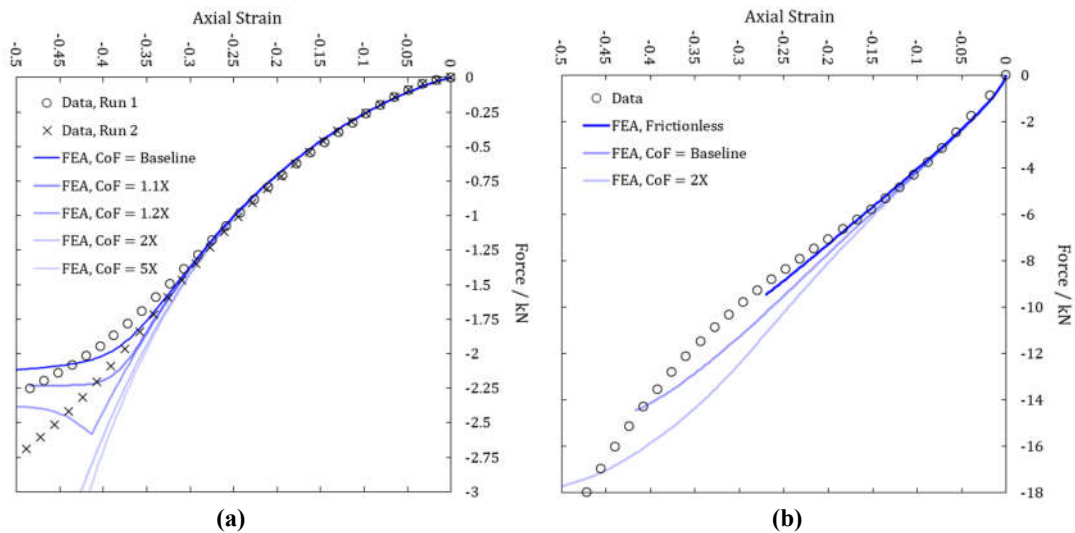


**Fig. 6.15:** Experimental and FE force-strain responses for bonded seals with:
**(a)** the unfilled NR compound; **(b)** the filled EPDM compound.

For the EPDM material, the compressibility parameter was $D_1 = 5.998 \cdot 10^{-4}$ MPa$^{-1}$ which corresponded to a Poisson's ratio of 0.4975, a value that has been found accurate for a variety of filled sealing materials used by the project sponsor. Similar to the NR case, the Poisson's ratio was converted to a $D_1$ parameter via the modulus of the UT stress-strain curve in Fig. 6.13b where $G = E/3 \approx 16.7$ MPa. As Fig. 6.15b shows, force-strain correlations for the EPDM compound are accurate down to -15% compression, but then both qualitative and quantitative problems arise. Below this limit, the "FEA, CoF = Baseline" trend overpredicts the force magnitude until a softening behaviour, which is not observed in the experimental data, brings it back into agreement at about -42% strain (at which point the simulation failed to converge). In an effort to eliminate the softening behaviour in the

FE model, the "FEA, CoF = 2X" curve doubled the friction coefficients but showed no sign of removing the effect. Furthermore, a frictionless case in FEA (which admittedly terminated prematurely due to problems with convergence) predicted a stiffer response than the experimental data. This suggests that the discrepancy between the data and FE results does not arise from frictional uncertainties.

A possible explanation for a less satisfactory correlation with the EPDM compound might be that the hyperelastic model was determined from a loading mode that was not dominant in the experimental test, or the range of strain for curve fitting was not properly chosen. However, Figs. 6.16 and 6.17 suggest these scenarios are unlikely. The green contour in Fig. 6.16 corresponds to planar tension, and the blue contour corresponds to equibiaxial tension, confirming that the most dominant loading modes were fit in Fig. 6.12b. In addition, the strain levels are mostly less than 100%, so the fitting range for strain was acceptable. It is also unlikely that strain rate sensitivity explains the correlation problems in Fig. 6.15b because on average it was 1%/s in the validation tests.

It is more likely that the lower correlation for the EPDM compound arose from non-ideal hyperelasticity. Recall from Chapter 2 that in ideal hyperelasticity, a compressive loading mode is equivalent to a tensile loading mode. For instance, the energy consumed during a uniaxial compression can be expressed as an equivalent equibiaxial tension. Although the dominant loading mode in the present study was planar, which is theoretically equivalent in tension and compression, it is possible that the experimental characterisation was "compression dominant" and did not map well onto the planar tension characterisation test. If this is true, it is almost certainly a consequence of the material being highly filled. For further evidence of this claim, refer to Appendix K which shows imperfect hyperelasticity for a filled HNBR material.

Another potential problem with the EPDM correlation is that only pure modes of deformation were used in material characterisation tests. As Ansarri-Benham *et al.*[264] pointed out, sometimes it is necessary to introduce non-pure deformations such as simple shear or torsion to accurately characterise the hyperelastic response of a rubbery material. Regardless, this subject is not explored further because the maximum error of $\approx 12\%$ at $\varepsilon = -0.3$ is not entirely unacceptable for a filled compound, especially one that is difficult to curve fit.
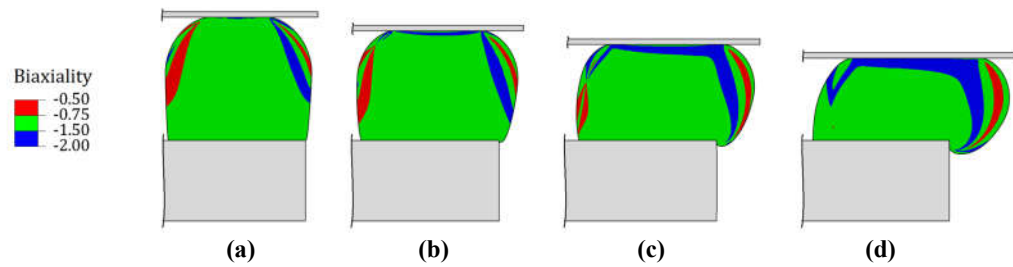
**Fig. 6.16:** Biaxiality using a compressible form of Eq. 2.21 (see Appendix D) in the EPDM bonded seal at different levels of compression: **(a)** 10% compression; **(b)** 20% compression; **(c)** 30% compression; **(d)** 40% compression.
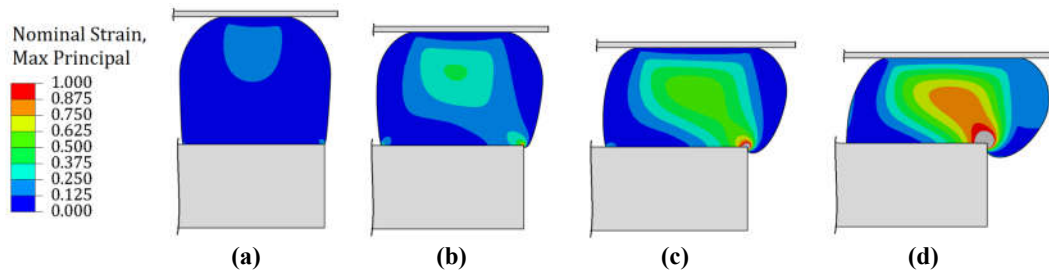


**Fig. 6.17:** Engineering strain in the EPDM bonded seal at different levels of compression: **(a)** 10% compression; **(b)** 20% compression; **(c)** 30% compression; **(d)** 40% compression.

## 6.8  Experimental Test Plan and Results for Elastic Leak of the Bonded Seals

The detailed test plan is given in Appendix L. Some important points to highlight are:

- Critical fixture and seal dimensions were measured prior to assembly.

- A hydrocarbon grease was used to lubricate sealing contact interfaces. Negligible absorption of the grease occurred as the time between assembly and full leakage ranged from 3-9 min for NR and 9-20 min for EPDM, with one outlier of 38 min for EPDM.

- The test fixture was maintained in an environment of $23 \pm 1°C$.

- Pressure was applied to the seals until leakage was detected via a plateau or drop in pressure. Before disassembly, the seals were pressured to leakage two more times to assess cyclic stress softening.

The test matrix and leak pressures for the seals are shown in Table 6.4. The extrusion gap, which is a function of the gauge ring height, is expressed as a percent of the nominal seal height. For instance, when no gauge ring was used, the extrusion gap was 100%. The compression is expressed as an average axial compressive strain based on the rubber seal height. For simplicity, the extrusion gaps and compressions are reported as nominal values, but values as tested are captured in Appendix L. Twenty seals of each material were made, but the table indicates that only 9 of each were tested with no repeats of any assembly condition. Therefore, the test matrix does not address statistical variation. This limitation is discussed later.

Fig. 6.18 shows leak pressures with identical assembly conditions (SNs 9 in Table 6.4) for the NR and EPDM seals and are representative of other conditions. The leak pressures

148

were an order of magnitude higher in the EPDM compound which is consistent with its modulus being an order of magnitude higher than the NR modulus. Three plateaus at 1.5 MPa in the NR compound indicated sustained leakage with the pump on. The material showed no signs of softening while leaking or with subsequent pressure cycles. The EPDM compound showed a softening behaviour when sustained leak occurred which is attributed to stress relaxation. The material also exhibited cyclic stress softening.

**Table 6.4:** Experimental test matrix and leak pressure results. "SN" indicates the serial number for the test. Each SN was pressured to full leakage three times without any disassembly between pressure cycles.

| Extrusion gap / % | Compression / % | NR leak pressure / MPa | | | | EPDM leak pressure / MPa | | | |
|---|---|---|---|---|---|---|---|---|---|
| | | SN | $P_1$ | $P_2$ | $P_3$ | SN | $P_1$ | $P_2$ | $P_3$ |
| 100 (no gauge ring) | 5 | 1 | 0.04 | 0.04 | 0.03 | 1 | 1.79 | 1.45 | 1.41 |
| | 10 | 2 | 0.12 | 0.12 | 0.12 | 2 | 1.92 | 1.74 | 1.69 |
| | 15 | 3 | 0.19 | 0.19 | 0.19 | 3 | 2.09 | 1.93 | 1.83 |
| 75 | 5 | 4 | 0.04 | 0.04 | 0.04 | 4 | 2.03 | 1.67 | 1.64 |
| | 10 | 5 | 0.22 | 0.22 | 0.22 | 5 | 2.50 | 2.25 | 2.20 |
| | 15 | 6 | 0.34 | 0.34 | 0.34 | 6 | 2.96 | 2.72 | 2.65 |
| 50 | 5 | 7 | 0.52 | 0.52 | 0.51 | 7 | 3.83 | 3.40 | 3.33 |
| | 10 | 8 | 0.84 | 0.84 | 0.82 | 8 | 5.98 | 5.31 | 5.03 |
| | 15 | 9 | 1.54 | 1.54 | 1.54 | 9 | 10.07 | 9.02 | 8.69 |
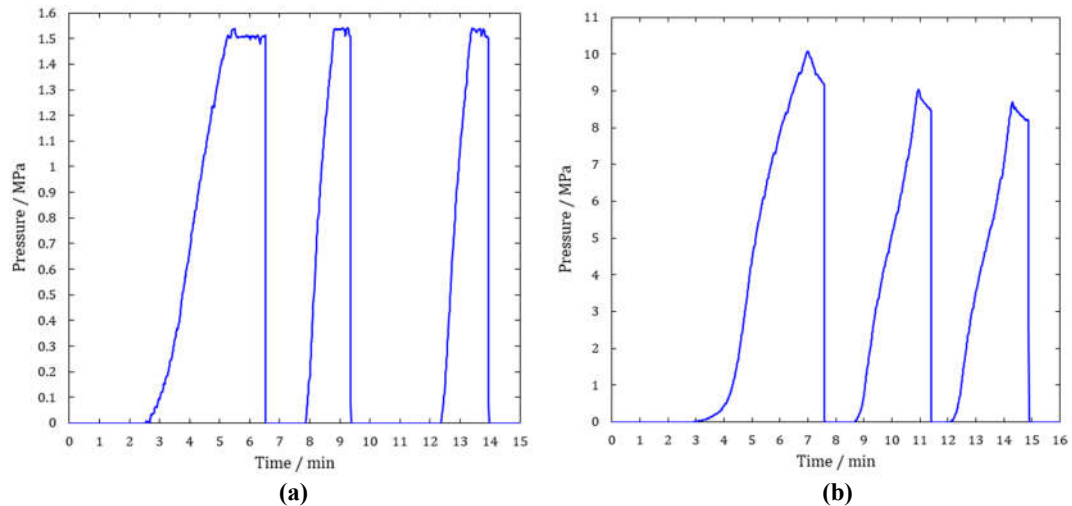


**Fig. 6.18:** Leak pressures with 15% compression and a 50% extrusion gap for:
**(a)** the unfilled NR compound; **(b)** the filled EPDM compound.

Fig. 6.19 plots the first-cycle leak pressures for both materials as a function of nominal compression with different nominal extrusion gaps. Refer to Appendix L for actual compressions and gaps. As expected, leak pressures increased with higher compressions and smaller extrusion gaps. In addition, two qualitative trends from Fig. 5.18 were observed. First, the extrusion gaps of 75% and 100% (which correspond to "$h_g$= 3.18 mm" and "No Gauge" in Chapter 5) had leak pressures that were linearly dependent on compression, whereas the extrusion gap of 50% (which corresponds to "$h_g$= 6.35 mm" in Fig. 5.18) predicted a non-linear dependence. Second, there was a much larger increase in

leak pressure when the extrusion gap was reduced from 75% to 50% as opposed to the change from 100% to 75%. These qualitative alignments somewhat mitigate the uncertainty of measuring only one data point per assembly condition. Exceptions are made for the two lowest pressures with the NR seal at $\varepsilon = 5\%$ because the transducer was not capable of accurately resolving them. The sensor resolution was 0.001 MPa with an accuracy of $\pm0.075$ MPa. For this reason, linear trends are not illustrated for the data sets. The trends in Fig. 6.19 are discussed further in the next chapter where they are compared to FE solutions.
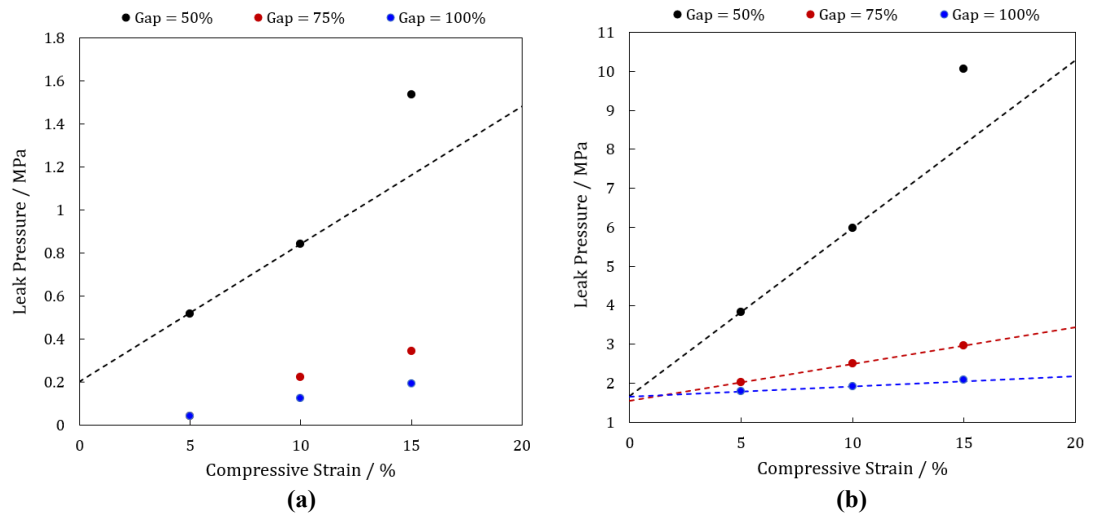


**Fig. 6.19:** Elastic leak pressures as a function of compression for different nominal extrusion gaps: **(a)** the unfilled NR compound; **(b)** the filled EPDM compound. The linear trends are fit to the data points at 5% and 10% compression to illustrate whether the point at 15% compression remains linear.

## 6.9 Summary

An experimental test fixture has been designed and tested with NR and EPDM bonded seals that had nominal heights of 12.7 mm. The seals were subjected to compression ratios within the range of 5-15% and nominal extrusion gaps within the range of 50-100%. This range for the extrusion gaps corresponds to a range of gauge ring heights from 6.35 mm to 0 mm, respectively.

Cure rheology characterisations of both materials was shown. The NR compound exhibited reversion which is common in sulphur cured rubber. DSC analysis gave confidence that the NR seals were suitably cured. The EPDM material exhibited a slight marching cure which is not uncommon for peroxide cured rubbers. A post-curing process was implemented to mitigate this effect. DSC analysis showed that the EPDM seals were sufficiently cured.

Both rubbers were characterised with planar tension and uniaxial compression tests, the two most critical loading modes according to biaxiality analyses. The unfilled NR compound exhibited minimal inelastic effects. The filled EPDM, being more typical of an industrial sealing material, had significant inelasticities. The hyperelastic characterisation

data were fit with the gen-Yeoh SEF. The fitting accuracy was excellent for the NR but less accurate although reasonable for the EPDM.

The hyperelastic material models were validated with compression tests of the bonded seals down to $\varepsilon$ = -50%. An FE model of the EPDM seal matched the experimental results well down to -15% compression, and the NR model fit well down to -30%. The former model probably deviated at a lower strain magnitude due to imperfect hyperelasticity. That is, the deformation mode during the validation exercise did not match well with that of the characterisation tests. The deviations of the NR seals at larger strain magnitudes were due to an elastic instability that was dependent on friction in the system.

The bonded seals were pressure tested, and experimental leak pressures were measured from 0.1-10 MPa. The EPDM seals had significantly higher leak pressures than the NR seals due to their stiffer stress-strain response. Significant inelasticities were observed in the EPDM tests but not in the NR tests. Only one test per assembly condition (that is, compression level and extrusion gap) was conducted, but based on expectations from Chapter 5, the experimental trends appear reliable. Thus, qualitative agreement between the numerical and experimental leak studies is established. The next order of business is to determine if quantitative agreement can also be made. To this end, Chapter 7 uses FPP modelling in Abaqus to predict leak pressures based on the rubber materials and physical measurements that are reported in this chapter and Appendix L.

# 7. Correlation of Experimental & Numerically Simulated Leak Pressures

## 7.1 Overview

This chapter applies lessons learned from the FPP simulations in Chapter 5 to numerically predict leak pressures for the experimental test conditions in Chapter 6. The simulated pressures are 10% to 55% higher than the test pressures. At low leak pressures with the NR material, the error is attributed to inaccuracies in the pressure transducers. With the EPDM seals, some of the error may arise from strain rate sensitivity. However, the large errors are not generally explained by these effects or any of the following: the friction model; volumetric compressibility; numerical discretisation; stress relaxation; the Mullin's effect; dynamic effects; deformation of the test fixture; asymmetries in the test configuration; and inhomogeneity of the rubber materials. The primary source of error appears to arise from the leak criterion itself, and this claim is supported by applying two different leak criteria that result in simulated leak pressures bounding experimental pressures.

## 7.2 The FE Models

All simulations in this chapter are built upon work in Chapters 5 and 6 as follows:

- The seal geometry was exactly as shown in Fig. 5.1, but the compression ratios and extrusion gaps were adjusted to match the precise conditions that were tested based on the measurements in Appendix L. This approximation eliminated the labourious exercise of partitioning the seal for trivial changes in its geometry while preserving the more critical features of compression ratio and extrusion gap.

- The hyperelastic material models from Fig. 6.12 were used with compressibility parameters as described in Section 6.7. Inelasticities were not simulated unless otherwise stated.

- The load steps and contact controls in Sections 5.4.1 and 5.4.2 were used.

- The contact pressure-dependent friction model from Fig. 5.9 was used since it had reasonable accuracy for the validation exercises in Section 6.7.

- Unless otherwise specified, pressure penetration was simulated with the DLOAD subroutine in Abaqus/Standard as described in Section 5.6.2. This ensured that contact closures were simulated. It also gave results that were better aligned with Abaqus' native R2017 FPP scheme which was demonstrated in Section 5.5 to be less sensitive to mesh sizing than the R2018 scheme.

- The metal components were simulated as rigid bodies. This will be justified based on the FE analysis of the test fixture in Section 6.2 and arguments in Section 7.4.4.

- Unless otherwise stated, the mesh from Fig. 5.26 which has a 0.03 mm mesh size along the sealing interface was used. Hence, simulated leak pressures were probably a few percent higher than a 1% mesh-converged solution.

## 7.3 Comparison of Experimental and FE Leak Pressures

Fig. 7.1 plots peak experimental (● symbols) and simulated (× symbols) leak pressures for both rubber materials during their first pressure cycle. The percentage differences for different test conditions are indicated next to the simulated pressures.
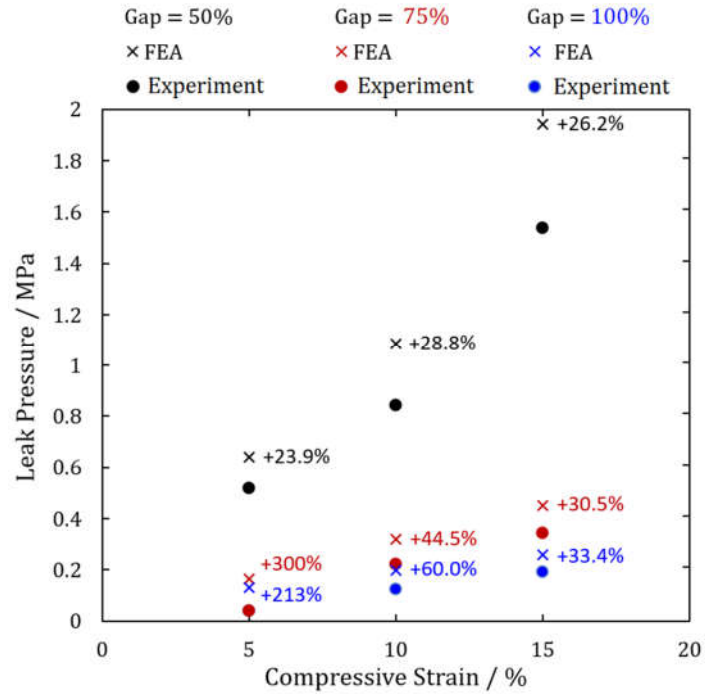


**(a)**
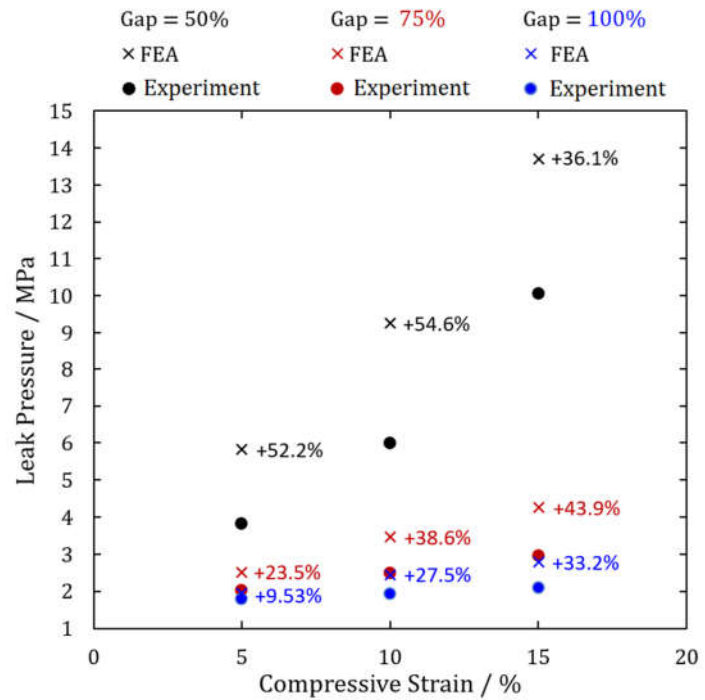


**(b)**

**Fig. 7.1:** Comparison of experimental and FE leak pressures for the bonded seals with: **(a)** the unfilled NR compound; **(b)** the filled EPDM compound. "Gap" refers to the nominal extrusion gap.

The accuracy of the pressure transducer for all tests was $\pm 0.075$ MPa and significant for some conditions. Table 7.1 summarises the maximum potential errors that may be attributed to the accuracy of the pressure transducer.

**Table 7.1:** Maximum potential errors for the first cycle leak pressures ($P_1$) due to the accuracy of the pressure transducer.

| Extrusion gap / % | Compression / % | NR pressure error / % | | EPDM pressure error / % | |
|---|---|---|---|---|---|
| | | SN | $P_1$ | SN | $P_1$ |
| 100 (no gauge ring) | 5 | 1 | 190 | 1 | 4.2 |
| | 10 | 2 | 65 | 2 | 3.9 |
| | 15 | 3 | 39 | 3 | 3.6 |
| 75 | 5 | 4 | 190 | 4 | 3.7 |
| | 10 | 5 | 34 | 5 | 3.0 |
| | 15 | 6 | 22 | 6 | 2.5 |
| 50 | 5 | 7 | 14 | 7 | 2.0 |
| | 10 | 8 | 8.9 | 8 | 1.3 |
| | 15 | 9 | 4.9 | 9 | 0.7 |

Based on the table and figures, the following observations are made:

- All simulated leak pressures are significantly higher than experimental pressures.

- The simulated leak pressures follow qualitative trends from Chapters 5 and 6. With extrusion gaps of 75% and 100%, leak pressure increases linearly with respect to the compression ratio. However, for an extrusion gap of 50%, leak pressure increases non-linearly with the seal compression.

- Comparing Table 7.1 and Fig. 7.1a, it is evident that the transducer accuracy introduces large uncertainties in the NR seal leak pressures for all cases when the extrusion gap is 75% and 100%. Potential errors due to the transducer diminish as leak pressures increase.

- For NR seals, the measurement error due to the transducer is much lower with extrusion gaps of 50% and cannot fully explain the systematically higher simulation pressures.

- Potential errors due the transducer are less than 5% for every EPDM seal and cannot explain the large differences between experimental and simulated leak pressures.

- In the EPDM tests, the percent differences between experimental and simulated leak pressures increase as the compression ratios increase and the extrusion gaps decrease. That is, the simulation errors increase as experimental leak pressures increase. An exception occurs with $\varepsilon = 15\%$ and an extrusion gap of 50%. This latter case would not converge with the implicit solver, so the VDLOAD subroutine from Section 5.6.3 was used in Abaqus/Explicit. As previously explained, the explicit solver handles contact differently, resulting in lower leak pressures. Inertia effects can also disrupt the sealing front in the explicit solver and pull nodes out of contact sooner than the implicit solver. See Appendix R for an illustration of this.

- Qualitative trends for the NR seals with an extrusion gap of 50% are similar to those with the EPDM seals. Presumably, the alignment occurs because the measurement errors do not significantly affect the NR seals at higher pressures. As with the EPDM seal, the VDLOAD subroutine was required to achieve convergence at the highest level of compression.

Overall, the results in Fig. 7.1 indicate that something is systematically and significantly incorrect with the simulated leak pressures, and it is for this reason that test repeats have not yet been conducted. That is, experimental uncertainty and statistical variation appear unlikely to reconcile the experimental and simulated results, so additional seals are being preserved for future testing. The sections that follow explore possible sources for the large discrepancies.

## 7.4  On Some Sources of Error in the Simulated Leak Pressures

### 7.4.1  Friction, Volumetric Compressibility, and the FE Mesh

Model sensitivities to friction and volumetric compressibility were assessed in Section 5.7. It was shown that reducing friction by a factor of two had almost no effect on leak pressures. In fact, the CoFs for rubber at high contact pressures in a lubricated condition approach the frictionless limit, so frictional uncertainty is not significant in the cases considered. What is particularly telling is considering the EPDM seal with 5% compression and an extrusion gap of 50%. The numerical result is 52.2% larger than the experimental results, yet the friction sensitivity study in Fig. 5.32b only shows 2.5% variation due to frictional sensitivity. Clearly this cannot explain the error.

Turning to compressibility and assuming a practical range of 0.495-0.4995 for Poisson's ratio, Fig. 5.32 suggests uncertainties lie in a range of $\pm 5\%$. In reality, the potential errors due to compressibility are lower. It is well established that unfilled NR has approximately $\nu = 0.4995$, and data from the project sponsor supports the value of 0.4975 that is used for the filled EPDM. Consequently, uncertainties in the volumetric compressibility cannot explain the large discrepancies in Fig. 7.1.

The FE mesh chosen for this chapter resulted in leak pressures that were not mesh-independent within 1%, and results were biased high. The comprehensive studies in Section 5.5 suggest that the mesh error was in the range of 2-6% which is also not adequate to explain the large overpredictions in this chapter.

### 7.4.2  Inelastic Effects

During the experimental tests for NR seals, the average time between seal compression and full leakage was 7 minutes. Fig. 6.11 shows that the maximum stress relaxation during this time span is 4.5%. Simulations were conducted with $K_i$ material model parameters relaxed by this amount, and the leak pressures scaled down in almost exact proportion with the moduli. In reality, full stress relaxation was not present when the seals leaked. Some recovery occurred during pressure application due to the Mullins effect, and the material tracked a virgin stress-strain path once strains became sufficiently large. Fig. 6.18a also provides strong evidence that stress relaxation was insignificant in the NR seals because

155

there was no appreciable change in the sustained leak pressure over the ≈1.5 minute time interval during the first cycle. Cyclic stress softening is also not observed in the figure. Therefore, it is improbable that inelasticities explain the large discrepancies in Fig. 7.1a. (Note: the potential for inaccuracies due to strain rate sensitivity is discussed later.)

Inelasticities must be considered in the EPDM seals. Neglecting one outlier, the average time between seal compression and leakage was 14 minutes during experimental testing. Over this time interval, Fig. 6.10b suggests that the worst-case seal relaxation is about 30%. Scaling the $K_i$ moduli in simulations again found that leak pressures decreased in almost exact proportion to the model parameters. Yet, even this worst-case relaxation cannot explain the magnitude of discrepancies in Fig. 7.1b. In addition, Fig. 6.10a shows that the relaxed EPDM material rapidly recovers to a virgin stress-strain path when larger strains occur, so some of the relaxation after compression in the experimental tests may have been recovered as the seal was pressurised.

Because the EPDM material showed significant inelasticity, an analysis of experimental strain rates is necessary. The strain rates could not be measured directly, but they could be approximated from FE results and experimental times. For instance, the average strain rate ranged from 0.1-0.9%/s when the seal was pressurised with $\varepsilon = 15\%$ and an extrusion gap of 50%. This was determined by sampling the maximum principal strains at the locations highlighted in Fig. 7.2 at times beginning near the point of full compression and ending near the point of leakage. The difference in strains at the time points was divided by the experimentally measured time between compression and leakage to estimate the strain rate. The average strain rate for all points in Fig. 7.2 was 0.3%/s. Strains in the lower right region of the seal were not considered because deformations there were small. Strain rates with the other test conditions and materials were similar to those illustrated here. Importantly, the average experimental strain rates were about one-third of those in the material characterisation tests. This is of little consequence for the NR material where inelastic effects are small, but the same cannot be said for the EPDM seals.
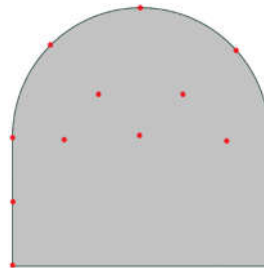


Fig. 7.2: Sampling locations for average strain rates during pressure application.

Although the Mullins effect mitigated the complication of stress relaxation due to pre-compression, the EPDM seals almost certainly exhibited a softer response than that in Fig. 6.8b due to a lower average strain rate. Unfortunately, only one strain rate was characterised

due to limited material for testing, but the order of the error can be established with data from another Shore A 80D commercially sensitive sealing material that was provided by the financial sponsor. Fig. 7.3 shows stress-strain curves for the material with strain rates of 1%/s and 15%/s, more than an order of magnitude different. The curves are normalised by the peak stress at the faster rate. The difference between the curves varies between 20-25% for strains above 25%. Since the average experimental strain rates were less than an order of magnitude different from the characterisation strain rates, it is reasonable to expect the order of the model error due to excessive stiffness to be within 25%. Referring to Fig. 7.1b, this is not sufficient to explain discrepancies in the experimental and simulated leak pressures.
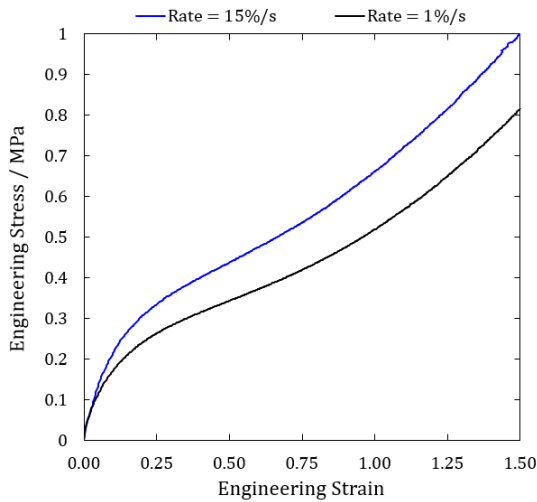


**Fig. 7.3:** Typical strain rate sensitivity for an 80 durometer (Shore A) sealing material.

It is tempting to suggest that the simulated errors arise from a combination of stress relaxation and the low experimental strain rate. Collectively, their sum gives an upper bound of 55% for the error which would bring the experimental and simulated pressures in good agreement for the two lower compression ratios with an extrusion gap of 50%. However, the two effects cannot be additively summed because they are not mutually independent.[90] Specifically, stress relaxation and strain rate sensitivity in a filled rubber arise primarily from a single physical phenomenon: constraints on polymer chain mobilities due to interactions with the filler. When a deformed rubber is held at constant strain, this manifests as stress relaxation. When deformations are continuous but strain rates vary, it manifests as a vertical shift in the stress magnitude for a given strain. The leak pressures would be overcorrected if both effects were applied to the numerical simulations.

To summarise the arguments in this section, inelasticities in the NR are demonstrably small and cannot explain the larger discrepancies between experimental and simulated leak pressures. Inelastic effects certainly contribute to some of the discrepancies for EPDM seals. The effect of stress relaxation is deemed small due to recovery from the Mullins effect, but the lower strain rate in the experimental cases probably results in non-trivial

errors in the simulated leak pressures. However, an order of magnitude analysis suggests that, as a worst case, ≈25% of the simulation error can be explained by strain rate sensitivity. Yet, even this pessimistic assumption does not account for the observed discrepancies.

### 7.4.3 Dynamic Effects Due to Inertia and Mass Scaling

In Table 5.2, dynamic effects have a small impact on the crack pressure, reducing it from 14.04 MPa to 13.92 MPa which is -0.9%. Differences in the implicit and explicit solutions are more significant in this chapter. As mentioned, there is a general trend for the simulation errors to increase as the leak pressures increase, but the two highest pressures for each material deviate from this trend. This occurs because the explicit scheme was required to solve these load cases. The difference is particularly notable for the EPDM seal and not entirely surprising since the mass was scaled by $10^6$. This created elastic waves in the material that disrupted the sealing interface, pulling the node at the sealing front out of contact at a lower pressure than in the quasi-static simulation. Fig. 7.4 illustrates this phenomenon with mass scaled by $10^8$, a large factor that was chosen to amplify the elastic waves. Perhaps counterintuitively, the leak pressure (19.1 MPa) with this mass scaling is much higher than that in Fig. 7.1b even though the sealing front was disrupted by elastic waves. This occurred because the mass significantly impeded deformation into the extrusion gap, raising the leak pressure. Therefore, dynamic effects can raise or lower leak pressures. For the case at hand, a scaling factor of $10^8$ is clearly not physically realistic for the rates of pressure application in the experimental testing. The factor of $10^6$ used for one point in Fig. 7.1b was also not physically realistic, but Table 5.2 does give merit for its use. Reducing the factor to a lower magnitude would probably increase simulated leak pressures due to a more stable sealing front. Further studies on mass scaling are not pursued here because the simulation errors are too large to be attributed to this issue alone.



|     (a)     |     (b)     |     (c)     |     (d)     |
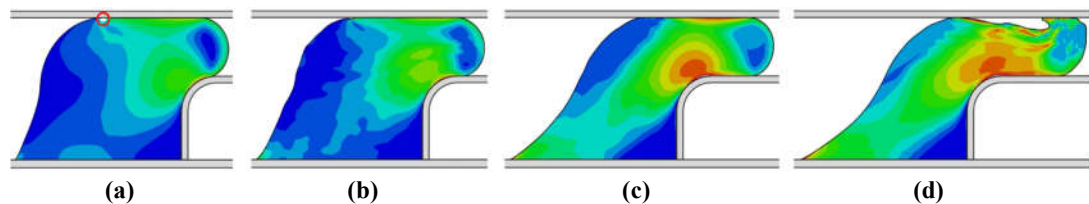
**Fig. 7.4:** Illustration of elastic waves in Abaqus/Explicit with mass scaled by a factor of $10^8$: **(a)** at 7.5 MPa, the nominal strain contours are smooth, but the sealing front is unstable as indicated by the void that is circled red; **(b)** at 8.1 MPa, strain contours become unstable, presumably due to an imbalance between the forces from friction, inertia, and strain-energy; **(c)** at 14.6 MPa, the seal has largely stabilised, and the contours are smoother; **(d)** at 19.1 MPa, pressure rapidly breaks through the seal.
(see also Appendix R.)

### 7.4.4 Deflection of the Test Fixture

As shown in Fig. 6.4, the separation between the top and bottom plates must increase when the test fixture is pressurised, so an analysis of this breathing effect is warranted. For simplicity, the plates were modelled as rigid, and their expected elastic displacement was addressed by reducing the seal compression by an equivalent amount. Because the test fixture remained in an elastic regime, it was reasonable to linearly scale the displacement of the top plate with the applied pressure instead of modelling its actual deformation. An upper bound for the simulation error due to breathing was established by adopting the worst-case deflection of 0.9 mm when $P_f = 52$ MPa from Section 6.2, and then scaling this deflection by the simulated leak pressure. For example, the simulated leak pressure was 9.25 MPa for the EPDM seal with $\varepsilon = 10\%$ and an extrusion gap of 50%, so the displacement of the top plate in the FE model was reduced by 0.9 mm $\times$ (9.25/52) = 0.16 mm to simulate the breathing effect. This resulted in a simulated leak pressure of 8.31 MPa, a 10.7% reduction. Unsurprisingly, test conditions with lower leak pressures gave less error due to breathing. For instance, the leak pressure of 1.96 MPa for the EPDM seal with $\varepsilon = 5\%$ and an extrusion gap of 100% was only 1.6% lower when breathing was considered. Hence, the breathing effect was only significant for some of the test conditions with EPDM seals. It was not critical for the NR seals because the highest leak pressure was only 1.54 MPa. In all cases, breathing effects do not fully account for the large discrepancies between experimental and simulated leak pressures.

### 7.4.5 The Critical Contact Node and the Leak Criterion for FPP

As illustrated in Fig. 5.25, the native FPP schemes in Abaqus/Standard monitor the contact pressure at a node that is not in physical contact with the sealing countersurface to determine when to propagate pressure. Another natural choice for the critical node is the one that is in physical contact with the sealing countersurface. Yet if this were chosen while maintaining a critical contact pressure of zero, it would amplify errors in the simulated leak pressures because the node that is in physical contact always has a larger contact pressure than the one that is not in contact. Clearly, choosing the node that is in physical contact with the sealing countersurface as the critical node for FPP (with Abaqus' default leak criterion of 0 MPa) cannot rectify the large errors in Fig. 7.1.

The preceding argument is premised on adopting Abaqus' default leak criterion of 0 MPa, and despite the common adoption of this criterion in most FE studies in Table 3.1, there is no physical basis for it. In fact, this criterion is never mentioned when analytical arguments are made; rather, leakage is stated to occur when the contact pressure equals the fluid pressure. Testing this criterion in Abaqus is not a trivial matter because the arguments that are called into the DLOAD and VDLOAD subroutines do not allow simple

computation of nodal contact pressures. Nevertheless, the leak criterion can be tested with manual implementation to determine if it gives better agreement with experimental results. Such a scheme is illustrated in Fig. 7.5 where the leak criterion of Fig. 5.25 is changed from $P_{contact} = 0$ to $P_{contact} \leq P_f$ (recall that $P_f$ is the fluid pressure). Such a scheme is expected to give a lower leak pressure than that with Abaqus' default criterion because as the contact pressure reduces, it must momentarily match the fluid pressure before it reaches zero.
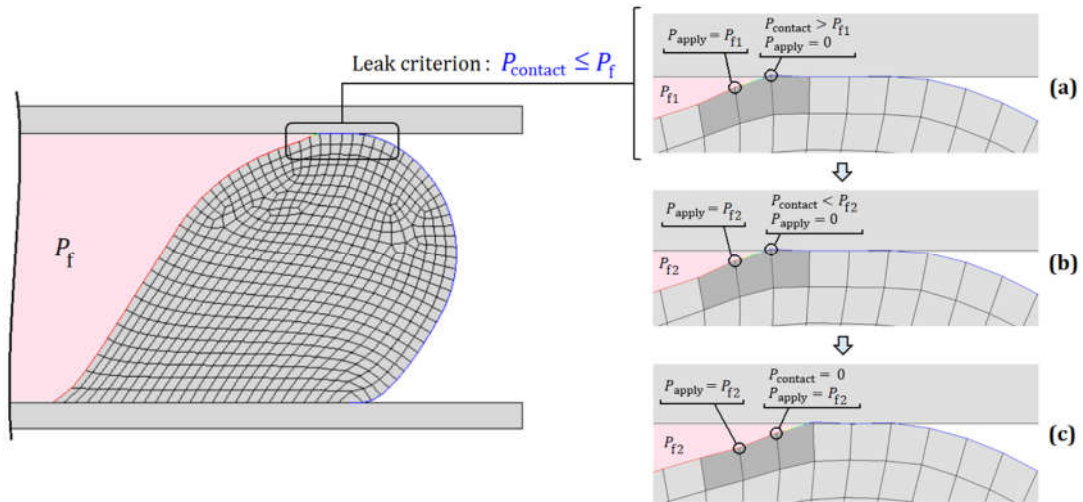


Fig. 7.5: Illustration of a manually implemented leak criterion where fluid pressure ($P_f$) propagates when the contact pressure at the sealing front is less than or equal to the fluid pressure. **(a)** The fluid pressure, $P_{f1}$, is applied to the left node but not the right. **(b)** The fluid pressure is incremented by a small amount from $P_{f1}$ to $P_{f2}$, causing the contact pressure at the right node to drop below the fluid pressure. **(c)** Since the leak criterion has been met, the fluid pressure is propagated to the next node which breaks contact at the node, and the scheme continues.

To explore the scheme in Fig. 7.5, the EPDM seal with $\varepsilon = 5\%$ and an extrusion gap of 50% was chosen. The lower compression was beneficial because, owing to its relatively low leak pressure, it reduced the number of manual iterations to cause leakage; yet the leak pressure was sufficiently high to limit transducer error to 2% (see Table 7.1), a small value compared to the simulation error of +52.2%, in Fig. 7.1b. The mesh size at the sealing interface was increased from 0.03 mm to 0.25 mm, again to reduce the number of manual iterations. This corresponded to the mesh that is illustrated in Fig. 5.21a and, depending on the FPP scheme (see Fig. 5.12), was expected to overpredict the leak pressure by 12-22% based on the mesh convergence studies in Fig. 5.23. Manual implementation of the classical leak criterion gave a simulated leak pressure of 2.32 MPa which is 39% lower than the experimental leak pressure in Fig. 7.1b. Based on previous arguments, refining the mesh would reduce the simulated leak pressure, further increasing the error.

It is conceivable that adopting the classical leak criterion and setting the critical node for FPP to the one just right of the sealing front would resolve the issue. This somewhat *ad hoc* adjustment is illustrated in Fig. 7.6. When the scheme was implemented, the simulated leak pressure increased to 3.18 MPa, still 17% lower than the experimental leak pressure. Refining the mesh to a size of 0.125 mm confirmed the expected trend: the simulated leak

pressure reduced to 2.85 MPa, or 26% lower than that from the experiment. Further mesh refinement would increase the error. It can be stated with reasonable confidence that neither the classical nor the Abaqus default leak criteria are physically accurate for the problem considered in this work, but they do establish bounds between which the seal actually leaks.
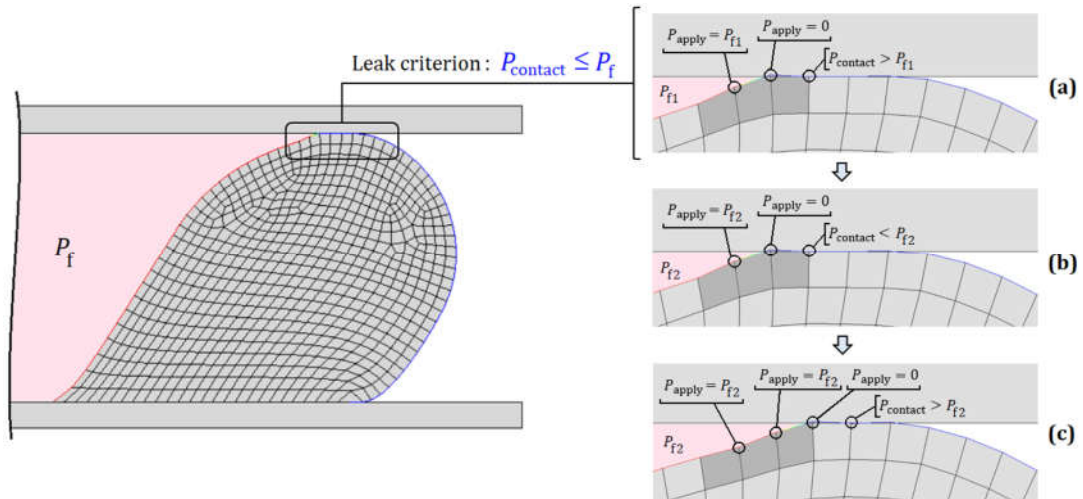


**Fig. 7.6:** Illustration of a manually implemented leak criterion where fluid pressure ($P_f$) propagates when the contact pressure at the sealing front is less than or equal to the fluid pressure. **(a)** The fluid pressure, $P_{f1}$, is applied to the left node but not the right, the latter of which is the sealing front. The leak scheme monitors the node to the right of the sealing front instead of the node at the sealing front. **(b)** The fluid pressure is incremented by a small amount from $P_{f1}$ to $P_{f2}$, causing the contact pressure at the node where the leak criterion is applied to drop below the fluid pressure. **(c)** Since the leak criterion has been met, the fluid pressure is propagated to the next node which breaks contact at the sealing front. The leak criterion also propagates to the right by one node, and the scheme continues.

### 7.4.6 Asymmetries in the Experimental Test Fixture

To the author's knowledge, all visual evidence suggests that seal leakage and failure are not symmetric even when a nominally symmetric test configuration is used.[159,160,161] For example, see Fig. 7.7. Internal data from the sponsor also supports this observation. This is not surprising given that a mechanical failure seeks the path of least resistance. Geometric variation and material anisotropy on a microstructural level always provide these paths, and the consequence is that axisymmetric models tend to overpredict sealing capability. Yet for the problem at hand, these uncertainties seem unlikely to explain the order of the errors in the simulated leak pressures. The metal components were machined within $\pm 0.01$ mm, and the previous section establishes that even with 0.16 mm variation in the compression (which is much too large for most test pressures in this work), the simulation of the leak pressure only changed by $\approx 10\%$. Although the EPDM material did not appear to follow ideal hyperelastic theory (see Section 6.7), it is unlikely that this explains errors as large as those in Fig. 7.1b. And certainly, the NR material closely followed ideal hyperelastic theory, yet its simulation errors are also large. Therefore, geometric and material variations cannot adequately account for the large simulation errors.
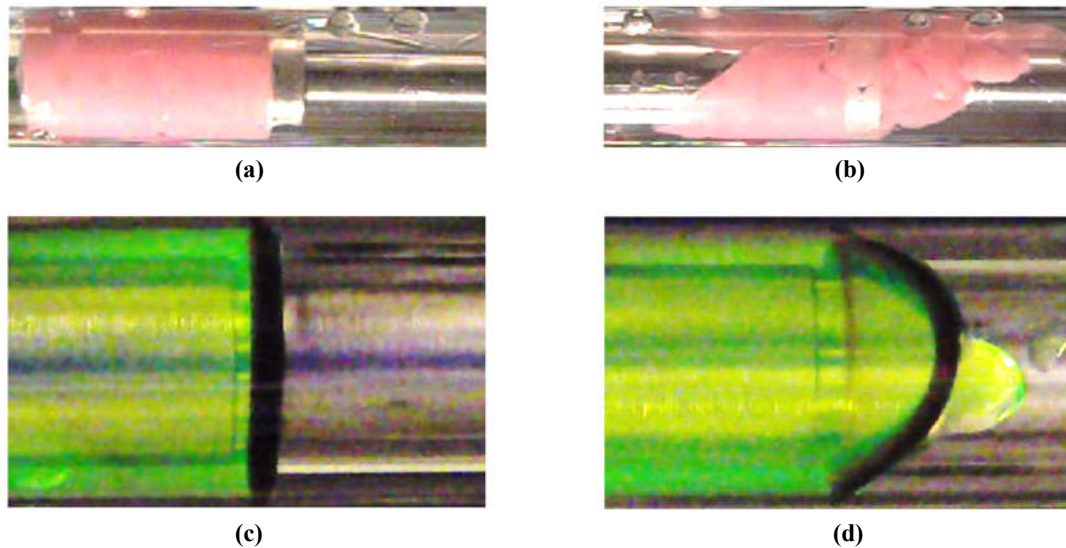
**Fig. 7.7:** Examples of asymmetric failures in axisymmetric seals: **(a)** a mini swell packer (see Fig. 3.10 for a full-scale schematic) with differential pressure from left to right and shortly before fracture; **(b)** the mini swell packer showing extrusion that is not axisymmetric; **(c)** an O-ring seal with pressurised fluid; **(d)** the O-ring seal exhibiting a non-axisymmetric leak. (Adapted from Druecke *et al*.)[161]

## 7.5 The Impact of Cumulative Errors on the Simulated Leak Pressures

Clearly, many factors can contribute to the errors in the simulated leak pressures in Fig. 7.1, so an attempt to assess these from a broader perspective is given in this section. Table 7.2 shows maximum potential errors based on evidence from this thesis alongside errors that the author deems more likely. The latter, subjective as they may be in some cases, are reasonably substantiated by trends that are observed in this work. These errors are discussed in greater detail in previous sections, so only brief notes are made in the table.

**Table 7.2:** Summary of the maximum and probable errors in the simulated leak pressures.

| Error Source | Error / % | | | Justification |
| --- | --- | --- | --- | --- |
| | Max. | Likely (EPDM) | Likely (NR) | |
| Hyperelastic model | N/A | ≤ 10 | ≤ 1 | Figs. 6.12, 6.14, & 6.15 illustrate good accord between characterisation data and the models, especially for NR. |
| Friction model | +1.7 | ≤ 1 | ≤ 1 | Fig. 5.32b shows leak pressures are not sensitive to reduction in CoFs. |
| Volumetric compressibility | +9.6 | ≤ 1 | ≤ 1 | Fig. 5.32a shows sensitivity to Poisson's ratio, but there is good certainty in assigned compressibilities for the NR and EPDM seals. |
| Mesh | +5 | ≤ 3 | ≤ 3 | Fig. 5.23 shows error in the mesh size ranges from 2-5% depending on the FPP scheme. |
| Stress relaxation | +30 | ≤ 1 | ≤ 1 | Figs. 6.10b and 6.11 show 5-30% relaxation, but the Mullins effect mitigates this, especially for EPDM as shown in Fig. 6.10a. Fig. 6.18a also shows no relaxation during sustained leakage of NR seals. |
| Strain rate | +25 | ≤ 20 | ≤ 1 | Fig. 7.3 sets the error bound for EPDM. Figs. 6.11 and 6.18 show that relaxation, and by extension strain rate, have limited effect in NR. |
| Dynamic effects | +10 | ≤ 1 | ≤ 1 | Fig. 7.1 suggests the explicit solution gives lower pressures than the implicit solver, but the effect is not present in most simulations. |
| Test fixture breathing | +10.7 | ≤ 10.7 | ≤ 1.6 | Section 7.4.4 establishes the max. error at the maximum leak pressure. Errors reduce for lower leak pressures. |
| FE implementation of FPP | ±30 | ±30 | ±30 | Section 7.4.5 shows that neither the default leak criterion in Abaqus or the classical leak criterion are correct for this problem. |
| Pressure transducer error | > 100 | < 5 | < 10* | Table 7.1 shows measurement error is low for EPDM seals. At the two highest leak pressures with NR, the measurement error is also low. |
| Physical asymmetries | N/A | N/A | N/A | This effect is challenging to assess, but it is at least partially addressed by the test fixture breathing analysis in Section 7.4.4. |

\* The value assigned here only applies for the two highest leak pressures with NR.

The main takeaway from Table 7.2 is this: the largest source of error lies in the finite-element implementation of fluid pressure penetration. Most troubling, neither the Abaqus default criterion nor the classical leak criterion have provided leak pressures that are reasonable, but it is encouraging that the experimental leak pressures were bounded by the two criteria. It is plausible to suggest that, at least where numerical implementation is concerned, reality lies somewhere between them.

## 7.6 Summary

There is poor correlation between numerically simulated leak pressures and their experimental counterparts. Even cumulative errors cannot fully explain the poor correlation, and this is especially true for the NR seals at their highest two leak pressures. The EPDM seals introduced some complexities in the material model that can account for a portion of the total error, but these uncertainties cannot fully account for the observed discrepancies. The large errors appear to arise primarily from inaccuracies in the leak criterion itself. This idea is supported by the fact that two different leak criteria, namely when $P_{\text{contact}} = 0$ and $P_{\text{contact}} = P_{\text{f}}$, resulted in leak pressures that bound the experimental leak pressures. The former predicted leak pressures that were too high, and the latter gave pressures that were too low. A leak criterion between these two limits seems more appropriate to adopt, for instance:

$$P_{\text{contact}} = \alpha P_{\text{f}} \tag{7.1}$$

with $0 < \alpha < 1$. Exploring this criterion is a natural next step to extend the work in this thesis and is discussed in the next chapter.

# 8. Conclusions and Outlook

As this thesis draws to a close, it is helpful to frame the current work on the prediction of seal leakage within the broader perspective of previous research. Analytical treatments of leak prediction, although qualitatively useful, appear incapable of accurately solving the leak problem, especially when finite deformations occur. Complications that arise in rubber material models, including hyperelasticity and viscoelasticity, also make analytical solutions intractable. Percolation theories have been proposed for modelling seal leakage, but these do not appear applicable for high pressure seals that, at least in practical terms, have near-zero leak rates. In these cases, leakage is abrupt (essentially an on-off mechanism) and often linked to an elastic instability. Therefore, the only recourse to tackle the general leak problem is numerical simulation. Different numerical techniques exist in the literature, and fluid pressure penetration modelling with mechanical FEA has received the most attention in industrial settings. Academics have explored more complicated methods that consider fluid-structure interactions, but these do not fundamentally resolve many complications that have been exposed in the present work. Hence, the focus of this research has been to assess and attempt to validate FPP algorithms in the commercial FE software Abaqus. In the next section, good modelling and test practices that are buttressed by the present work are consolidated and reiterated. The chapter closes the author's thoughts on a path forward, including a discussion of the leak criterion which has been shown to be the weakest link in FPP simulations.

## 8.1 Best Practices for Simulating and Testing Leak Problems with FPP

This section presents some best practices based on the findings in this thesis. The most relevant points from FE modelling, material characterisation, and experimental testing are revisited, and justifications for the practices are provided where applicable.

### 8.1.1 Material Characterisation and Curve Fitting a Hyperelastic Model

1. Before determining which characterisation tests are most suitable for a given problem, conduct a biaxiality analysis (Section 5.4.7 and 6.7) with FEA to determine the dominant loading modes. The hyperelastic material model for this exercise need not be exact, as strains (from which biaxiality is computed) are primarily determined by the geometry of deformation. In fact, a Neo-Hookean material model with an appropriate order for the rubber's shear modulus will usually suffice for the exercise.

2. Consider loading mode equivalencies (Section 2.5.2) when choosing characterisation tests. For example, the ET test is quite difficult to execute, but the UC test (ET's theoretical equivalent) is simple on a uniaxial test machine. The equivalency of these two modes is particularly important for high temperature testing because ET specimens can fracture at very low (and practically useless) strains due to grip constraint. UC compression buttons are much more robust. The drawback of UC tests is that they are sensitive to friction, but this is often a reasonable tradeoff for modelling purposes.

3. Conduct characterisation tests to levels of strain that are experienced in actual parts. The strain limits can be readily determined while conducting an FE biaxiality analysis. The levels of strain should also be considered with respect to the loading modes that occur (Section 5.4.7).

4. Material characterisation data in UT is the worst choice for building an FE material model for axisymmetric seals. They are better approximated by a plane-strain condition. The equibiaxial loading condition can also be significant in axisymmetric seals with large deformation. Therefore, it is usually best to build a hyperelastic material model from PT and ET (or UC) stress-strain data, with a fitting bias toward the former.

5. When characterising a material in planar tension, compensate for the change in gauge height due to grip compression because it is a non-trivial portion of the nominal height (Section 6.5).

6. When determining a hyperelastic material model for FEA, plot the model's UT, PT, and ET stress-strain responses on a single graph to ensure that $\sigma_{ut} < \sigma_{pt} < \sigma_{et}$ for all positive strains (Section 5.3). Strictly speaking, this criterion must only hold for true stresses, not engineering stresses.

7. A rubber's volumetric compressibility should be accurately modelled even when a seal has unloaded surfaces (Section 5.7.2). In the absence of characterisation data, a range of Poisson's ratio from $v = 0.495$ to $0.4975$ should be considered for a filled rubber. For an unfilled rubber, assigning $v = 0.4995$ is generally acceptable and more computationally stable than assuming an incompressible material.

8. To mitigate the variability that is inherent in rubber compounds, use the same batch of material for characterisation coupons and manufactured test components. If the same batch cannot be used, try to assess variability by reviewing historical manufacturing data (Sections 6.3 and 6.5).

9. Ensure that manufactured parts have a state-of-cure that is comparable to characterisation coupons. Try to achieve a state-of-cure of 90% or better in both (Section 6.4).

10. When characterising and modelling rubber compounds, consider inelastic phenomena such as stress relaxation, the Mullins effect, compression set, and the strain rate. This is especially important for filled rubber, but may be negligible for unfilled compounds (Sections 6.5 and 7.4.2).

11. Validate hyperelastic material models by conducting physical tests with inhomogeneous deformations. Use loads, displacements, and where possible, measurements on the deformed sample. Compare all measurements with FE predictions to assess the accuracy of the material model (Section 6.7).

### 8.1.2 General Finite-Element Considerations

1. Use a contact pressure-dependent friction model. Multiple sources suggest a large diminution of the CoF at high pressures, and in the absence of better data use or scale the data from Fig. 5.9 (Section 5.4.3 and 5.7.1).

2. To prevent premature termination of a solution in Abaqus/Standard: (a) reduce the minimum load increment from $10^{-5}$ to $10^{-8}$; (b) increase the number of iteration attempts from 5 to 10 (Section 5.4.1).

3. In Abaqus/Standard, the penalty contact formulation appears to converge better than the Augmented Lagrange formulation, but the accuracy of different

formulations for leak problems (including the kinematic formulation in Abaqus/Explicit) was not assessed in this work (Section 5.4.2).

4. When meshing, use reduced integration hybrid quadrilateral elements and conduct mesh sensitivity studies. Use partitions to highly refine the mesh at sealing interfaces. When mesh-independent solutions are not possible, it is still helpful to monitor convergence trends as the mesh size reduces (Section 5.5).

5. Quadrilaterals should be the dominant element shape, but limited and careful use of triangular elements is acceptable, especially if they are sufficiently far from sealing surfaces. When element sizes or types transition, monitor field contour plots such as stress and strain for discontinuities (Sections 5.4.6 and 5.5).

6. When assessing the possibility of fracture in FEA, use experimentally measured fracture strains as a first proxy, but realise that this method is imperfect. Also recognise that the fracture strain is loading mode dependent; for instance, the fracture strain in planar tension is lower than that uniaxial tension (Section 5.4.7).

7. When using mass scaling in Abaqus/Explicit, conduct a sensitivity analysis to understand if inertia is affecting the solution (Section 5.6.3).

8. Use rigid boundaries for metal countersurfaces with caution, especially for high pressure applications. Even if metal sealing surfaces are expected to deform, it may be possible to preserve them as rigid bodies by adjusting kinematic boundary conditions (Sections 6.2 and 7.4.4).

### 8.1.3  Specific Considerations for FPP in Finite-Element Analysis

1. In Abaqus/Standard, one should first attempt FPP solutions without contact controls. If contact convergence is a problem, apply local contact stabilisation to troublesome interfaces. Use as small a damping factor as possible. Compare undamped solutions (prior to their failure to converge) to damped solutions to check for excessive energy dissipation. Review ALLSD for a low order relative to ALLIE. If convergence still cannot be achieved, or the load increment is cut back excessively, try to simulate the problem in Abaqus/Explicit (which requires a subroutine or manual FPP). Adjusting contact stiffness can also be explored but was not helpful in this research (Sections 5.4.2 and 5.6.3). Abaqus recently released a general contact algorithm that has not been explored in this work.

2. When using Abaqus' native FPP algorithms, monitor pressure penetration solutions for contact closure because the default schemes cannot address the closure of pressurised surfaces. This shortcoming lowers simulated leak pressures, but when the default leak criterion is adopted (that is, $P_{\text{contact}} = 0$), the inaccuracy can be artificially masked by the leak criterion itself. Problems with contact closure require particularly careful judgement (compare results in Sections 5.4.4 and 5.6.1).

3. When using Abaqus' native FPP algorithms, the default penetration time of $0.001\,\text{s}$ is usually acceptable. If convergence problems are encountered when pressure is advanced from one node to the next, increase the penetration time by an order of magnitude to try smoothing the transition and facilitate convergence (Section 5.4.4).

4. In Abaqus, a subroutine (or manual pressure manipulation) is required to close contact on nodes that are exposed to fluid pressure (Sections 5.4.4 and 5.6).

5. Regardless of the solution scheme, it appears that the greatest source of error is the leak criterion. To date, no generally reliable leak criterion has been established or

implemented in Abaqus for the problem that has been studied (Section 5.6).

6. When conducting FPP simulations, monitor for rapid changes in contact status. They may be indicative of an elastic instability in the problem, so even if full convergence is not achieved, the pressure at an unconverged step may be practically equivalent to the leak pressure.

## 8.2  Toward a Better Leak Criterion for Modelling FPP

As previously highlighted, two criteria that are commonly employed in the literature, namely $P_{\text{contact}} = 0$ and $P_{\text{contact}} = P_{\text{f}}$, yield leak pressures that bound the experimental leak pressures. Based on this observation, it is suggested to explore a leak criterion according to $P_{\text{contact}} = \alpha P_{\text{f}}$ (Eq. 7.1). Applying this equation with $0 < \alpha < 1$ to the problem studied in this work would yield numerical leak pressures that fall between those that were reported with the conventional leak criteria.

The use of Eq. 7.1 may seem *ad hoc*, but there are arguments that it has a physical basis. In a finite-element solver, there is a discontinuity in the nodal force due to fluid pressure at the sealing front (see Fig. 3.17a for this definition). That is, a nodal force due to fluid pressure in FE solvers is applied as an "on-off" mechanism according to the leak criterion. This means that a distributed load (the pressure) is not smoothly distributed in a discretised model. Furthermore, Sections 5.5 and 7.4.5 suggest that this problem is not a consequence of the mesh size itself; even mesh-converged leak pressures are inaccurate. In an actual seal, there is probably a smooth fluid pressure gradient near the sealing front, and the net force due to this gradient lies somewhere between the forces that arise from the two conventional leak criteria. The factor $\alpha$ in Eq. 7.1 acts as a "lumped" parameter to capture this effect, and it could be calibrated with FE methods. The author suspects that $\alpha$ would depend on the seal geometry and perhaps the sealing material.

Possibly, a more physically realistic model would implement a shape function where $\alpha = \alpha(x)$ and $x$ is the distance along the sealing front (see Fig. 3.18 for a typical illustration of this variable $x$). This more complicated form could arise from fluid partially penetrating through the sealing interface due to the surface roughness. If this were the case, it may be appropriate to adapt percolation theories[185-187] to mechanical FE models of seal leakage. The shape function could possibly take a form of $\alpha = \alpha(x, R_{\text{a}})$ where $R_{\text{a}}$ is a surface roughness parameter. In any case, experimentally determining the shape of $\alpha(x)$ or $\alpha(x, R_{\text{a}})$ would be difficult if not impossible for most high pressure seals because, even if pressure gradients could be resolved at small scales near the sealing front, measurements would have to discern between contact pressure and fluid pressure near the sealing front. Setting this complication aside, a first step could be to assume a linear shape function at the sealing front.

Experimental evidence supports the notion of a fluid pressure gradient along a sealing interface. This is most apparent by observing swell packers (see Fig. 3.10) that have been damaged during pressure testing. Fig. 8.1 shows a swell packer with damage imparted by fluid penetrating though the inner diameter of the rubber seal. This type of damage may occur without leakage across the seal because the fluid does not fully penetrate the entire length of rubber. Partial leakage could also occur along the outer diameter of the rubber without completely bypassing the seal. Presumably, this partial leak phenomenon (which implies development of a fluid pressure gradient) may occur on a smaller scale with seals that have more typical length-to-diameter aspect ratios. The presence of pressure gradients across a sealing interface is also supported by the work of Wang *et al*.,[267] though these authors demonstrated the concept with partial leakage across discrete sealing elements instead of a continuous one.



**Fig. 8.1:** Evidence of fluid penetration along the inner diameter of a swell packer. The leak paths are indicated by the pink curves. (Adapted from Eatwell.)[268]

To motivate a plan forward, Table 8.1 summarises strengths and areas for improvement in this thesis. The table also notes where novel contributions to the literature are made.

**Table 8.1:** Summary of strengths and weaknesses in the FE models of this thesis.

| Feature | Novel | Comments |
|---|---|---|
| Model type = 2D | No | • 2D is acceptable because the large modelling errors cannot be fully attributed to 3D effects.<br>• 3D modelling of FPP is cost prohibitive due to the mesh size that is required for accurate leak predictions. |
| SEF = gen-Yeoh | Yes | • A new SEF and subroutines have been developed for highly filled rubber seals. |
| Hyperelastic characterisation | Yes | • The most critical loading modes (PT, UC) were determined with biaxiality analyses.<br>• Mechanical characterisation used these most critical modes. |
| Volumetric compressibility | No | • Realistic values based on measurements by the project sponsor were adopted.<br>• Most studies in the literature assume $\nu = 0.5$. |
| Rheology characterisation | Yes | • DSC was used to validate the state-of-cure in the bonded seals, giving confidence that their material properties matched those of the test coupons. |
| Hyperelastic model validation | Yes | • Compression tests on bonded rubber seals gave good confidence in the material models. |
| Viscoelastic modelling | Yes | • Inelastic effects were quantified and considered but not explicitly modeled.<br>• They were insignificant for the unfilled NR seals.<br>• The order of error due to inelasticities was established for the filled EPDM seals.<br>• Other studies in the literature on modelling seal leakage have not addressed these effects. |
| Friction model = variable CoF | Yes | • A contact pressure-dependent model was developed from tests on FKM, FEPM, and HNBR materials.[245,256]<br>• Characterisation testing of the NR and EPDM materials would be beneficial.<br>• Most studies in the literature assume a Coulomb model. |
| Max. leak pressure $\approx$10 MPa | Yes | • Test pressures were an order of magnitude higher than those in previous rubber seal literature. |
| FPP modelling | Yes | • New subroutines removed pressure from nodes with closing contact.<br>• The first mesh sensitivity studies were reported.<br>• Systematic comparisons of the Abaqus R2017 and R2018 pressure integration schemes were reported.<br>• The FPP subroutine for Abaqus/Explicit enabled the study of dynamic effects on seal leakage.<br>• Different leak criteria were studied, and none were found satisfactory for the problem studied. |
| Test fixture deformation | No | • Deformation of the test fixture was not explicitly modeled. |
| Statistical variation | No | • Only one leak pressure was measured for each experimental test condition. |

To advance the present work, an accurate leak propagation criterion must be established. This can be studied by developing a subroutine[†††] to implement the leak criterion given in Eq. 7.1. If an Abaqus subroutine is developed, it will require computation of nodal contact pressures at the sealing front. This is not a straightforward exercise but should be possible. Alternatively, the leak criterion could be implemented by manually propagating pressure, but this method would be too cumbersome to be generally useful. In either case, deformation of the test fixture could be readily included in these models because leakage would not be dictated by the kinematic location of a node at the sealing front.

Because the leak prediction errors in this thesis are too large to be explained by anything other than the leak criterion itself, the experiments in this work provide a basis for other researchers to study the leak equation of Eq. 7.1 without generating new experimental data. Once the error due to the leak criterion is reduced to a reasonable level, statistical variation can be addressed by conducting replicate experimental tests. To minimise uncertainties due to viscoelasticity, it would be most appropriate to restrict future tests to an unfilled compound, at least until there is confidence in the chosen leak criterion. If filled materials are tested, inelastic effects will require more careful attention, especially those related to strain rate sensitivity.

---

[†††] Personal correspondence with Abaqus indicates that an option to update the critical contact pressure during a load step may be incorporated in a future software release, in which case a user-defined subroutine may no longer be necessary.

# References

1   International Organization for Standardization, (2012). "Rubber – Vocabulary". ISO Standard No. 1382:2012. https://www.iso.org/standard/60252.html.

2   H.H. Buchter, (1979). *Industrial Sealing Technology*. John Wiley & Sons. USA.

3   R. Mody, D. Gerrard, & J. Goodson, (2013). "Elastomers in the Oilfield". *Rubber Chemistry and Technology*, **86** (3), 449-469.

4   United States Coast Guard, (2011). *On Scene Coordinator Report Deepwater Horizon Oil Spill*. https://repository.library.noaa.gov/view/noaa/283. Accessed Sep. 27th, 2022.

5   United States Department of Justice, (2015). *Fact Sheet Proposed Consent Decree with BP for the Deepwater Horizon/Macondo Well Oil Spill*. https://www.justice.gov/enrd/file/834511/download. Accessed Sep. 27th, 2022.

6   Engineering Services LP, (2014). *Deepwater Horizon Blowout Preventer Failure Analysis Report*. For the US Chemical Safety and Hazard Investigation Board. https://www.csb.gov/assets/1/20/appendix_2_a__deepwater_horizon_blowout_preventer_failure_analysis1.pdf?15262. Accessed Sep. 27th, 2022.

7   T. Hohenberger, (2021). "WPS Expert Talk – EiE Overview". Schlumberger Technology Corporation. GEMS 104571156.

8   T. Hohenberger, (2015). "Project Retrospective and Value Stream Map – 9625 XCP v4". Schlumberger Technology Corporation. GEMS 101750064.

9   J. Tully, (2011). *The Devil's Milk: A Social History of Rubber*. Monthly Review Press. New York, NY, USA.

10  K. Memmler, (1934). *The Science of Rubber*. Reinhold Publishing Corp. New York, USA. https://archive.org/details/in.ernet.dli.2015.206122. Accessed Oct. 17th, 2021.

11  C.E. Akers, (1914). *The Rubber Industry in Brazil and the Orient*. Metheun & Co. Ltd. London, UK. https://archive.org/details/rubberindustryin00akerrich. Accessed Oct. 17th, 2021.

12  J. Priestley, (1770). *A Familiar Introduction to the Theory and Practice of Perspective*. London. p.xv. https://archive.org/details/afamiliarintrod00conggoog. Accessed Oct. 17th, 2021.

13  B.D. Porritt, (1927). "The Early History of the Rubber Industry". *London Rubber Growers Association*, **5**. (Cited from Tully)[9].

14  P. Martyr, (1511). *De Orbe Novo*. (Cited from Tully)[9].

15  C. Rodriguez & P. Ortiz, (1994). "El Manati, un Espacio Sagrado de los Olmeca". Universidad Veracruzana, Jalapa, Veracruz, Mexico. (Cited from Hosler *et al.*)[16].

16  D. Hosler, S.L. Burkett, & M.J. Tarkanian, (1999). "Prehistoric Polymers: Rubber Processing in Ancient Mesoamerica". *Science*, **284** (5422), 1988-1991.

17  M.J. Tarkanian & D. Hosler, (2011). "America's First Polymer Scientists: Rubber Processing, Use and Transport in Mesoamerica". *Latin American Antiquity*, **22** (4), 469-486.

18  Anonymous. https://sumatfeet.wordpress.com/2012/10/29/rubber-farming/. Accessed Oct. 17th, 2021.

19  I. Mursell, Mexicolore. https://www.mexicolore.co.uk/aztecs/ask-experts/have-any-ancient-rubber-balls-been-found. Accessed Oct. 17th, 2021.

20  L.B. Tunnicliffe, (2015). *Particulate Reinforcement of Elastomers at Small Strains*. PhD Thesis, Queen Mary University of London. London, UK.

21  T. Hancock, (1857). *Personal Narrative of the Origin and Progress of the Caoutchouc or India-rubber Manufacture in England*. Longman, Brown, Green, Longmans, & Roberts. London, UK. https://play.google.com/store/books/details?id=Sd1IAAAAMAAJ&rdid=book-Sd1IAAAAMAAJ&rdot=1. Accessed Oct. 17th, 2021.

22  H. Wolf & R. Wolf, (2009 reprint, originally 1936). *Rubber – A Story of Glory and Greed*. J.J. Little & Ives Co. New York, USA.

23  H. Morawetz, (2000). "History of Rubber Research". *Rubber Chemistry and Technology*, **73**

(3), 405-426.

24  R.A. Solo, (1959) "Synthetic Rubber: A Case Study in Technological Development under Government Direction". United States Senate Report, U.S. Government Printing Office. Washington, U.S.A. https://babel.hathitrust.org/cgi/pt?id=uc1.a0003264645&view=1up&seq=5. Accessed Oct. 17th, 2021.

25  F.A. Howard, (1947). *Buna Rubber: The Birth of an Industry*. D. van Nostron Co., Inc. New York.

26  K.W. Whitten, R.E. Davis, M.L. Peck, & G.G. Stanley, (2004). *General Chemistry*. 7th Ed. Thomson Brooks/Cole. USA.

27  R.T. Morrison & R.N. Boyd, (1992). *Organic Chemistry*. 6th Ed. Prentice Hall Inc. New Jersey, USA. https://archive.org/details/MorrisonBoydOrganicChemistry. Accessed Oct. 17th, 2021.

28  H. Bergwerf, (2015). molview.org. Accessed May 12th, 2020.

29  W. Gratzer, (2009). *Giant Molecules: From Nylon to Nanotubes*. Oxford University Press. Oxford, UK. (See Chapters 2 & 7).

30  A.Y. Coran, (2005). "Vulcanization". In *Science and Technology of Rubber*. 3rd Ed. Eds. J.E. Mark, B. Erman, & F.R. Eirich. Academic Press. Ch. 7, 321-366.

31  D.L. Hertz Jr., (1984) "Theory and Practice of Vulcanization". *Elastomerics*, **116**, 17-21.

32  J.A. Brydson, (1999). "Aliphatic Polyolefins other than Polyethylene, and Diene Rubbers" and "Fluorine-containing Polymers". In *Plastics Materials*. 7th Ed. Elsevier, Ltd. Ch. 11, 247-310 & Ch. 13, 363-385.

33  G.R. Hamed, (2001). "Materials and Compounds". In *Engineering with Rubber. How to Design Rubber Components*. 2nd Ed. Ed. A.N. Gent. Hanser Publishers. Munich, Germany. Ch. 2, 11-34.

34  P.R. Dluzneski, (2001). "Peroxide Vulcanization of Elastomers". *Rubber Chemistry and Technology*, **74** (3), 451-492.

35  Y.A. Cengel & M.A. Boles, (2006). *Thermodynamics: An Engineering Approach*. 6th Ed. McGraw Hill. Boston, MA, USA.

36  J.M.G. Cowie & V. Arrighi, (2008). *Polymers: Chemistry and Physics of Modern Materials*. 3rd Ed. Taylor & Francis Group, LLC. Boca Raton, FL, USA.

37  J.H. Gibbs & E.A. DiMarzio, (1959). "Nature of the Glass Transition and the Glassy State". *The Journal of Chemical Physics*, **28** (3), 373-383.

38  G. Adam & J.H. Gibbs, (1965). "On the Temperature Dependence of Cooperative Relaxation Properties in Glass-Forming Liquids". *The Journal of Chemical Physics*, **43** (1), 139-146.

39  J.M. O'Reilly, (1962). "The Effect of Pressure on Glass Temperature and Dielectric Relaxation Time of Polyvinyl Acetate". *Journal of Polymer Science*, **57** (165), 429-444.

40  M.S. Paterson, (1964). "Effect of Pressure on Young's Modulus and the Glass Transition in Rubbers". *Journal of Applied Physics*, **35** (1), 176-179.

41  A. Aulova, A. Oseli, M. Bek, T. Prodan, & I. Emri, (2019). "Effect of Pressure on Mechanical Properties of Polymers". In *Encyclopedia of Continuum Mechanics*. Live Edition. Eds. H. Altenbach & A. Öchsner. Springer-Verlag. Berlin, Germany.

42  N. Bekkedahl, (1934). "Forms of Rubber as Indicated by Temperature-Volume Relationship". *Journal of Research of National Bureau of Standards*, **13** (3), 411-431. (Reprinted in *Rubber Chem. & Tech.*, **8** (1), 5-22).

43  L.H. Adams & R.E. Gibson, (1930). "The compressibility of rubber". *Journal of the Washington Academy of Sciences*, **20** (12), 213-223. (Reprinted in *Rubber Chem. & Tech.*, **3** (4), 555-562).

44  L.E. Nielsen & R.F. Landel, (1993). *Mechanical Properties of Polymers and Composites*. 2nd Ed. Taylor & Francis Group, LLC. Boca Raton, FL, USA.

45  D.W. Brazier, (1980). "Applications of Thermal Analytical Procedures in the Study of Elastomers and Elastomer Systems". *Rubber Chemistry and Technology*, **53** (3), 437-511.

46  H. Singh & A.W. Nolle, (1959). "Pressure Dependence of the Viscoelastic Behavior of Polyisobutylene". *Journal of Applied Physics*, **30** (3), 337-341.

47  A.W. Nolle & J.J. Billings, (1959). "Proton Magnetic Resonance in Polyisobutylene at Various Temperatures, Pressures, and Frequencies". *The Journal of Chemical Physics*, **30** (1), 84-90.

48  A. Eisenberg & M. Shen, (1970). "Recent Advances in Glass Transitions in Polymers". *Rubber Chemistry and Technology*, **43** (1), 156-170.

49  L. Mullins, (1947). "Effect of Temperature on Resilience". *Transactions of the Institution of the Rubber Industry*, **22** (5), 235-258. (Reprinted in *Rubber Chem. & Tech.*, **20** (4), 998-1019).

50  L.R.G. Treloar, (1975). *The Physics of Rubber Elasticity*. 3rd Ed. Oxford University Press. Oxford, UK.

51  C.M. Roland, (2011). *Viscoelastic Behavior of Rubbery Materials*. Oxford University Press. Oxford, UK.

52  C.M. Roland, (2005). "Structure Characterization in the Science and Technology of Elastomers". In *Science and Technology of Rubber*. 3rd Ed. Eds. J.E. Mark, B. Erman, & F.R. Eirich. Academic Press. Ch. 3, 105-155.

53  L.C.E. Struik, (1978). *Physical Aging in Amorphous Polymers and Other Materials*. Elsevier Science, Oxford, UK.

54  M.C. Shen & A. Eisenberg, (1966). "Glass Transitions in Polymers". *Progress in Solid State Chemistry*, **3**, 407-481. (Reprinted in *Rubber Chem. & Tech.*, **43** (1), 95-155).

55  A.N. Gent, (2001). *Engineering with Rubber: How to Design Rubber Components*. 2nd Ed. Hanser Publishers. Munich, Germany.

56  W.D. Callister & D.G. Rethwisch, (2010). *Materials Science and Engineering: An Introduction*. 8th Ed. John Wiley & Sons, Inc. Hoboken, NJ, USA.

57  J. Brandrup, E.H. Immergut, & E.A. Grulke, (1999). *Polymer Handbook*. 4th Ed. Wiley. New York, NY, USA.

58  J.E. McKinney, H.V. Belcher, & R.S. Marvin, (1960). "The Dynamic Compressibility of a Rubber-Sulfur Vulcanizate and Its Relation to Free Volume". *Transactions of the Society of Rheology*, **4** (1), 347-362.

59  C.A. Byrne, (1979). "Studies of Aflas Polymers". US Army Laboratory Command Report MTL TR 89-69. Charlottesville, NC.

60  M.R. Ambler, (1973). "Studies on the Nature of Multiple Glass Transitions in Low Acrylonitrile, Butadiene-Acrylonitrile Rubbers". *Journal of Polymer Science*, **11** (7), 1505-1515.

61  A.K. Sircar & T.G. Lamond, (1978). "Total Thermal Analysis of NBR Vulcanizates". *Rubber Chemistry and Technology*, **51** (4), 647-654.

62  S. Bhattacharjee, A.K. Bhomwick, & B.N. Avasthi, (1991). "High-Pressure Hydrogenation of Nitrile Rubber: Thermodynamics and Kinetics". *Industrial and Engineering Chemistry Research*, **30** (6), 1086-1092.

63  S. Hayashi, H. Sakakida, M. Oyama, & T. Nakagawa, (1991). "Low-Temperature Properties of Hydrogenated Nitrile Rubber (HNBR)". *Rubber Chemistry and Technology*, **64** (4), 534-544.

64  N.W. Tschoegl, W.G. Knauss, & I. Emri, (2002). "The Effect of Temperature and Pressure on the Mechanical Properties on Thermo- and/or Piezorheologically Simple Polymeric Materials in Thermodynamic Equilibrium – A Critical Review". *Mechanics of Time-Dependent Materials*, **6** (1), 53-99.

65  W.W. Schmiegel, (2003). "A Review of Recent Progress in the Design and Reactions of Base-Resistant Fluoroelastomers". DuPont Dow Elastomers Report. Wilmington, DE, USA.

66  G. Kojima & H. Kojima, (1977). "A New Fluoroelastomer Derived from Tetrafluoroethylene and Propylene". *Rubber Chemistry and Technology*, **50** (2), 403-412.

67 Anonymous, (2012). "Low Temperature Sealing Capability of O-Rings: The Relationship between Laboratory Tests and Service Performance". James Walker Report. James Walker & Co., Ltd., Woking, Surrey, UK. https://www.jameswalker.biz/nb/pdf_docs/129-low-temperature-sealing-capability-of-o-rings-the-relationship-between-laboratory-tests-and-service-performance. Accessed Oct. 17th, 2021.

68 H. Tu, (2014). "Pressure Effect on the Glass Transition Temperature of AFLAS" Schlumberger Technology Corporation. GEMS Report 101692827.

69 Anonymous, (2017). "Elastomer Engineering Guide". James Walker Report. James Walker & Co., Ltd., Woking, Surrey, UK. https://www.jameswalker.biz/system/pdf_docs/fichiers/148/original_Elastomer_engineering_guide.pdf. Accessed October 17th, 2021.

70 J.H. Fielding, (1943). "Flex Life and Crystallization of Synthetic Rubber". *Industrial and Engineering Chemistry*, **35** (12), 1259-1261. (Reprinted in *Rubber Chem. & Tech*., **17** (2), 398-403).

71 D. Parkinson, (1945). "Carbon Blacks in GR-S". *Transactions of the Institution of the Rubber Industry*, **21** (1), 7-30. (Reprinted in *Rubber Chem. & Tech*., **19** (1), 100-122).

72 A. Ciesielski, (1999). *An Introduction to Rubber Technology*. Rapra Technology Limited. Shawbury, UK.

73 B. Shaw & J.J.C. Busfield, (2020). *Characterisation of Elastomers for Dynamic Sealing Applications*. PhD Thesis, Queen Mary University of London. London, UK.

74 H. Wang, L. Yang, & G.L. Rempel, (2013). "Homogeneous Hydrogenation Art of Nitrile Butadiene Rubber: A Review". *Polymer Reviews*, **53** (2), 192-239.

75 R.J. Windslow, (2018). *Computational Modelling of Fracture Processes in Elastomeric Seals*. PhD Thesis, Queen Mary University of London.

76 R.G. Arnold, A.L. Barney, & D.C. Thompson, (1973). "Fluoroelastomers". *Rubber Chemistry and Technology*, **46** (3), 619-652.

77 J. Gough, (1805). "A Description of a Property of Caoutchouc or Indian Rubber". *Memoirs of the Literary and Philosophical Society of Manchester (Series 2)*, **1**, 288-295.

78 L.R.G. Treloar, (1942). "The Structure and Elasticity of Rubber". *Reports on Progress in Physics*, **9** (1), 113-136.

79 L.R.G. Treloar, (1943). "The Elasticity of a Network of Long-Chain Molecules. I." *Transactions of the Faraday Society*, **39**, 36-41.

80 L.R.G. Treloar, (1943). "The Elasticity of a Network of Long-Chain Molecules. II." *Transactions of the Faraday Society*, **39**, 241-246.

81 S. Timoshenko & J.N. Goodier, (1951). *Theory of Elasticity*. 2nd Ed. McGraw-Hill Book Co. Section 6, "Hooke's Law", p. 8.

82 M. Wadham-Gagnon, P. Hubert, C. Semler, M.P. Paidoussis, M. Vezina, & D. Lavoie, (2006). "Hyperelastic modeling of rubber in commercial finite element software (ANSYS)". *Proceedings of the SAMPE '06: Creating New Opportunities for the World Economy*.

83 W.V. Mars, (2006). "Heuristic Approach for Approximating Energy Release Rates of Small Cracks Under Finite Strain, Multiaxial Loading". In *Elastomers and Components: Service Life Prediction – Progress and Challenges*. Ed. V.A. Coveney. Ch. 7, 91-111.

84 R.J. Windslow, T.W. Hohenberger, & J.J.C. Busfield, (2020). "Determination of the Loading Mode Dependence of the Proportionality Parameter for the Tearing Energy of Embedded Flaws in Elastomers under Multiaxial Deformations". In: *Fatigue Crack Growth in Rubber Materials*. *Advances in Polymer Science* **286**. Eds. G. Heinrich, R. Kipscholl, & R. Stocek.

85 P. Steinmann, M. Hossain, & G. Possart, (2012). "Hyperelastic models for rubber-like materials: Consistent tangent operators and suitability for Treloar's data". *Archive of Applied Mechanics*, **82** (9), 1183-1217.

86    M. Hossain & P. Steinmann, (2013). "More hyperelastic models for rubber-like materials: consistent tangent operators and comparative study". *Journal of the Mechanical Behavior of Materials*, **22** (1-2), 1-24.

87    H. Dal, Y. Badienia, K. Acikgoz, & F.A. Denli, (2019). "A Comparative Study on Hyperelastic Constitutive Models on Rubber: State of the Art after 2006". In *Constitutive Models for Rubber XI: Proceedings of the 11th ECCMR*, Nantes, France, June 25–27, 2019. Eds. B. Huneau, J.-B. Le Cam, Y. Marco, and E. Verron. CRC Press, Boca Raton, FL.

88    R.S. Rivlin, (1948). "Large Elastic Deformations of Isotropic Materials. I. Fundamental Concepts". *Philosophical Transactions of the Royal Society of London. Series A, Mathematical and Physical Sciences*, **240** (822), 459-490.

89    R.S. Rivlin, (1956). "Large Elastic Deformations". In *Rheology: Theory and Applications*. Ed. F.R. Eirich. Elsevier, New York. Vol. 1, Ch. 10, 351-385.

90    A.F.S.M Amin, S.I. Wiraguna, A.R. Bhuiyan, & Y. Okui, (2006). "Hyperelasticity Model for Finite Element Analysis of Natural and High Damping Rubbers in Compression and Shear". *Journal of Engineering Mechanics*, **132** (1), 54-64.

91    C.K.L. Davies, D.K. De, & A.G. Thomas, (1994). "Characterization of the Behavior of Rubber for Engineering Design Purposes. 1. Stress-Strain Relations". *Rubber Chemistry and Technology*, **67** (4), 716-728.

92    O.H. Yeoh, (1990). "Characterization of Elastic Properties of Carbon-Black-Filled Rubber Vulcanizates". *Rubber Chemistry and Technology*, **63** (5), 792-805.

93    J.M. Gere, (2004). *Mechanics of Materials*. 6th Ed. Thomson Learning, Inc., Belmont, CA, Ch. 7, "Analysis of Stress & Strain", Section 7.2, p.465 & 469.

94    D.C. Kay, (2011). *Tensor Calculus*. McGraw Hill, USA. Section 3.5, "The Stress Tensor".

95    D.S. Chandrasekharaiah & L. Debnah, (1994). *Continuum Mechanics*. Academic Press, Inc., San Diego, CA, "Generalized Hooke's Law", Section 9.2, p.364-367.

96    G.A. Holzapfel, (2000). *Nonlinear Solid Mechanics: A Continuum Approach for Engineering*. John Wiley & Sons, Ltd, New York.

97    J.S. Bergström, (2015). *Mechanics of Solid Polymers: Theory and Computational Modeling*. Elsevier, London.

98    G. Wertheim, (1848). "L'Equilibre des Corps Solides Homogenes". *Annales de Chimie et de Physique, 3 serie*, **23**, 52-57. https://babel.hathitrust.org/cgi/pt?id=hvd.hnycwf&view=1up&seq=167.

99    J.P. Joule, (1859). "On Some Thermo-Dynamic Properties of Solids". *Philosophical Transactions of the Royal Society of London*, **149**, 91-131, (see Section 45). https://ia802301.us.archive.org/33/items/scientificpapers01joul/scientificpapers01joul.pdf.

100    W. Thomson & P.G. Tait, (1871). *Handbuch der Theoretischen Physik*. Vol. 1, Part 2, Section 684, p. 211-212. https://archive.org/details/handbuchdertheo00taitgoog/page/n432/mode/2up. An English reprint was issued in 1883. *Treatise on Natural Philosophy*. Vol. 1, Part 2, Section 684, p. 221-222. https://archive.org/details/b21987312/page/n3/mode/2up.

101    W.C. Röntgen, (1876). "Ueber das Verhältniss der Quercontraction zur Längendilatation bei Kautschuk". *Annalen der Physik*, **235** (12), 601-616.

102    H. Bouasse, (1903). "Sur le Coefficient s de Poisson pour le Caoutchouc Vulcanisé". *Journal de Physique Théorique et Appliquée*, **2** (1), 490-498. https://doi.org/10.1051/jphystap:019030002004001.

103    G.S. Whitby, (1920). *Plantation Rubber and the Testing of Rubber*. Ed. Longman, Greens & Co., New York. Ch. 21, "Poisson's Ratio", p. 486-502. https://archive.org/details/plantationrubbe00whitgoog/page/n18/mode/2up.

104    R.G. Young & P.A. Lovell, (1991). *Introduction to Polymers*. 2nd Ed. Chapman & Hall.

105    A.N. Gent & K.W. Starr, (2001). "Dynamic Mechanical Properties". In *Engineering with Rubber. How to Design Rubber Components*. 2nd Ed. Ed. A.N. Gent. Hanser Publishers. Munich, Germany. Ch. 4, p. 73-96.

106    L. Mullins, (1950). "Thixotropic Behavior of Carbon Black in Rubber". *Journal of Physical and Colloid Chemistry*, **54** (2), 239-251. (Reprinted in *Rubber Chem. & Tech.*, **23** (4), 733-743).

107    L. Mullins & R.W. Whorlow, (1951). "Effect of Fillers on Plasticity of Unvulcanized Rubber". *Transactions of the Institution of the Rubber Industry*, **27** (1), 55-74. (Reprinted in *Rubber Chem. & Tech.*, **24** (2), 232-249).

108    J.G. Williams, (1973). *Stress Analysis of Polymers*. Longmans Harlow, Essex, UK.

109    R.J. Windslow & J.J.C. Busfield, (2019). "Viscoelastic modeling of extrusion damage in elastomer seals". *Soft Materials*, **17** (3), 228-240.

110    A.Y. Malkin & A.I. Isayev, (2012). *Rheology Concepts, Methods, and Applications*. 2nd Ed. ChemTec Publishing.

111    E. Catsiff & A.V. Tobolsky, (1955). "Stress-Relaxation of Polyisobutylene in the Transition Region (1,2)". *Journal of Colloid Science*, **10** (4), 375-392.

112    M.L. Williams, R.F. Landel, & J.D. Ferry, (1955). "The Temperature Dependence of Relaxation Mechanisms in Amorphous Polymers and Other Glass-forming Liquids". *Journal of the American Chemical Society*, **77** (14), 3701-3707.

113    W.K. Moonan & N.W. Tschoegl, (1985). "The Effect of Pressure on the Mechanical Properties of Polymers. IV. Measurements in Torsion". *Journal of Polymer Science: Polymer Physics Edition*, **23** (4), 623-651.

114    G. Oenslager, (1926). "Changes in the Rubber Industry during the Past Fifty Years". *Industrial Engineering and Chemistry*, **18** (9), 902-905.

115    D. Parkinson, (1929). "Some properties of carbon black". *Transactions of the Institution of the Rubber Industry*, **5** (4), 263-280. (Reprinted in *Rubber Chem. & Tech.*, **3** (3), 418-430).

116    H.J. Stern, (1954). *Rubber: Natural and Synthetic*. Maclaren & Sons, London, UK.

117    H.W. Greider, (1922). "Some Physical Properties of Rubber Compounded with Light Magnesium Carbonate". *Industrial and Engineering Chemistry*, **14** (5), 385-394.

118    H.W. Greider, (1923). "The Resilient Energy and Abrasion Resistance of Vulcanized Rubber". *Industrial and Engineering Chemistry*, **15** (5), 504-511.

119    J. Plagge & M. Klüppel, (2018). "Determining strain-induced crystallization of natural rubber composites by combined thermography and stress-strain measurements". *Polymer Testing*, **66**, 87-93.

120    D. Parkinson, (1944). "Effect of Diameter & Surface Area of Carbon Black Particles on Certain Properties of Rubber Compounds". *Rubber Chemistry and Technology*, **17** (2), 451-474.

121    W.W. Vogt & R.D. Evans, (1923). "Poisson's Ratio and Related Properties for Compounded Rubber". *Industrial and Engineering Chemistry*, **15** (10), 1015-1018.

122    H. Greider, (1924). "The Influence of Glue on the Reinforcing Effect of Light Magnesium Carbonate in Rubber". *Industrial and Engineering Chemistry*, **16** (2), 151-155.

123    H. Endres, (1924). "Factors Determining the Reinforcing Value of Fillers in Compounded Rubber". *Industrial and Engineering Chemistry*, **16** (11), 1148-1152.

124    W. Wiegand, (1925). "The More Complete Evaluation of the Pigment Reinforcement of Rubber". *Industrial and Engineering Chemistry*, **17** (9), 939-941.

125    A.R. Payne, (1962). "The Dynamic Properties of Carbon Black Loaded Natural Rubber Vulcanizates. Part II". *Journal of Applied Polymer Science*, **6** (21), 368-372. (Reprinted in *Rubber Chem. & Tech.*, **36** (2), 444-450).

126    A. Einstein, (1906). "A New Determination of Molecular Dimensions". *Annalen der Physik*, **324** (2), 289-306. (original volume: *Annalen der Physik IV*, **19**). English translation available at: http://www.zhenzhubay.com/zzw/upload/up/2/378598b.pdf.

127    H.M. Smallwood, (1944). "Limiting Law of the Reinforcement of Rubber". *Journal of Applied Physics*, **15** (11), 758-766.

[128] E. Guth, (1945). "Theory of Filler Reinforcement". *Journal of Applied Physics*, **16** (20), 20-25.

[129] L.H. Cohan, (1947). "The Mechanism of Reinforcement of Elastomers by Pigments". *India Rubber World*, **117** (3), 343-348. (Reprinted in *Rubber Chem. & Tech.*, **21** (3), 667-681).

[130] C.M. Roland, (2016). "Reinforcement of Elastomers". *Reference Module in Materials Science and Engineering*. https://doi.org/10.1016/B978-0-12-803581-8.02163-9.

[131] V. Vand, (1948). "Viscosity of Solutions and Suspensions. I. Theory". *Journal of Physical and Colloid Chemistry*, **52** (2), 277-299.

[132] N. Warasitthinon, A.-C. Genix, M. Sztucki, J. Oberdisse, & C.G. Robertson, (2019). "The Payne Effect: Primarily Polymer-Related or Filler-Related Phenomenon?" *Rubber Chemistry and Technology*, **92** (4), 599-611. The image in Fig. 2.35 is from a related conference.

[133] W.P. Fletcher & A.N. Gent, (1953). "Nonlinearity in the Dynamic Properties of Vulcanized Rubber Compounds". *Transactions of the Institution of the Rubber Industry*, **29** (5), 266-280. (Reprinted in *Rubber Chem. & Tech.*, **27** (1), 209-222).

[134] A.R. Payne & R.E. Whittaker, (1971). "Low Strain Dynamic Properties of Filled Rubbers". *Rubber Chemistry and Technology*, **44** (2), 440-478.

[135] H. Bouasse & Z. Carrière, (1903). "Sur les Courbes de Traction du Caoutchouc Vulcanisé". *Annales de la Faculté des Sciences de Toulouse*, **5** (3) 257-283. https://afst.centre-mersenne.org/article/AFST_1903_2_5_3_257_0.pdf.

[136] L. Mullins, (1947). "Effect of Stretching on the Properties of Rubber". *Journal of Rubber Research*, **16** (12), 275-289. (Reprinted in *Rubber Chem. & Tech.*, **21** (2), 281-300).

[137] M. Klüppel, (2009). "Evaluation of viscoelastic master curves of filled elastomers and applications to fracture mechanics". *Journal of Physics: Condensed Matter*, **21** (3), 035104.

[138] J. Fritzsche & M. Klüppel, (2011). "Structural dynamics and interfacial properties of filler-reinforced elastomers". *Journal of Physics: Condensed Matter*, **23** (3), 035104.

[139] J. Hallet & L.B. Tunnicliffe, (2020). "Using Carbon Black to Meet the Design Challenges of EV Applications". *Elastomer Use in Electric Vehicles. Proceedings of the Rubber in Engineering Group (RIEG)*. Webinar. https://www.iom3.org/sites/default/files/event-documents/Birla_0.pdf.

[140] J.-B. Donnet, R.C. Bansal, & M.-J. Wang, (1993). *Carbon Black: Science and Technology*. 2nd Ed. Marcel Dekker, Inc., New York.

[141] R. Zafarmehrabian, S.T. Gangali, M.H.R. Ghoreishy, & M. Davallu, (2012). "The Effects of Silica/Carbon Black Ratio on the Dynamic Properties of the Tread Compounds in Truck Tires". *E-Journal of Chemistry*, **9** (3), 1102-1112.

[142] J.-B. Donnet, (1998). "Black and White Fillers and Tire Compound". *Rubber Chemistry and Technology*, **71** (3), 323-341.

[143] Anonymous, (2017). Hiwa Engineering Company. http://www.hiwaco.com/odr.htm.

[144] X. Ren, (2017). "Method Comparison for elastomer state-of-cure evaluation". Schlumberger Technology Corporation. GEMS Reports 101469861 and 102742058.

[145] F. Carleo, E. Barbieri, R. Whear, & J.J.C. Busfield, (2018). "Limitations of Viscoelastic Constitutive Models for Carbon-Black Reinforced Rubber in Medium Dynamic Strains and Medium Strain Rates". *Polymers*, **10** (9), 988.

[146] F. Carleo, (2019). *Modelling the Viscoelastic Behaviour of Rubber*. PhD Thesis, Queen Mary University of London. London, UK.

[147] F. Carleo, J. Plagge, R. Whear, J. Busfield, & M. Klüppel, (2020). "Modeling the Full Time-Dependent Phenomenology of Filled Rubber for Use in Anti-Vibration Design". *Polymers*, **12** (4), 841.

[148] J. Vorel & Z.P. Bažant, (2014). "Review of Energy Conservation Errors in Finite Element Softwares Caused by Using Energy-Inconsistent Objective Stress Rates". *Advances in Engineering Software*, **72**, 3-7.

149  H. Müller & B. Nau, (1998). *Fluid Sealing Technology: Principles and Applications*. CRC Press.

150  Y. Lou, A. Robisson, S. Cai, & Z. Suo, (2012). "Swellable elastomers under constraint". *Journal of Applied Physics*, **112**, 034906.

151  B. Nau, (1987). "The State of the Art of Rubber-Seal Technology". *Rubber Chemistry and Technology*, **60** (3), 381-416.

152  B. Nau, (1999). "An historical review of studies of polymeric seals in reciprocating hydraulic systems". *Proceedings of the Institution of Mechanical Engineers, Part J: Journal of Engineering Tribology*, **213** (3), 215-226.

153  R. Flitney, (2014). *Seals and Sealing Handbook*. 6th Edition. Elsevier. USA.

154  B. Lorenz, (2012). *Contact Mechanics and Friction of Elastic Solids on Hard and Rough Substrates*. PhD Thesis, Rheinisch-Westphalia Technical University of Aachen, Germany.

155  K. Braden, (2016). "Packer Elements". Schlumberger Technology Corporation. GEMS Report 100850803.

156  T. Wu, H. Yang, & J. Zhang, (2016). "Test Plan and Report: 13-3/8 (68-72) Blueplug Max CMR Element Test – V3". Schlumberger Technology Corporation. GEMS Report 102790320.

157  American Petroleum Institute, (2015). *Packers and Bridge Plugs*, 3rd Edition. API Specification 11D1.

158  International Organization for Standardization, (2008). *Downhole equipment – Packers and bridge plugs*. ISO Standard No. 14310:2008.

159  Q. Liu, Z. Wang, Y. Lou, & Z. Suo, (2014). "Elastic leak of a seal". *Extreme Mechanics Letters*, **1**, 54-61.

160  B. Druecke, (2018). "Mechanics of Swellable Elastomeric Seals". Massachusetts Institute of Technology. PhD Thesis. https://dspace.mit.edu/handle/1721.1/115609. Accessed Dec. 16, 2019.

161  B. Druecke, E.B. Dussan, N. Wicks, & A.E. Hosoi, (2015). "Large Elastic Deformation as a Mechanism for Soft Seal Leakage". *Journal of Applied Physics*, **117** (10), 104511.

162  H. Estrada & I. Parsons, (1999). "Strength and leakage finite element analysis of a GFRP flange joint". *International Journal of Pressure Vessels and Piping*, **76** (8), 543-550.

163  K.L. Johnson, (1985). *Contact Mechanics*. Cambridge University Press. Cambridge, UK.

164  P.B. Lindley, (1967). "Compression characteristics of laterally unrestrained 'O' rings". *Journal of the Institution of the Rubber Industry*, **1**, 202-213.

165  A.F. George, A. Strozzi, & J.I. Rich, (1987). "Stress fields in a compressed unconstrained elastomeric O-ring seal and a comparison of computer predictions and experimental results". *Tribology International*, **20** (5), 237-247.

166  E. Dragoni & A. Strozzi, (1988). "Analysis of an Unpressurized, Laterally Restrained, Elastomeric O-Ring Seal". *Journal of Tribology*, **110** (2), 193-200.

167  E. Dragoni & A. Strozzi, (1989). "Theoretical Analysis of an Unpressurized Elastomeric O-ring Seal Inserted into a Rectangular Groove". *Wear*, **130** (1), 41-51.

168  G.K. Nikas, (2003). "Analytical study of the extrusion of rectangular elastomeric seals for linear hydraulic actuators". *Proceedings of the Institution of Mechanical Engineers, Part J: Journal of Engineering Tribology*, **217** (5), 365-374.

169  R. Eshel, (1984). "Prediction of Extrusion Failures of O-Ring Seals". *ASLE Transactions*, **27** (4), 332-340.

170  A. Karaszkiewicz, (1990). "Geometry and Contact Pressure of an O-Ring Mounted in a Seal Groove". *Industrial and Engineering Chemistry Research*, **29** (10), 2134-2137.

171  H.K. Kim, J.H. Nam, J.S. Hawong, & Y.H. Lee, (2009). "Evaluation of O-ring stresses subjected to vertical and one side lateral pressure by theoretical approximation comparing with photoelastic experimental results". *Engineering Failure Analysis*, **16** (6), 1876-1882.

172 J.H. Nam, J.S. Hawong, D.C. Shin, & B.R. Mose, (2011). "A study on the behaviors and stresses of O-ring under uniform squeeze rates and internal pressure by transparent type photoelastic experiment". *Journal of Mechanical Science and Technology*, **25** (9), 2427-2438.

173 A.O. Bernard, J.S. Hawong, D.C. Shin, & B. Dong, (2015). "Contact behavior analysis of elastomeric x-ring under uniform squeeze rate and internal pressure before and after forcing-out using the photoelastic experimental hybrid method". *Journal of Mechanical Science and Technology*, **29** (5), 2157-2168.

174 N.I. Muskhelishvili, (1953). *Some Basic Problems of the Mathematical Theory of Elasticity*. P. Noordhoff, Ltd., Groningen, Netherlands.

175 D. Wu, S. Wang, & X. Wang, (2017). "A novel stress distribution analytical model of O-ring seals under different properties of materials". *Journal of Mechanical Science and Technology*, **31** (1), 289-296.

176 M. Beghini, L. Bertini, C. Santus, A. Guglielmo, & G. Mariotti, (2015). "Partially open crack model for leakage pressure analysis of bolted metal-to-metal flange". *Engineering Fracture Mechanics*, **144**, 16-31.

177 D. Broek, (1989). *The Practical Use of Fracture Mechanics*. Springer Netherlands.

178 R. Brighenti & F. Artoni, (2016). "A Fracture Mechanics Based Model for the Analysis of Seal Effectiveness". *Fatigue and Fracture of Engineering Materials and Structures*, **39** (12), 1445-1460.

179 B. Druecke, D.M. Parks, & A.E. Hosoi, (2018). "Effect of compressibility and aspect ratio on performance of long elastic seals". https://arxiv.org/pdf/1707.08166.pdf. (Pre-print).

180 S.A. Al-Hiddabi, T. Pervez, S.Z. Qamar, F.K. Al-Jahwari, F. Marketz, S. Al-Houqani, & M. van de Velden, (2015). "Analytical model of elastomer seal performance in oil wells". *Applied Mathematical Modelling*, **39** (10-11), 2836-2848.

181 P. Thirion, (1948). "The Coefficients of Adhesion of Rubber". *Rubber Chemistry and Technology*, **21** (2), 505-515.

182 A. Schallamach, (1953). "The Load Dependence of Rubber Friction". *Rubber Chemistry and Technology*, **26** (2), 297-301.

183 E.F. Yanes, J.J.C. Busfield, N. Pugno, R. Manson, H.L. Chen, & J. Ramier, (2019). "Application of Rubber Friction to FEA Models of Rubber Sealing". In *Constitutive Models for Rubber XI*, Proceedings of the 11th European Conference on Constitutive Models for Rubber, Nantes, France, June 25-27, Eds: B. Huneau, J.-B. Le Cam, Y. Marco, & E. Verron. CRC Press, Boca Raton, Florida.

184 F. Bottiglione, G. Carbone, L. Mangialardi, & G. Mantriota, (2009). "Leakage mechanism in flat seals". *Journal of Applied Physics*, **106** (10), 104902.

185 B. Lorenz & B.N.J. Persson, (2009). "Leak rate of seals: Comparison of theory with experiment". *Europhysics Letters*, **86** (4), 44006.

186 B. Lorenz & B.N.J. Persson, (2010). "Leak rate of seals: Effective-medium theory and comparison with experiment". *The European Physical Journal E*, **31** (2), 159-167.

187 B.N.J. Persson, (2016). "Leakage of Metallic Seals: Role of Plastic Deformations". *Tribology Letters*, **63** (3), 42.

188 I. Green & C. English, (1992). "Analysis of Elastomeric O-ring Seals in Compression Using the Finite Element Method". *Tribology Transactions*, **35** (1), 83-88.

189 K. Alzebdeh, T. Pervez, & S.Z. Qamar, (2010). "Finite Element Simulation of Compression of Elastomeric Seals in Open Hole Liners". *Journal of Energy Resources Technology*, **132** (3), 031002.

190 C. Gong, W. Ding, K. Soga, K.M. Mosalam, & Y. Tuo, (2018). "Sealant behavior of gasketed segmental joints in shield tunnels: An experimental and numerical study". *Tunnelling and Underground Space Technology*, **77**, 127-141.

191   T. Wu, (2005). "Stress and Sealing Performance Analysis of Containment Vessel". *Proceedings of ASME Pressure Vessels and Piping Division Conference*, July17th-21st, Denver, CO, USA.

192   X.-G. Song, L. Wang, & Y. Park, (2009). "Analysis and optimization of nitrile butadiene rubber sealing mechanism of ball valve". *Transactions of Nonferrous Metals Society of China*, **19** (Supplement 1), s220-s224.

193   H. Zhang & J. Zhang, (2016). "Static and Dynamic Sealing Performance Analysis of Rubber D-Ring Based on FEM". *Journal of Failure Analysis and Prevention*, **16** (1), 165-172.

194   J. Jung, I. Hwang, & D. Lee, (2017). "Contact Pressure and Strain Energy Density of Hyperelastic U-shaped Monolithic Seals under Axial and Radial Compressions in an Insulating Joint: A Numerical Study". *Applied Sciences*, **7** (8), 792.

195   G. Hu, G. Wang, L. Dai, P. Zhang, M. Li, & Y. Fu, (2018). "Sealing Failure Analysis on V-Shaped Sealing Rings of an Inserted Sealing Tool for Multistage Fracturing Processes". *Energies*, **11** (6), 1432.

196   L.-Q. Wang, Z.-L. Wei, S.-M. Yao, Y. Guan, & S.-K. Li, (2018). "Sealing Performance and Optimization of a Subsea Pipeline Mechanical Connector", *Chinese Journal of Mechanical Engineering*, **31**, 18.

197   SIMULIA, (2020). "Pressure penetration loading with surface-based contact". In *Abaqus R2020 Theory Guide*. Dassault Systèmes Simulia Corp. Providence, Rhode Island, USA.

198   R. Möller & M. Stey, (2004). "Dichtungsausgelung mit Abaqus: Ein Ansatz zur Berechnungung der 'Pressure Penetration' in 3D". *ABAQUS 2004 User's Conference Proceedings*, September 20th-21st Königswinter, Germany.

199   A.J. Slee, D.T. Gethin, J. Stobbart, & S.J. Hardy, (2014). "Case Study on a Complex Seal Design for a High Pressure Vessel". *Proceedings of the ASME Pressure Vessels and Piping Conference*, July 20th-24th, Anaheim, CA.

200   X. Li, J. Wan, X. Du, & H. Xiao, (2015). "Structure Analysis of Flexible Pipe End Fitting Seal System". *Proceedings of the ASME 2015 34th International Conference on Ocean, Offshore, and Arctic Engineering*, May 31st-June 5th , St. John's Newfoundland, Canada.

201   U.S. Fernando & G.K. Karabelas, (2014). "Analysis of End Fitting Barrier Seal Performance in High Pressure Unbonded Flexible Pipes". *Proceedings of the ASME 2014 33rd International Conference on Ocean, Offshore, and Arctic Engineering*, June 8th-13th , San Francisco, CA.

202   L. Tang, W. He, X. Zhu, & Y. Zhou, (2019). "Sealing Performance Analysis of an End Fitting for Marine Unbonded Flexible Pipes Based on Hydraulic-Thermal Finite Element Modeling". *Energies*, **12** (11), 2198.

203   L. Tang, W. He, X. Zhu, & Y. Zhou, (2020). "Sealing Performance of the End Fitting of a Marine Unbonded Flexible Pipe under Pressure Penetration". *Journal of Applied and Computational Mechanics*, **6** (3), 543-553.

204   G. Hu, G. Wang, M. Li, X. He, & W. Wu, (2018). "Study on sealing capacity of packing element in compression packer". *Journal of the Brazilian Society of Mechanical Sciences and Engineering*, **40** (9), 438.

205   B. Zhao, Y.J. Zhao, X.Y. Wu, & H.C. Xiong, (2018). "Sealing performance analysis of P-shape seal with fluid pressure penetration loading method". *IOP Conference Series: Materials Science and Engineering*, **397**, 012126.

206   C. Gong & W. Ding, (2018). "A computational framework to predict the water-leakage pressure of segmental joints in underwater shield tunnels using an advanced finite element method". *International Journal for Numerical and Analytical Methods in Geomechanics*, **42** (16), 1957-1975.

207   C. Gong, W. Ding, K. Soga, & K.M. Mosalam, (2019). "Failure mechanism of joint waterproofing in precast segmental tunnel linings". *Tunnelling and Underground Space Technology*, **84**, 334-352.

208   C. Gong, W. Ding, & D. Xie, (2020). "Parametric investigation on the sealant behavior of

tunnel segmental joints under water pressurization". *Tunnelling and Underground Space Technology*, **97**, 103321.

209    Institution of Civil Engineers. https://www.ice.org.uk/ICEDevelopmentWebPortal/media/Events/Lectures/shieldhall-tunnel.jpg?ext=.jpg.

210    Y. Gorash, W. Dempster, W.D. Nicholls, R. Hamilton, & A.A. Anwar, (2016). "Study of mechanical aspects of leak tightness in a pressure relief valve using advanced FE-analysis". *Journal of Loss Prevention in the Process Industries*, **43**, 61-74.

211    Y. Gorash, A. Bickley, & F. Gozalo, (2017). "Improvement of leak tightness for swellable elastomeric seals through the shape optimization". In *Constitutive Models for Rubber X: Proceedings of the 10th ECCMR*, Munich, Germany, August 28th-31st, 2017. Eds. A. Lion & M. Johlitz. CRC Press, Boca Raton, FL.

212    Y. Gorash, A. Bickley, & F. Gozalo, (2018). "Application of the CEL Approach to Consider FSI for the Assessment of Leak Tightness for Elastomeric Seals". *Proceedings of the ASME 2018 Pressure Vessels & Piping Conference*, July 15th-20th, Prague, Czech Republic.

213    M. Raous, (1999). "Quasistatic Signorini Problem with Coulomb Friction and Coupling to Adhesion". In *New Developments in Contact Problems*. Eds. P. Wriggers & P. Panatiotopoulos. Springer-Verlag, Vienna. Chapter 3, Section 1.4.5.

214    P. Wriggers, (2006). "Discretization, Large Deformation Contact". In *Computational Contact Mechanics*, Spring, Berlin, Heidelberg. Section 9.5.7 (Press-fit Problem).

215    N. Morrison, Y. Gorash, & R. Hamilton, (2018). "Comparison of Single-Solver FSI Techniques for the FE-Prediction of a Blow-Off Pressure for an Elastomeric Seal". *6th European Conference on Computational Mechanics*, June 11th-15th, Glasgow, UK.

216    L. Foucard, A. Aryal, R. Duddu, & F. Vernerey, (2015). "A coupled Eulerian–Lagrangian extended finite element formulation for simulating large deformations in hyperelastic media with moving free boundaries". *Computer Methods in Applied Mechanics and Engineering*, **283**, 280-302.

217    J. Parraga, (2015). *Tutorial 24: Threaded Connector & Pressure Penetration*. Available from simuleon.com. https://info.simuleon.com/abaqus-tutorial-threaded-connector-pressure-penetration. Accessed August 6th, 2020.

218    S. Morlacchi, (2014). *Tutorial Number 17: CEL model of a boat in a wavy sea*. Available from simuleon.com. https://info.simuleon.com/abaqus-tutorial-cel-model-of-a-boat-floating. Accessed August 6th, 2020.

219    Y. Gorash, (2018). "CEL simulation of a leakage through a SEAL". https://www.youtube.com/watch?v=60Jve9cA-5w. Accessed August 6th, 2020.

220    L.R.G. Treloar, (1944). "Stress-strain data for vulcanised rubber under various types of deformation". *Transactions of Faraday Society*, **40**, 59-70.

221    M. Fujikawa, N. Maeda, J. Yamabe, & M. Koishi, (2020). "Performance Evaluation of Hyperelastic Models for Carbon-Black-Filled SBR Vulcanizates". *Rubber Chemistry & Technology*, **93** (1), 142-156.

222    W. Press, B. Flannery, S. Teukolsky, & W. Vetterlin, (1992). *Numerical Recipes in FORTRAN 90: The Art of Parallel Scientific Computing*. 2nd Ed. Cambridge University Press, Cambridge, UK, 1992. Section 15.5.

223    SIMULIA, (2020). "Hyperelastic behavior of rubberlike materials". In *Abaqus R2020 Materials Manual*. Dassault Systèmes Simulia Corp. Providence, Rhode Island, USA.

224    SIMULIA, (2020). "Mass scaling". In *Abaqus R2020 Analysis Guide*. Dassault Systèmes Simulia Corp. Providence, Rhode Island, USA.

225    SIMULIA, (2020). "Stress rates". In *Abaqus R2020 Theory Manual*. Dassault Systèmes Simulia Corp. Providence, Rhode Island, USA.

226    Anonymous. Veryst Engineering. https://www.veryst.com/services/testing/material-test-library/uniaxial-tension-testing.

227   B. Engel & R. Steinheimer, (2008). "Obtaining more precise flow curves from uniaxial tensile tests for FE-Simulations". *International Conference on Technology of Plasticity*, 2253-2258.

228   S.Y. Yang & W. Tong, (2009). "A finite element analysis of a tapered flat sheet tensile specimen". *Experimental Mechanics*, **49** (2), 317-330.

229   B. Song, B. Sanborn, D. Susan, K. Johnson, J. Dabling, J. Carroll, A. Brink, S. Grutzik, & A. Kustas, (2019). "Correction of specimen strain measurement in Kolsky tension bar experiments on work-hardening materials". *International Journal of Impact Engineering*, **132**, 103328.

230   H. Mei, L. Lang, K. Liu, & X. Yang, (2018). "Evaluation study on iterative inverse modeling procedure for determining post-necking hardening behavior of sheet metal at elevated temperature". *Metals*, **8** (12), 1044.

231   A. Arriaga, J.M. Lazkano, R. Pagaldai, A.M. Zaldua, R. Hernandez, R. Atxurra, & A. Chrysostomou, (2007). "Finite-element analysis of quasi-static characterisation tests in thermoplastic materials: Experimental and numerical analysis results correlation with ANSYS". *Polymer Testing*, **26** (3), 284-305.

232   J. Day & K. Miller, (2000). "Equibiaxial Stretching of Elastomeric Sheets, An Analytical Verification of Experimental Technique". *ABAQUS 2000 User's Conference Proceedings*, Newport, RI. May 30th - June 2nd, 2000.

233   L.R.G. Treloar, (1948). "Stresses and birefringence in rubber subjected to general homogeneous strain". *Proceedings of the Physical Society*, **60** (2), 135-144.

234   M. Fujikawa, N. Maeda, J. Yamabe, Y. Kodama, & M. Koishi, (2014). "Determining Stress-Strain in Rubber with In-Plane Biaxial Tensile Tester". *Experimental Mechanics*, **54** (9), 1639-1649.

235   ASTM D412-16, (2016). *Standard Test Methods for Vulcanized Rubber and Thermoplastic Elastomers – Tension*. ASTM International, West Conshohocken, Pennsylvania, USA.

236   R. Brown, (2006). *Physical Testing of Rubber*. 4th Ed. Spring, New York.

237   D. De Focatiis, (2003). *Inverting domes for needle-less powder injection*. PhD Thesis. University of Oxford.

238   D. Zwillinger, (2003). *CRC Standard Mathematical Tables and Formulae*. 31st Edition. CRC Press.

239   R.W. Ogden, (1972). "Large deformation isotropic elasticity – on the correlation of theory and experiment for incompressible rubberlike solids". *Proceedings of the Royal Society. Series A. Mathematical and Physical Sciences*, **326** (1567), 565-584.

240   SIMULIA, (2020). "Choosing the master and slave roles in a two-surface contact pair". In *Abaqus R2020 Interactions Manual*. Dassault Systèmes Simulia Corp. Providence, Rhode Island, USA.

241   SIMULIA, (2020). "Adjusting contact controls in Abaqus/Standard". In *Abaqus R2020 Interactions Manual*. Dassault Systèmes Simulia Corp. Providence, Rhode Island, USA.

242   C. Obbink-Huizer, (2016). "6 Tips solving non convergence with Abaqus FEA". *Simuleon FEA blog*. https://info.simuleon.com/blog/6-tips-solving-non-convergence-with-abaqus-fea.

243   SIMULIA, (2020). "Automatic stabilization of unstable problems". In *Abaqus R2020 Interactions Manual*. Dassault Systèmes Simulia Corp. Providence, Rhode Island, USA.

244   R. Weyler, J. Oliver, T. Sain, & J.C. Cante, (2012). "On the contact domain method: A comparison of penalty and Lagrange multiplier implementations". *Computer Methods in Applied Mechanics and Engineering*, **205-208**, 68-82.

245   E. Yanes, N.M Pugno, J. Ramier, B. Berryhill, & J.J.C. Busfield, (2021). "Characterising the friction coefficient between rubber O-rings and a rigid surface under extreme pressures". *Polymer Testing*, **104**, 107378.

246   E. Yanes, (2020). Personal correspondence from a friction data library for oilfield sealing materials.

247  SIMULIA, (2020). "Solid isoparametric quadrilaterals and hexahedra". In *Abaqus R2020 Theory Manual*. Dassault Systèmes Simulia Corp. Providence, Rhode Island, USA.

248  SIMULIA, (2020). "UVARM". In *Abaqus R2020 User Subroutines Manual*. Dassault Systèmes Simulia Corp. Providence, Rhode Island, USA.

249  Z. Wang, C. Chen, Q. Liu, Y. Lou, & Z. Suo, (2017). "Extrusion, slide, and rupture of an elastomeric seal". *Journal of the Mechanics and Physics of Solids*, **99**, 289-303.

250  SIMULIA, (2020). "Pressure penetration loading". In *Abaqus R2020 Interactions Manual*. Dassault Systèmes Simulia Corp. Providence, Rhode Island, USA.

251  SIMULIA, (2020). "Restarting an analysis". In *Abaqus R2020 Analysis Manual*. Dassault Systèmes Simulia Corp. Providence, Rhode Island, USA.

252  SIMULIA, (2020). "DLOAD". In *Abaqus R2020 User Subroutines Manual*. Dassault Systèmes Simulia Corp. Providence, Rhode Island, USA.

253  SIMULIA, (2020). "VDLOAD". In *Abaqus R2020 User Subroutines Manual*. Dassault Systèmes Simulia Corp. Providence, Rhode Island, USA.

254  SIMULIA, (2020). "Contact constraint enforcement methods in Abaqus/Explicit". In *Abaqus R2020 Interactions Manual*. Dassault Systèmes Simulia Corp. Providence, Rhode Island, USA.

255  ABAQUS, Inc., (2004). "Automatic time incrementation and stability". In *Getting Started with ABAQUS/Explicit: Keywords Version*. Dassault Systèmes Simulia Corp. Providence, Rhode Island, USA.

256  L. Chan, (2021). EiE Elastomer Property Library. Schlumberger Technology Corporation. GEMS 103132319 Rev. 4. The value cited here is consistent with https://promo.parker.com/promotionsite/oring-ehandbook/us/en/ehome/Coefficient-of-Thermal-Expansion.

257  SIMULIA, (2020). "Contact Formulations and Numerical Methods". *Abaqus R2020 Interactions Manual*. Dassault Systèmes Simulia Corp. Providence, Rhode Island, USA.

258  ANSI/ASME B1.1-2003, (2003). "Unified Inch Screw Threads (UN and UNR Thread Form)". American Society of Mechanical Engineers. The standard is also well-documented in the book *Machinery's Handbook* by Industrial Press.

259  Guangzhou JST Seals, Co., Ltd. https://jst-seals.en.alibaba.com/. Accessed Aug. 23rd, 2021.

260  Cameron Brookshire. https://www.slb.com/companies/cameron. Accessed Aug. 23rd, 2021.

261  A.F.S.M. Amin, M.S. Alam, & Y. Okui, (2002). "An improved hyperelasticity relation in modeling viscoelasticity response of natural and high damping rubbers in compression: experiments, parameter identification and numerical verification". *Mechanics of Materials*, **34** (2), 75-95.

262  Parker Hannafin Corp., (2021). "Selecting the Right O-Ring Seal Squeeze Ratio". http://blog.parker.com/selecting-the-right-o-ring-seal-squeeze-ratio. Accessed Sep. 18th, 2021.

263  C.G. Robertson & N.J. Hardman, (2021). "Nature of Carbon Black Reinforcement of Rubber: Perspective on the Original Polymer Nanocomposite". *Polymers* **13** (4), 538.

264  A. Anssari-Benam, A. Bucchi, C.O. Horgan, & G. Saccomandi, (2021). "Assessment of a New Isotropic Hyperelastic Constitutive Model for a Range of Rubberlike Materials and Deformations". *Rubber Chemistry & Technology*. Online only.

265  J. Heczko, R. Kottner, & A. Kossa, (2021). "Rubber ageing at elevated temperature – Model calibration". *European Journal of Mechanics / A Solids*, **89**, 104320.

266  X. Ren & W. Kyei-Manu, (2017). Oil Swell Packer Predictor. Schlumberger Technology Corporation. GEMS Report 101335451.

267  Z. Wang, Q. Liu, Y. Lou, H. Jin, & Z. Suo, (2015). "Elastic Leak for a Better Seal". *Journal of Applied Mechanics*, **82** (8), 081010.

268  B. Eatwell, (2010). "ET201006340 - 8.13 X 5.50 APS SWELL PACKER W/ COMPOUND C900-7 (RETEST)". Schlumberger Technology Corporation. GEMS Report 100830885.

269     Axel Physical Testing Services, (Unknown). "Compression or Biaxial Extension?" http://www.axelproducts.com/downloads/CompressionOrBiax.pdf. Accessed Oct. 9th, 2021.

270     S.W. Stratton, (1912). "The Testing of Mechanical Rubber Goods". *Circular of the Bureau of Standards*, **38**, 1-38. https://archive.org/details/circularofbureau38unse/mode/1up.

271     W.B. Weigand & H.A. Braendle, (1923). "Persistence of Calendar Grain after Vulcanization". *Industrial and Engineering Chemistry*, **15** (3), 259-262.

272     M. Brieu, J. Diani, N. Bhatnagar, (2007). "A New Biaxial Tension Test Fixture for Uniaxial Testing Machine – A Validation for Hyperelastic Behavior of Rubber-like Materials". *Journal of Testing and Evaluation*, **35** (4), 364-372.

273     J. Day & K. Miller, (Unknown). "Equibiaxial Stretching of Elastomeric Sheets, An Analytical Verification of Experimental Technique". http://www.axelproducts.com/downloads/BiaxialExtension.pdf.

274     J.R. Sheppard & W.J. Clapson, (1932). "Compression Stress Strain of Rubber". *Industrial Engineering and Chemistry*, **24** (7), 782-790.

275     P.A. Przybylo & E.M. Arruda, (1998). "Experimental Investigations and Numerical Modeling of Incompressible Elastomers during Non-homogeneous deformations". *Rubber Chemistry and Technology*, **71** (4), 730-749.

276     SIMULIA, (2020). "UHYPER". In *Abaqus R2020 User Subroutines Manual*. Dassault Systèmes Simulia Corp. Providence, Rhode Island, USA.

277     S.A. Chester, (2008). VUMAT and UMAT for a neo-Hookean material. https://web.njit.edu/~sac3/Software.html. Accessed Oct. 3rd, 2022.

278     SIMULIA, (2019). "WRITING USER SUBROUTINES WITH ABAQUS," Dassault Systèmes Simulia Corp. Providence, Rhode Island, USA. https://eduspace.3ds.com/CompanionManager/ui/#/course/en/222402//false/false/publicSearch//abaqus//. Accessed Oct. 3rd, 2022.

279     SIMULIA, (2020). "VUMAT". In *Abaqus R2020 User Subroutines Manual*. Dassault Systèmes Simulia Corp. Providence, Rhode Island, USA.

# Appendix A: A gen-Yeoh SEF UHYPER Subroutine for Abaqus/Standard

```fortran
C ***********************************************************************
C  Author:    Travis Hohenberger
C  Date:      2021-10-06
C  E-mail:    twhohen@gmail.com
C  Version:   0 (see bottom of code for version history)
C ***********************************************************************
C
C  This subroutine is built from the template in Simulia (2020) (see re-
C  ferences at bottom of page). The strain-energy function is the gener-
C  alized-Yeoh model described in Hohenberger et al. (2019) and has the
C  form:
C
C  W = K1*(I1-3)^m + K2*(I1-3)^p + K3*(I1-3)^q + (1/D1)*(J-1)^2
C
C  where K1, K2, K3, m, p, q are distortional fitting parameters and D1
C  is a volumetric fitting parameter. I1 is the first invariant of the
C  modified stretch tensor. J is the volumetric ratio. Refer to Holzapf-
C  el (2000) for theoretical details.
C
C ***********************************************************************
      SUBROUTINE UHYPER(BI1,BI2,AJ,U,UI1,UI2,UI3,TEMP,NOEL,CMNAME,
     1                  INCMPFLAG,NUMSTATEV,STATEV,NUMFIELDV,
     2                  FIELDV,FIELDVINC,NUMPROPS,PROPS)
C
      INCLUDE 'ABA_PARAM.INC'
C
      CHARACTER*80 CMNAME
      DIMENSION U(2),UI1(3),UI2(6),UI3(6),STATEV(*),FIELDV(*),
     1          FIELDVINC(*),PROPS(*)
C
C     PARAMETERS
C     ----------
      REAL*8    zero,     one,      two,      three
      PARAMETER( zero=0.d0, one=1.d0, two=2.d0, three=3.d0 )
C
C     LOCAL VARIABLES
C     ---------------
      REAL*8 k1, k2, k3, em, pe, qu, d1
C
C ***********************************************************************
C ------------------------ MODEL PARAMETERS -------------------------
C ***********************************************************************
      k1 =  props(1)
      k2 =  props(2)
      k3 =  props(3)
      em =  props(4)
      pe =  props(5)
      qu =  props(6)
      d1 =  props(7)
C
C ***********************************************************************
C ---------------------- STRAIN-ENERGY FUNCTION ----------------------
C ***********************************************************************
      IF (d1.GT.zero) THEN
         U(1) =   k1*(BI1-three)**em +
     $            k2*(BI1-three)**pe +
     $            k3*(BI1-three)**qu +
     $            1/d1*(AJ-one)**two
       ELSE
         U(1) =   k1*(BI1-three)**em +
     $            k2*(BI1-three)**pe +
     $            k3*(BI1-three)**qu
       END IF
C
C ***********************************************************************
C -- IF-THEN statement initializes dU/dI1 to finite value if EM < 1.0 --
C ***********************************************************************
      IF (BI1.EQ.three .AND. em.LT.one) THEN
        UI1(1) = one
       ELSE
        UI1(1) = em*k1*(BI1-three)**(em-one) +
     $           pe*k2*(BI1-three)**(pe-one) +
     $           qu*k3*(BI1-three)**(qu-one)
       END IF
C
```

```fortran
C ************************************************************************
C ---------- IF-THEN statement prevents d2U/dI1 --> Infinity -----------
C ************************************************************************
      IF (BI1.EQ.three .AND.
     $   (em.LT.two .OR. pe.LT.two .OR. qu.LT.two)) THEN
         UI2(1) = zero
      ELSE
         UI2(1) = em*(em-one)*k1*(BI1-three)**(em-two) +
     $            pe*(pe-one)*k2*(BI1-three)**(pe-two) +
     $            qu*(qu-one)*k3*(BI1-three)**(qu-two)
      END IF
C
C ************************************************************************
C ------------------ DERIVATIVES OF COMPRESSIBLE TERM ------------------
C ************************************************************************
      IF (d1.GT.zero) THEN
         UI1(3) = two/d1*(AJ-one)
         UI2(3) = two/d1
      ELSE
         UI1(3) = zero
         UI2(3) = zero
      END IF
C
C ************************************************************************
C ----------------- SET NON-ESSENTIAL VARIABLES TO ZERO ---------------
C ************************************************************************
      U(2)   = zero
      UI1(2) = zero
      UI2(2) = zero
      UI2(4) = zero
      UI2(5) = zero
      UI2(6) = zero
      UI3(1) = zero
      UI3(2) = zero
      UI3(3) = zero
      UI3(4) = zero
      UI3(5) = zero
      UI3(6) = zero
C
      RETURN
C
      END SUBROUTINE UHYPER
C ************************************************************************
C  References:
C
C  T.W. Hohenberger, R.J. Windslow, N.M. Pugno, & J.J.C. Busfield, (2019
C  ). "A Constitutive Model for both Low and High Strain Nonlinearities
C  in Highly Filled Elastomers and Implementation with User-Defined Mat-
C  erial Subroutines in Abaqus". Rubber Chemistry and Technology, 92 (4)
C  , 653-686.
C
C  G.A. Holzapfel, (2000). Nonlinear Solid Mechanics: A Continuum Appro-
C  ach for Engineering. John Wiley & Sons, Ltd.
C
C  SIMULIA, (2020). "UHYPER" In: Abaqus R2020 User Subroutines Manual.
C  Dassault Systèmes Simulia Corp., Providence, RI, USA.
C
C ************************************************************************
C  Revision History
C
C  0: Initial release.
C
C ************************************************************************
```

# Appendix B: A gen-Yeoh SEF VUMAT Subroutine for Abaqus/Explicit

```
C **********************************************************************
C  Authors:  Travis Hohenberger & Richard Windslow
C  Date:     2021-10-06
C  E-mail:   twhohen@gmail.com
C  Version:  4 (see bottom of code for version history)
C **********************************************************************
C
C This subroutine builds on the Neo-Hookean VUMATs published in Bergst-
C rom (2015), Chester (2008), and Simulia (2020) (see references at bo-
C ttom of page). The strain-energy function is the generalized-Yeoh mo-
C del described in Hohenberger et al. (2019) and has the form:
C
C  W = K1*(I1-3)^m + K2*(I1-3)^p + K3*(I1-3)^q + (1/D1)*(J-1)^2
C
C where K1, K2, K3, m, p, q are distortional fitting parameters and D1
C is a volumetric fitting parameter. I1 is the first invariant of the
C modified stretch tensor. J is the volumetric ratio. Refer to Holzapf-
C el (2000) for theoretical details.
C
C **********************************************************************
      SUBROUTINE VUMAT(
     1     nblock, ndir, nshr, nstatev, nfieldv, nprops, lanneal,
     2     stepTime, totalTime, dt, cmname, coordMp, charLength,
     3     props, density, strainInc, relSpinInc,
     4     tempOld, stretchOld, defgradOld, fieldOld,
     5     stressOld, stateOld, enerInternOld, enerInelasOld,
     6     tempNew, stretchNew, defgradNew, fieldNew,
     7     stressNew, stateNew, enerInternNew, enerInelasNew )
C
      INCLUDE 'vaba_param.inc'
C
      DIMENSION props(nprops), density(nblock), coordMp(nblock,*),
     1          charLength(nblock), strainInc(nblock,ndir+nshr),
     2          relSpinInc(nblock,nshr), tempOld(nblock),
     3          stretchOld(nblock,ndir+nshr),
     4          defgradOld(nblock,ndir+nshr),
     5          fieldOld(nblock,nfieldv), stressOld(nblock,ndir+nshr),
     6          stateOld(nblock,nstatev), enerInternOld(nblock),
     7          enerInelasOld(nblock), tempNew(nblock),
     8          stretchNew(nblock,ndir+nshr),
     9          defgradNew(nblock,ndir+nshr),
     1          fieldNew(nblock,nfieldv),
     2          stressNew(nblock,ndir+nshr), stateNew(nblock,nstatev),
     3          enerInternNew(nblock), enerInelasNew(nblock)
C
      CHARACTER*80 cmname
C
C     PARAMETERS
C     ----------
      REAL*8   oneThrd, half, twoThrd, zero, one, two, three,
     $         thresh
      PARAMETER(oneThrd=1.d0/3.d0, half=0.5d0, twoThrd=2.d0/3.d0,
     $         zero=0.d0, one=1.d0, two=2.d0, three=3.d0,
     $         thresh=10.d0**-12.d0)
C
C     LOCAL VARIABLES
C     ---------------
      REAL*8 g0      , k0      , twoG    , lmda    , trace   , d1      ,
     $       k1      , k2      , k3      , em      , pe      , qu      ,
     $       Bxx     , Byy     , Bzz     , Bxy     , Bxz     , Byz     ,
     $       BbarXX  , BbarYY  , BbarZZ  , BbarXY  , BbarXZ  , BbarYZ  ,
     $       dBbarXX , dBbarYY, dBbarZZ, dBbarXY, dBbarXZ, dBbarYZ ,
     $       J       , J23     , duDi1   , duDi3   , I1      , g1      ,
     $       p0      , j1      , u1
C
      k1 = props(1)
      k2 = props(2)
      k3 = props(3)
      em = props(4)
      pe = props(5)
      qu = props(6)
      d1 = props(7)
C
      g0 = two * k1
      k0 = two / d1
```

```
C
C        ******************************************************************
C        ------------ INITIALIZE MATERIAL AS LINEARLY ELASTIC--------------
C        ******************************************************************
C
         twoG = two * g0
         lmda = k0 - twoG * oneThrd
C
         IF (totalTime.EQ.0.0) THEN
C
            DO k = 1,nblock
               trace = strainInc(k,1) + strainInc(k,2) + strainInc(k,3)
               stressNew(k,1) = stressOld(k,1) + twoG*strainInc(k,1) +
     $                          lmda*trace
               stressNew(k,2) = stressOld(k,2) + twoG*strainInc(k,2) +
     $                          lmda*trace
               stressNew(k,3) = stressOld(k,3) + twoG*strainInc(k,3) +
     $                          lmda*trace
               stressNew(k,4) = stressOld(k,4) + twoG*strainInc(k,4)
            END DO
C
            RETURN
C
         END IF
C
C        ******************************************************************
C        ----------- START LOOP FOR MATERIAL POINT CALCULATIONS -----------
C        ******************************************************************
C
         DO k = 1,nblock
C
C           CALCULATE LEFT CAUCHY-GREEN STRAIN TENSOR, B = U*U
C           --------------------------------------------------
            Bxx = stretchNew(k,1) * stretchNew(k,1) +
     $            stretchNew(k,4) * stretchNew(k,4)
            Byy = stretchNew(k,2) * stretchNew(k,2) +
     $            stretchNew(k,4) * stretchNew(k,4)
            Bzz = stretchNew(k,3) * stretchNew(k,3)
            Bxy = stretchNew(k,1) * stretchNew(k,4) +
     $            stretchNew(k,4) * stretchNew(k,2)
C
C           CALCULATE J = |F| = |U|
C           -----------------------
C
            J = stretchNew(k,1) * (stretchNew(k,2)*stretchNew(k,3)) -
     $          stretchNew(k,4) * (stretchNew(k,3)*stretchNew(k,4))
C
C           CALCULATE MODIFIED STRAIN TENSOR, Bbar = J^(-2/3)*B
C           ---------------------------------------------------
            J23 = J**(-twoThrd)
C
            BbarXX = J23 * Bxx
            BbarYY = J23 * Byy
            BbarZZ = J23 * Bzz
            BbarXY = J23 * Bxy
C
C           FIRST INVARIANT OF Bbar = tr(Bbar)
C           ----------------------------------
            I1 = BbarXX + BbarYY + BbarZZ
C
C           DEVIATORIC PART OF Bbar
C           -----------------------
            p0 = I1 * oneThrd
C
            dBbarXX = BbarXX - p0
            dBbarYY = BbarYY - p0
            dBbarZZ = BbarZZ - p0
            dBbarXY = BbarXY
C
C           DERIVATIVES OF STRAIN-ENERGY FUNCTION
C           -------------------------------------
            j1 = I1 - three
C
            IF (j1.LT.thresh) THEN
               duDi1 = zero
            ELSE
               duDi1 = em * k1 * j1**(em-one) +
     $                 pe * k2 * j1**(pe-one) +
     $                 qu * k3 * j1**(qu-one)
```

188

```fortran
          END IF
C
          duDi3 = two/d1 * (J - one)
C
C         COROTATIONAL CAUCHY (TRUE) STRESSES
C         -----------------------------------
          g1 = two/J * duDi1
C
          stressNew(k,1) = g1 * dBbarXX + duDi3
          stressNew(k,2) = g1 * dBbarYY + duDi3
          stressNew(k,3) = g1 * dBbarZZ + duDi3
          stressNew(k,4) = g1 * dBbarXY
C
C         UPDATE SPECIFIC INTERNAL ENERGY
C         -------------------------------
          u1 = half * ( (stressOld(k,1)+stressNew(k,1))*strainInc(k,1) +
     $                  (stressOld(k,2)+stressNew(k,2))*strainInc(k,2) +
     $                  (stressOld(k,3)+stressNew(k,3))*strainInc(k,3) +
     $                   two * (stressOld(k,4)+stressNew(k,4))*
     $                            strainInc(k,4) )
C
          enerInternNew(k) = enerInternOld(k) + u1 / density(k)
C
      END DO
C
      RETURN
C
      END SUBROUTINE VUMAT
C
C **********************************************************************
C References:
C
C J.S. Bergstrom, (2015). Mechanics of Solid Polymers: Theory and Comp-
C utational Modeling. Elsevier, Inc.
C
C S.A. Chester, (2008). VUMAT and UMAT for a neo-Hookean material. htt-
C ps://web.njit.edu/~sac3/Software.html
C
C T.W. Hohenberger, R.J. Windslow, N.M. Pugno, & J.J.C. Busfield, (2019
C ). "A Constitutive Model for both Low and High Strain Nonlinearities
C in Highly Filled Elastomers and Implementation with User-Defined Mat-
C erial Subroutines in Abaqus". Rubber Chemistry and Technology, 92 (4)
C , 653-686.
C
C G.A. Holzapfel, (2000). Nonlinear Solid Mechanics: A Continuum Appro-
C ach for Engineering. John Wiley & Sons, Ltd.
C
C Simulia, (2020). "VDLOAD". In: Abaqus R2020 User Subroutines Manual.
C Dassault Systèmes Simulia Corp., Providence, RI, USA.
C
C **********************************************************************
C Revision History
C
C 0: Initial version for beta testing performance of the VUMAT in diff-
C    erent modes of deformation with different material models (Neo-Ho-
C    okean, Yeoh, and gen-Yeoh).
C
C 1: Removed 'IF-THEN statements to enter loops for 3D case. The code
C    was converted to only cover 3D geometry. A separate 2D code will
C    be written to optimize computational efficiency.
C
C    In LOCAL VARIABLE declarations, dBbarYZ was dvBbarYZ. This did no-
C    t have significant impact on the code because later declaration of
C    the correct variable, dBbarYZ, would initialize the variable to 0.
C
C    Updated with introductory content, references, revision history,
C    and general clean-up for release to Schlumberger.
C
C 2: BUG FIX: When testing a unit cube with twist on its top face (and
C    no extension), it was found that tr(Bbar)=3 which makes j1=0 which
C    makes duDi1 --> Infinity. This was a known issue when developing
C    the UHYPER subroutine, but it was thought that the linear elastic
C    step in the VUMAT would always introduce some strain along the di-
C    agonal of Bbar; this is not the case. Therefore, an 'IF-THEN' sta-
C    tement has been added to assign a finite value to duDi1 if j1 is
C    less than 1e-12. Ideally, this value would be 0, and 0 was found
C    to work with single-precision accuracy. However, when double-prec-
C    ision was used, the solution was found to be unstable. If problems
C    occur when running this VUMAT, the first thing to check is the be-
```

189

```
C      havior of duDi1 (and possibly duDi3). It may be necessary to chan-
C      ge 1e-12 to a larger value.
C
C  3: Added PARAMETER thresh=10.d0**-12.d0 to control the threshold @ w-
C      hich duDi1=zero. This had been previously specified by manually t-
C      yping out 0.000000000001.
C
C      Removed local variable jInv since it is not used in the code.
C
C  4: Added missing parameter "zero=0.d0". The code can have problems r-
C      unning if left implicitly defined.
C
C  ********************************************************************
```

# Appendix C: An n-Block Model Fortran Code for Correction of UT Data

```fortran
PROGRAM nBlock11                                              ! v11.0
!
!     *********************************************************************
!     Author:     Travis Hohenberger
!     Date:       2019-11-04
!     E-mail:     twhohen@gmail.com
!     System:     Windows 10
!     Software:   Netbeans IDE Dev (201804200002)
!                 Java 1.8.0_101; Java Hotspot 64 Bit Server VM 25.101-b13
!                 Java Runtime Environment 1.8.0_101-b13
!     *********************************************************************
!
!     Dumbbells are often stretched in uniaxial extension to collect stre-
!     ss-strain data. When a dumbbell is gripped at a section wider than
!     its gage section, and strain is computed from displacement of the g-
!     rips, the calculated strain is lower than the actual strain in the
!     gage section. This program corrects stress-strain data when direct
!     measurement of strain (for instance, with a video extensometer) in
!     the gage section is not possible, and therefore must be estimated f-
!     rom grip (ie. crosshead) displacement. The program decomposes a dum-
!     bbell into a series of blocks as illustrated in SCHEMATIC 1. As cur-
!     rently written, the code creates 200 'n-blocks' between the upper (
!     ie. tab) and lower (ie. gage) sections.
!                                              _____
!      &&&&&&&&&&&&&&&&&&            |                            |
!      &&&&&&&&&&&&&&&&&&            |                            |
!      &&&&&&&&&&&&&&&&&&            |                            |
!      &&&&&&&&&&&&&&&&&&            |             UPPER          |
!      &&&&&&&&&&&&&&&&&& ==> Tab section   |        BLOCK        |
!      &&&&&& TAB &&&&&&            |        index = 202          |
!      &&&&&&&&&&&&&&&&&&            |           in code          |
!      &&&&&&&&&&&&&&&&&&            |_____|
!      &&&&&&&&&&&&&&&&            |_____|
!      &&&&&&&&&&&&&&&  ==> Smooth radius  |_____|
!      &&&&&&&&&&&&&&            |_____|
!      &&&&&&&&&&&& ==> Tangent of radii   |_____|   Seven
!      &&&&&&&&&&&            |_____|  ==> n-Block
!      &&&&&&&&&& ==> Smooth radius    |_____|    transitions,
!      &&&&&&&&&            |_____|    index = 2, 3, .
!      &&&&&&&&            |       |        .., 201 in code
!      &&&&&&&&            |       |
!      &&&&&&&&            |       |
!      &&&&&&&&            | LOWER |
!      & GAGE &            | BLOCK |
!      &&&&&&&&            |       |
!      &&&&&&&& ==> Gage section    | index |
!      &&&&&&&&            |  = 1  |
!      &&&&&&&&            |  in   |
!      &&&&&&&&            | code  |
!      &&&&&&&&            |_____|
!
!        (a)                          (b)
!
!     SCHEMATIC 1: (a) Quarter-dumbbell with "smooth" geometry;
!                  (b) dumbbell decomposed into "block" geometry
!
!     *********************************************************************
!
!     The code uses the incompressible form of the generalized Yeoh strai-
!     n-energy function:
!
!     W = K1*(I1-3)^m + K2*(I1-3)^p + K3*(I1-3)^q
!
!     which can be replaced by the user by changing the force equation. S-
!     ee the user guide at the end of this code for more details.
!
!     References:
!
!     Hohenberger et al, (2019). A constitutive model for both low and hi-
!     gh strain nonlinearities in highly filled elastomers and implementa-
!     tion with user-defined material subroutines in Abaqus. Rubber Chemi-
!     stry and Technology, 92 (4), 653-686.
!
!     Hohenberger & Busfield, (2022). A method to generate accurate elast-
!     ic and hyperelastic uniaxial tension stress-strain data without an
!     extensometer. Rubber Chemistry and Technology, In press.
!
!     Disclaimer: This code is not computationally optimal, but it has wo-
!                 ked for multiple cases tested by the author.
!
!     *********************************************************************
!
      IMPLICIT NONE
!
      REAL K1    , K2    , K3    , deL(202), w(202)  , t     , Delta ,&
           Fo    , Lam0  , F(202), Lam(202), ErrF(202), delNew, Fout  ,&
```

```fortran
       deLtot, ErrDel, R1        , R2      , w0         , wTab   , SigOut,&
       alpha , h1     , h2       , L0      , dh1        , dh2    , y(202),&
       Lgrip , Lbell , em       , pe      , qu         , MxErrF, DelEnd,&
       SigStore(200) , LamStore(200)    , LamFact    , ForcFac
!
       INTEGER i, j, k, int1, int2
!
!      ********************************************************************
!      - MATERIAL MODEL PARAMETERS FOR GEN-YEOH STRAIN-ENERGY FUNCTION --
!      ********************************************************************
!
       K1 =  5.38    ! MPa
       K2 = -2.85    ! MPa
       K3 =  0.40    ! MPa
       em =  0.89
       pe =  1.08
       qu =  1.85
!
!      ********************************************************************
!      ------ CONVERGENCE FACTORS FOR STRETCH AND FORCE ITERATIONS ------
!      ********************************************************************
!
       LamFact = 10.      ! Increasing values speed up convergence but can
       ForcFac = 0.1      ! result in unacceptable error. Monitor 'ErrDel'
!                         ! and 'MaxErrF' in the output window to ensure
!                         ! they remain << 1.
!
!      ********************************************************************
!      ----------- DUMBBELL DIMENSIONS (mm), SEE SCHEMATIC 2 ------------
!      ********************************************************************
!
       Lbell  = 57.5      ! Dumbbell length (half-length, die C = 57.5)
       Lgrip  = 27.899    ! Grip separation (half-length)
       L0     = 16.5      ! Gage length (half-length, die C = 16.5)
       w0     = 3.12305   ! Width of gage section (half-width)
       wTab   = 12.5      ! Width of tab (half-width, die C = 12.5)
       t      = 2.3335    ! Dumbbell thickness (not illustrated)
       R1     = 14.       ! Dumbbell radius at gage (die C = 14)
       R2     = 25.       ! Dumbbell radius at tab (die C = 25)
       Delta  = 0.078     ! Initial displacement for starting iterations
       DelEnd = 32.       ! Target end displacement (half-displacement)
!
!                                 |               |
!                                 |<--- wTab ---->|    Delta, DelEnd
!                                 |               |        ^
!          --------------------- &&&&&&&&&&&&&&&&&&         |
!               ^                 &&&&&&&&&&&&&&&&&&         |
!               |                 &&&&&&&&&&&&&&&&&&         |
!               |                 &&&&&&&&&&&&&&&&&&         |
!               |                 &&&&&&&&&&&&&&&&&&         |
!               |      ----------- &*************&  ------------
!               |         ^        &&&&&&&&&&&&&&&&
!               |         |        &&&&&&&&&&&&&&&&
!               |         |        &&&&&&&&&&&&&&&& <---- R2
!               |         |        &&&&&&&&&&&&&&&
!               |         |        &&&&&&&&&&&&&&
!            Lbell        |        &&&&&&&&&&&&
!               |         |        &&&&&&&&&& <---------- R1
!               |         |        &&&&&&&&&
!               |       Lgrip      &&&&&&& -----------
!               |         |        &&&&&&&&         ^
!               |         |        &&&&&&&&         |
!               |         |        &&&&&&&&         |
!               |         |        &&&&&&&&         |
!               |         |    --->&  w0  &<---     L0
!               |         |        &&&&&&&&         |
!               |         |        &&&&&&&&         |
!               v         v        &&&&&&&&         v
!          --------------------- &&&&&&&& -----------
!
!          SCHEMATIC 2: Illustration of dimensions to be input by user
!
!      ********************************************************************
!      ------------------- INITIALIZE SOME VARIABLES -------------------
!      ********************************************************************
!
!      NOTE: The guess values for 'Lam0' and 'Fo' affect convergence and
!            in addition to 'LamFact' & 'ForcFac', may result in unaccep-
!            table error if they are too large. If large errors are enco-
!            untered even with very small 'LamFact' & 'ForcFac', try red-
!            ucing the initial guess values for 'Lam0' and 'Fo'.
!
       Lam0 = 1.000001    ! Initial guess value for stretch
       Fo = 0.1           ! Initial load increment (units = Newtons)
       Lam = Lam0         ! Initialize all Lam(i)'s to Lam0
       F = 0.             ! Initialize pulling force to 0
       ErrF = 500.        ! Initialize force error to a large value
!
!      ********************************************************************
!      ---------- CALCULATION OF HEIGHTS & WIDTHS OF n-BLOCKS -----------
!      ********************************************************************
```

```
!
      int1 = 100    ! Number of intervals in which to decompose dumbbell
      int2 = 100    ! radius transitions. This code must be updated if
                    ! '100' is not specified for 'int1' or 'int2'. When
!                   ! testing the code, 100 intervals were found to give
!                   ! less than 0.1% discretization error.
!
!     The geometric calculations below do not require modification if t-
!     he default dimensioning scheme for an ASTM dumbbell applies.
!
      alpha = ACOS((R1+R2+w0-wTab)/(R1+R2))   ! Angle b/t horizontal and
                                              ! the line connecting the
                                              ! centers of R1 & R2.
!
      h1 = L0 + R1*SIN(alpha)      ! Height to tangent of R1 and R2
      h2 = h1 + R2*SIN(alpha)      ! Height to transition b/t R2 & wTab
      dh1 = (h1-L0) / int1         ! n-block interval height in R1 zone
      dh2 = (h2-h1) / int2         ! n-block interval height in R2 zone
      y(1) = L0                    ! Set y(1) equal to gage length
      w(1) = w0                    ! Set w(1) equal to gage width
      w(202) = wTab                ! Set w(202) equal to tab width
!
      DO i=2,101                      ! Loop to calculate the height to
         IF (i.EQ.2) THEN             ! the n-blocks and respective wid-
            y(i) = y(i-1) + dh1/2.    ! ths in the R1 transition zone.
         ELSE
            y(i) = y(i-1) + dh1
         END IF
         w(i) = -((R1**2 - (y(i)-L0)**2))**0.5 + w0 + R1
      END DO
!
      DO i=102,201                    ! Loop to calculate the height to
         IF (i.EQ.102) THEN           ! the n-blocks and respective wid-
            y(i) = h1 + dh2/2.        ! ths in the R2 transition zone.
         ELSE
            y(i) = y(i-1)+dh2
         END IF
         w(i) = (R2**2 - (y(i) - (L0 + (R1+R2)*SIN(alpha)))**2)**0.5&
              + wTab - R2
      END DO
!
      IF (Lgrip.GT.h2) THEN    ! Compute the height of the upper tab se-
         y(202) = Lgrip - h2   ! ction. Neglect this section if the grip
      ELSE                     ! location is below the upper tab region.
         y(202) = 0.
      END IF
!
!     *****************************************************************
!     --------- ITERATIVE CALCULATIONS FOR FORCE AND STRETCH ----------
!     *****************************************************************
!
      k = 1           ! Index k is used for data storage / output.
!
 220  j = 1           ! Restart location if the current target displace-
!                     ! ment, 'Delta', has not been reached after force
!                     ! and stretch iterations.
!
 210  DO i = j,202    ! Loop for force calculations in each n-block.
!
!     Force from generalized Yeoh strain-energy function:
!
         F(i) = 2*w(i)*t*(Lam(i)-1/(Lam(i)**2))*&
                (em * K1 * (Lam(i)**2 + 2/Lam(i) - 3)**(em-1.) + &
                 pe * K2 * (Lam(i)**2 + 2/Lam(i) - 3)**(pe-1.) + &
                 qu * K3 * (Lam(i)**2 + 2/Lam(i) - 3)**(qu-1.))
!
         ErrF(i) = Fo - F(i)                   ! Residual force error
!
         IF (ErrF(i).GT.500.0) THEN            ! Convergence check
            WRITE(*,*) 'ErrF = ' , ErrF(i)
            WRITE(*,*)
            WRITE(*,*) 'Force error > 500. Try adjusting Fo.'
            STOP
         END IF
!
         IF (ErrF(i).GT.0.) THEN                         ! If error in force
            IF (ErrF(i).LT.0.05) THEN                    ! is positive, incr-
               Lam(i) = Lam(i) + 0.000001*LamFact ! ement stretch and
            ELSE IF (ErrF(i).LT.0.5) THEN                ! use the GOTO stat-
               Lam(i) = Lam(i) + 0.00001*LamFact  ! ement to recalcul-
            ELSE IF (ErrF(i).LT.5.) THEN                 ! ate the force unt-
               Lam(i) = Lam(i) + 0.0001*LamFact   ! il the force resi-
            ELSE IF (ErrF(i).LT.50.) THEN                ! dual, 'ErrF(i)',
               Lam(i) = Lam(i) + 0.001*LamFact    ! becomes negative.
            ELSE IF (ErrF(i).LT.500.) THEN
               Lam(i) = Lam(i) + 0.01*LamFact
            END IF
            GO TO 210
         END IF
!
      j = j+1     ! Increment j so that later, if necessary, the outer
```
193

```fortran
      END DO          ! loop will restart until the final target displacem-
!                     ! ent, 'DelEnd', is reached or exceeded.
!
      deL(1)   =  L0*(Lam(1)-1)            ! Displacement of gage section
      deL(202) =  y(202)*(Lam(202)-1)     ! Displacement of tab section
!
      DO i=2,101                          ! Displacement of each n-block
         deL(i) = dh1*(Lam(i)-1)          ! in R1 section
      END DO
!
      DO i=102,201                        ! Displacement of each n-block
         deL(i) = dh2*(Lam(i)-1)          ! in R2 section
      END DO
!
      DO i = 2,201                        ! Set each n-block displacement
         IF (y(i).GT.Lgrip) THEN          ! to 0 if the n-block is above
            deL(i) = 0.                   ! the grip location.
         END IF
      END DO
!
      deLtot = 0.                         ! Initialize total displacement.
!
      DO i=1,202                          ! Compute total displacement.
         deLtot = deLtot + deL(i)
      END DO
!
      ErrDel = Delta - deLtot             ! Compare the sum of all n-block
!                                         ! displacements to the target d-
      IF (ErrDel.GT.0.) THEN              ! isplacement, 'Delta'. If error
         IF (ErrDel.LT.0.1) THEN          ! is positive, increment force &
            Fo = Fo + 0.01*ForcFac        ! restart the force and stretch
         ELSE IF (ErrDel.LT.1.) THEN      ! iteration loops with the GOTO
            Fo = Fo + 0.1*ForcFac         ! statement.
         ELSE IF (ErrDel.LT.10.) THEN
            Fo = Fo + 1.0*ForcFac
         ELSE IF (ErrDel.LT.100.) THEN
            Fo = Fo + 10.*ForcFac
         ELSE IF (ErrDel.LT.1000.) THEN
            Fo = Fo + 100.*ForcFac
         END IF
         GO TO 220
      END IF
!
!     *****************************************************************
!     --------- END OF ITERATION LOOPS FOR FORCE AND STRETCH ----------
!     *****************************************************************
!
      DO i = 1,202                        ! Store the maximum force er-
         IF (ErrF(i+1).LT.ErrF(i)) THEN   ! ror of all the n-blocks.
            MxErrF = ErrF(i+1)
         ELSE
            MxErrF = ErrF(i)
         END IF
      END DO
!
      Fout = F(1)              ! Store the force in the gage section.
      SigOut = F(1)/w(1)/t     ! Store the stress in the gage section.
!
      LamStore(k) = Lam(1)     ! Store stress and stretch as output that
      SigStore(k) = SigOut     ! the user can copy from output window.
!
!     This next sequence of commands may seem confusing. The desired st-
!     ress & stretch outputs are stored in arrays LamStore(k) & SigStor-
!     e(k), but a stress corresponding to an n-block corrected stretch
!     is stored one increment behind the current increment due to the m-
!     anner in which this code increments displacement from 'Delta' to
!     'DelEnd'. Specifically, stress and stretch during the first itera-
!     tion are not n-block corrected. The code forces the crosshead str-
!     etch at iteration 'k+1' to equal the gage stretch at iteration 'k'
!     , and then maps the updated gage stretch (at 'k+1') to the stress
!     at 'k', creating an n-block corrected (stretch, stress) pair.
!
      IF (k.EQ.1) THEN     ! Write headings for stress & stretch outputs.
         WRITE(*,*)
         WRITE(*,*) '  Gage Stretch' , '     Nominal Stress / MPa',&
                    '      ErrDel    ' , '     MaxErrF    '
         WRITE(*,*) '  ------------    ' , '--------------------',&
                    '  -----------    ' , '-------------'
      ELSE
         WRITE(*,360) LamStore(k),SigStore(k-1),&  ! Write stress, str-
                      ErrDel,MxErrF                 ! etch, and errors.
      END IF
!
      k = k+1                             ! Increment k for the next target di-
!                                         ! displacement, 'Delta'.
!
      delNew = Lgrip*(Lam(1)-1.)    ! Set the next displacement incremen-
!                                   ! t, 'Delta', so that the stretch ba-
      IF (delNew.LT.delEnd) THEN    ! sed on crosshead displacement in i-
         Delta = delNew             ! ncrement 'k+1' is equal to the str-
         Fo = Fout                  ! etch in the gage section at increm-
```

194

```
            GO TO 220                 ! ent 'k'. If the total target displ-
         END IF                       ! acement, 'DelEnd', has not been re-
!                                      ! ached, conduct another iteration of
!                                      ! the entire sequence.
         WRITE(*,*)
         WRITE(*,*) 'Final errors, force, displacement, & average stretch'
         WRITE(*,*) '-------------------------------------------------'
         WRITE(*,310) 'ErrDel = ' , ErrDel ,' mm   Max. displacement error'
         WRITE(*,320) 'MxErrF = ' , MxErrF ,'N' , 'Max. force error'
         WRITE(*,330) 'F = '    , Fout     ,'N' , 'Pulling force'
         WRITE(*,340) 'Delta = ', Delta    ,'mm','Crosshead displacement'
         WRITE(*,350) 'LamT = ' , Delta/Lgrip+1.,'Crosshead (avg) stretch'
         WRITE(*,*)
!
 310     FORMAT(A10,F12.6,A29)
 320     FORMAT(A10,F12.6,A3,A19)
 330     FORMAT(A10,F12.3,A3,A16)
 340     FORMAT(A10,F12.3,A3,A25)
 350     FORMAT(A10,F12.4,A29)
 360     FORMAT(F12.4,F18.3,F26.6,F17.6)
!
END PROGRAM nBlock11
!
!  **********************************************************************
!  --------------------- USER GUIDE / INSTRUCTIONS --------------------
!  **********************************************************************
!
!  1. Plot uniaxial tension stress-strain data with strain based on grip
!     (ie. crosshead) displacement.
!
!  2. Fit a strain-energy function to the stress-strain data and record
!     model parameters.
!
!  3. Input model parameters in the n-block code, and update the force
!     equation if the generalized Yeoh strain-energy function is not us-
!     ed.
!
!  4. Run the program to generate corrected stress-strain data for the
!     material. If more data points are desired, adjust inputs 'Delta'
!     and 'DelEnd' to result in different starting and ending points in
!     the calculator. See SCHEMATIC 3 for an illustration of n-block co-
!     rrected stress-strain data.
!
!
!
!        |                                        /            /
!        |    Hyperelastic model             /          __/
!        |    fit to stress-strain ___      /        ___/
!        |    data based on cross-   |     /      ___/
!        |    head displacement      |    /    __/
!        |                           V__/    _/
!     S |                      __/     /    ^
!     T |                   __/    __/      |
!     R |                __/    __/         |__ n-block corrected
!     E |             __/    __/            |    stress-strain output
!     S |          __/    __/
!     S |       __/    __/
!        |     /    __/
!        |    /   _/
!        |   / __/
!        |  / _/
!        | / /
!        | /_/
!        |/_____
!                              STRAIN
!
!       SCHEMATIC 3: Illustration of n-block corrected stress-strain data
!                    which, via a hyperelastic material model, shifts st-
!                    ress-strain data based on grip (ie. crosshead) disp-
!                    lacement.
```
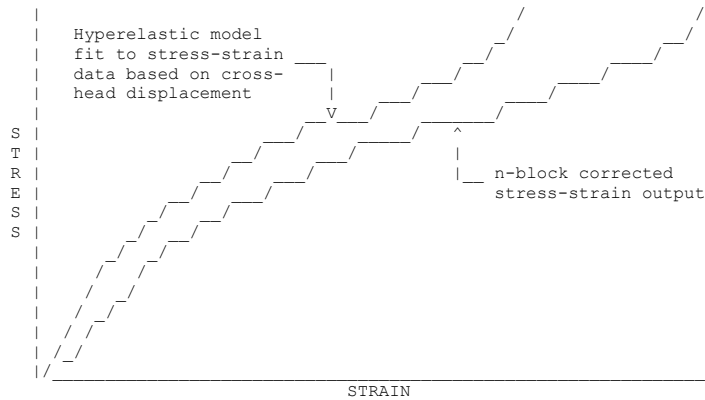
195

# Appendix D: A Biaxiality UVARM Subroutine for Abaqus/Standard

```fortran
C ************************************************************************
C  Authors:  Richard Windslow & Travis Hohenberger
C  Date:     2021-10-06
C  E-mail:   twhohen@gmail.com
C  Version:  0
C ************************************************************************
C
C  This subroutine computes element biaxiality for a hyperelastic mater-
C  ial. The definition is described in Windslow et al. (2020) (see below
C  for references) and given here:
C
C        B = log(L_min) / log(L_max)
C
C  where B is the element biaxiality, L_min is the minimum principal st-
C  retch, and L_max is the maximum principal stretch in an individual e-
C  lement. When a material is compressible, B must be scaled by the Jac-
C  obian, J_vol, according to:
C
C        J_vol = L_min * L_mid * L_max
C
C        B_comp = log(L_min * J_vol^(-1/3)) / log(L_max * J_vol^(-1/3))
C
C  where L_mid is the middle principal stretch and B_comp is the scaled
C  biaxiality.
C
C ************************************************************************
      SUBROUTINE UVARM(UVAR,DIRECT,T,TIME,DTIME,CMNAME,ORNAME,NUVARM,
     1                 NOEL,NPT,LAYER,KSPT,KSTEP,KINC,NDI,NSHR,COORD,
     2                 JMAC,JMATYP,MATLAYO,LACCFLA)
C
      INCLUDE 'ABA_PARAM.INC'
C
      DIMENSION UVAR(NUVARM),DIRECT(3,3),T(3,3),TIME(2)
      CHARACTER*80 CMNAME,ORNAME
      DIMENSION ARRAY(15),JARRAY(15),JMAC(*),JMATYP(*),COORD(*)
      CHARACTER*3 FLGRAY(15)
C
C ************************************************************************
C ----------------- COMPUTE MIN, MID, & MAX STRETCHES ----------------
C ************************************************************************
      CALL GETVRM('NEP',ARRAY,JARRAY,FLGRAY,JRCD,JMAC,JMATYP,MATLAYO,
     1            LACCFLA)
      L_min = ARRAY(1) + 1.0
      L_mid = ARRAY(2) + 1.0
      L_max = ARRAY(3) + 1.0
C
C ************************************************************************
C ---------------------- COMPUTE THE JACOBIAN -----------------------
C ************************************************************************
      J_vol = L_min * L_mid * L_max
C
C ************************************************************************
C ------------------- COMPUTE DEVIATORIC STRETCHES -------------------
C ************************************************************************
      L_minC = L_min * ((J_vol) ** (-1.0 / 3.0))
      L_midC = L_mid * ((J_vol) ** (-1.0 / 3.0))
      L_maxC = L_max * ((J_vol) ** (-1.0 / 3.0))
C
C ************************************************************************
C ----------------------- COMPUTE BIAXIALITY ------------------------
C ************************************************************************
      uvar(1) = log(L_minC) / log(L_maxC)
C
      RETURN
      END SUBROUTINE UVARM
C
C ************************************************************************
C  References:
C
C  R.J. Windslow, T.W. Hohenberger, & J.J.C. Busfield, (2020). "Determi-
C  nation of the Loading Mode Dependence of the Proportionality Paramet-
C  er for the Tearing Energy of Embedded Flaws in Elastomers under Mult-
C  iaxial Deformations". In: Fatigue Crack Growth in Rubber Materials.
C  Eds. G. Heinrich, R. Kipscholl, & R. Stocek.
C
C  Simulia, (2020). "UVARM". In: Abaqus R2020 User Subroutines Manual.
C  Dassault Systèmes Simulia Corp., Providence, RI, USA.
C ************************************************************************
```

# Appendix E: Conversion of ET Stress to Equivalent UC Stress

Treloar[50] presented the equivalence of equibiaxial tension and uniaxial compression for an incompressible rubbery material in terms of true stress, but (in this author's opinion) his nomenclature was somewhat convoluted. He did not illustrate the transformation in terms of nominal stress, so this gap is closed here.

Consider the compression button in Fig. 2.14 with initial height, $h_o$, and initial diameter, $d_o$. When subjected to uniform (nominal) radial stress, $\sigma_{et}$, the button undergoes equibiaxial extension (Fig. 2.14b) and the stress is given by:

$$\sigma_{et} = \frac{F_r}{A_r} = \frac{F_r}{\pi d_o h_o} \tag{E.1}$$

where $F_r$ is total radial force and $A_r$ is the initial radial surface area of the cylindrical wall. For this exercise, true radial stress $\hat{\sigma}_{et}$ will be needed:

$$\hat{\sigma}_{et} = \frac{F_r}{\hat{A}_r} = \frac{F_r}{\pi d_f h_f} \tag{E.2}$$

where $\hat{A}_r$, $d_f$, and $h_f$ are final area, diameter, and height of the cylinder, respectively. $d_f$ follows from measurements of radial strain $\varepsilon_r$:

$$\varepsilon_r = \frac{d_f - d_o}{d_o} \quad \Rightarrow \quad d_f = (\varepsilon_r + 1)d_o = \lambda_r d_o \tag{E.3}$$

where the stretch ratio $\lambda_r = \varepsilon_r + 1$ has been substituted for notational convenience. $h_f$ follows from incompressibility (that is, conservation of volume):

$$V_o = V_f = \frac{\pi}{4}d_o^2 h_o = \frac{\pi}{4}d_f^2 h_f \quad \Rightarrow \quad h_f = \left(\frac{d_o}{d_f}\right)^2 h_o = \lambda_r^{-2} h_o \tag{E.4}$$

where $V_o$ and $V_f$ are volumes before and after deformation, respectively. The last equality is obtained by rearranging and substituting Eq. E.3. With initial and final geometry fully described, axial strain $\varepsilon_a$ is computed:

$$\varepsilon_a = \frac{h_f - h_o}{h_o} \quad \Rightarrow \quad \lambda_a = \frac{h_f}{h_o} = \frac{1}{\lambda_r^2} \tag{E.5}$$

where $\lambda_a = \varepsilon_a + 1$ and the last equality follows from Eq. E.4.

The next step is key to transform radial stress to equivalent uniaxial stress. Superimposing hydrostatic pressure $P = -\hat{\sigma}_{et}$ on the specimen cancels $\hat{\sigma}_{et}$ on the radial surface, leaving only compressive stress $\hat{\sigma}_{et} = \hat{\sigma}_{uc}$ on the top and bottom faces (Fig. 2.14c). It is critical to realize this step must use true stresses, and it is valid strictly for incompressible, isotropic materials.

At this stage, there are expressions for $\hat{\sigma}_{et}$, $\sigma_{et}$, $\hat{\sigma}_{uc}$, $\lambda_r$, and $\lambda_a$. To arrive at $\sigma_{uc}$, first construct expressions analogous to Eqs. E.1 and E.2 in the axial direction:

$$\sigma_{uc} = \frac{F_a}{A_a} = \frac{F_a}{\frac{\pi}{4}d_o^2} \tag{E.6}$$

$$\hat{\sigma}_{uc} = \frac{F_a}{\hat{A}_a} = \frac{F_a}{\frac{\pi}{4}d_f^2} \tag{E.7}$$

where $A_a$ and $\hat{A}_a$ are initial and final areas of the axial faces, respectively, and $F_a$ is the axial force. Solving for $F_a$ in Eq. E.7, substituting in Eq. E.6, and invoking Eq. E.3:

$$\sigma_{uc} = \frac{\frac{\pi}{4}d_f^2}{\frac{\pi}{4}d_o^2}\hat{\sigma}_{uc} = \left(\frac{d_f}{d_o}\right)^2 \hat{\sigma}_{uc} = \lambda_r^2 \hat{\sigma}_{uc} \tag{E.8}$$

A similar manipulation of Eq. E.1 and Eq. E.2 gives:

$$\hat{\sigma}_{et} = \frac{\pi d_o h_o}{\pi d_f h_f}\sigma_{et} = \frac{\sigma_{et}}{\lambda_r \lambda_a} = \frac{\sigma_{et}}{\lambda_r \frac{1}{\lambda_r^2}} = \lambda_r \sigma_{et} \tag{E.9}$$

where the relationships for stretch ratios follow from Eq. E.3 and Eq. E.5. Since $\hat{\sigma}_{et} = \hat{\sigma}_{uc}$, Eqs. E.8 and E.9 give:

$$\sigma_{uc} = \lambda_r^3 \sigma_{et} \tag{E.10}$$

Axel Physical Testing Services[269] has published the strain form of this equation without derivation.

# Appendix F: Proof of the Uniformity
## of Stress in Equibiaxial Tension

A radial stress distributed about the perimeter of a disc is given. To illustrate, consider a quarter section of a cylindrical disc that is subjected to a uniform radial force, $F_1$, along its outer perimeter with reaction forces, $F_2$ and $F_3$, in orthogonal directions (Fig. N.4a). All forces can be converted to distributed loads (that is stresses) through the areas on which they act. Hence, the force on a differential element along the perimeter of the disc is:

$$dF_1 = \sigma_1 dA_1 \tag{F.1}$$

Decomposing the force into $x$ and $y$ components, Eq. F.1 becomes:

$$dF_{1.x} = \sigma_1 \cos(\theta) \, dA_1 \tag{F.2a}$$

$$dF_{1.y} = \sigma_1 \sin(\theta) \, dA_1 \tag{F.2b}$$

where $\theta$ is an angle measured counterclockwise from the $x$-axis. The differential area is given by:

$$dA_1 = hr_1 d\theta \tag{F.3}$$

so that the net force in the $x$ and $y$ directions due to $\sigma_1$ becomes:

$$F_{1.x} = \sigma_1 r_1 h \int_0^{\pi/2} \cos(\theta) \, d\theta = \sigma_1 r_1 h \tag{F.4a}$$

$$F_{1.y} = \sigma_1 r_1 h \int_0^{\pi/2} \sin(\theta) \, d\theta = \sigma_1 r_1 h \tag{F.4b}$$

The solutions are identical due to the symmetry of the problem. Summing all forces in the $x$ and $y$ directions:

$$\sigma_1 r_1 h = \sigma_2 r_1 h \tag{F.5a}$$

$$\sigma_1 r_1 h = \sigma_3 r_1 h \tag{F.5b}$$

from which it follows that $\sigma_1 = \sigma_2 = \sigma_3$. This proves that the applied radial stress is equal to the tangential reaction stresses, but it does not prove that the radial stress at an arbitrary location inside the disc equals the applied radial stress. To prove the equivalence of the latter, consider a partition of the quarter geometry as given in Fig. N.4b. By analogy with Eqs. F.4a,b, the net forces in the $x$ and $y$ directions due to the internal force, $F_4$, are:

$$F_{4.x} = F_{4.y} = \sigma_4 r_4 h \tag{F.6}$$

Summing all forces in the $x$ direction:

$$\sigma_1 r_1 h - \sigma_2 (r_1 - r_4)h - \sigma_4 r_4 h = 0 \tag{F.7a}$$

$$\sigma_1 r_1 - \sigma_2 r_1 + \sigma_2 r_4 - \sigma_4 r_4 = 0 \tag{F.7b}$$

Since it has already been shown that $\sigma_1 = \sigma_2$, then Eq. F.7b reduces to $\sigma_2 = \sigma_4$. It immediately follows that $\sigma_1 = \sigma_4$; hence, for a uniform, homogeneous equibiaxial deformation, the radial stress applied at the perimeter equals the radial stress at any location that has a diameter smaller than the perimeter.

# Appendix G: Levenberg-Marquardt Code to Determine SEF Model Parameters

## THE TOP-LEVEL PROGRAM

```fortran
PROGRAM LvMrqGenYeohUni   !  Travis Hohenberger  |  2019-04-04   |  v1.1
!
!    ***********************************************************************
!  This program uses the Levenberg-Marquardt curve-fitting method for n-
!  on-linear functions to fit uniaxial tension and/or compression data
!  to a generalized Yeoh strain-energy function (gen-Yeoh SEF) which has
!
!             W = K1(I1-3)^m + K2(I1-3)^p + K3(I1-3)^q
!
!  where (K1,K2,K3,m,p,q) are fitting parameters and I1 is the first in-
!  variant of the stretch tensor. The algorithm and subroutines are imp-
!  lemented precisely as described in Press et al. 1992. See the bottom
!  of this program for more details.
!
      IMPLICIT NONE
      INTEGER   NDATA,NCA,I,MA,NITER,IA(6),KK
      REAL      X,Y,SIG,A(6),COVAR(6,6),ALPHA(6,6),CHISQ,&
                ALAMDA,ACC,C1,C2
      EXTERNAL  FUNCS
!
!    ******************************************************************
!    ----------------  START OF USER INPUT SECTION  -----------------
!    ******************************************************************
!
      DIMENSION   X(876),&       !  Set each dimension = NDATA
                  Y(876),&
                  SIG(876)
!
      NDATA =      876           !  Enter # of lines in input data.
!
!    (A1,A2,A3,A4,A5,A6) = (K1,K2,K3,m,p,q)
      A(1)  =   1.35
      A(2)  =  -0.07
      A(3)  =   0.051
      A(4)  =   0.75
      A(5)  =   1.505
      A(6)  =   1.97
!
      IA(1) =   0               !  Parameter solve switches.
      IA(2) =   1               !
      IA(3) =   1               !  Set = '0' to fix a parameter.
      IA(4) =   0               !  Set = '1' to iterate a parameter.
      IA(5) =   1               !
      IA(6) =   1               !  IA(J) corresponds to A(J).
!
      OPEN(16,FILE='DataNewX1')  !  Enter file name for STRETCH data.
      OPEN(17,FILE='DataNewY1')  !  Enter file name for stress data.
!
!    ******************************************************************
!    ----------------  END OF USER INPUT SECTION  --------------------
!    ******************************************************************
!
      READ(16,*)(X(KK),KK=1,NDATA)    !  Load stretch test data.
      READ(17,*)(Y(KK),KK=1,NDATA)    !  Load stress test data.
      CLOSE(16)                       !  Close stretch test data.
      CLOSE(17)                       !  Close stress test data.
!
      DO 20 I=1,NDATA    !  SIG(I)'s are StDev's (weight functions) for
        SIG(I)=1.        !  data points used in MRQMIN. In this code
 20   ENDDO             !  all weights are equal.
!
      CHISQ=100          !  Initialize fitting error to large value.
      NITER=0            !  Initialize iteration count for MRQMIN.
!
!    ******************************************************************
!    -------  SET UP DISPLAY FOR OUTPUT OF PARAMETERS & ERROR  -------
!    ******************************************************************
!
      WRITE(*,110)
 110    FORMAT(2X,'ITER',8X,'K1',12X,'K2',12X,'K3',13X,'m',13X,'p',&
               13X,'q',10X,'CHISQ')
      WRITE(*,120)
 120    FORMAT(2X,'----',4X,'----------',4X,'----------',4X,&
               '----------',4X,'----------',4X,'----------',&
               4X,'----------',4X,'----------')
      WRITE(*,130)NITER,A,CHISQ
 130    FORMAT(2X,I3,4X,F11.6,3X,F11.6,3X,F11.6,3X,F11.6,3X,F11.6,3X,&
```

199

```fortran
               F11.6,3X,F11.6)
!
!     ******************************************************************
!     ------------------- START MRQMIN SUBROUTINE --------------------
!     ******************************************************************
!                 ---------------------------------
!     ----------------| Initialization Call for MRQMIN |---------------
!                 ---------------------------------
!
      ALAMDA=-1.              !  Set ALAMDA < 0 to initialize MRQMIN.
      MA=6                    !  Number of parameters in gen-Yeoh model = 6.
      NCA=MA                  !  Variable req'd for some subroutines.
!
      CALL MRQMIN(X,Y,SIG,NDATA,A,IA,MA,COVAR,ALPHA,NCA,CHISQ,&
                 FUNCS,ALAMDA)
!
!                   ---------------------------
!     ------------------| Iteration Call for MRQMIN |------------------
!                   ---------------------------
!
  27  CONTINUE                           !  Start of iteration loop.
      WRITE(*,130)NITER+1,A,CHISQ    !  Display parameters & error.
      NITER=NITER+1
      C1=CHISQ                           !  Error before iteration.
!
      CALL MRQMIN(X,Y,SIG,NDATA,A,IA,MA,COVAR,ALPHA,NCA,CHISQ,&
                 FUNCS,ALAMDA)
!
      C2=CHISQ                           !  Error after iteration.
      ACC=ABS((C2-C1)/C2)               !  Change in error.
      IF(ACC.GT.1.E-06)THEN             !  Set convergence criterion.
          IF(NITER.LT.50)GOTO 27        !  Cap max. # of iterations.
      ENDIF
!           ---------------------------------------
!     |-----------|Final Call for MRQMIN (to sort COVAR)|------------|
!           ---------------------------------------
!
      ALAMDA=0.
!
      CALL MRQMIN(X,Y,SIG,NDATA,A,IA,MA,COVAR,ALPHA,NCA,CHISQ,FUNCS,&
                 ALAMDA)
!
!         --------------------------------------------------
!     |------|Write Final Values for Easy Transcription in Excel|------|
!         --------------------------------------------------
!
      WRITE(*,*)'-------------------------'
      WRITE(*,140)A(1)
 140    FORMAT(' K1 = ',F7.3)
      WRITE(*,141)A(4)
 141    FORMAT('  m = ',F7.3)
      WRITE(*,142)A(2)
 142    FORMAT(' K2 = ',F7.3)
      WRITE(*,143)A(5)
 143    FORMAT('  p = ',F7.3)
      WRITE(*,144)A(3)
 144    FORMAT(' K3 = ',F7.3)
      WRITE(*,145)A(6)
 145    FORMAT('  q = ',F7.3)
!
      STOP
!
END PROGRAM LvMrqGenYeohUni
!
!  ******************************************************************
!  ------------------------- MORE DETAILS --------------------------
!  ******************************************************************
!
!  The function fit by this program is the uniaxial stress equation:
!
!      S = 2*(L-1/L^2)*[K1*m*(L^2+2/L-3)^(m-1) +
!                       K2*p*(L^2+2/L-3)^(p-1) +
!                       K3*q*(L^2+2/L-3)^(q-1)]
!
!  where L is the stretch ratio at a given uniaxial stress S.
!
!  The following subroutines from Press et al. 1992 are required:
!  MRQMIN, MRQCOF, GAUSSJ, & COVSRT. The program also requires a user-
!  defined subroutine FUNCS that contains the function to be fit. Press
!  et al. 1992 describes one such function, but this has been replaced
!  by the stress equation above. See comments in FUNCS for details on h-
!  ow to adjust the FUNCS subroutine for different functions.
!
!  De 1994 adopted and published a program similar to this one for the
!  Davies-De-Thomas SEF (Davies et al. 1994) in his PhD thesis. The ori-
```
200

```
! ginal author of that code was James Busfield, and the program could
! fit multiple loading modes by using so-called 'reduced' stress and s-
! train data. See De 1994 for guidance on how to adjust the current pr-
! ogram if multiple modes must be fit simultaneously.
!
! ************************************************************************
! ---------  DEVELOPMENT NOTES & INSTALLATION INSTRUCTIONS  -----------
! ************************************************************************
!
! This code was developed with NetBeans IDE Dev (Build 201804200002) r-
! unning on top of packages from MinGW with the gfortran compiler. f90
! codes replace the f77 codes in Press et al. 1992. This required repl-
! acement of PAUSE commands with WRITE(*,*)('TEXT INFORMATION') follow-
! ed by READ(*,*). Some useful links on software installation are:
!
! Install video:  https://www.youtube.com/watch?v=wGv2kGl8OV0
! MinGW link:     https://sourceforge.net/projects/mingw/
! Netbeans link:  http://137.254.56.27/download/trunk/nightly/latest/
!
! Follow the steps in the installation video, stopping at 3:20 where i-
! nstructions about the terminal window are given. Try to run a simple
! 'Hello World' application. If the code will not compile, you may need
! to manually specify the location of the Fortran compiler by going th-
! ru the top menu: Tools --> Options --> C/C++. Make sure the gfortran
! compiler is specified. If not, search for the compiler on your compu-
! ter (defaults to C:\MinGW\bin\gfortran.exe) and provide a link to it.
! Also make sure as.exe (assembler command), make.exe (make command),
! and gdb.exe (debugger) are properly linked.
!
! To run the program:
!
! 1. Create a new project in Netbeans thru the top menu: File -->
!    C/C++ Application --> Next --> Fortran90 Free (specify this from
!    the drop-down box) --> Finish.
!
! 2. Expand the application tree in the project panel on the left (de-
!    fault name is CppApplication1).
!
! 3. Expand 'Source Files'.
!
! 4. Copy text from LvMrqGenYeohUni.txt and paste over all text in
!    source file 'main.f90' (or another title if you changed the de-
!    fault name).
!
! 5. For each subroutine file:
!
!       a. Right click 'Source Files' and select: New --> Fortran File
!          (Free Format)...
!
!       b. Name the file according to the subroutine that will be
!          pasted, and then paste all text over any default text in
!          the file that is generated. Ensure file extension is .f90.
!
! 6. Right click 'Source Files' and select: New --> Empty File...
!
! 7. Name the file for stretch test data, for instance 'DataX'.
!
! 8. Paste stretch test data into the file.
!
! 9. Repeat steps 6 thru 8 for stress data, for instance 'DataY'.
!
! 10. The Netbeans output panel may not allow keyboard input which is
!     required for some programs. Although the current program does not
!     require keyboard input, it is still recommended to activate outp-
!     ut in an external terminal window where keyboard input is possib-
!     le. To do this, right click the project name in the project panel
!     and select: Properties --> Run --> Console Type -->
!     External Terminal.
!
! 11. Follow steps in the USER GUIDE below for further instructions.
!
! ************************************************************************
! --------------------------  USER GUIDE  ----------------------------
! ************************************************************************
!
! 1. The program requires stretch data instead of stain data.
!
! 2. Test data are read from 2 separate files. Create different files
!    for stretch and stress data, for instance with file names 'DataX'
!    and 'DataY', respectively. These are read into variables X(NDATA)
!    and Y(NDATA). The number of points in each file must match.
!
! 3. Enter the number of data points to define variable dimensions for
!    X, Y, and SIG (lines 25, 26, & 27, respectively). Also record this
!    number in NDATA (line 29).
```

```
!
! 4. Using line 31 as a guide, enter values for K1, K2, K3, m, p, and
!    q.
!
! 5. Set the IA switches (lines 39 thru 44) to determine which paramet-
!    ers, if any, to keep fixed (IA=0) and which to iterate (IA=1).
!
! 6. Enter the name of the stretch data file (for instance 'DataX') on
!    line 46. Do similar for the stress data file on line 47.
!
! 7. Run the program to solve the parameters. In general, best fit sol-
!    utions are not unique (ie. outputs will depend on initial guesses.
!    Errors may occur during computation if initial guesses are far fr-
!    om stable values and/or the test data is poorly represented by the
!    SEF.
!
! 8. Inspect output parameters. In practice, the following constraints
!    often work well for modeling oilfield sealing materials:
!
!      (K1 > |K2| > K3)        (K2 < 0)             (K3 > 0)
!         (m < p < q)        (0.5 < m < 1.1)     (1 < p < 1.5)
!
!    None of these constraints are algorithmically enforced. Manual ad-
!    justment of parameters and selective manipulation of the IA switc-
!    hes may be required to achieve 'sensible' parameters.
!
! 9. The Neo-Hookean SEF can be solved with inputs:
!
!                  (K1,K2,K3,m,p,q) = (1,0,0,1,2,3)
!         (IA1,IA2,IA3,IA4,IA5,IA6) = (1,0,0,0,0,0)
!
! 10. The Yeoh SEF can usually be solved with inputs:
!
!                  (K1,K2,K3,m,p,q) = (1, -0.1, 0.01, 1, 2, 3)
!         (IA1,IA2,IA3,IA4,IA5,IA6) = (1,1,1,0,0,0)
!
! 11. If all 6 parameters are not known reasonably well a priori, achi-
!     eving an accurate solution with all parameters initially free is
!     unlikely. If initial guess values cannot be estimated, one techn-
!     ique to proceed is to:
!
!         a. Fit a Yeoh SEF (see preceding step for details).
!         b. Enter the Yeoh parameters as new guess values. Set IA4=1.
!            Run the program to get updated parameters.
!         c. Repeat step b, but unlock p by setting IA5 = 1.
!         d. Repeat step c, but unlock q by setting IA6 = 1.
!
! 12. If step 11 is unsuccessful, retry the technique with initial gue-
!     sses:
!
!                  (K1,K2,K3,m,p,q) = (5, -1.5, 0.2, 0.9, 1.2, 2)
!         (IA1,IA2,IA3,IA4,IA5,IA6) = (1,1,1,0,0,0)
!
! **********************************************************************
! ------------------------  KNOWN ISSUES  --------------------------
! **********************************************************************
!
! 1. A singularity occurs in the stress equation at no load if m, p, or
!    or q are less than 1. To avoid computational errors (for instance
!    IEEE_INVALID_FLAG and IEEE_DIVIDE_BY_ZERO), delete any data point
!    at (and possibly near) a stretch of 1.
!
! 2. Setting m, p, or q = 0 causes a computation error (for instance
!    IEEE_INVALID_FLAG and IEEE_DIVIDE_BY_ZERO) even if their correspo-
!    nding parameters (K1,K2,K3) are also set to zero. Always ensure f-
!    inite values for the exponents.
!
! **********************************************************************
! ------------------------  VERSION NOTES  --------------------------
! **********************************************************************
!
!   v1.0: initial release
!   v1.1: corrected 'n' to 'p' and 'p' to 'q' on write output, lines
!         132 & 136, respectively; removed write(*,*)chisq from line
!         138.
!
! **********************************************************************
! -------------------------  REFERENCES  ---------------------------
! **********************************************************************
!
! C. Davies, D. De, & A. Thomas, (1994). "Characterization of the Beha-
! vior of Rubber for Engineering Design Purposes. 1. Stress-Strain Rel-
! ations". Rubber Chemistry and Technology 67(4), 716.
!
! D. De, (1994). "The effect of particulate fillers on the strain ener-
```

202

```
!  gy function and crack growth in rubbers". PhD Thesis. Queen Mary Uni-
!  versity of London Library. Contact James Busfield (j.busfield@qmul.a-
!  c.uk or Travis Hohenberger (twhohen@gmail.com) for an electronic cop-
!  y.
!
!  T.W. Hohenberger, R.J. Windslow, N.M. Pugno, & J.J.C. Busfield, (2019
!  ). "A Constitutive Model for both Low and High Strain Nonlinearities
!  in Highly Filled Elastomers and Implementation with User-Defined Mat-
!  erial Subroutines in Abaqus". Rubber Chemistry and Technology, 92 (4)
!  , 653-686.
!
!  W. Press, B. Flannery, S. Teukolsky, & W. Vetterlin, (1992). Numeric-
!  al Recipes in FORTRAN. 2nd Ed. Cambridge University Press. See secti-
!  on 15.5.
!
!  ***********************************************************************
```

## SUBROUTINES CALLED BY THE TOP-LEVEL PROGRAM

```
!  ***********************************************************************
!
SUBROUTINE MRQMIN(X,Y,SIG,NDATA,A,IA,MA,COVAR,ALPHA,NCA,CHISQ,FUNCS,&
                  ALAMDA)
!
!  Subroutine transcribed from Numerical Recipes in Fortran, 2nd Ed. (P-
!  ress et al. 1992) with no significant alterations. Each call of the
!  subroutine conducts one solution iteration. The initial call uses AL-
!  AMDA < 0 to initialize a solution. Iteration scaling parameter ALAMDA
!  is automatically altered for subsequent iterations. When convergence
!  is satisfied, the subroutine must be called one last time with ALAMDA
!  = 0 to finalize the solution. The routine calls the following variab-
!  les:
!
!    X:      array of stretch test data with DIMENSION = NDATA
!
!    Y:      array of stress test data with DIMENSION = NDATA
!
!    SIG:    St.Dev. weight functions for the solution algorithm which
!            are set to 1 for the current application
!
!    NDATA:  number of test data points in input files
!
!    A:      array of parameters to solve with DIMENSION = MA
!
!    IA:     switches to fix (IA=0) or iterate (IA=1) model parameters
!
!    MA:     number of parameters in the model
!
!    COVAR:  covariance matrix that characterizes 'components' of error
!            between the model parameters
!
!    ALPHA:  curvature matrix which is the inverse of COVAR; used for
!            iteration calculations
!
!    NCA:    equal to MA in this application
!
!    CHISQ:  overall error metric for the model fit
!
!    FUNCS:  user-defined subroutine that contains function to be mini-
!            mized
!
!    ALAMDA: scaling parameter that determines step size between param-
!            eter calculation iterations
!
      IMPLICIT NONE
      INTEGER   MA,NCA,NDATA,IA(MA),MMAX,J,K,L,MFIT
      REAL      ALAMDA,CHISQ,FUNCS,A(MA),ALPHA(NCA,NCA),&
                COVAR(NCA,NCA),SIG(NDATA),X(NDATA),Y(NDATA),OCHISQ
!
!  ***********************************************************************
      PARAMETER (MMAX=20)          !  Set to largest number of parameters
!                                     that the algorithm can fit.
!
      REAL      ATRY(MMAX),BETA(MMAX),DA(MMAX)
      SAVE      OCHISQ,ATRY,BETA,DA,MFIT
!
      IF(ALAMDA.LT.0.)THEN                  !  Initialization statement
          MFIT=0
          DO 11 J=1,MA                      !  Set # of parameters to fit
             IF(IA(J).NE.0)MFIT=MFIT+1
 11       ENDDO
          ALAMDA=0.001      !  Set initial value for scaling parameter
!
```

```fortran
          CALL MRQCOF(X,Y,SIG,NDATA,A,IA,MA,ALPHA,BETA,NCA,CHISQ,FUNCS)
!
          OCHISQ=CHISQ         !  'Old' error metric
!
          DO 12 J=1,MA
              ATRY(J)=A(J)
12        ENDDO
      ENDIF
!
      DO 14 J=1,MFIT                   !  Alter linearized fitting matrix
          DO 13 K=1,MFIT              !  by augmenting diagonal elements
              COVAR(J,K)=ALPHA(J,K)
13        ENDDO
          COVAR(J,J)=ALPHA(J,J)*(1.+ALAMDA)
          DA(J)=BETA(J)
14    ENDDO
!
      CALL GAUSSJ(COVAR,MFIT,NCA,DA,1,1)    !  Matrix solution for COVAR
!
      IF(ALAMDA.EQ.0.)THEN                       !  Once converged, evalu-
          CALL COVSRT(COVAR,NCA,MA,IA,MFIT)   !  ate the covariance ma-
          RETURN                                  !  trix.
      ENDIF
      J=0
      DO 15 L=1,MA                      !  Did the trial succeed?
          IF(IA(L).NE.0)THEN
              J=J+1
              ATRY(L)=A(L)+DA(J)
          ENDIF
15    ENDDO
!
      CALL MRQCOF(X,Y,SIG,NDATA,ATRY,IA,MA,COVAR,DA,NCA,CHISQ,FUNCS)
!
      IF(CHISQ.LT.OCHISQ)THEN         !  Success. Accept the new solution.
          ALAMDA=0.1*ALAMDA
          OCHISQ=CHISQ
          DO 17 J=1,MFIT
              DO 16 K=1,MFIT
                  ALPHA(J,K)=COVAR(J,K)
16            ENDDO
              BETA(J)=DA(J)
17        ENDDO
          DO 18 L=1,MA
              A(L)=ATRY(L)
18        ENDDO
      ELSE
          ALAMDA=10.*ALAMDA     !  Failure, increase ALAMDA and proceed.
          CHISQ=OCHISQ
      ENDIF
!
      RETURN
!
END SUBROUTINE MRQMIN
!
!   *********************************************************************
!
SUBROUTINE MRQCOF(X,Y,SIG,NDATA,A,IA,MA,ALPHA,BETA,NALP,CHISQ,FUNCS)
!
!  Subroutine transcribed from Numerical Recipes in Fortran, 2nd Ed. (P-
!  ress et al. 1992) with no significant alterations. This routine is c-
!  alled by MRQMIN to evaluate the linearized fitting matrix ALPHA and
!  vector BETA as well as calculate CHISQ.
!
      IMPLICIT NONE
      INTEGER    MA,NALP,NDATA,IA(MA),MMAX,MFIT,I,J,K,L,M
      REAL       CHISQ,A(MA),ALPHA(NALP,NALP),BETA(MA),SIG(NDATA),&
                 X(NDATA),Y(NDATA),DY,SIG2I,WT,YMOD
      EXTERNAL   FUNCS
      PARAMETER (MMAX=20)
      REAL       DYDA(MMAX)

      MFIT=0
!
      DO 11 J=1,MA
          IF(IA(J).NE.0)MFIT=MFIT+1
11    ENDDO
!
      DO 13 J=1,MFIT            !  Initialize (symmetric) ALPHA and BETA
          DO 12 K=1,J
              ALPHA(J,K)=0.
12        ENDDO
          BETA(J)=0.
13    ENDDO
!
      CHISQ=0.
```

```fortran
!
      DO 16 I=1,NDATA                     !  Summation loop over all data
          CALL FUNCS(X(I),A,YMOD,DYDA,MA)
          SIG2I=1./(SIG(I)*SIG(I))
          DY=Y(I)-YMOD
          J=0
          DO 15 L=1,MA
              IF(IA(L).NE.0)THEN
                  J=J+1
                  WT=DYDA(L)*SIG2I
                  K=0
                  DO 14 M=1,L
                      IF(IA(M).NE.0)THEN
                          K=K+1
                          ALPHA(J,K)=ALPHA(J,K)+WT*DYDA(M)
                      ENDIF
 14               ENDDO
                  BETA(J)=BETA(J)+DY*WT
              ENDIF
 15       ENDDO
          CHISQ=CHISQ+DY*DY*SIG2I                       !  Calculate CHI^2
 16   ENDDO
!
      DO 18 J=2,MFIT                      !  Fill in the symmetric side
          DO 17 K=1,J-1
              ALPHA(K,J)=ALPHA(J,K)
 17       ENDDO
 18   ENDDO
!
      RETURN
!
END SUBROUTINE MRQCOF
!
!  **********************************************************************
!
SUBROUTINE GAUSSJ(A,N,NP,B,M,MP)
!
!  Subroutine transcribed from Numerical Recipes in Fortran, 2nd Ed. (P-
!  ress et al. 1992) with no significant alterations. This routine is c-
!  alled by MRQMIN to solve an error matrix. It is a linear equation so-
!  lution via Gauss-Jordan elimination. Argument A is an NP X NP input
!  matrix. B is an N X M input matrix containing M vectors stored in an
!  array of dimension NP X MP. On output, A is replaced by its inverse,
!  and B is replaced by solution vectors.
!
      IMPLICIT NONE
      INTEGER   M,MP,N,NP,NMAX,I,ICOL,IROW,J,K,L,LL
      REAL      A(NP,NP),B(NP,NP)
      PARAMETER (NMAX=50)                 !  Largest anticipated value of N
      INTEGER   INDXC(NMAX),INDXR(NMAX),IPIV(NMAX)     !  Pivot indices
      REAL      BIG,DUM,PIVINV
!
      DO 11 J=1,N
        IPIV(J)=0
 11   ENDDO
!
      DO 22 I=1,N                 !  Start main loop for column reduction
          BIG=0.
          DO 13 J=1,N                         !  Start loop to search for
              IF(IPIV(J).NE.1)THEN            !  pivot element.
                  DO 12 K=1,N
                      IF(IPIV(K).EQ.0)THEN
                          IF(ABS(A(J,K)).GE.BIG)THEN
                              BIG=ABS(A(J,K))
                              IROW=J
                              ICOL=K
                          ENDIF
                      ELSEIF(IPIV(K).GT.1)THEN
                          WRITE(*,'(''Warning! Singular matrix...'')')
                          READ(*,*)
                      ENDIF
 12               ENDDO
              ENDIF
 13       ENDDO
!
!         Pivot element is now identified. Next, interchange rows, if n-
!         eeded, to put the pivot element on the diagonal. Columns are
!         not physically interchanged, only relabeled: INDXC(I), the co-
!         lumn of Ith pivot element, is the Ith column that is reduced,
!         while INDXR(I) is the row in which that pivot element was ori-
!         ginally located. If INDXR(I).NE.INDXC(I) there is an implied
!         column interchange. With this form of bookkeeping, the soluti-
!         on B's will end up in the correct order, and the inverse matr-
!         ix will be scrambled by columns.
!
```

```fortran
                IPIV(ICOL)=IPIV(ICOL)+1
                IF(IROW.NE.ICOL)THEN
                    DO 14 L=1,N
                        DUM=A(IROW,L)
                        A(IROW,L)=A(ICOL,L)
                        A(ICOL,L)=DUM
 14                 ENDDO
                    DO 15 L=1,M
                        DUM=B(IROW,L)
                        B(IROW,L)=B(ICOL,L)
                        B(ICOL,L)=DUM
 15                 ENDDO
                ENDIF
                INDXR(I)=IROW                   !  Now ready to divide pivot
                INDXC(I)=ICOL                   !  row by pivot element located
                IF(A(ICOL,ICOL).EQ.0.)THEN      !  at IROW and ICOL.
                    WRITE(*,'(''Warning! Singular matrix in GAUSSJ.'')')
                    READ(*,*)
                ENDIF
                PIVINV=1./A(ICOL,ICOL)
                A(ICOL,ICOL)=1.
                DO 16 L=1,N
                    A(ICOL,L)=A(ICOL,L)*PIVINV
 16             ENDDO
                DO 17 L=1,M
                    B(ICOL,L)=B(ICOL,L)*PIVINV
 17             ENDDO
                DO 21 LL=1,N                    !  Reduce the rows...
                    IF(LL.NE.ICOL)THEN          !     ...except for the pivot one.
                        DUM=A(LL,ICOL)
                        A(LL,ICOL)=0.
                        DO 18 L=1,N
                            A(LL,L)=A(LL,L)-A(ICOL,L)*DUM
 18                     ENDDO
                        DO 19 L=1,M
                            B(LL,L)=B(LL,L)-B(ICOL,L)*DUM
 19                     ENDDO
                    ENDIF
 21             ENDDO
 22         ENDDO
!
!   The main loop is now complete. Next, unscramble the solution in lig-
!   ht of any column interchanges. This is done by interchanging pairs
!   of columns in the reverse order in which the permutation was built
!   up.
!
        DO 24 L=N,1,-1
            IF(INDXR(L).NE.INDXC(L))THEN
                DO 23 K=1,N
                    DUM=A(K,INDXR(L))
                    A(K,INDXR(L))=A(K,INDXC(L))
                    A(K,INDXC(L))=DUM
 23             ENDDO
            ENDIF
 24     ENDDO
!
        RETURN
!
END SUBROUTINE GAUSSJ
!
!   *********************************************************************
!
SUBROUTINE COVSRT(COVAR,NPC,MA,IA,MFIT)
!
!  Subroutine transcribed from Numerical Recipes in Fortran, 2nd Ed. (P-
!  ress et al. 1992) with no significant alterations. This routine is c-
!  alled by MRQMIN to organize the COVAR matrix in proper rows and colu-
!  mns with 0 variances / covariances for parameters held fixed.
!
        IMPLICIT NONE
        INTEGER MA,MFIT,NPC,IA(MA)
        REAL    COVAR(NPC,NPC)       !  Expand dimension of COVAR, if nec-
        INTEGER I,J,K                !  essary, to account for parameters
        REAL    SWAP                 !  that were held fixed.
!
        DO 12 I=MFIT+1,MA
            DO 11 J=1,I
                COVAR(I,J)=0.
                COVAR(J,I)=0.
 11         ENDDO
 12     ENDDO
!
        K=MFIT
!
        DO 15 J=MA,1,-1
```

```fortran
             IF(IA(J).NE.0)THEN
                 DO 13 I=1,MA
                     SWAP=COVAR(I,K)
                     COVAR(I,K)=COVAR(I,J)
                     COVAR(I,J)=SWAP
  13             ENDDO
                 DO 14 I=1,MA
                     SWAP=COVAR(K,I)
                     COVAR(K,I)=COVAR(J,I)
                     COVAR(J,I)=SWAP
  14              ENDDO
                 K=K-1
             ENDIF
  15     ENDDO
!
         RETURN
!
END SUBROUTINE COVSRT
!
!   *********************************************************************
!
SUBROUTINE FUNCS(XS,A,YS,DYDA,NA)
!
!  This function only applies to the uniaxial stress equation with the
!  gen-Yeoh SEF. If pure shear or equibiaxial data should be fitted, th-
!  e function must be modified as follows:
!
!      Pure Shear:   AO = 2 * (XS - 1/XS**3)
!                    BO = XS**2 + 1/XS**2 - 2
!
!      Equibiaxial:  AO = 2 * (XS - 1/XS**5)
!                    BO = 2 * XS**2 + 1/XS**4 - 3
!
!      AO and BO are effectively constants so the partial derivatives re-
!      main unchanged.
!
         IMPLICIT NONE
         INTEGER NA
         REAL     XS,YS,A(NA),DYDA(NA),AO,BO
!
         AO=2*(XS-1/XS**2)           !  Variables defined for more compact
         BO=XS**2+2/XS-3             !  expression of stress equation.
!
         YS=AO*(A(1)*A(4)*BO**(A(4)-1)+&      !  Uniaxial stress equation
                A(2)*A(5)*BO**(A(5)-1)+&      !  derived from SEF.
                A(3)*A(6)*BO**(A(6)-1))
!
!      Partial derivatives with respect to each model parameter are requ-
!      ired, ie. d(YS)/d(A1), d(YS)/d(A2), ... , d(YS)/d(A6):
!
         DYDA(1)=AO*A(4)*BO**(A(4)-1)
         DYDA(2)=AO*A(5)*BO**(A(5)-1)
         DYDA(3)=AO*A(6)*BO**(A(6)-1)
         DYDA(4)=AO*A(1)*(A(4)*BO**(A(4)-1)*LOG(BO)+BO**(A(4)-1))
         DYDA(5)=AO*A(2)*(A(5)*BO**(A(5)-1)*LOG(BO)+BO**(A(5)-1))
         DYDA(6)=AO*A(3)*(A(6)*BO**(A(6)-1)*LOG(BO)+BO**(A(5)-1))
!
         RETURN
!
END SUBROUTINE FUNCS
!
!   *********************************************************************
```

207

# Appendix H: A DLOAD Subroutine for FPP in Abaqus/Standard

```
C  **********************************************************************
C  Author:   Travis Hohenberger
C  Date:     2021-10-07
C  E-mail:   twhohen@gmail.com
C  Version:  0
C  **********************************************************************
C
C  This subroutine is built from the template in Simulia (2020) (see re-
C  ference below). It has been developed to apply fluid pressure penetr-
C  ation to the surface of an axisymmetric seal that is compressed betw-
C  een two plates. A bonded interface is used to fix the seal to the bo-
C  ttom plate. A frictional interface is used with the top plate. When
C  developed, the plates were assumed to be rigid bodies, so plate defl-
C  ection is not accounted for. The geometry used when developing this
C  code is in Schematic 1. Some important notes:
C
C    1. The schematic is shown after the seal has been compressed.
C
C    2. Pressure of magnitude "F_Lim" is applied to the left surface of
C       the seal.
C
C    3. As the seal deforms under pressure, nodes on the seal that init-
C       ially contact the top plate may be pulled out of contact. If th-
C       ese nodes fall below the user-defined y-coordinate "y_Lim", pre-
C       ssure propagates to that node. Therefore, this code uses a kine-
C       matic definition to propagate pressure, as opposed to the built-
C       -in pressure penetration schemes in Abaqus/Standard which use n-
C       odal contact pressure. The different solutions have similar res-
C       ults when a sufficiently small mesh is used.
C
C    4. For the problems tested, it was found acceptable to set "y_Lim"
C       exactly equal to the y-coordinate of the top plate.
C
C    y (Axis of Symmetry)
C    ^
C    |
C    |_____
C    |                                                 |
C    |            TOP PLATE         FRICTIONAL INTERFACE  |
C    |_____|  ____
C    |                       ----->/**********\        ^
C    |                       ---->/***********\        |
C    |                       --->|* COMPRESSED *|        |
C    |               F_Lim --->|**** SEAL ****|        |
C    |                       --->|*************|      y_Lim
C    |                       --->|*************|        |
C    |--------------------------------------------------      |
C    |            BOTTOM PLATE         BONDED INTERFACE  |    |
C    |_____|    |
C    |--------------------------------------------------------> x
C
C      Schematic 1: Fixture geometry for developing the subroutine.
C
C  REFERENCE:
C  ---------
C      SIMULIA, (2020). "DLOAD". In: Abaqus R2020 User Subroutines Manua-
C      l. Dassault Systèmes Simulia Corp. Providence, Rhode Island, USA.
C
C  **********************************************************************
       SUBROUTINE DLOAD(f, kstep, kinc, time, noel, npt, layer, kspt,
      1                 coords, jltyp, sname)
C
       INCLUDE 'aba_param.inc'
C
       DIMENSION time(2), coords(3)
       CHARACTER*80 sname
C
C      PARAMETERS
C      ----------
       REAL*8    one, two
       PARAMETER(one=1.d0, two=2.d0)
C
C      LOCAL VARIABLES
C      ---------------
       REAL*8 y_Lim, F_Lim, y
```

```fortran
C
C      *******************************************************************
C      ----------------- USER INPUTS (SEE SCHEMATIC 1) ------------------
C      *******************************************************************
       y_Lim = 11.177
       F_Lim = 11.
C
C      *******************************************************************
C      ------ ASSIGN THE VARIABLE y TO y-COORDINATES IN THE MODEL -------
C      *******************************************************************
       y = coords(2)
C
C      *******************************************************************
C      |     IN A FIRST STEP, APPLY PRESSURE TO NODES BELOW "y_Lim",     |
C      |          AND THEN DEPRESSURIZE IN THE FOLLOWING STEP.           |
C      |       FOR MORE DETAILS, SEE THE NOTES BELOW THIS SECTION.       |
C      *******************************************************************
       IF (time(2).LE.two) THEN
          IF (y.LT.y_Lim) THEN
             F = F_Lim * time(1)
          END IF
       ELSE IF (time(2).GT.two) THEN
          IF (y.LT.y_Lim) THEN
             F = F_Lim * (one-time(1))
          END IF
       END IF
C
       RETURN
       END SUBROUTINE DLOAD
C
C **********************************************************************
C ------------------------ SOME MORE NOTES -------------------------
C **********************************************************************
C
C  1. With the code as currently written, the pressurization step must
C     be defined with a step time of 1. The same time must be assigned
C     for the depressurization step to give a total time of 2.
C
C  2. The variable "time" stores the current step time in "time(1)" and
C     the total time in "time(2)".
C
C  3. During the pressurization step, the pressure ramps up from 0 to
C     "F_Lim". During the depressurization step, the pressure ramps do-
C     wn from "F_Lim" to 0.
```

# Appendix J: A VDLOAD Subroutine
# for FPP in Abaqus/Explicit

```
C **********************************************************************
C  Author:    Travis Hohenberger
C  Date:      2021-10-07
C  E-mail:    twhohen@gmail.com
C  Version:   0
C **********************************************************************
C
C  This subroutine is built from the template in Simulia (2020) (see re-
C  ference below). It has been developed to apply fluid pressure penetr-
C  ation to the surface of an axisymmetric seal that is compressed betw-
C  een two plates. A bonded interface is used to fix the seal to the bo-
C  ttom plate. A frictional interface is used with the top plate. When
C  developed, the plates were assumed to be rigid bodies, so plate defl-
C  ection is not accounted for. The geometry used when developing this
C  code is in Schematic 1. Some important notes:
C
C    1. The schematic is shown after the seal has been compressed.
C
C    2. Pressure of magnitude "F_Lim" is applied to the left surface of
C       the seal.
C
C    3. As the seal deforms under pressure, nodes on the seal that init-
C       ially contact the top plate may be pulled out of contact. If th-
C       ese nodes fall below the user-defined y-coordinate "y_Lim", pre-
C       ssure propagates to that node. Therefore, this code uses a kine-
C       matic definition to propagate pressure, as opposed to the built-
C       -in pressure penetration schemes in Abaqus/Standard which use n-
C       odal contact pressure. The different solutions have similar res-
C       ults when a sufficiently small mesh is used.
C
C    4. For the problems tested, a kinematic contact definition (as opp-
C       osed to the penalty option that is also available in Abaqus/Exp-
C       licit) was used at the top interface. To prevent premature seal
C       leakage, it was found necessary to set "y_Lim" slightly below t-
C       he y-coordinate of the top plate in some cases. As one example,
C       when the compressed seal height was 10.619 mm, y_Lim=10.6185 was
C       used. The lower value is required because elastic waves due to
C       inertia can cause the sealing front to be unstable.
C
C    y (Axis of Symmetry)
C    ^
C    |
C    |_____
C    |                                                 |
C    |           TOP PLATE        FRICTIONAL INTERFACE |
C    |_____| _____
C    |                    ----->/*********\            ^
C    |                    ---->/***********\           |
C    |                    --->|* COMPRESSED *|         |
C    |            F_Lim --->|**** SEAL ****|           |
C    |                    --->|*************|         y_Lim
C    |                    --->|*************|           |
C    |-------------------------------------------       |
C    |           BOTTOM PLATE       BONDED INTERFACE |  |
C    |_____|  |
C    |----------------------------------------------------> x
C
C     Schematic 1: Fixture geometry for developing the subroutine.
C
C  REFERENCE:
C  ---------
C     SIMULIA, (2020). "VDLOAD". In: Abaqus R2020 User Subroutines Manu-
C     al. Dassault Systèmes Simulia Corp. Providence, Rhode Island, USA.
C
C **********************************************************************
      SUBROUTINE VDLOAD(nBlock, ndim, stepTime, totalTime, amplitude,
     1                  curCoords, velocity, dirCos, jltyp, sname, value)
C
      INCLUDE 'vaba_param.inc'
C
      DIMENSION curCoords(nBlock,ndim)   , velocity(nBlock,ndim),
     1          dirCos(nBlock,ndim,ndim) , value(nBlock)
      CHARACTER*80 sname
C
C     LOCAL VARIABLES
```

```
C      ---------------
       INTEGER  km
       REAL*8    y_Lim , F_Lim , y
C
C      ******************************************************************
C      ----------------- USER INPUTS (SEE SCHEMATIC 1) ------------------
C      ******************************************************************
       y_Lim = 10.6185
       F_Lim = 17.
C
C      ******************************************************************
C      ---------- APPLY PRESSURE TO THE ELEMENTS IN THE MODEL -----------
C      ******************************************************************

       DO 100 km = 1,nBlock
          IF (curCoords(km,2).LT.y_Lim) THEN
             value(km) = amplitude * F_Lim
          END IF
  100 CONTINUE
C
       RETURN
       END SUBROUTINE VDLOAD
C ************************************************************************
C ------------------------- SOME MORE NOTES ----------------------------
C ************************************************************************
C
C   There are various ways of implementing this type of pressure penetr-
C   ation subroutine in Abaqus/Explicit. One simple method is to set the
C   step time for pressurization equal to the target pressure that is s-
C   pecified by "F_Lim", and then define an amplitude with a time inter-
C   val that begins at 0 and ends at the same value as "F_Lim". The mag-
C   nitudes at each time are then specified as 0 and 1, respectively.
C
C   Using the method described thus far, the default amplitude called i-
C   nto the VDLOAD subroutine will be incorrect. The correct amplitude
C   cannot be specified in Abaqus/CAE, so it must be manually entered in
C   the input file. Below is some example text from an input file. It s-
C   hows an amplitude definition from 0 to 17 seconds with magnitudes of
C   0 and 1. The step time is 17 which matches the amplitude time. The
C   bold red text is manually added to the input file to call the corre-
C   ct amplitude into the Dsload pressure (which is itself defined by a
C   VDLOAD subroutine.
C
C   *Amplitude, name=Amp-P01-0000-1700
C             0.,                 0.,                 17.,                1.
C   ** ------------------------------------------------------------------
C   **
C   ** STEP: P-01
C   **
C   *Step, name=P-01, nlgeom=YES
C   *Dynamic, Explicit, element by element
C   , 17.
C   *Bulk Viscosity
C   0.06, 1.2
C   **
C   ** LOADS
C   **
C   ** Name: P-01   Type: Pressure
C   *Dsload, amplitude=Amp-P01-0000-1700
C   Surf-Pressure, PNU, 0.
```

# Appendix K: A Rubber Compound
# with Imperfect Hyperelasticity

Fig. K.1 shows uniaxial tension and compression data for a sealing compound. The "Equivalent ET" dots are computed from the uniaxial compression data according to the theory in Appendix E. In Fig. K.1a, the curve fits to the uniaxial compression data and equivalent equibiaxial data are good. The good fit in both modes is a consequence of their theoretical equivalence. However, the fit to the uniaxial tension data is poor. Due to the large separation between the equivalent equibiaxial "data" and the uniaxial tension data, the material is not well-conditioned for fitting with a hyperelastic strain-energy function. That is, the material exhibits imperfect hyperelastic behaviour. Fig. K.1b adjusts the model parameters to achieve a good fit to the uniaxial tension data which results in a poor fit to the uniaxial compression data. If the uniaxial tension and compression test data were converted to a reduced form according to Eq. 4.4, they would not overlap in the linear region (on a logarithmic scale) as was the case in Fig. 4.5a.
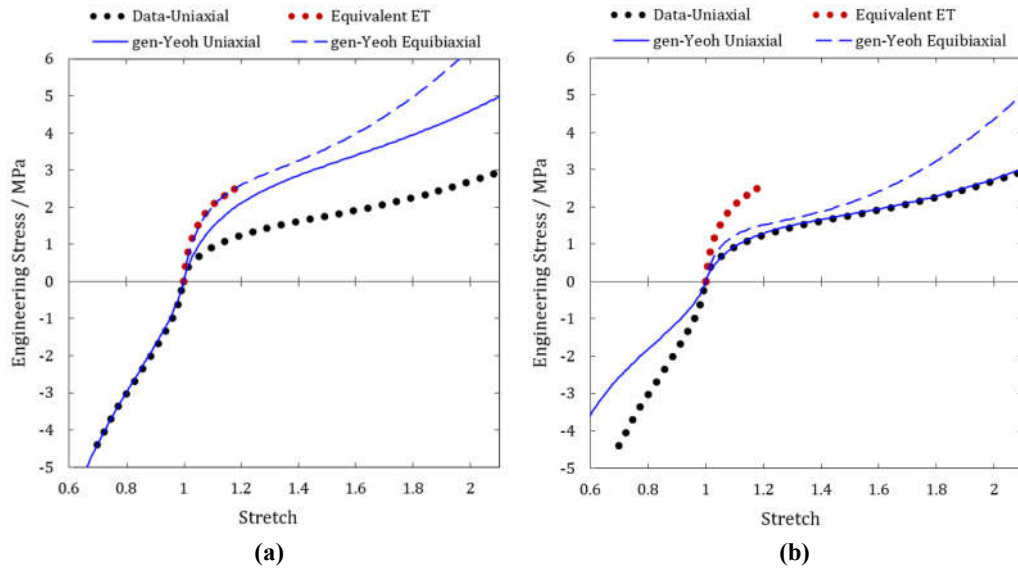


**Fig. K.1:** Illustration of imperfect hyperelasticity in a rubber material: **(a)** a gen-Yeoh SEF fit to uniaxial compression data (and by corollary the equivalent equibiaxial data that is computed from the uniaxial compression data as described in Appendix E); **(b)** a gen-Yeoh SEF fit to the uniaxial tension data. No set of model parameters can achieve a good fit to both uniaxial compression and tension data because the rubber material does not follow ideal hyperelastic model theory.

# Appendix L: Test Fixture Dimensions and Test Plan for Experimental Testing

Critical test fixture dimensions are illustrated in Fig. L.1. The components are identified in Fig 6.1 and Table 6.1. Table L.1 shows actual measurements that were determined with digital calipers. For simulations in Chapter 7, average dimensions were used when multiple measurements of a single feature were recorded.
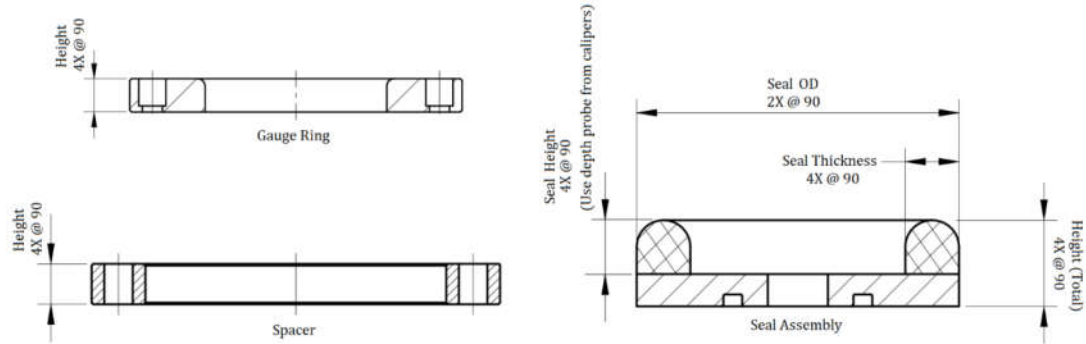


**Fig. L.1:** Critical dimension locations for test fixture components.

**Table L.1:** Critical test fixture dimensions for experimental testing. Units are mm.

| Description | SN | Height (total) 4X @ 90° | Seal Height 4X @ 90° | Seal Thickness 4X @ 90° | Seal OD 2X @ 90° |
|---|---|---|---|---|---|
| Spacer, 0.775" | – | 19.70/19.71 /19.70/19.70 | N/A | N/A | N/A |
| Spacer, 0.750" | – | 19.05/19.04/19.05/19.05 | N/A | N/A | N/A |
| Spacer, 0.725" | – | 18.41/18.41/18.41/18.41 | N/A | N/A | N/A |
| Gauge Ring, 0.425" | – | 10.8/10.8/10.8/10.8 | N/A | N/A | N/A |
| Gauge Ring, 0.300" | – | 7.62/7.62/7.62/7.62 | N/A | N/A | N/A |
| Gauge Ring, 0.125" | – | 3.16/3.15/3.16/3.16 | N/A | N/A | N/A |
| Seal Assembly, NR | 1 | 20.30/20.31/20.35/20.30 | 12.56/12.61/12.65/12.60 | 12.61/12.61/12.63/12.65 | 76.20/76.30 |
| Seal Assembly, NR | 2 | 20.25/20.26/20.34/20.31 | 12.56/12.57/12.65/12.62 | 12.64/12.68/12.65/12.62 | 76.20/76.25 |
| Seal Assembly, NR | 3 | 20.28/20.27/20.30/20.25 | 12.61/12.60/12.63/12.58 | 12.59/12.62/12.64/12.61 | 76.25/76.25 |
| Seal Assembly, NR | 4 | 20.23/20.35/20.28/20.25 | 12.56/12.68/12.61/12.58 | 12.60/12.64/12.61/12.58 | 76.25/76.25 |
| Seal Assembly, NR | 5 | 20.29/20.29/20.32/20.32 | 12.59/12.59/12.62/12.56 | 12.61/12.67/12.68/12.62 | 76.25/76.25 |
| Seal Assembly, NR | 6 | 20.37/20.34/20.32/20.32 | 12.67/12.64/12.62/12.62 | 12.67/12.62/12.63/12.60 | 76.25/76.25 |
| Seal Assembly, NR | 7 | 20.27/20.35/20.32/20.28 | 12.56/12.64/12.61/12.57 | 12.62/12.66/12.63/12.60 | 76.25/76.25 |
| Seal Assembly, NR | 8 | 20.29/20.32/20.28/20.35 | 12.60/12.62/12.59/12.65 | 12.57/12.62/12.59/12.60 | 76.25/76.25 |
| Seal Assembly, NR | 9 | 20.31/20.25/20.31/20.31 | 12.60/12.54/12.60/12.60 | 12.59/12.63/12.60/12.61 | 76.20/76.20 |
| Seal Assembly, EPDM | 1 | 20.48/20.48/20.49/20.49 | 12.61/12.60/12.60/12.60 | 12.72/12.72/12.71/12.73 | 76.20/76.20 |
| Seal Assembly, EPDM | 2 | 20.50/20.51/20.50/20.51 | 12.61/12.60/12.60/12.62 | 12.75/12.72/12.71/12.75 | 76.20/76.20 |
| Seal Assembly, EPDM | 3 | 20.45/20.47/20.45/20.47 | 12.61/12.60/12.64/12.61 | 12.73/12.73/12.71/12.75 | 76.20/76.20 |
| Seal Assembly, EPDM | 4 | 20.45/20.45/20.45/20.45 | 12.61/12.61/12.60/12.61 | 12.73/12.73/12.71/12.75 | 76.20/76.20 |
| Seal Assembly, EPDM | 5 | 20.45/20.44/20.47/20.48 | 12.61/12.61/12.62/12.62 | 12.72/12.72/12.71/12.73 | 76.20/76.20 |
| Seal Assembly, EPDM | 6 | 20.37/20.37/20.41/20.41 | 12.61/12.61/12.63/12.63 | 12.72/12.72/12.71/12.75 | 76.20/76.20 |
| Seal Assembly, EPDM | 7 | 20.45/20.45/20.48/20.48 | 12.61/12.60/12.60/12.62 | 12.76/12.72/12.71/12.73 | 76.20/76.20 |
| Seal Assembly, EPDM | 8 | 20.56/20.56/20.56/20.56 | 12.61/12.62/12.61/12.61 | 12.76/12.76/12.73/12.73 | 76.16/76.23 |
| Seal Assembly, EPDM | 9 | 20.47/20.47/20.47/20.49 | 12.61/12.60/12.60/12.60 | 12.72/12.72/12.71/12.73 | 76.20/76.20 |

## Assembly Procedure

1. Lubricate O-ring #216 with Krytox GPL 206 grease and install the seal carrier that has natural rubber (NR) and serial number 1.

2. Fix the seal carrier to the bottom plate with the button head cap screw.

3. Install the 0.300" (7.62 mm) gauge ring on the bottom plate with 8 low profile socket head screws.

4. Lubricate the top of the gauge ring with Lubriplate L0161-05 or Krytox GPL 206 grease because the seal will contact this surface when pressure forces it into the extrusion gap.

5. Position the 0.775" (19.7 mm) spacer on the bottom plate.

   Note: Both EPDM and NR swell in hydrocarbon fluids. There is no need to rush the following steps, but do not allow the seals to sit in the fixture for an extended period of time (for instance during a lunch break or overnight) after installation.

6. Lubricate the bonded seal and the sealing countersurface of the top plate with Lubriplate L0161-05 or Krytox GPL 206 grease. Be sure to also apply grease to the region of the top plate that will sit above the gauge ring as the seal will contact this surface when pressure forces it into the extrusion gap.

7. Install the top plate and secure with 8 socket screws), 16 washers, and 8 nuts. These hardware items must be grade 8 for adequate strength. Be sure to fully compress the bonded seal until the top and bottom plates are flush with the spacer ring. Record the time.

8. Connect a pressure line to the top plate. The test medium shall be water to prevent swelling of the rubber.

9. Place the device under test (DUT) in a thermally controlled environment such as a test chamber with a temperature of 23±1°C.

## Pressure Test Procedure

1. Slowly apply pressure to the DUT, trying to maintain the curve as smooth as reasonably possible. There may be pressure fluctuations (stick-slip) as the seal displaces. Continue adding pressure until there are indications of leakage across the seal. Stop increasing pressure if 5,400 psi (37.2 MPa) is reached. No pressure hold time is required for this step. Simply try to capture the peak pressure when leakage occurs.

2. Record the leak pressure "P1". If no leak occurred, write "No Leak".

3. Bleed pressure to atmosphere.

4. Repeat steps 1 and 2 in this section two times, recording pressures in columns "P2" and "P3".

5. Disassemble and reassemble the fixture according to the test matrix, taking note of the following:

   a. If at any time elastomer fracture is found, put the test on hold and contact Schlumberger for further instruction.

   b. Be sure to match the serial numbers of the seal assemblies to the correct spacers and gauge rings.

   c. Remember to apply the required grease to the bonded seal, top plate, and gauge ring when changing seal assemblies.

   d. For the gauge ring indicated as 0.425"+0.125" (10.8 mm + 3.18 mm), be sure to place the 0.125" (3.18 mm) gauge ring under the 0.425" (10.8 mm) gauge ring.

# Appendix M: Some Notes on Sources of Error in the Uniaxial Tension Test

A uniaxial tension test is commonly used for constructing a hyperelastic material model. The test specimen is often a flat or cylindrical dumbbell clamped at its ends and extended until it fractures in its gauge section. Fig. 4.8 shows two different test configurations, each with its own benefits which are discussed in Section 4.3. Dumbbell geometry is governed by ASTM D412,[235] and it includes tolerances on the geometric form, such as width variation in the gauge section. Obviously, the width varies along the length of the dumbbell, but in some cases, it also varies through the thickness; that is, the cross-sections may be trapezoidal instead of rectangular. This is a problem particularly when dies are used to cut dumbbells from rubber plaques and the material is resistant to cutting. The rubber is subjected to non-uniform compression during the cutting which develops the trapezoidal shape. For the sealing materials in this work, the width variation through the thickness is about $\pm 3\%$, admittedly small but easily corrected with careful measurements as shown in Fig. M.1.



**Fig. M.1:** Measurement of the dumbbell width with the tip of the calipers positioned at the top face of the specimen. The bottom face would also be measured. Multiple positions along the length, for instance 6 total places, can be measured and averaged.

Thermal expansion is an important consideration when testing rubber, but it is difficult to address it properly when testing at high temperatures. For example, when HNBR dumbbells at 163℃ are removed from a thermal chamber, they start to cool down and contract immediately, rendering cross-sectional measurements inaccurate. Therefore, one must measure dimensions inside the thermal chamber, or estimate them from an independent measure of their thermal expansivity. The first solution is not always possible. The second solution is complicated by rubber's non-linear thermal expansivity, as well as anisotropy that is inherent in thin rubber sheets.[121,270,271] These complications aside, consider an HNBR dumbbell with nominal cross-sectional gauge dimensions of 6 mm $\times$ 2 mm and a thermal expansion coefficient (assumed linear) of 0.000245 mm/(mm $\cdot$ ℃) over the temperature range of 20–163℃.[256] Under such conditions, thermal expansion can introduce up to 7% error in the cross-sectional area (and hence, stress) if not properly addressed.

When dumbbells are gripped at their narrow section and strain is computed from grip displacement, constraint at the grips introduces uncertainty in the nominal length that is used for strain calculations. For the sealing materials tested in this work, the length increased about 0.5–1 mm when compressed by the grips. It is simple enough to use this to offset the nominal length for strain calculations, but it does not address the fact that the rubber width cannot contract at the grip constraint when the dumbbell is stretched. This source of error decreases as the nominal length increases, but the maximum length of the dumbbell should not exceed the length of the straight portion of the dumbbell, about 30 mm for an ASTM (die C) dumbbell.[235] Therefore, it is plausible to assume that the order of this error is 1 mm / 30 mm $\approx$ 3%. By itself, this error is negligibly low for practical purposes, but it becomes problematic when coupled with other errors. The composite error based on the three sources above is 13%, a more concerning number. Thus, there are two points to emphasise. First, even the well-known uniaxial tension test has nontrivial complications when testing rubber. Second, attention must be given to small sources of error when testing rubber because they collectively generate larger composite errors.

# Appendix N: Assessment of the Equibiaxial Tension Test with a Disc Specimen

The biaxial tension test is difficult to execute because it requires loading in two perpendicular directions. Treloar's[233] pioneering work in this regard (Fig. N.1a,b) has been enduring with the concept still being used and refined to this day. (Note: It appears that the image of Treloar's biaxial test piece did not make it into the digital scan for the online version of his article from 1948, but it can be found in his textbook[50] published in 1975.) He attached wires to tabs extending from a nominally square test section. Weights were hung from the wires to stretch the rubber in two directions.
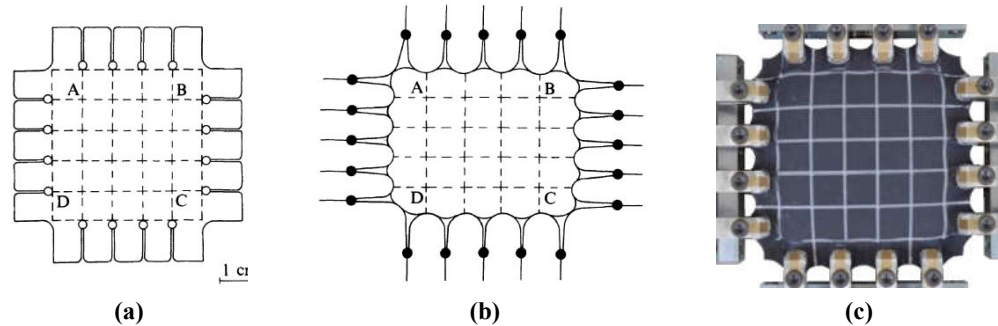


**Fig. N.1:** Biaxial test specimens: **(a)** an unstretched specimen as proposed by Treloar;[50] **(b)** a specimen with tabs loaded by weights; **(c)** a more recent specimen in equibiaxial tension as given by Fujikawa *et al.*[234]

Various contraptions have been proposed for biaxial testing. One concept that transforms a uniaxial extension into a biaxial deformation is shown in Fig. N.2.[272] When the green bar and linkages are pulled vertically, blue cylinders traverse along the red linkages to pull the test specimen in a horizontal direction. The ratio of vertical to horizontal extension is controlled by the angle of red linkages with respect to the horizontal bracket on which they mount. The primary drawbacks of such contraptions are that they are kinematically complicated, and tight machine tolerances are required to minimise play between interacting components.
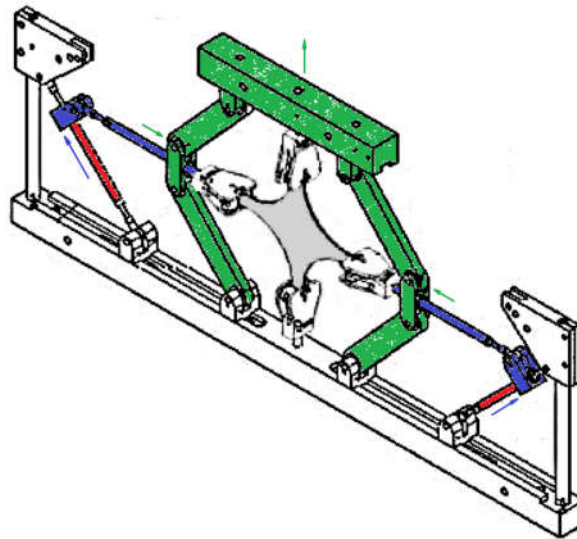


**Fig. N.2:** A biaxial test contraption for a uniaxial tension test machine. (Adapted from Brieu *et al.*)[272]

Axel Physical Testing Services provides a unique solution for equibiaxial testing. The company uses a disc-shaped specimen with radial tabs that are pulled by wires (Fig. N.3a). Pulleys redirect the radial loads into an axial direction so that a uniaxial load causes a radial stretch. The test piece geometry is shown in Fig. N.3b. Strain is optically measured across a ∅25 mm section of the specimen. A finite-element study by Day & Miller[232,273] indicates that the strain through this location is indeed uniform (Fig. N.3c). Nominal (engineering) stress is reported as $\sigma = F_r/A_r$ where

$F_r$ is the total radial force (assumed equivalent to the total axial force), $A_r = \pi dh$, $d = 50$ mm, and $h$ is the specimen thickness. However, Fig. N.3c shows that the strain at the location nominally defined by $d = 50$ mm is not uniform in the deformed configuration; therefore, stress cannot be uniform. In addition, the nominally cylindrical area, $A_r$, does not remain cylindrical in the deformed configuration.
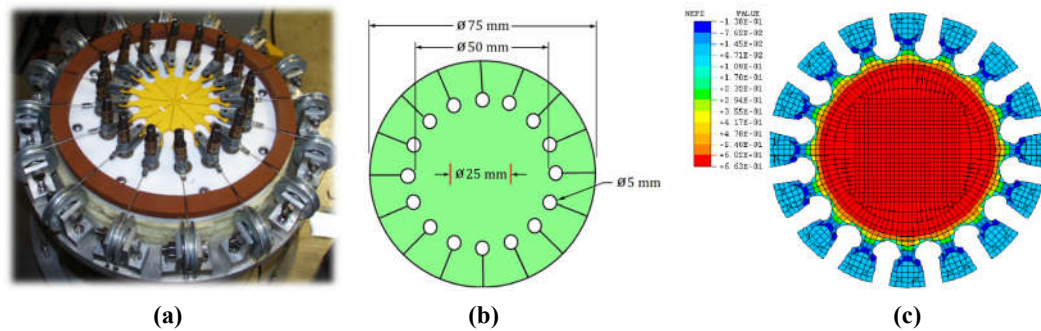


**Fig. N.3:** Disc-shaped equibiaxial test specimen: **(a)** undergoing deformation at Axel Physical Testing Services; **(b)** nominal specimen dimensions; **(c)** FE study showing that strain is uniform in the location nominally defined at $d = 25$ mm, but strain at the location nominally defined by the location at $d = 50$ mm is not uniform. (Adapted from Day & Miller.)[232,273]

Inhomogeneous deformation through the tab transition casts doubt on the validity of reporting stress in the equibiaxial test specimen as $\sigma = F_r/A_r$, but force equilibrium offers some justification. It can be shown that, given a radial stress applied to the perimeter of a disc with known dimensions, the internal stress at any interior location is equal to the applied radial stress. Referring to Fig. N.4, the proof, which is shown in Appendix F, shows that $\sigma_1 = \sigma_2 = \sigma_3 = \sigma_4$. To quantify how well this result, which is what Axel's calculation is based on, applies to the actual test specimen, a finite-element study with a finer mesh and larger strain than that shown in Fig. N.3c has been conducted as part of this work.
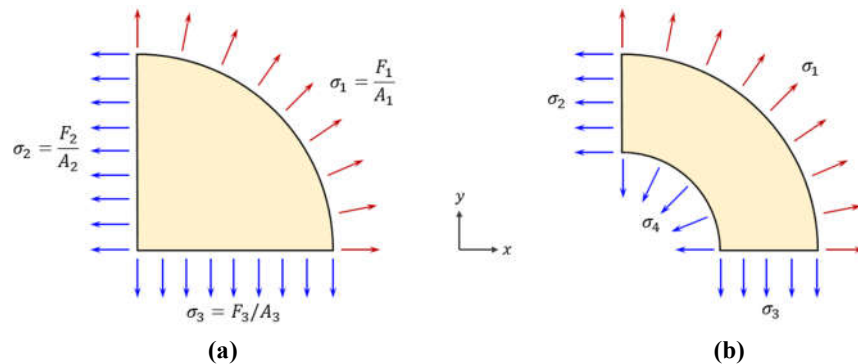


**Fig. N.4:** Free body diagrams of a quarter of a disc held in equibiaxial tension: **(a)** before a cut along an internal radial surface; **(b)** after a cut along an internal radial surface.

2D plane stress and 3D analyses of Axel's equibiaxial specimen were conducted, and the results differed by less than 2%. The detailed results presented here refer to 2D models with the settings shown in Table N.1. To reduce the number of elements, a $1/16^{th}$ model was used with tangential symmetry constraints. Incompressible Neo-Hookean and Yeoh SEFs were used. The former used a shear modulus typical of unfilled rubber, and the latter used model parameters for the 90D (Shore A) HNBR sealing material from Section 4.2. The tabs were loaded at their centres with Ø5 mm circular imprints to simulate clamp surfaces. Mesh independence was confirmed to be within 0.5% by comparing radial force reactions while using element seed sizes of 0.125 mm and 0.0625 mm. Fig. N.5 shows the undeformed and deformed geometry, with strain based on nodal displacement (which is an average across the test specimen) also indicated. For reference, the maximum equivalent uniaxial compression (see Eq. 2.20) for the specimen is $\bar{\varepsilon} \approx -0.75$.

**Table N.1:** 2D plane stress finite-element model settings for an equibiaxial test specimen.

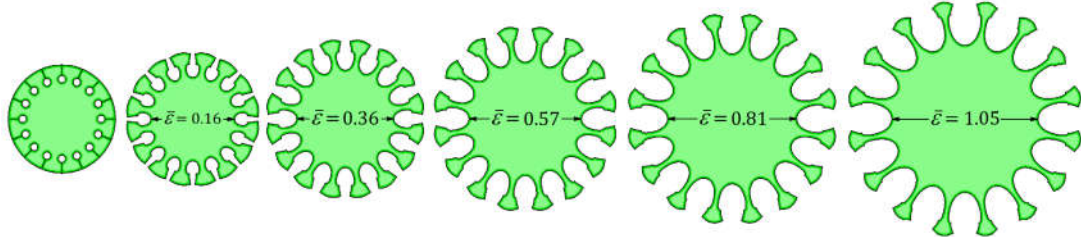| Parameter | Value |
|---|---|
| Strain-energy function | Neo-Hookean, $C_{10} = G/2 = 1$ MPa<br>Yeoh, $(C_{10}, C_{20}, C_{30}) = (2.9, -0.15, 0.025)$ MPa |
| Volumetric behaviour | Incompressible |
| Element type | CPS4R (quadrilateral, linear, reduced integration) |
| Test type | Displacement controlled |
| Tab displacement | Ø90 mm |
| Mesh seed size | 0.0625 mm |



**Fig. N.5:** An equibiaxial test specimen with clamp displacements in Ø18 mm increments, up to a total displacement of Ø90 mm. $\bar{\varepsilon}$ denotes average strain across the specimen.
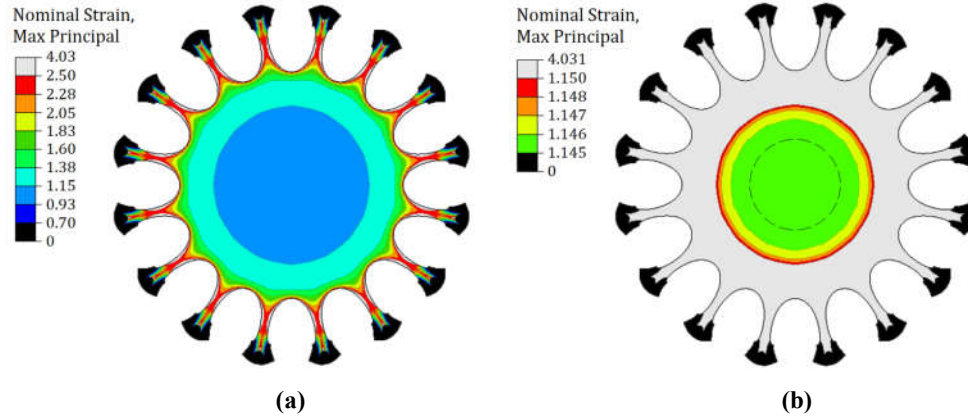


**Fig. N.6:** Maximum principal strains (nominal) in an equibiaxial test specimen with a clamp displacement of Ø90 mm: **(a)** with a broad contour band to show inhomogeneous strain through the tab transition zone; **(b)** with a narrow contour band to illustrate the homogeneity in the gauge section. The dashed line indicates the location of marks that were initially at Ø25 mm.

Fig. N.6 shows maximum principal strain contours in the equibiaxial specimen when stretched by Ø90 mm. There is a rapid transition through the tab section. The contour scale is reduced in Fig. N.6b to illustrate that the strain in the central region of the specimen is uniform over a 0.001 range, and the diameter defined by Axel's gauge marks (indicated by the dashed circle) falls well within this range. Therefore, measurement of strain along a nominal diameter of 25 mm is justified.

Fig. N.7 shows stress-strain responses predicted by inspection of elements nominally located at Ø25 mm in the finite-element models. The stress-strain response is also computed from Axel's equation, $\sigma = F_r/A_r$, with $F_r$ determined by the force reaction at the tab and $A_r = 50\pi$ for a specimen of unit thickness. The errors indicated along the curves show that the calculation systematically overpredicts stress, but it reproduces all salient features of the FE models.
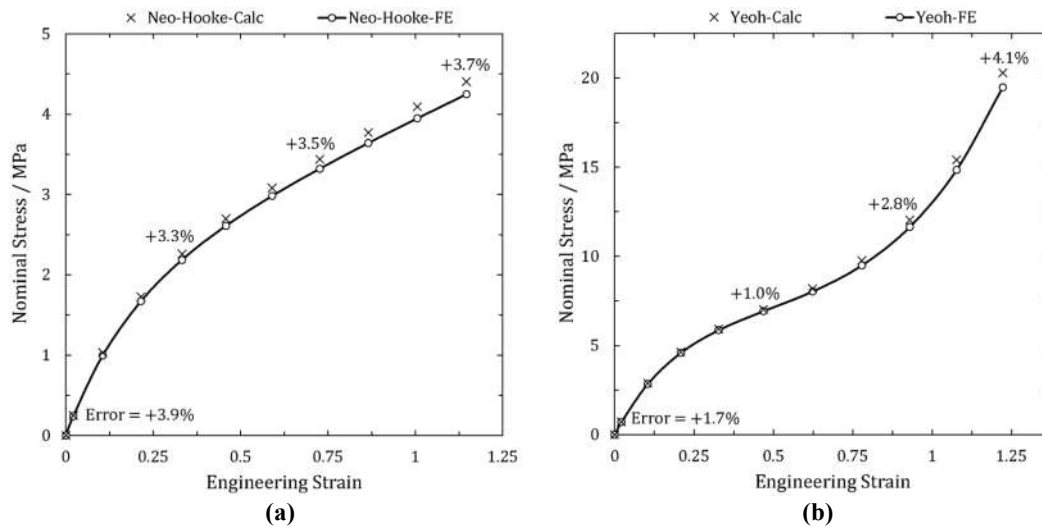
**Fig. N.7:** Stress-strain responses as predicted by an incompressible finite-element solution and Axel's approximate calculation. Some typical errors are shown assuming the FE solution is exact. **(a)** Neo-Hookean SEF; **(b)** Yeoh SEF.

To explain why Axel's calculation overpredicts stress, it is easiest to analyse true stress. Referring to Fig. N.7a, the true stress according to Axel's model at the maximum strain is computed as $\hat{\sigma} = (1 + \varepsilon)\sigma = 9.46$ MPa.[50] When comparing this value to true stress in the finite-element model, a problem is encountered because, as Fig. N.8 shows, the diameter nominally defined at 50 mm is variable in the deformed configuration, so selecting an area for the true stress calculation is not straightforward. Using the minimum and maximum extents of the red curve in Fig. N.8b to define cylindrical areas, the range of true stress is computed as 9.01– 9.76 MPa which are limits that bound Axel's solution. Using the average diameter along the red curve, which is not the arithmetic average of the range but is determined from measurements in the FE model, the true stress is computed to be 9.45 MPa, nearly identical to Axel's calculation. Hence, it appears that Axel's calculation systematically overpredicts stress because it relies on an averaging assumption that does not strictly apply to an equibiaxial specimen with tabs. Regardless, the error is acceptable for most, if not all, practical applications. It is worth commenting that the systematic error is not restricted to Axel's equibiaxial test specimen; it arises from the inherently complex boundary conditions required for all equibiaxial test setups. For completeness, it is noted that some authors[274,275] have used inflation of rubber sheets to approximate the equibiaxial loading condition. These test rigs are also prone to complications at the clamp boundary.
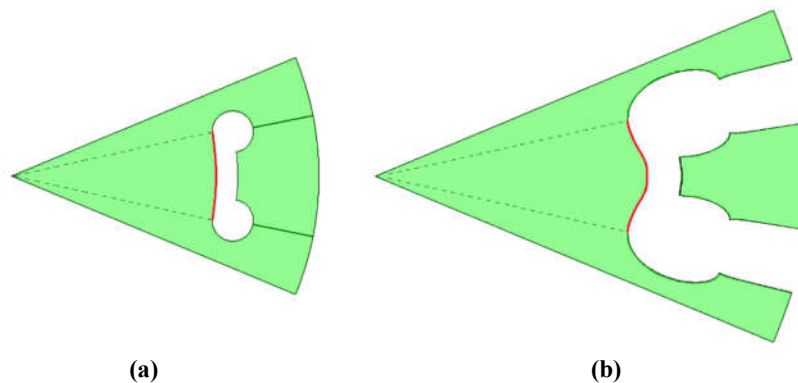


**Fig. N.8:** $1/8^{th}$ model of an equibiaxial specimen with elements removed to show how the initially circular curve at $\varnothing 50$ mm deforms when a load is applied: **(a)** undeformed configuration; **(b)** deformed configuration.

# Appendix P: User Guidelines for a UHYPER Subroutine

Implementing the gen-Yeoh SEF with a UHYPER subroutine[276] only requires a user to specify Eq. 4.6 and appropriate derivatives which for the gen-Yeoh SEF are:

$$\frac{\partial W}{\partial \bar{I}_1} = mK_1(\bar{I}_1 - 3)^{m-1} + pK_2(\bar{I}_1 - 3)^{p-1} + qK_3(\bar{I}_1 - 3)^{q-1} \tag{P.1}$$

$$\frac{\partial^2 W}{\partial \bar{I}_1^2} = (m^2 - m)K_1(\bar{I}_1 - 3)^{m-2} + (p^2 - p)K_2(\bar{I}_1 - 3)^{p-2} + (q^2 - q)K_3(\bar{I}_1 - 3)^{q-2} \tag{P.2}$$

$$\frac{\partial W}{\partial J} = \frac{2}{D_1}(J - 1) \tag{P.3}$$

$$\frac{\partial^2 W}{\partial J^2} = \frac{2}{D_1} \tag{P.4}$$

A mathematical indeterminacy arises if $m$, $p$, or $q$ are less than one (see Section 4.2). Because the UHYPER subroutine requires the second derivative of the SEF, the numerical issue also arises if $m$, $p$, or $q$ are non-integer and less than two. The following logic can address the indeterminacy:

IF $(\bar{I}_1 = 3$ AND $(m < 1$ OR $p < 1$ OR $q < 1))$ THEN

$\quad \dfrac{\partial W}{\partial \bar{I}_1} = 1$

ELSE

$\quad \dfrac{\partial W}{\partial \bar{I}_1} = mK_1(\bar{I}_1 - 3)^{m-1} + pK_2(\bar{I}_1 - 3)^{p-1} + qK_3(\bar{I}_1 - 3)^{q-1}$

END IF

IF $(\bar{I}_1 = 3$ AND $(m < 2$ OR $p < 2$ OR $q < 2))$ THEN

$\quad \dfrac{\partial^2 W}{\partial \bar{I}_1^2} = 0$

ELSE

$\quad \dfrac{\partial^2 W}{\partial \bar{I}_1^2} = (m^2 - m)K_1(\bar{I}_1 - 3)^{m-2} + (p^2 - p)K_2(\bar{I}_1 - 3)^{p-2} + (q^2 - q)K_3(\bar{I}_1 - 3)^{q-2}$

END IF

Even though $\partial W/\partial \bar{I}_1 \to \infty$ when, for instance, $m < 1$, the first IF-THEN statement assigns a finite value to $\partial W/\partial \bar{I}_1$ because Abaqus will not initialise a solution if $\partial W/\partial \bar{I}_1$ is too close to zero or tends to infinity. The choice of finite value does not appear to affect the solution as long as convergence is achieved. Abaqus can initialise a solution with $\partial^2 W/\partial \bar{I}_1^2 = 0$, so that has been used. The full code for the UHYPER subroutine is in Appendix A.

# Appendix Q: User Guidelines for a VUMAT Subroutine

VUMATs have been implemented by many researchers, but detailed codes are rarely published. Some Neo-Hookean VUMATs can be found. Bergström provides a partially complete but obsolete example,[97] and Chester[277] gives a partial code that, while correct, is not computationally optimal. Simulia also provides some code blocks for the Neo-Hookean SEF in training materials in its 3DS Academy.[278] However, finding a complete and validated code for a hyperelastic VUMAT is not easy.

Guidelines on writing a VUMAT can be found in Abaqus documentation.[279] The Cauchy stress tensor, stretch tensor, and strain increment tensor are stored in vectors with six components. For instance, Cauchy stress components are:

$$\hat{\boldsymbol{\sigma}} = \begin{bmatrix} \hat{\sigma}_{11} & \hat{\sigma}_{12} & \hat{\sigma}_{13} \\ \hat{\sigma}_{21} & \hat{\sigma}_{22} & \hat{\sigma}_{23} \\ \hat{\sigma}_{31} & \hat{\sigma}_{32} & \hat{\sigma}_{33} \end{bmatrix} = (\hat{\sigma}_{11}, \hat{\sigma}_{22}, \hat{\sigma}_{33}, \hat{\sigma}_{12}, \hat{\sigma}_{23}, \hat{\sigma}_{13}) = (\hat{\sigma}_1, \hat{\sigma}_2, \hat{\sigma}_3, \hat{\sigma}_4, \hat{\sigma}_5, \hat{\sigma}_6) \qquad \text{(Q.1)}$$

where the symmetry of $\hat{\sigma}_{ij} = \hat{\sigma}_{ji}$ has been invoked to reduce storage space.

In Abaqus/Explicit, VUMAT subroutines require stresses to be expressed in the reference (undeformed) configuration. This is achieved by using the rotation tensor to convert the Cauchy stress to its corotational form with the definition:

$$\hat{\boldsymbol{\sigma}}_{co} = \mathbf{R}^T \hat{\boldsymbol{\sigma}} \mathbf{R} \qquad \text{(Q.2)}$$

Another useful definition for numerical implementation is the modified stretch tensor:

$$\overline{\mathbf{U}} = J^{-1/3} \mathbf{U} \qquad \text{(Q.3)}$$

Combining Eqs. 2.37, 2.45, 2.49, Q.2, Q.3 and applying the properties $\mathbf{R}^T \mathbf{R} = \mathbf{R}\mathbf{R}^T = \mathbf{I}$ and $\text{tr}(\mathbf{R}\overline{\mathbf{U}}^2 \mathbf{R}^T) = \text{tr}(\overline{\mathbf{U}}^2)$, corotational stresses may be expressed as:

$$\hat{\boldsymbol{\sigma}}_{co} = \frac{2}{J}\left(\frac{\partial W}{\partial \bar{I}_1}\right)\left(\overline{\mathbf{U}}^2 - \frac{1}{3}\text{tr}(\overline{\mathbf{U}}^2)\mathbf{I}\right) + \frac{\partial W}{\partial J}\mathbf{I} \qquad \text{(Q.4)}$$

The forms of Eq. 2.49 and Eq. Q.4 are identical, but it is important to recognize that $\overline{\mathbf{B}} \neq \overline{\mathbf{U}}^2$; each tensor returns stress in different configurations. The following steps will execute a hyperelastic VUMAT with the gen-Yeoh SEF in Abaqus:

1. Compute the strain tensor, $\mathbf{B}^* = \mathbf{U}^2$.

2. Compute the volume ratio, $J = \det \mathbf{U}$.

3. Compute the modified strain tensor, $\overline{\mathbf{B}}^* = J^{-2/3}\mathbf{B}^*$.

4. Compute derivatives of the strain-energy function, $\frac{\partial W}{\partial \bar{I}_1}$ and $\frac{\partial W}{\partial J}$.

5. Compute corotational stresses, $\hat{\boldsymbol{\sigma}}_{co} = \frac{2}{J}\left(\frac{\partial W}{\partial \bar{I}_1}\right)\left(\overline{\mathbf{B}}^* - \frac{1}{3}\text{tr}(\overline{\mathbf{B}}^*)\mathbf{I}\right) + \frac{\partial W}{\partial J}\mathbf{I}$.

6. Compute the internal energy density, for instance with direct application of the SEF.

As a mathematical shortcut, the strain tensor $\mathbf{B}^*$ has been defined to remove rotations from the left Cauchy-Green strain tensor of Eq. 2.37, and a slightly altered version of Eq. Q.4 is used. The corotational stresses computed in the fifth step are identical to those from Eq. Q.4.

When a model uses more than one finite-element, Abaqus may process multiple material points during a VUMAT call. These are stored in an Abaqus-defined parameter, nblock, that increases the dimension of the stress, stretch, and strain increment vectors.

Explicit analyses require calculation of a stable time increment to advance the solution. The increment is initialised with a linearly elastic approximation for the material during the first call of the VUMAT. This is completed by using Abaqus-defined strain increments ($d\varepsilon_i$), the initial stress vector ($\sigma_i'$), and elastic material parameters ($G, \kappa$) to calculate the new stress vector ($\sigma_i''$) as shown in the following logic:

```
IF (totalTime = 0) THEN
   DO k = 1, nblock
```

$$\sigma_{k,1}'' = \sigma_{k,1}' + 2G(d\varepsilon_{k,1}) + \left(\kappa - \frac{2}{3}G\right)\left(\varepsilon_{k,1} + \varepsilon_{k,2} + \varepsilon_{k,3}\right)$$

$$\sigma_{k,2}'' = \sigma_{k,2}' + 2G(d\varepsilon_{k,2}) + \left(\kappa - \frac{2}{3}G\right)\left(\varepsilon_{k,1} + \varepsilon_{k,2} + \varepsilon_{k,3}\right)$$

$$\sigma_{k,3}'' = \sigma_{k,3}' + 2G(d\varepsilon_{k,3}) + \left(\kappa - \frac{2}{3}G\right)\left(\varepsilon_{k,1} + \varepsilon_{k,2} + \varepsilon_{k,3}\right)$$

$$\sigma_{k,4}'' = \sigma_{k,4}' + 2G(d\varepsilon_{k,4})$$

$$\sigma_{k,5}'' = \sigma_{k,5}' + 2G(d\varepsilon_{k,5})$$

$$\sigma_{k,6}'' = \sigma_{k,6}' + 2G(d\varepsilon_{k,6})$$

```
   END DO
   RETURN
END IF
```

Next, the hyperelastic block of the code executes with the six steps previously outlined in this section. In some cases, the linear elastic step does not sufficiently deform elements and stress indeterminacy occurs in the hyperelastic coding block due to numerical precision or truncation. To avoid this, the following logic can be applied:

```
IF ((Ī₁ − 3) < 10⁻¹²) THEN
```
$$\frac{\partial W}{\partial \bar{I}_1} = 0$$
```
ELSE
```
$$\frac{\partial W}{\partial \bar{I}_1} = mK_1(\bar{I}_1 - 3)^{m-1} + pK_2(\bar{I}_1 - 3)^{p-1} + qK_3(\bar{I}_1 - 3)^{q-1}$$
```
END IF
```

The user must set the threshold at which $\partial W / \partial \bar{I}_1 = 0$. Larger values help convergence but introduce larger rounding error. Smaller values do the opposite.

Parameters for the hyperelastic material model can be directly specified in the subroutine, read from the input file, or read from Abaqus' .cae file. If this latter option is preferred, the material properties must be specified as shown in Fig. Q.1.
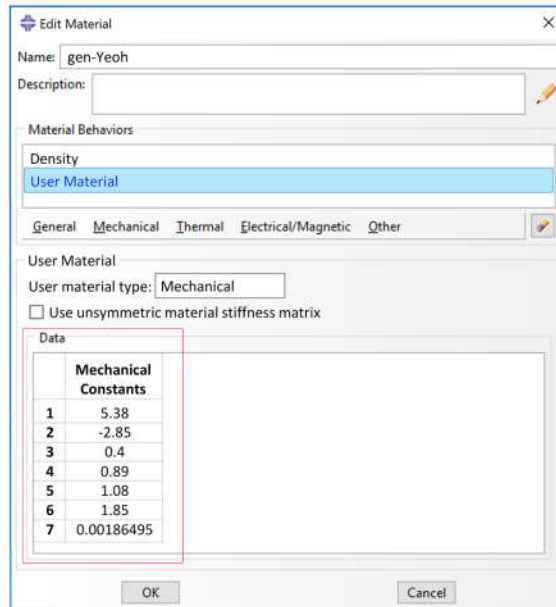


**Fig. Q.1:** Material parameters read by `props(n)` variable in a VUMAT.

222

The material properties are then read with the following statements in the subroutine:

```
C      MATERIAL PROPERTIES
C      -------------------
       k1 = props(1)
       k2 = props(2)
       k3 = props(3)
       em = props(4)
       pe = props(5)
       qu = props(6)
       d1 = props(7)
```

When updating the internal energy density, the strain-energy function can be directly applied. Alternatively, the following equation adopted from Abaqus documentation correctly increments the energy:

$$W = \frac{1}{2}\{(\sigma'_{k,1} + \sigma''_{k,1})d\varepsilon_{k,1} + (\sigma'_{k,2} + \sigma''_{k,2})d\varepsilon_{k,2} + (\sigma'_{k,3} + \sigma''_{k,3})d\varepsilon_{k,3} + 2[(\sigma'_{k,4} + \sigma''_{k,4})d\varepsilon_{k,4} + (\sigma'_{k,5} + \sigma''_{k,5})d\varepsilon_{k,5} + (\sigma'_{k,6} + \sigma''_{k,6})d\varepsilon_{k,6}]\}$$

Finally, plane strain and axisymmetric versions of the code can be built by removing any references to the fifth and sixth elements of the stress, stretch, and strain increment vectors. Alternatively, one can follow Bergström's example[97] and implement logic to handle 2D and 3D cases with a single subroutine. A plane stress subroutine requires additional modification to account for out-of-plane strains.

# Appendix R: More Illustrations of Seal Deformations[‡‡‡]

This appendix illustrates seal deformations as pressure increases. Figs. R.1–R.6 show a simulation that was completed in Abaqus/Standard. Nodes at a sealing front (see Fig. 3.11) had fluid pressures manually removed or added to them as their contact status changed. The captions provide more details.
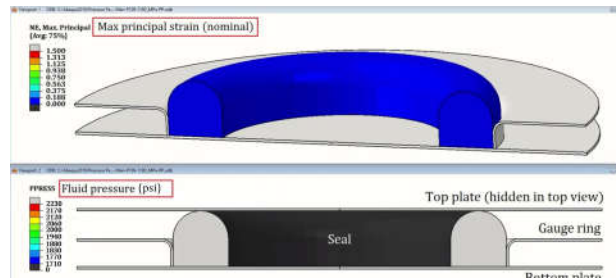


**Fig. R.1:** A seal in isometric view with the top plate removed and strain contours (top) and in section view with the top plate shown and fluid pressure contours (bottom). Gauge ring height is 6.35 mm. $P_f = 0$ MPa.
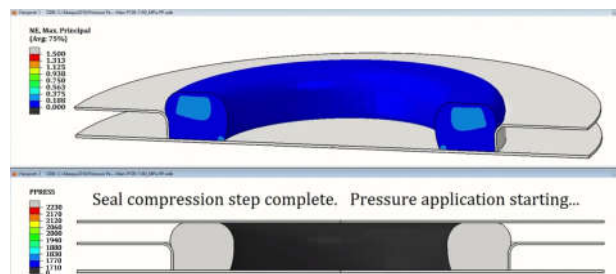


**Fig. R.2:** The seal immediately after compression. $P_f = 0$ MPa.
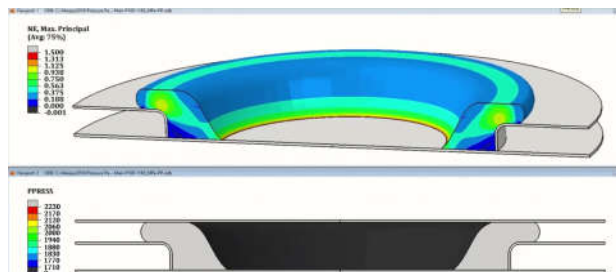


**Fig. R.3:** The seal with $P_f < 11$ MPa.
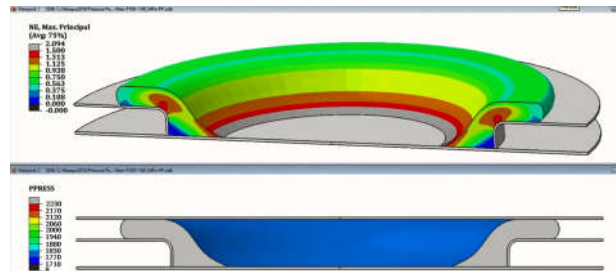


**Fig. R.4:** The seal with $P_f = 12$ MPa.

---

[‡‡‡] The images in this section are taken from the following videos, available online as of October 2022:
https://www.youtube.com/watch?v=SsQt0vBJn2U
https://www.youtube.com/watch?v=qp1fB17OhsE
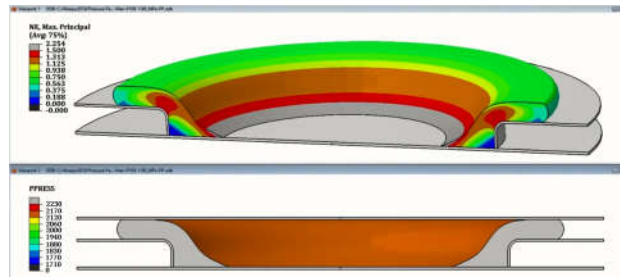
**Fig. R.5:** The seal with $P_f = 14.8$ MPa.



The solution does not converge beyond this point.
The final pressure is 15.08 MPa.
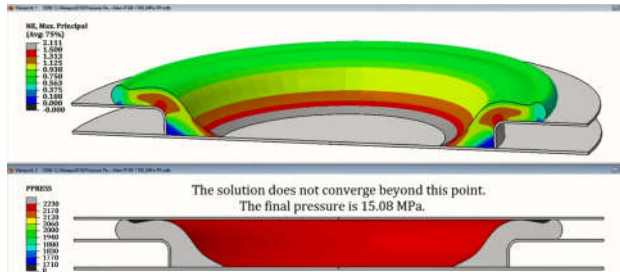
**Fig. R.6:** The seal at its last converged step and $P_f = 15.08$ MPa, a point at which leak is imminent.

Figs. R.7–R.13 show images from a video in Abaqus/Explicit. The VDLOAD subroutine from Appendix J was used to propagate fluid pressure. Elastic instabilities are observed over two different ranges of pressure.
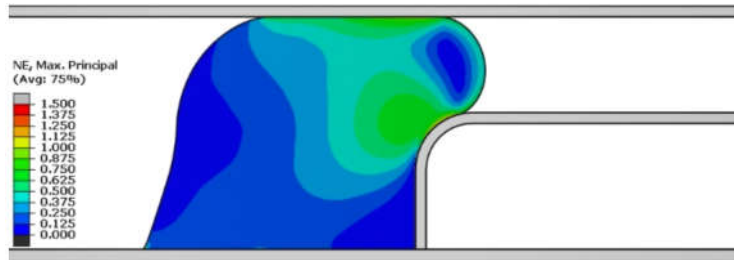


**Fig. R.7:** The seal with $P_f = 6.20$ MPa. Strain contours are smooth.
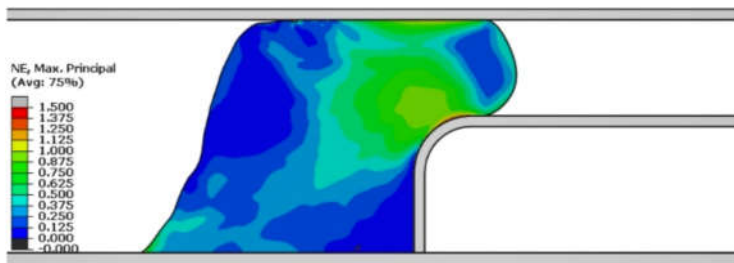


**Fig. R.8:** The seal with $P_f = 8.25$ MPa. Elastic waves due to an instability significantly disrupt the strain contours.
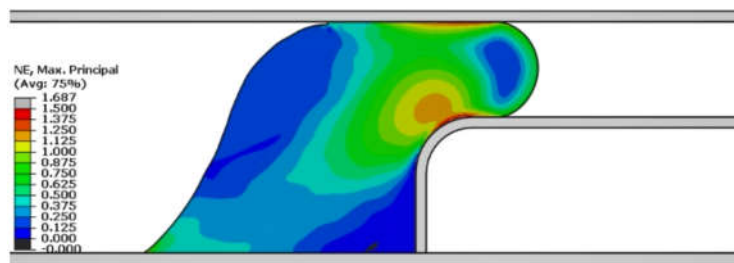


**Fig. R.9:** The seal with $P_f = 12.07$ MPa. The instability has largely vanished due to viscous dissipation that is present in the Abaqus/Explicit solver.
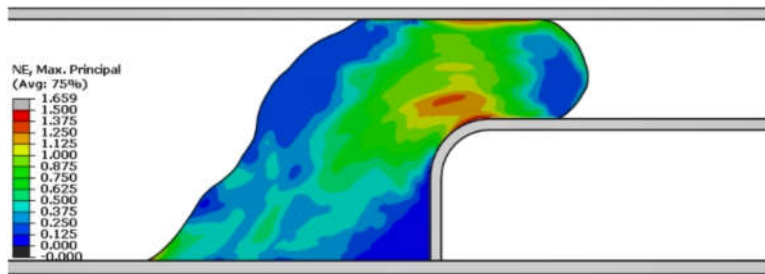
225

**Fig. R.10:** The seal with $P_f = 12.28$ MPa. Another elastic instability is encountered.
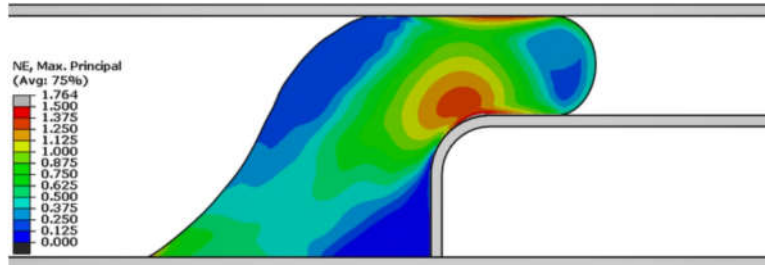


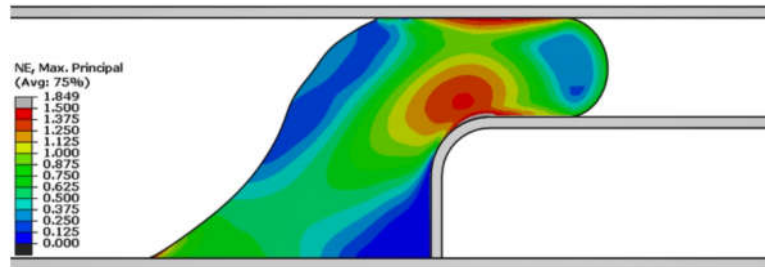**Fig. R.11:** The seal with $P_f = 14.60$ MPa. Again the instability has dissipated.



**Fig. R.12:** The seal with $P_f = 18.85$ MPa. The sealing front is largely stable at this point, but the fluid pressure is close to the leak pressure.
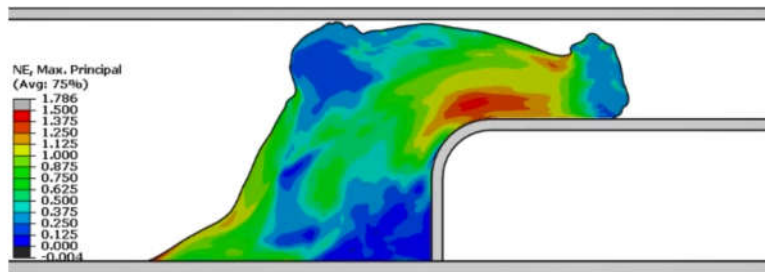


**Fig. R.13:** The seal with $P_f = 19.20$ MPa. The fluid pressure has completely bypassed the seal.